MALDI and SIMS Microscope Mode Imaging Mass Spectrometry

Natasha Smith

Worcester College
University of Oxford

A thesis submitted for the degree of Doctor of Philosophy

Michaelmas 2023

Abstract

Mass spectrometry imaging (MSI) is a powerful tool, mapping the spatial distribution of molecules with micron or sub-micron resolutions using their molecular mass. Microscope MSI is a great technique with a high throughput, but is used less commonly than microprobe MSI as it achieves lower mass and spatial resolution. This thesis presents methods for improving the mass and spatial resolution with a microscope MSI instrument, as well as expanding the imaging field of view. A new microscope MSI instrument is also presented, utilising secondary ion mass spectrometry (SIMS).

Using a reflectron ToF mass spectrometer, by generating a stronger field, the spatial resolution can be increased from 13 ± 1 μm o 8 ± 1 μm experimentally, and could potentially reach <7 μm according to simulations. Variable magnification has been explored in simulation, and the application of an additional einzel lens proved capable of changing the magnification from $\times 92$ to $\times 20$, which can expand the field of view from 270 μm to 1242 μm. This can increase the scope of the instrument by acquiring larger images first, with a <50 μm spatial resolution and $\sim$ 2,500 mass resolution, before increasing the magnification on a region of interest and attaining higher resolution data. Such a feature would be very desirable in commercial applications and improve the throughput of the instrument.

Using a Timepix3 camera, the timing precision can be improved by using a more intense trigger, reaching a 4.5 ns full width half maximum (FWHM). Through the use of time-over-threshold data, mass peaks can be reduced from a FWHM of 50 μm to 32 μm, improving the attainable mass resolution with the Timepix3 camera, bringing it closer to the true mass resolution of the instrument.

A SIMS ToF mass spectrometer has been presented, taking a similar design to the reflectron ToF instrument. Work was done to characterise this instrument in order for it to be used in tandem with the reflectron ToF mass spectrometer.

MALDI and SIMS Microscope Mode Imaging Mass Spectrometry



Natasha Smith

Worcester College

University of Oxford

A thesis submitted for the degree of

Doctor of Philosophy

Michaelmas 2023

Acknowledgements

Firstly I would like to thank Professor Mark Brouard. I am incredibly grateful to have had this experience, and for all of the mentoring and help offered. Without his insight, this thesis would not have been possible. A very big thank you to the National Physical Laboratory for funding my iCASE award, and Professor Josephine Bunch and Dr Rory Steven, for supporting this endeavour and always offering support when needed.

I owe a debt of gratitude to many members of the Brouard group, including Dr Michael Burt, who spent a great deal of time answering my many questions at the start of my DPhil. His attention to detail and ability to explain concepts incredibly clearly awes me. Dr James Pickering, for the many hours spent helping me move the reflectron ToF instrument, and for helping me fix it each time it stopped working. Your knowledge about lasers was a huge help, and I'm glad you've succeeded and moved towards bigger and better things. To Dr Robert Burleigh, for guiding me when I was new to the group, and spending so much time training me on how to use the instrument. Dr Felicia Green, who inspires me as a woman in STEM. Dr Elena Castellani and Yifeng Jia, best of luck with the work going forwards!

I would like to thank the PTCL electronics team, and in particular Phil, who spent far too much time visiting the reflectron Instrument every time something broke. The CRL facilities team, you were all invaluable when the entire instrument had to be relocated, thank you for being so generous with your time!

To the many fantastic people in Oxford who have helped me get through the past two years, and especially the process of writing this thesis. Liam, for answering my numerous coding questions and helping me every time I got stuck, and Jimmy for being the most emotionally intelligent person I know, always knowing what to say. It was a far brighter experience being able to go through undergrad together. The many friends I have made during this DPhil: Helen, Camilla, Jack, Q, Tom, your friendship has made this a far richer experience. The Worcester College porters, "Mama Max", Dylan, Chris, and Roger, for the countless hours aiding my procrastination in the lodge. An extra special thank you to Mifforc, for proofreading my entire thesis and sending me far too many kind messages of support. I feel privileged to know you. Ty, for sharing your wisdom and reminding me that setbacks aren't the end of the world. Max, for always being the calm in the storm, and being slightly absurd in the best way. Finally, my parents, who have absolutely no idea what it is that I do, but support me with every thing I have ever set my mind to.

Abstract

Mass spectrometry imaging (MSI) is a powerful tool, mapping the spatial distribution of molecules with micron or sub-micron resolutions using their molecular mass. Microscope MSI is a great technique with a high throughput, but is used less commonly than microprobe MSI as it achieves lower mass and spatial resolution. This thesis presents methods for improving the mass and spatial resolution with a microscope MSI instrument, as well as expanding the imaging field of view. A new microscope MSI instrument is also presented, utilising secondary ion mass spectrometry (SIMS).

Using a reflectron ToF mass spectrometer, by generating a stronger field, the spatial resolution can be increased from 13 $\pm$ 1 μm o 8 $\pm$ 1 μm experimentally, and could potentially reach <7 μm according to simulations. Variable magnification has been explored in simulation, and the application of an additional einzel lens proved capable of changing the magnification from $\times$92 to $\times$20, which can expand the field of view from 270 μm to 1242 μm. This can increase the scope of the instrument by acquiring larger images first, with a <50 μm spatial resolution and $\sim$ 2,500 mass resolution, before increasing the magnification on a region of interest and attaining higher resolution data. Such a feature would be very desirable in commercial applications and improve the throughput of the instrument.

Using a Timepix3 camera, the timing precision can be improved by using a more intense trigger, reaching a 4.5 ns full width half maximum (FWHM). Through the use of time-over-threshold data, mass peaks can be reduced from a FWHM of 50 μm to 32 μm, improving the attainable mass resolution with the Timepix3 camera, bringing it closer to the true mass resolution of the instrument.

A SIMS ToF mass spectrometer has been presented, taking a similar design to the reflectron ToF instrument. Work was done to characterise this instrument in order for it to be used in tandem with the reflectron ToF mass spectrometer.

Contents

List of Abbreviations **xi**

1 Introduction **1**
- 1.1 Short history of mass spectrometry . . . 2
- 1.2 Time-of-flight MS . . . 6
- 1.3 Ionisation sources . . . 11
  - 1.3.1 LDI . . . 14
  - 1.3.2 MALDI . . . 15
  - 1.3.3 SIMS . . . 19
- 1.4 Ion Imaging . . . 20
- 1.5 Ion Detection . . . 30
- 1.6 Summary . . . 33

2 Experimental Methods **35**
- 2.1 Reflectron ToF Mass Spectrometer . . . 36
  - 2.1.1 Ion Optics . . . 37
  - 2.1.2 Laser . . . 40
  - 2.1.3 Triggering . . . 43
- 2.2 SIMS MSI . . . 44
  - 2.2.1 Preparation Chamber and Sample Plate . . . 47
  - 2.2.2 Ion Optics . . . 47
  - 2.2.3 C_{60}^{+} ion gun . . . 50
- 2.3 Sample preparation . . . 52
  - 2.3.1 Electrosprayer . . . 52
  - 2.3.2 Dried droplet . . . 56
- 2.4 Detector assembly . . . 56
  - 2.4.1 Microchannel plates . . . 58
  - 2.4.2 Scintillator screen . . . 59
  - 2.4.3 Photomultiplier Tube . . . 61
- 2.5 Cameras . . . 63
  - 2.5.1 CCD . . . 63
  - 2.5.2 Timepix3 camera . . . 65

2.5.3 Image processing . . . 67
2.6 m/z calibration . . . 68
2.7 Summary . . . 71

3 Characterisation of a Reflectron Ion Microscope 73
3.1 SIMION . . . 75
3.1.1 Potential Arrays . . . 75
3.1.2 Defining Ions . . . 77
3.1.3 Workbench . . . 80
3.1.4 LUA . . . 81
3.1.5 Output Results . . . 81
3.1.6 Genetic Algorithm . . . 84
3.2 Improving the Spatial Resolution . . . 85
3.2.1 Theory . . . 86
3.2.2 Simulations . . . 87
3.2.3 Experimental Results . . . 89
3.3 Zoom lens . . . 92
3.3.1 Reflectron lens . . . 93
3.3.2 Additional einzel lens . . . 101
3.3.3 Using the existing einzel lens as a zoom lens . . . 113
3.4 Conclusion . . . 118

4 Improving Time Precision with a Timepix3 Camera 121
4.1 Timepix3 Camera and Data Processing . . . 122
4.1.1 Timepix3 Camera . . . 123
4.1.2 Methods . . . 125
4.1.3 Data Processing . . . 126
4.2 Experimental Verification . . . 130
4.2.1 Experimental jitter . . . 131
4.2.2 Laser intensity . . . 134
4.2.3 LED . . . 139
4.2.4 Effects on Mass Spectra . . . 146
4.3 Conclusion . . . 150

5 Comparing the reflectron instrument with the SIMS instrument 153
5.1 Ionisation method . . . 154
5.1.1 Nd:YAG Laser Beam . . . 154
5.1.2 C_{60}^{+} Ion Beam . . . 159
5.2 Mass Spectra . . . 172
5.3 Mass resolution . . . 179
5.4 Spatial resolution . . . 180
5.5 Conclusion . . . 184

6 Conclusions and Future Work **187**

References **191**

List of Abbreviations

CCD . . . . . Charge Coupling Device

CMOS . . . . . Complementary Metal Oxide Sensor

FWHM . . . . Full Width Half Maximum

ITO . . . . . Indium Titanium Oxide

LDI . . . . . Laser Desorption ionisation

MALDI . . . . Matrix Assisted Laser Desorption Ionisation

MCP . . . . . Microchannel Plate

MSI . . . . . Mass Spectrometry Imaging

m/z . . . . . mass to charge ratio

$m/\Delta m$ . . . . . Mass resolution

PEDA . . . . . Post Extraction Differential Acceleration

PImMS . . . . Pixel Imaging Mass Spectrometry

PMT . . . . . Photomultiplier Tube

SIMS . . . . . Secondary Ion Mass Spectrometry

1 Introduction

Contents

1.1 Short history of mass spectrometry 2
1.2 Time-of-flight MS 6
1.3 Ionisation sources 11
1.3.1 LDI 14
1.3.2 MALDI 15
1.3.3 SIMS 19
1.4 Ion Imaging 20
1.5 Ion Detection 30
1.6 Summary 33

Mass Spectrometry (MS) is an analytical technique, determining the mass-to-charge ratio, m/z, of ions, as well as their intensity. By converting neutral molecules to gas-phase ions and fragments and separating them using their m/z, typically using their time-of-flight (ToF), the structure of complex molecules can be explored, aiding in the identification of unknown substances. Imaging Mass Spectrometry (MSI) pairs MS with a spatial component, providing positional information while maintaining chemical specificity. The information provided can provide the spatial distribution of molecules, such as biomarkers, metabolites, and peptides, giving the locations for particular m/z ions [1].

There are two main techniques used for MSI: microprobe-mode, and microscope-

mode. The former utilises a focused ionisation source, generating ions over a small region on the sample surface, while the latter uses a defocused ionisation source, ablating a large surface area and generating ions as a plane. The differences between the two methods will be explored in more detail in Section 1.4.

This thesis develops and characterises two ion microscope instruments, beginning with a detailed description of each mass spectrometer in Chapter 2. An exploration of the capabilities of a reflectron ToF mass spectrometer is conducted, investigating the spatial resolution limits and the capabilities of variable magnification. This is followed by use of a fast time stamping camera, the Timepix3 camera, researching the time precision when paired with the reflectron ToF instrument. Finally, a comparison of two different ionisation methods is performed, contrasting the reflectron ToF instrument against a secondary ion mass spectrometry (SIMS).

This chapter will introduce the history of mass spectrometry, followed by a discussion on time-of-flight MS, the types of ionisation sources commonly used, ion imaging methods, and means for ion detection.

1.1 Short history of mass spectrometry

The field of mass spectrometry began in the mid nineteenth century with Julius Plücker. Using vacuum tubes and an electromagnet, Plücker found that electrical discharge in rarefied gases causes a fluorescent glow to form - this glow was later determined to be produced by cathode rays [2]. This glow could be shifted with the electromagnet, suggesting that these cathode rays are electrically charged, and the direction of the deflection indicated that they are likely negatively charged.

In 1866, Eugen Goldstein also observed canal rays, by applying a high voltage across a discharge tube with a perforated cathode [3, 4]. Passing a current through them would produce a faint luminous ray originating from the holes in the cathode. The ionised gas includes positive ions - it is the positively charged ions which generate the canal ray. The canal rays in an electric and magnetic field behaved in the opposite way to the cathode rays, indicating the positive charge. A schematic of a canal ray ion source is show in Figure 1.1.

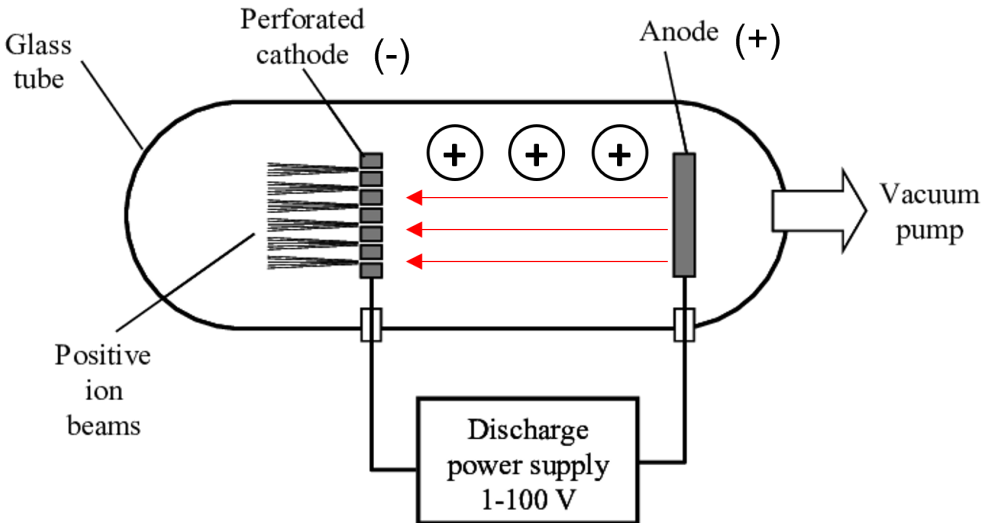


Figure 1.1: Schematic of a canal ray tube, adapted from ref. [5].

J. J. Thomson won the race to determine the nature of cathode rays, proving they were negatively charged particles, later named electrons [6]. Thomson created the "parabola ion spectrograph", which became known as the first mass spectrometer [7, 8]. A stream of ionised neon were channelled through a magnetic and an electric field. This stream experienced a deflection, which was measured with a photographic plate located in the beam path. As a result, a mass spectrum is formed, consisting of a series of parabolas, indicating different parabolas of deflection. Each parabola corresponds to a single m/z, the kinetic energy for each determining its position along the parabola. Thomson concluded that neon must be composed of two atoms, discovering isotopes neon-20 and neon-22 in 1913, as depicted in Figure 1.2 [8]. For his work on the conduction of electricity in gases, Thompson was awarded the 1906 Nobel Prize in Physics .

From this work, a student of Thomson's, Francis Aston, built the first mass spectrometer at Cambridge in 1919 [9, 10]. Returning to the Cavendish Laboratory after World War I, Aston built an instrument similar to Thomson's parabola apparatus, however this new device applied parallel magnetic and electric fields in different regions of the flight tube. This caused particles of the same m/z ratio, but different velocities, to be focused on the same point on the screen, producing a more intense beam. With the introduction of a series of slits to filter ions of different

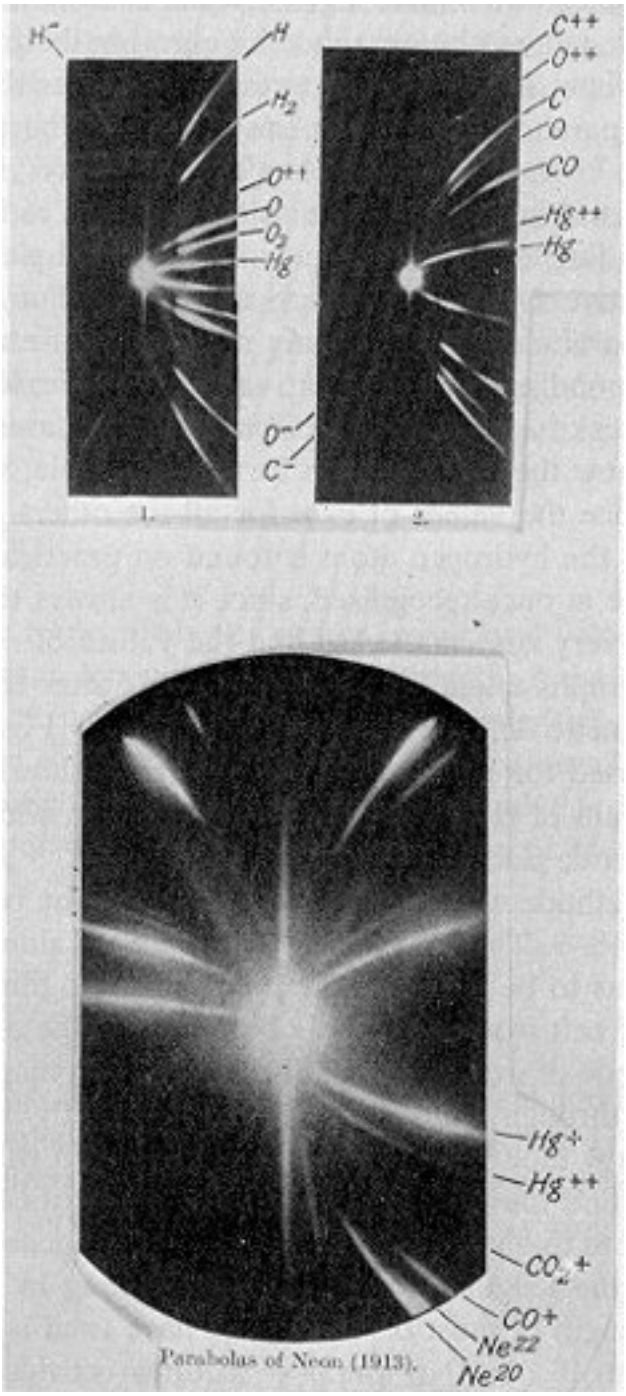


Figure 1.2: Photographic plate from the 1913 experiment performed by Thomson, adapted from ref. [8].

velocity and energy, an improved mass resolution and accuracy could be achieved. Aston identified isotopes of chlorine (35 and 37 Da), bromine (79 and 81 Da), and krypton (78, 80, 82, 83, 84, and 86 Da). For this significant contribution to the field, he was awarded the Nobel Prize in Chemistry in 1922.

The field shifted from physics to analytical chemistry in the 1940's, with the work of Alfred Nier [11]. Having designed and built several instruments, Nier revolutionised the field and made it more useful to the scientific community. His most notable achievement was his use of a mass spectrometer to separate the two isotopes ^{238}U and ^{235}U - one of which was known to undergo slow neutron fission, but scientists were unsure which one [12]. This proved to be a significant contribution to U enrichment efforts during World War II.

The next phase in the development of the field was to expand the scope of mass spectrometry. McLafferty, Biemann, and Djerassi lead the way, piecing together fragmentation mechanisms of different classes of organic molecules [13–17]. Prior to this, only molecules of known identity and structure could be tested, MS being used as a quantitative tool for measuring concentration. The three chemists changed the field of MS, enabling the use of the technique for structure determination of unknown molecules.

The applications of MS expanded further with the development of gas chromatography mass spectrometry (GC-MS) in the 1950s [18, 19]. Based on their interaction with the coating on a capillary column, mixtures of molecules could be separated with a gas chromatogram. From this, these chemicals could be quantified and identified with MS. Applications include drug detection, environmental analysis, investigation of explosives, and the identification of unknown samples. In 1955, developments with the time-of-flight mass spectrometer (ToF-MS) [20] grew, followed by Fourier-transform ion cyclotron resonance MS (FTICR) [21] in 1974, further expanding the technique and its applications.

By the 1980s, MS was a routine analysis technique for small organic molecules, large molecules such as proteins had yet to conquered. Existing techniques relied on gas-phase collisions between the analyte, all of which resulted in significant

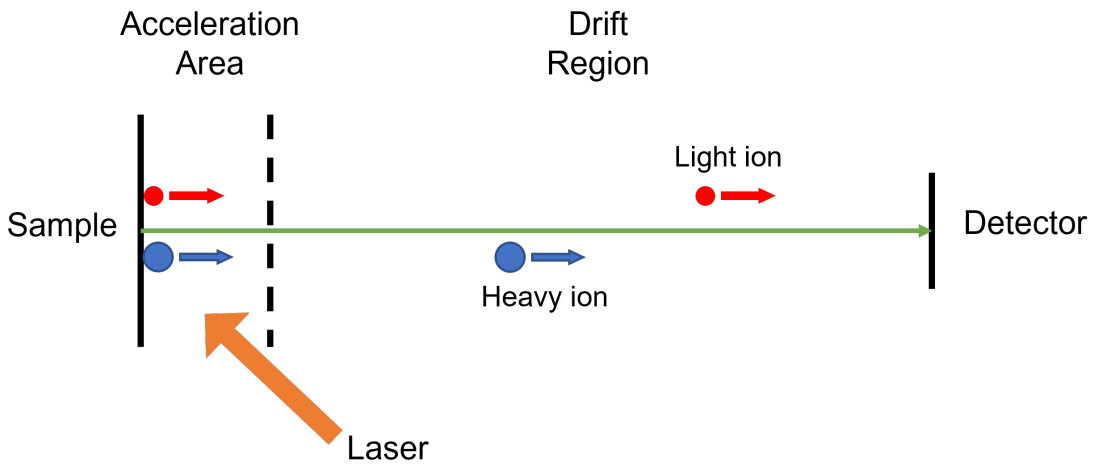


Figure 1.3: Diagram of the principle of ToF-MS. A light ion travels faster than a heavier ion, reaching the detector earlier.

fragmentation when applied to large molecules. From this problem, Electrospray Ionisation (ESI) and Matrix Assisted Laser Desorption Ionisation (MALDI) were born in 1988 [22–25]. Both of these techniques will be discussed in more detail later in this chapter. Each of these techniques has its advantages and disadvantages, however they are the still the favourite choice for ionising proteins and peptides.

1.2 Time-of-flight MS

The mass analyser used in the work described in this thesis will focus on time-of-flight. ToF-MS involves separating ions according to mass-to-charge ratio based on the time taken for an ion to travel to a detector. By applying an electric field, ions can be accelerated along a field free flight path. This method supplies the ions with the same amount of kinetic energy for a given charge. The ions will then continue along a field-free flight tube of known length, typically 1-2 m, until impacting upon a detector. During the field-free flight, heavier ions will travel at a lower velocity compared to lighter ions, hence will arrive at the detector later. Thus the time taken to reach the detector serves as a measure of the velocity, and hence the mass-to-charge ratio [26]. This is depicted in Figure 1.3.

An ion with mass m, has a charge $q = ze$ where q is the total charge, z the charge number, and e the electronic charge [27]. The ion is then accelerated using an

electric field, experiencing a potential V_s. Hence the ion electric potential energy, E_p, is $E_p = zeV_s$. Given that kinetic energy of the ion, E_k is given by $E_k = (1/2)mv^2$, where v is the ion velocity, and the potential energy at the exit of the acceleration region is converted to kinetic energy, the following can be shown:

$$E_p = E_k \tag{1.1}$$

$$zeV_s = \frac{1}{2}mv^2. \tag{1.2}$$

This can then be rearranged to determine the velocity of the ion,

$$v = \sqrt{\frac{2zeV_s}{m}}. \tag{1.3}$$

The ion travels at a constant velocity in the field-free region, thus the length of the drift path, L can be used to determine the flight time, t, of the ion:

$$v = \frac{L}{t} \Rightarrow t = \frac{L}{v}. \tag{1.4}$$

Substituting Equation 1.3 into Equation 1.4, gives the following equation, describing time in a ToF analyser:

$$t = \sqrt{\left(\frac{m}{z}\right)\left(\frac{L^2}{2eV_s}\right)}. \tag{1.5}$$

Rearrangement supplies an expression for m/z

$$\frac{m}{z} = \left(\frac{2eV_s}{L^2}\right)t^2. \tag{1.6}$$

Equation 1.6 proves the relationship between m/z and t can be described with:

$$t = k\sqrt{\frac{m}{z}}, \tag{1.7}$$

where k is a proportionality constant. For a particular ion acceleration (dependent on instrument settings and field strength), this relationship allows for the mass-to-charge ratio to be determined from the time-of-flight. In practice, this is done by collecting a spectrum of ion current signal (from the detector) against arrival time

at the detector. m/z can be extracted through the use of a calibration function, as detailed in Section 2.6. Additionally, Equation 2.6 demonstrates there is no upper m/z limit, although physical constraints will introduce other problems. The physical size of the instrument, collisions of ions with other gas molecules, and angular dispersion of the ion beam, impose an upper limit of around 300 kDa for a linear ToF instrument [28].

Ion mass resolution for a mass spectrometer can be described by differentiating Equation 1.6 with respect to m and t:

$$\frac{1}{z}dm = \left(\frac{2eV_s}{L^2}\right) 2tdt. \tag{1.8}$$

By rearranging Equations 1.6 and 1.8, different m/z can be resolved

$$\frac{m}{dm} = \frac{t}{2dt}. \tag{1.9}$$

Hence, the mass resolution, R, for a ToF mass spectrometer, can be expressed by

$$R = \frac{m}{\Delta m} = \frac{t}{2\Delta t}, \tag{1.10}$$

where m and t refer to the ion mass and time-of-flight respectively, and Δm and Δt are the mass and ToF peak width at half the maximum.

Δt describes the flight time spread of the ions, which can be caused by a variety of factors. The most significant factor is the distribution of initial kinetic energies from the ionisation method. In the case of a laser pulse with a typical Gaussian profile, different areas will receive different amounts of energy. This creates a distribution of arrival times for a given m/z. Additionally, the detector response time can play a factor, but the impact is small in comparison to the ionisation method. If the sample surface is inhomogenous, the ions generated will have different starting locations - a small difference but enough to create a distribution in arrival times for the same m/z, although there will likely be a difference in kinetic energy in such a case. Other factors include different starting times, resulting in ions arriving at the detector at different times even with the same kinetic energy, and

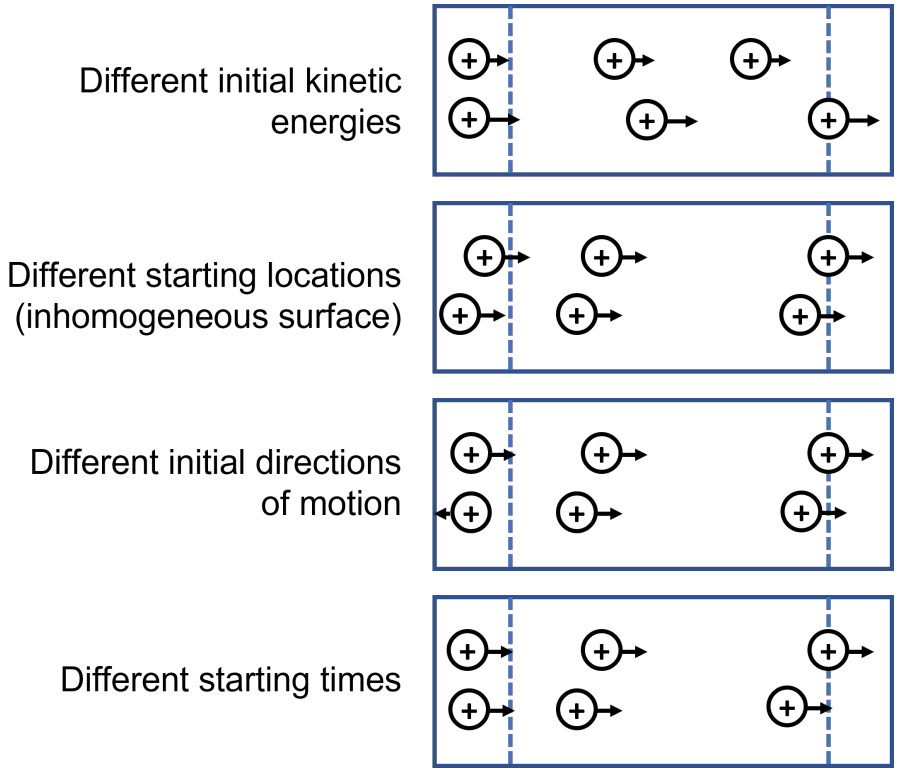


Figure 1.4: Factors affecting mass resolution in a linear ToF mass analyser. Ions are represented as circles, with an arrow indicating the size and direction of each ions' kinetic energy. Adapted from ref. [29]

different initial directions of motion, effectively changing the flight path length. These factors have been depicted in Figure 1.4.

In addition to the factors affecting Δt, the mass resolution for an instrument can be affected by the flight time, t. Such factors include the length of the ionising pulse, the space distribution of the ions, kinetic energy distribution, space charge effects, power supply stability, and mechanical precision of the instrument [30]. A greater t, by increasing the flight path L or decreasing the ion velocity, could improve the mass resolution. From the inception of MS, mass resolution has improved from 13 $m/\Delta m$ with Thomspon in 1913 [31], to 2,000 $m/\Delta m$ with Aston and the mass spectrograph in 1937 [32], to 8,000,000 $m/\Delta m$ using FTICR in 1998 [33].

One method of improving the mass resolution in ToF-MS is using a reflectron. First proposed by Alikhanov, a reflectron acts as an ion mirror, reflecting ions using a constant electric field, returning the ions back towards the detector [34]. The

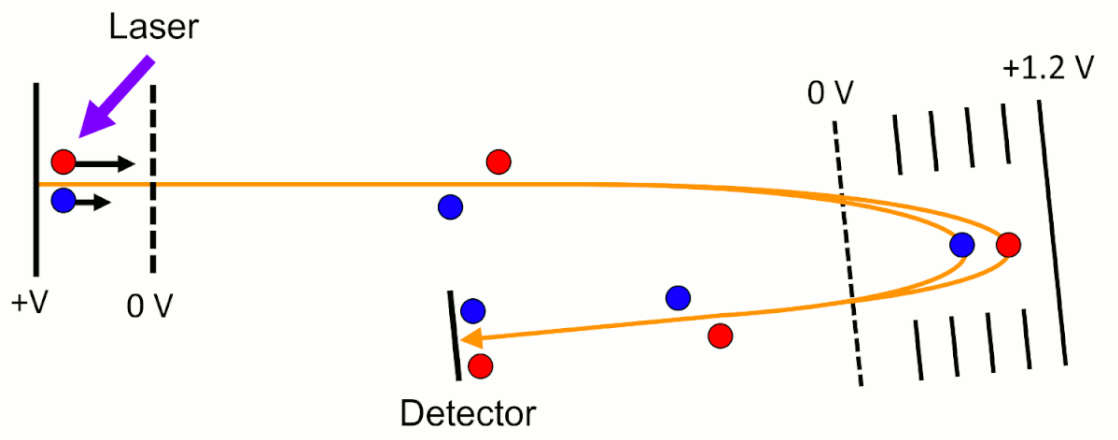


Figure 1.5: Schematic of a reflectron. Two ions of the same mass and charge but differing kinetic energies are accelerated towards a reflectron, which reflects the ions towards the detector. The higher energy ion (red) penetrates deeper into the reflectron. The detector is located at the focal point of the ions. Reprinted from [36].

simplest type of reflectron consists of a series of equally spaced grid electrodes or ring electrodes connected through a chain of resistors.

This helps to correct the kinetic energy distribution of the ions [35]. An ion of a given m/z with a high kinetic energy, and hence a greater velocity, will penetrate more deeply into the reflectron compared with an ion of lower kinetic energy (see Figure 1.5). The faster ions will spend more time in the reflectron and will reach the detector at the same time as slower ions with the same m/z. The reflectron field can be tuned such that the ions are temporally focused at the detector, minimising Δt, and thus increasing the mass resolution.

The reflectron exists in a number of variations, the simplest being single-stage, with a single electric field region (linear or non-linear). Single-stage reflectrons minimise the first derivative of time-of-flight with respect to ion energy, thus providing first order energy focusing. Meanwhile, a dual-stage reflectron, with two regions of different fields, features a high and low-field region. With this, it is possible to achieve both first and second order temporal focusing. Dual-stage reflectrons can hence compensate for larger variations in kinetic energy compared to single-stage reflectrons, causing ions to decelerate rapidly upon entrance to the first stage of the reflectron, losing approximately $2/3^{rds}$ of the ions kinetic energy here [37]. The second stage (low-field) is then responsible for repelling the ions

back. A dual-stage reflectron is more compact than a single-stage, however, it suffers from a lower transmission.

An additional benefit of a reflectron is owed to the extended flight path. The flight path is increased by twice the distance for a given length of ToF instrument, further aiding in the improved mass resolution. However this positive effect on the resolution is of less significance when compared to the initial kinetic energy correction.

While mass resolution is the primary metric for a mass spectrometer, mass accuracy must also be considered. Mass accuracy, A, describes the proximity of the experimental m/z measurement, γ, to the true m/z value, β, and is given by:

$$A = \frac{\gamma - \beta}{\beta} 10^6 \tag{1.11}$$

and is measured in parts per million (ppm). This effectively quantifies how close the experimentally determined value is to the true value. A high mass accuracy, paired with high precision, reduces the number of possible molecular formula which could be considered for an ion. The degree of accuracy required is relative to the m/z; with increasing m/z, the number of formulae which could fit a particular measured mass, increases, such that it becomes impossible to determine the molecular ion composition. The extent of this is illustrated in Figure 1.6. A mass spectrometer should have both high mass accuracy, and high mass resolution, allowing for accurate peak assignment.

1.3 Ionisation sources

In order for ions to travel the length of a ToF mass spectrometer, the ions must first be generated. There are numerous ways to produce ions, with the main distinction being hard vs soft ionisation, which differ in the amount of energy transferred to the analyte and hence the amount of fragmentation which occurs.

Hard ionisers provide large amounts of energy to the sample, resulting in fragmentation, thus the parent ion, M^+, is unlikely to be produced with a hard ionisation source. Such methods include electron ionisation (EI), and secondary ion mass spectrometry (SIMS) with small primary ions such as Cs^+.

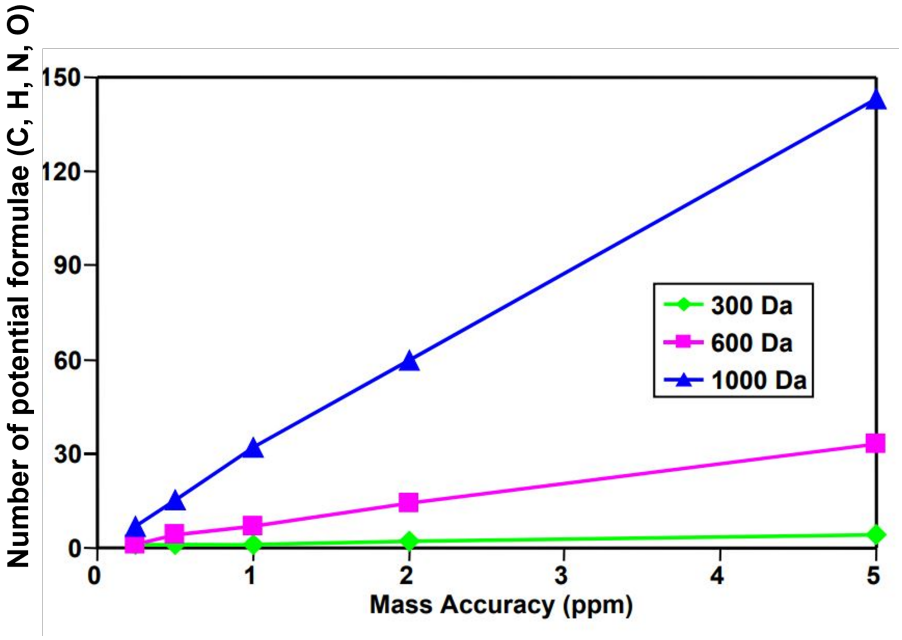


Figure 1.6: The effect of mass accuracy and molecular weight on the number of potential formulae, comprised of C, H, N, and O. Adapted from ref. [38]

On the other hand, soft ionisers produce fewer fragment ions and are more likely to produce the molecular ion. Methods for soft ionisation include laser desorption ionisation (LDI), matrix-assisted laser desorption ionisation (MALDI), SIMS with large primary ions such as C_{60}^{+}, chemical ionisation (CI), field ionisation (FI), atmospheric-pressure chemical ionisation, and electrospray ionisation. The difference in spectra produced by hard vs soft ionisation can be demonstrated in Figure 1.7.

The ionisation source used depends on what the experimental conditions are, and the extent of fragmentation desired. For samples in the gas phase, electron ionisation (a hard ionisation method) is often used. Electron ionisation was first developed by Dempster in 1918 [40], during which electrons released from a heated filament are accelerated towards an anode. The electrons collide with the gaseous analyte molecules, producing positive ions. The electrons produced have significant amounts of energy, the excess energy from the collision results in the analyte ion fragmenting bonds to produce a more stable daughter ion. This method is commonly applied to volatile substances with a low molecular weight [41].

Unlike electron ionisation, chemical ionisation is a soft ionisation method. Some

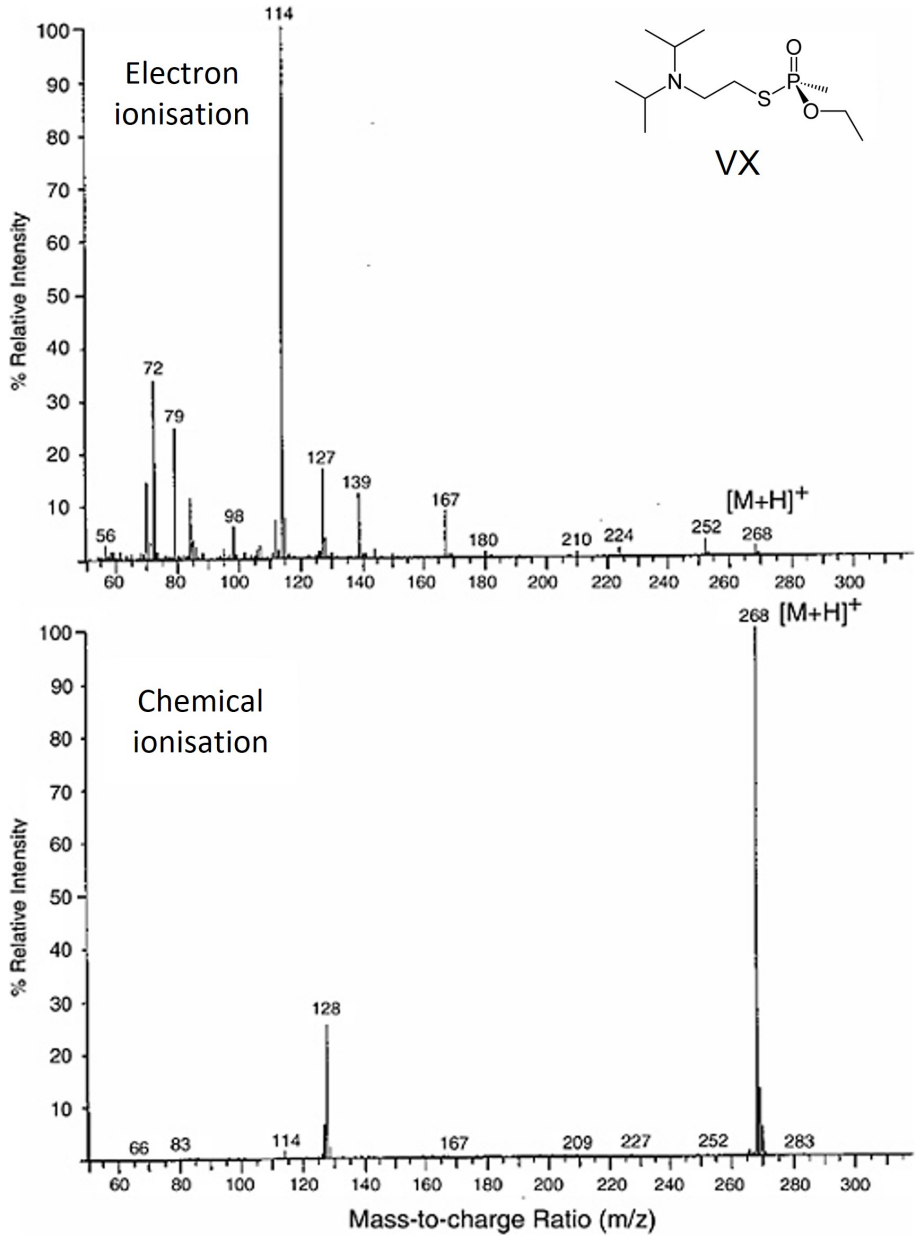


Figure 1.7: The mass spectra obtained for the nerve agent known as VX (structure provided in the top right corner). Performed using a hard ionisation source (top), electron ionisation (EI), and a soft ionisation source (bottom), chemical ionization (CI), with VX in acetonitrile. EI produces more numerous fragmentation peaks, whereas CI has a dominant peak produced by the protonated VX. Adapted from [39]

functional groups (such as alcohols, ethers, amines, amino acids) make molecules more prone to extensive fragmentation. In these cases, chemical ionisation may be preferable, and can act as a complementary technique to electron ionisation. Ions are produced through a collision of the analyte with primary ions present in the source [42]. A carrier gas is introduced to the electron ionisation chamber at a concentration greater than that of the analyte, the carrier gas interacts with the electrons, producing molecular ions, which subsequently react with the analyte to form analyte molecular ions [43]. Such a method is low energy, hence is a soft ionisation source and allows for easy determination of molecular mass.

Not all compounds can be investigated in the gas phase; many are not thermally labile. In order to obtain mass spectra, such compounds require ionisation sources compatible with liquid-phase or solid state analytes. With liquids, the analyte exists in solution, which can be nebulised into a source chamber at atmospheric pressure and ionised. Atmospheric pressure ionisation (API) allows for ionisation of the droplets, after which the ions are transferred into the high vacuum of a mass analyser. Examples of API sources include electrospray (ESI), atmospheric pressure chemical ionisation (APCI), atmospheric pressure photoionisation ionisation (APPI), and desorption electrospray ionisation (DESI) [44].

Solid-state ionisation is utilised for non-volatile deposits, with ions generated by the ablation of the sample using a high-energy source of protons or photons. The generated ions can be extracted using an electric field and travel along a flight path to a detector. Examples of such ionisation methods include laser desorption ionisation (LDI), matrix assisted laser desorption ionisation (MALDI), and secondary ion mass spectrometry (SIMS). In this thesis, LDI, MALDI and SIMS will be discussed; each method will be explored in more detail below.

1.3.1 LDI

Laser desorption ionisation uses a laser pulse with an intensity of $10^6 - 10^{10}$ Wcm^{-2}, focused on a sample surface of $10^{-3} - 10^{-4}$ cm^2, to ionise the analyte [45]. Given its ease of use and efficiency for producing gaseous ions, it is most commonly used

on solid samples. With a solid sample, the laser pulses ablate material from the surface, generating a microplasma of both ions and neutral molecules. The dense vapour produced near the sample surface can result in reactions between the ions and neutral molecules, leading to some fragmentation with heavy mass molecules. The laser serves to both vaporise, and ionise the sample.

LDI is often used to explore the surface of a sample and its local composition. The typical method uses infrared LDI, which generates a thermal spike and removes the need to match the wavelength to the sample, however, it is possible to perform selective ionisation by adjusting the laser wavelength [44]. The mass spectrum produced using this method is dependent on the analyte properties (e.g., photoabsorption, volatility, etc.). Additionally, if the mass is above approximately 900 Da, fragmentation almost always occurs [46, 47]. As a result, within this thesis, LDI has been used on analytes with molecular weights below 750 Da to minimise the likelihood of fragmentation.

1.3.2 MALDI

While LDI can result in fragmentation of heavier mass molecules, MALDI is a powerful alternative, producing intact gas-phase ions from a broad range of large, non-volatile, and thermally labile compounds. This can include proteins, oligonucleotides, synthetic polymers, and large inorganic compounds. Introduced in 1988 predominately by Karas and Hillenkamp, MALDI offers easy sample preparation, and a large tolerance for contamination by salts, buffers, detergents etc. [46, 48–50].

MALDI is preformed in two stages, depicted in Figure 1.8. Firstly, the analyte is dissolved in a solvent containing a matrix. A matrix describes a small organic molecule which has a strong absorption in the laser wavelength. This mixture is then dried onto a surface, with any liquid solvent removed, forming a ‘solid solution’ deposit of analyte-doped matrix crystals. As the liquid solvent is removed, the matrix crystallises, while the analyte is embedded throughout the crystals. After

the sample has been prepared, the sample is placed under vacuum inside a mass spectrometer, after which laser ablation occurs with short intense pulses.

Following ablation, intact analyte ions are produced, however the exact mechanism for the MALDI process is not fully understood [51, 52]. It is thought to be through a process of rapid heating of the matrix crystals from the laser irradiation, accumulating a large amount of energy in the condensed phase through excitation of the matrix molecules. This rapid heating results in localised sublimation of the matrix, ablation of a portion of the crystal surface, culminating in an expansion of the matrix into the gas phase. When this expansion occurs, the analyte is carried in the expanding plume [53].

The mechanism for production of ions from this plume is unclear, but ionisation reactions can occur under vacuum conditions at any point during this process [54, 55]. Theories for the process include gas-phase photoionisation, excited state proton transfer, ion-molecule reactions, and desorption of preformed ions. The most popular explanation suggests proton transfer occurs in the solid phase before desorption, or gas-phase proton transfer in the expanding plume from photoionised matrix molecules. Once the ion has been formed, they are then accelerated along a flight path.

The key advantage for MALDI lies in its increased sensitivity compared to other laser ionisation techniques. During the sample preparation, the concentration of the matrix exceeds that of the analyte, typically with a ratio of 1:1000 (analyte:matrix). This results in the individual analyte molecules being distributed and isolated throughout the sample surface. This prevents the formation of sample clusters, thus increasing the appearance of molecular ions in the resulting spectra. LDI is a harder ionisation source, whereby the energy from the laser pulse is transferred to the analyte directly. However, with MALDI, the matrix absorbs most of the incident energy, minimising sample damage and increasing the efficiency of energy transfer from the laser to the analyte. MALDI requires no wavelength adjustment to match the analyte, as the matrix absorbs the energy instead. Furthermore, high molecular masses can be analysed as the process is independent of the absorption

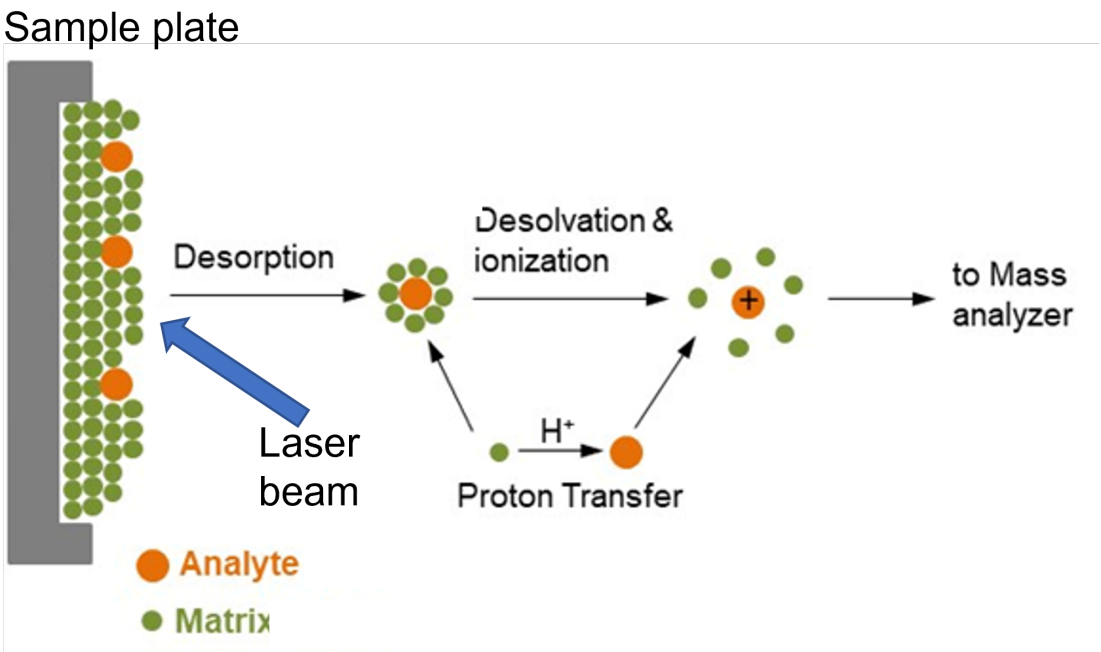


Figure 1.8: Diagram of the principle of MALDI. Adapted from [56]

properties and size of the analyte. This allows for molecular weights in excess of 100 kDa to be ionised.

The efficacy of the technique does depend on the choice of matrix the sample is placed in, and the analyte being investigated. An effective matrix compound is typically low in mass, ensuring that the sample is easily vaporised into the gas phase. Some examples of commonly used matrices are given in Figure 1.9.

These MALDI samples are often ionised using a UV laser, although IR lasers can also be used, with the key factor being the power supplied over the duration of the pulse at a given wavelength [57]. A balance of wavelength, pulse duration, and laser spot diameter is necessary to result in the onset of desorption of the matrix, while excessive laser power leads to more fragmentation and induces a loss of mass resolution.

The most important step in the analysis is matrix selection and sample preparation. The most effective matrix is strongly related to the class of analyte, and it can be a case of trial and error to determine the optimal matrix for a compound. The matrix must meet a number of requirements, including a strong absorbance for the laser wavelength, low enough mass to sublimate, vacuum stability, promotion of

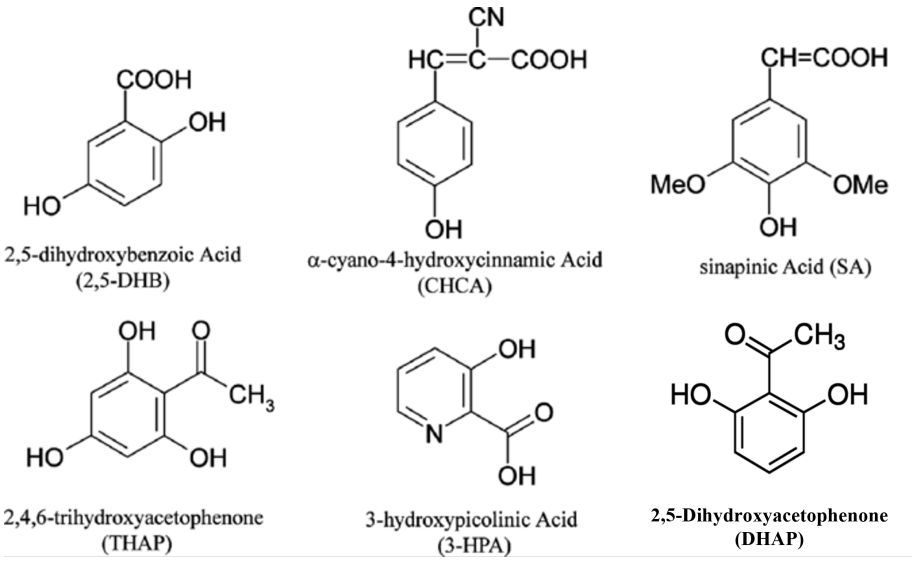


Figure 1.9: List of commonly used MALDI matrices. Adapted from [58]

Table 1.1: List of common matrices used for UV-MALDI, and the class of compounds with which they are used. The acronyms refer to: PA, picolinic acid; HPA, 3-hydroxypicolinic acid; SA, 3,5-dimethoxy-4-hydroxycinnamic acid; THAP, 2,4,6-trihydroxyacetophenone. Adapted from [59].

Matrix	Compound class
3-HPA	Oligonucleotides, DNA, and biopolymers
2,5-DHB	Oligosaccharides
CHCA	Peptides and triacylglycerol
SA	Proteins
THAP	Oligonucleotides

analyte ionisation, solubility in the same solvents as the analyte, and low chemical reactivity. Common UV-MALDI matrices are shown in Figure 1.1, alongside the class of compound for which they are frequently paired with.

MALDI does have disadvantages, such as low shot-to-shot reproducibility. Each laser shot removes a few layers of the sample, which can produce variation in the shot-by-shot spectrum. This can be improved through sample deposition homogeneity, which can give a better reproducibility of the signal. If the sample needs to be ablated for an extensive period of time, the sample can be moved during acquisition to expose fresh sample to the laser irradiation spot.

1.3.3 SIMS

Secondary ion mass spectrometry (SIMS) involves radiating a solid surface with a primary ion beam, and analysing the secondary ions emitted after this bombardment [60, 61]. The first prototype experiments were performed in the 1940s by Herzon and Viehböck [62], and the field developed quickly with the design proposed by Castaing and Slodzian [63, 64]. A typical SIMS instrument comprises of a primary ion gun, which generates the primary ion beam and is directed onto the surface of a sample, and a secondary ion column, including an extraction lens to accelerate ions away from the sample surface and towards a detector. All of this is performed under a high vacuum.

There are a few different types of ion guns employed, depending on the atom or molecule used. In the case of gaseous elements, noble gases ($^{40}Ar^+$, Xe^+), oxygen ($^{16}O^-$, $^{16}O_2^+$, $^{16}O_2^-$), or molecules such as SF_6 and C_{60}^+, a high current of roughly focused ion beams is produced. If $^{133}Cs^+$ is used, primary ions are generated through surface ionisation, with caesium atoms vaporising through a porous tungsten plug and ionising during evaporation [65]. An ion gun of this type provides fine focus or high current, depending on the gun design. The final source type is a liquid metal gun, using metals or alloys which are liquid at approximately room temperature. The liquid metal covers a tungsten tip, and emits ions when under the influence of a strong electric field. This produces a tightly focused beam (<50 nm), with moderate intensity, and the ability to generate short pulse widths. Selection of an ion species and ion gun is dependent on whether a pulsed or continuous mode of operation is desired, the required beam dimensions, and the sample.

The solid sample surface is bombarded by primary ions of a few keV energy. From this, a fraction of the particles emitted from the target are ionised (Figure 1.10). The yield of secondary ions will vary depending on the chemical environment, and the sputtering conditions (ion, energy, angle). This does add complexity to the quantitative aspect of SIMS, however, the technique offers high sensitivity, and low background, and can be applied to any solid which can be kept under vacuum.

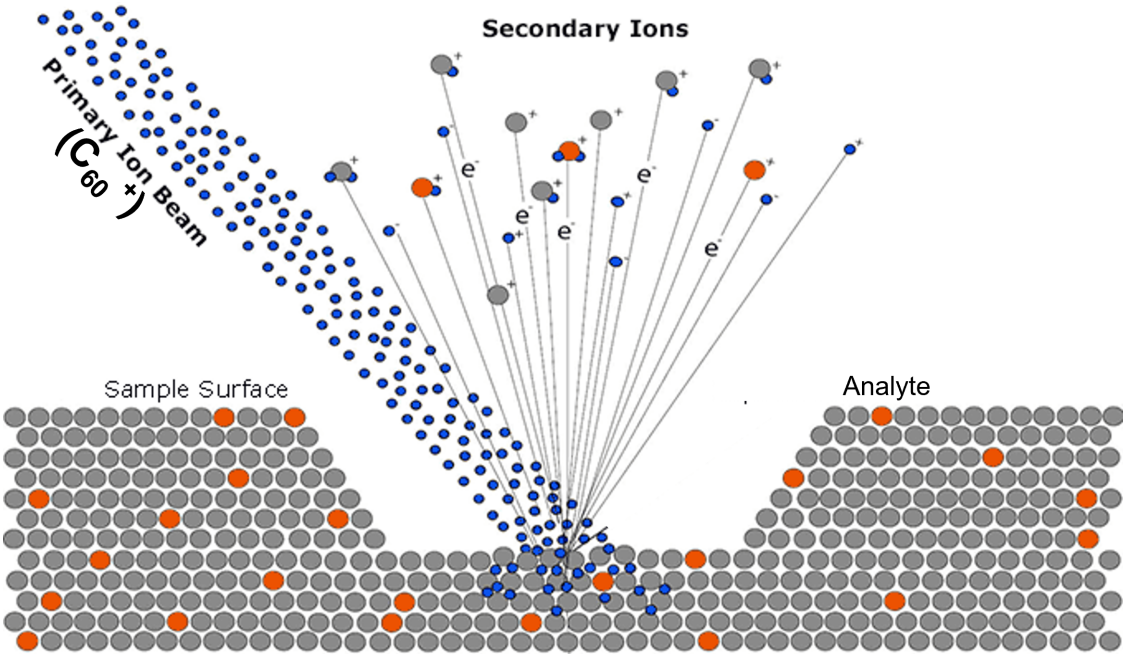


Figure 1.10: Cartoon of ion generation using SIMS. The primary ion beam strikes the analyte surface, producing secondary ions, including electrons. Adapted from [66]

SIMS can be further split into static SIMS and dynamic SIMS. Static SIMS uses low-current primary ion beams which do not cause damage to the surface of the sample, unlike dynamic sources that produce surface erosion. The static method usually uses a pulsed ion beam and is paired with ToF-MS, causing limited damage to any molecules on the surface. This is most often used with solids and is a useful means of studying conductive sources [67]. Dynamic secondary ion mass spectrometry (DSIMS) is used to obtain depth profiles of materials and is used for characterising surfaces, including the elemental, molecular, and isotopic composition. By continuing to bombard the surface, the erosion will be visible over a period of time as the crater becomes visible. Static SIMS is the typical method for acquiring mass information, while dynamic SIMS provides additional depth information but is less commonly used.

1.4 Ion Imaging

Mass Spectrometry Imaging (MSI) can be used to visualise the spatial distribution of molecules according to their molecular masses. Using a focused or defocused

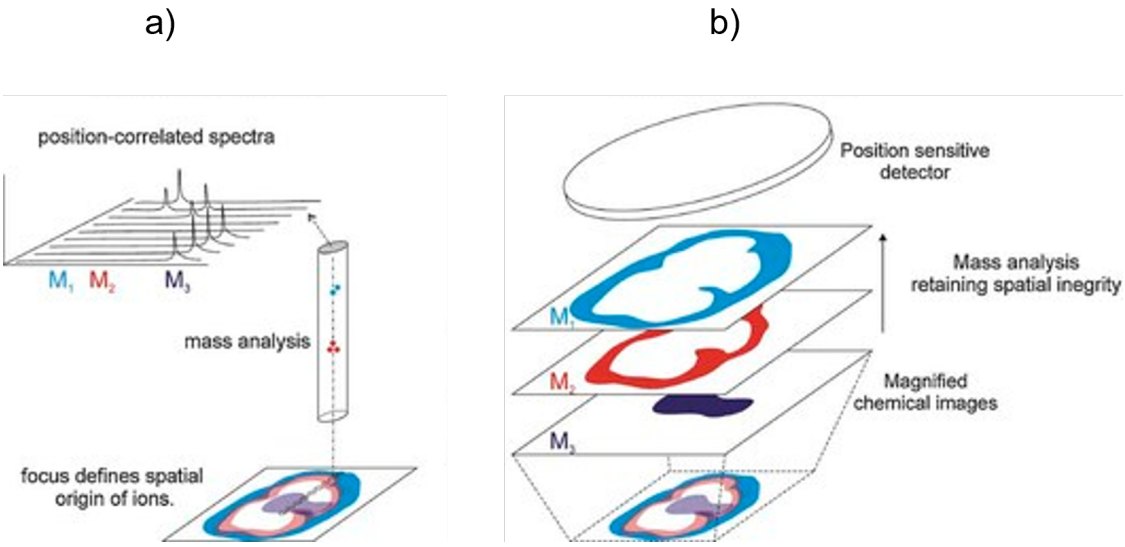


Figure 1.11: Cartoons illustrating the two approaches for molecular imaging mass spectrometry. a) Microprobe mode imaging - a focused ionisation source records mass spectra from a small area, rastering the surface, after which a molecular image can be constructed. b) Microscope mode imaging - using an ion-optical microscope and a defocused ionisation source, magnified images of mass resolved ion distributions are recorded with a 2D detector. Adapted from [68].

ionisation source, a chemically specific three dimensional ion image of a sample surface can be developed, whereby two of the dimensions are positional, x and y, and the third is the ion, m/z [68]. This can be done through two different operating principles, known as microprobe-mode, utilising a focused ionisation source, and microscope mode, using a defocused ionisation source.

Microprobe mode is the most common technique for imaging mass spectrometry. It is performed using a focused ionisation beam, analysing a specific region of the sample by generating a mass spectrum from the ionisation area. This mass spectrum is then recorded with the spatial coordinates of the laser ablation location assigned to it, as defined by the focus of the ionisation beam. A new location on the sample is then selected and analysed, the process being repeated until the desired sample area has been scanned. The output is a distribution map of intensities as a function of x and y locations. This process is illustrated in Figure 1.11a). Using this method, all spatial information from within each individual ionisation spot is lost, and thus the spatial resolution is dependent on the size of the ionisation spot.

Table 1.2: Comparison of typical parameters among MSI techniques. Adapted from [72].

	Nano-SIMS	ToF-SIMS	MALDI
Spatial resolution	$\tilde{1}0$ nm	$\tilde{1}$ μm	20 - 50 μm
Mass range m/z	<100	<1000 - 1500	>200
Type of biological compounds	Elements (iodine), small fragments	Lipids, drugs, metabolites	Peptides, proteins, lipids, drugs, metabolites

Microscope mode differs in its use of a defocused ionisation source, generating ions from the entire sample surface simultaneously. This is then projected onto a position-sensitive detector, as depicted in Figure 1.11b). Spatial information is acquired from within the ionisation spot, thus is independent of the ionising beam spot size, and is instead determined by the magnification of the microscope, the ion optics used, and the position-sensitive detector resolution. The decoupling of the spatial information from the spot size allows for a larger area of the sample surface to be imaged without needing to move the sample or ionisation beam.

These techniques for MSI have been paired with SIMS [67], MALDI [48], DESI [69], and LDI [70], to generate and image ions from a range of samples. It has the capability to image molecules such as metabolites, lipids, peptides, proteins, and glycans without labelling [71]. The combination of m/z information and the ability to visualise the spatial distributions in thin sample sections make this a valuable technique for biological characterisation. Figure 1.12 shows an example of images obtained by MSI of select ions contained in a rat brain tissue section, and typical parameters of three MSI techniques are given in Table 1.2.

The field of MSI is dominated by microprobe instruments, owed to its ability to pair any mass spectrometer with a focused ionisation source with a mass analyser of choice. The mass resolution is a product of the mass analyser chosen, while the spatial resolution is determined by the size of the ionisation spot - a smaller probe would result in a higher spatial resolution. The drawback from this is the time requirement; the time necessary for image acquisition is inversely proportional to the area of the ionisation spot size. For example, imaging a 10×10 mm^2 tissue

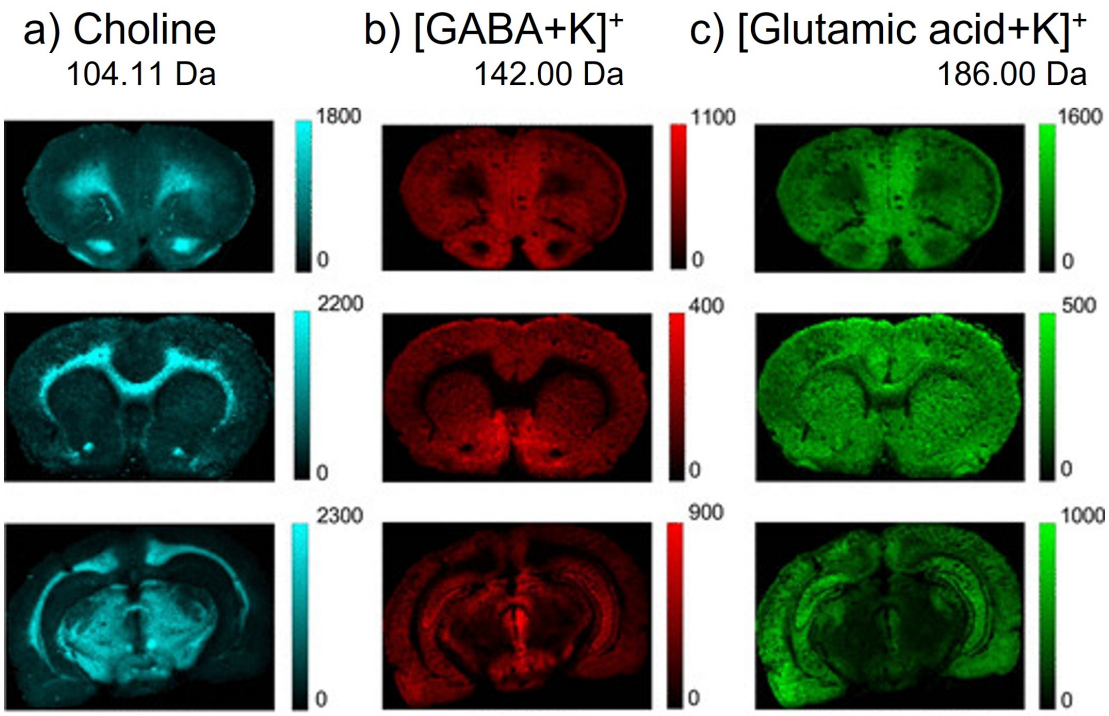


Figure 1.12: Ion images of rat brain tissue at three different masses (left to right) and three different anatomical locations (top to bottom), acquired using LDI-MSI . Adapted from [70].

section, with a spatial resolution of 10 μm, 1 million spots (pixels) is required. At a speed of 10 pixels per second, such an image would take approximately 28 hours. This not only decreases experimental throughput, but also introduces issues with samples which degrade over time.

The advantage microscope MSI has over microprobe MSI lies in its high-throughput potential. The spatial resolution is decoupled from the ionisation beam size, with ions electrostatically projected onto a position sensitive detector at the end of a ToF mass analyser. This has the potential to significantly reduce acquisition time, however does result in the coupling of spatial and mass resolution. The efficacy of the method has been demonstrated with a fast mass microscopy method performed by Heeren *et al.*, utilising microscope MSI to successfully obtain a gigapixel image in 34 minutes, which would take 2 months for a comparable image to be acquired using a microprobe technique [73].

The technique is dependent on the ion optics used and the capabilities of a

position-sensitive detector. The principles were established in the 1960's, but progress was limited by the imaging technology available [74]. Early research conducted with Charge-Coupled Device (CCD) cameras restricted imaging to a single m/z, as time gates must be applied to the detector, however, developments with Complementary Metal-Oxide Semiconductor (CMOS) based cameras have conquered this problem [75–77]. Ion images can now be recorded over a range of m/z within a single experiment [78–81]. These cameras will be discussed in further detail 2.5.

Following from the work of Castaing and Slodzian [63], where the conception of the ion microscope began, the development of microscope MSI began with CAMECA, a SIMS instrument. This first SIMS imaging instrument used high energy beams, which were destructive to the sample. This system used a 500 μm diameter Ar^+ primary ion beam, obtaining spatial resolution of 1 to 0.5 μm, and mass resolution of 5,000 $m/\Delta m$ [82–85]. This spatial resolution obtained is dependent on the analyte, its chemical environment, and the nature of the primary ions [63]. The limitations of the design mean only ions of less than 100 Da could be analysed, thus restricting its use to only low mass ions.

Another early instrument appeared in 1992; a stigmatic imaging ToF-SIMS mass spectrometer was presented by Schueler [86]. A pulsed primary ion beam impacts a sample source, resulting in secondary ions being emitted. The ions are electrostatically extracted and focused with an immersion lens. Following this are three 90° hemispherical electrostatic analysers (ESAs), helping to focus the image and ion flight times. An aperture located at the focal point between each ESA filters ions with extreme trajectories. Finally, the magnified ion image is projected onto an imaging detector. This instrument is depicted in Figure 1.13, and produced a field of view of 300 μm with a spatial resolution of 1-5 μm and mass resolution of $\geq$7,500 $m/\Delta m$. A mass resolution of approximately 15,000 $m/\Delta m$ was achieved with $C_2F_5^+$ secondary ions [87].

A further iteration of the technique was developed Heeren *et al.* with the triple focusing time-of-flight mass spectrometer (TRIFT) [88]. TRIFT II is a commercial instrument, similar to that used by Schueler, which was modified to perform MALDI

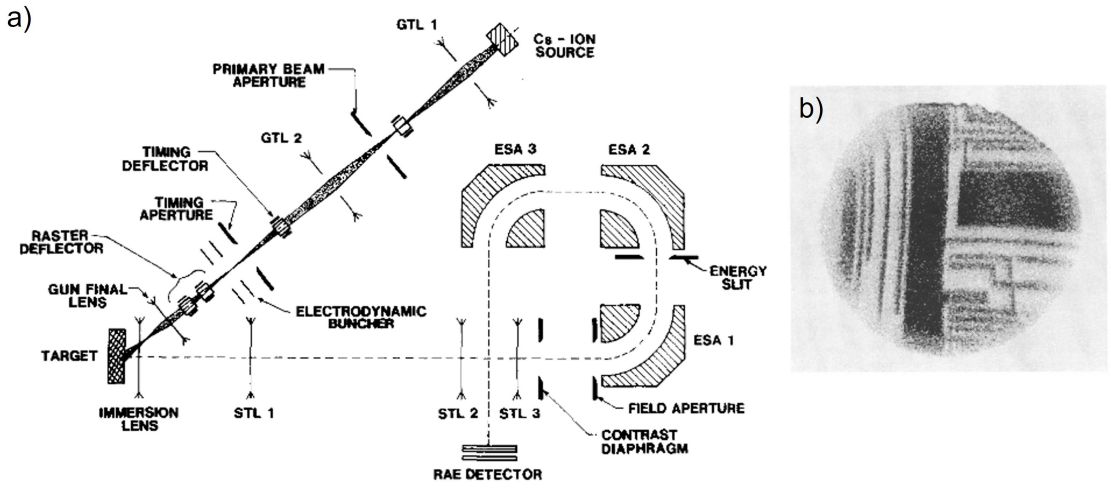


Figure 1.13: a) Layout of the direct imaging ToF mass spectrometer, developed by B. W. Schueler and b) ion images of Al^+ obtained with the ToF-MS SIMS instrument. Adapted from [86].

and produce the first macromolecular ion microscope images. 2,5-DHB was chosen as a matrix, and prepared in a 10,000:1:1 ratio with matrix/substance P (mass 1348 Da)/insulin (mass 5733 Da). The solution was allowed to crystallise while being agitated, producing a near-homogeneous layer of crystals. A fine mesh grid was pressed into the sample, producing a regular pattern which could be easily recognised during imaging. Using this sample, the instrument provided a magnification of $\sim \times 10$, and a spatial resolution of 4 μm, with a field of view of 150-300 μm. Heeren's work has shown the potential of microscope MSI for increased throughput compared to microprobe MSI, with the TRIFT instrument able to achieve μm-resolution [89].

Later developments in the field of miscroscope MSI by the Heeren group were done with TRIFT II, using a C_{60}^+ primary source paired with the Medipix Pixelated detector [90], followed by the Timpeix Camera [91, 92], and then a Timepix3 camera [73]. With the Timepix3 camera and metal-assisted C_{60}^+ SIMS on the BioTrift (an iteration of TRIFT II), a 1.2 gigapixel mass image was acquired. The output image, featuring a set of fingerprints, covered a 42 $\times$ 23.5 mm^2 area and was recorded in 33.3 minutes (see Figure 1.14). An image of this size was acquired by rastering the surface while simultaneously performing microscope MSI, allowing for a large image to be obtained in a fraction of the time required for microprobe MSI. The spatial

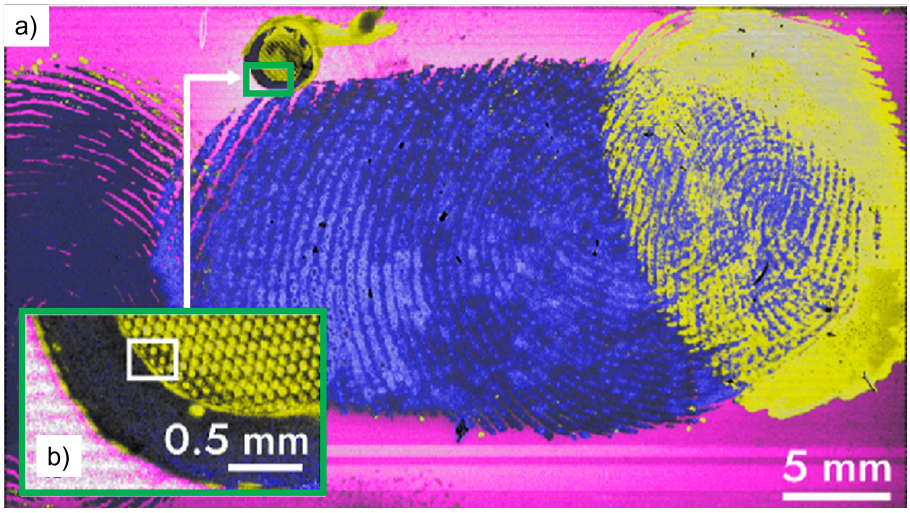


Figure 1.14: Mass image recorded using the BioTRIFT instrument and Timepix3 camera, displaying the 42 × 23.5 mm 2 area recorded in 33.3 min. a) A false-colour mass image of three fingerprints and a TEM grid on an ITO slide with blue, magenta, and yellow colours assigned to mass-to-charge values of 55, 115, and 23 m/z. b) Displays the TEM grid, shown at a pixel size of 10 µm. Adapted from [73].

resolving power for this image was determined to be 2.5 μm, however the technique is limited in its mass resolution, offering a low mass resolution of $\approx$ 100 $m/\Delta m$ at 395 m/z. The broad mass peak is a consequence of the phosphor screen having a slow rise and decay time (discussed in further detail in 2), and a broad ion pulse width, thus future iterations will likely improve this.

Another group researching microscope MSI instrument development is the Toyoda group at Osaka University. Toyoda *et al.* developed a multi-turn time-of-flight mass spectrometer (MULTUM-IMG) with a laser desorption ionisation source (Figure 1.15) [93, 94]. The instrument uses MALDI in conjunction with multi-turn ToF ion optics, comprising of four toroidal electric field sectors created by a cylindrical electric condenser paired with plane electrodes (Matsuda plates). Ions travel along this figure of eight path until allowed to exit by one of the condensers being switched off. The instrument is capable of achieving a high mass resolution $\approx$ 130,000 $m/\Delta m$ for ions of mass 1046.5 m/z, produced after 500 revolutions within the MULTUM-IMG. However this resolution is limited to a mass range of approx 6 Da, as lower m/z ions may overtake higher m/z within the closed flight path [93]. Further publications suggest methods for expanding the mass window, done using

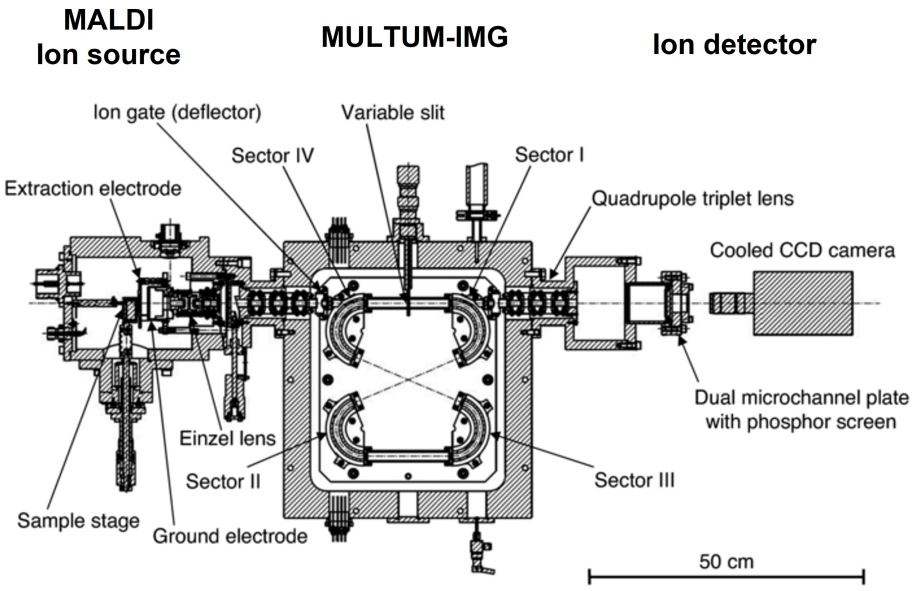


Figure 1.15: Schematic of the MULTUM-IMG mass spectrometer. Adapted from [94].

algorithms to determine lap numbers and the time-of-flight for a given m/z, enabling identification from a mass spectrum, even when lap-superimposition is present [95].

The MULTUM-IMG performs stigmatic MALDI microscope MSI, producing a spatial resolution of about 3 μm from a fine grid of crystal violet [94], however this was performed with the instrument on linear mode, rather than using the multi-turn optics. After ten revolutions, the mass resolution was increased from 150 $m/\Delta m$ in linear mode, to 2,000 $m/\Delta m$, for an ion of mass 372.2 m/z. The instrument is unable to simultaneously produce high spatial and mass resolution, with the ion image becoming increasingly more distorted after only a small number of revolutions (see Figure 1.16).

In order to combat the limited simultaneous mass and spatial resolution, Aoki *et al.* developed a new ion extraction method [96]. Delayed extraction is often used in conventional ToF mass spectrometers, in which an accelerating voltage is applied at a short delay after ionisation has occurred. This accelerating voltage can compensate for the ion energy spread, allowing ions of the same m/z to achieve a focal window, arriving at the detector at the same time thus improving mass resolution [20, 97, 98]. This technique cannot be used in conjunction with microscope MSI, as it results in the ion image being distorted during the delay time before the extraction.

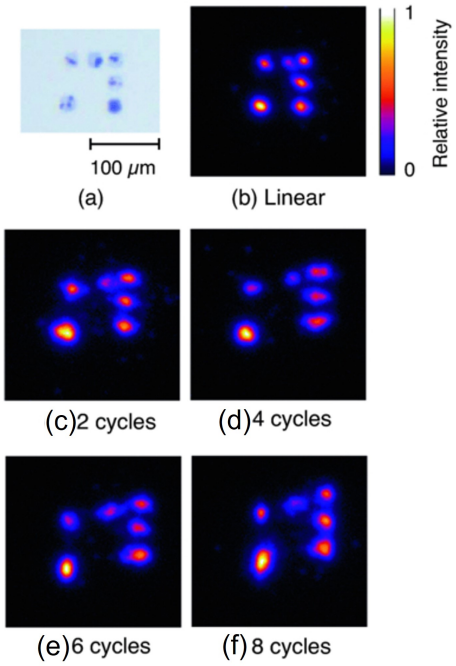


Figure 1.16: MULTUM-IMG ion images obtained from a microdot pattern of crystal violet. (a) an optical microphotograph, and (b)-(f) stigmatic ion images obtained in linear mode, and after an increasing number of cycles through the MULTUM-IMG. Adapted from [94].

The alternative proposed is pulsed extraction differential acceleration (PEDA), which increases the voltage on the extractor plate, rather than pulsing the repeller plate (Figure 1.17). This allows for retention of the spatial resolution. Careful selection of the pulse time and magnitude enable ions with lower kinetic energies to experience an increase in potential, and hence an increase in velocity. Using a MULTUM-IMG instrument in linear mode, a mass resolution of 1,450 $m/\Delta m$ for a peak at 373.25 m/z was achieved using PEDA, while maintaining an equal spatial resolution as without PEDA [96]. This can be compared to a mass resolution of 60 $m/\Delta m$ without pulsed extraction.

The PEDA technique was further developed by Guo *et al.* [99, 100]. In its original form, the technique is limited to a small mass window, estimated to be ± 20% of the optimised m/z, in which both spatial and mass resolution is simultaneously well resolved [96]. Aoki proposed a single-field method, whereby the extractor potential is increased to a single voltage at the trigger time, increasing the potential of one specific m/z, allowing it reach a temporal focus despite differing initial

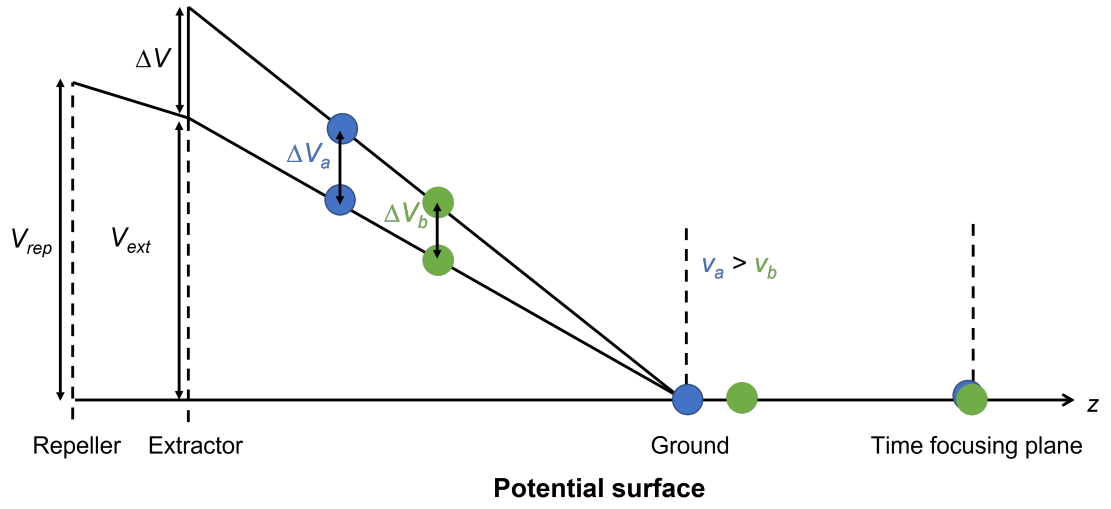


Figure 1.17: A cartoon representing single-field PEDA, and the potential energy of ions travelling through the electrodynamics ion optics. Two ions of the same mass but differing kinetic energies are represented by the blue and green circles. V_{rep} is the repeller voltage, V_{ext} is the extractor voltage, ΔV is the additional voltage applied to V_{ext} at t_{PEDA}, ΔV_a and ΔV_b describe the increase in potential experience by the ions, and v_a and v_b describe the velocity of the respective ion. At t_{PEDA}, the potential increases from V_{ext} to $V_{ext} + \Delta V$, increasing the velocity for ions between the extractor and grounded einzel lens plate. This results in the two ions reaching a time focusing plane.

velocities (see Figure 1.17). The next evolution proposed was titled double-field PEDA, and required an additional electrode located between the extractor and einzel lens entrance, allowing for a second pulse, focusing a second mass. The two focused masses can be selected such that the effective mass range can be increased to 165 Da with a mass resolution >1500 $m/\Delta m$. This produced a spatial resolution of 50 μm over a field of view of 5 mm^2 for ions within the focused mass range.

The effective mass range has been expanded with a time-dependent variation [101]. This electrodynamic version applies single-field PEDA to a wider mass range by increasing the extraction electrode potential with time. The result is a range of m/z which are sequentially focused as the ions pass through the acceleration region. With a Wiley-McLaren configuration ToF imaging mass spectrometer, the optimal pulse shape is a quadratic rise, as t is proportional to $\sqrt{m/z}$. Producing a quadratic pulse experimentally is non-trivial, however a linear rise is a close approximation. With the linear pulse, a 300-600 Da mass range was optimised for, achieving at least 75% of the maximum mass resolution, a ten-fold increase

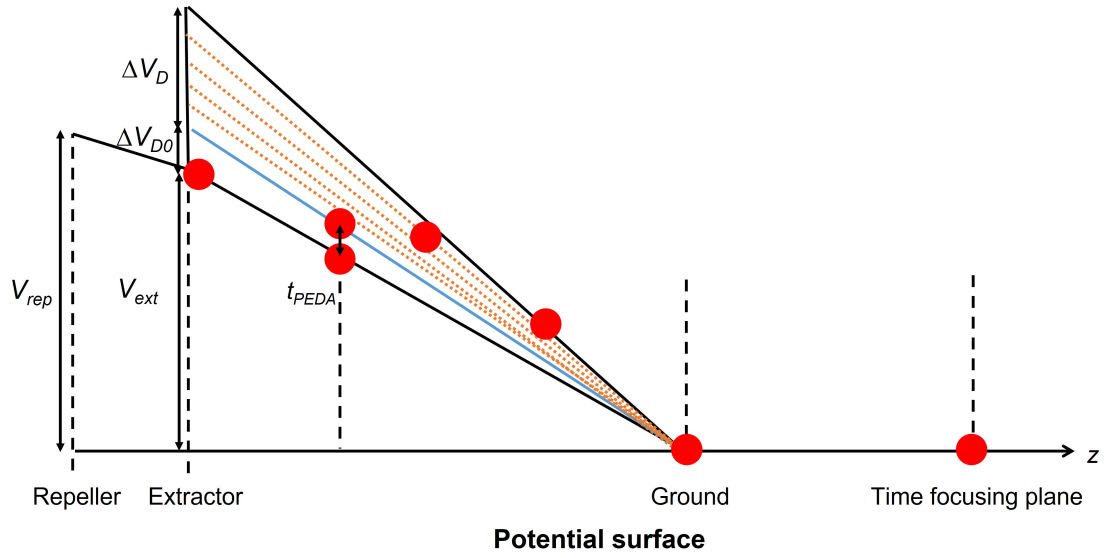


Figure 1.18: A cartoon representing time-variable PEDA, and the potential energy of ions travelling through the electrodynamics ion optics. V_{rep} is the repeller voltage, V_{ext} is the extractor voltage, ΔV_{D0} is the additional voltage applied to V_{ext} at t_{PEDA}, ΔV_D is the maximum additional voltage applied to $V_{ext} + \Delta V_D$ after t_{PEDA}, applying the time variable pulse. An ion is represented by the red circles. At t_{PEDA}, the potential increases from V_{ext} to $V_{ext} + \Delta V_{D0}$, increasing the velocity for ions between the extractor and grounded einzel lens plate in a similar way to single-field PEDA. The extractor potential is then time-varied, increasing up to a maximum of $V_{ext} + \Delta V_{D0} + V_D$. This results in a time focusing plane for ions which are within the extractor region as the pulse is applied.

compared to single-field PEDA. The spatial resolution also experienced a similar improvement, with an average of 25 μm between 300 and 600 Da.

A further iteration of the MULTUM instrument employed PEDA, achieving a mass resolution of ~10,000 $m/\Delta m$ and a spatial resolution of 1 μm with a fine mesh sample of crystal violet [95]. The ion optics of this instrument were designed such that the ion beam was injected to the MULTUM in a narrow beam, allowing for image quality to be conserved after circulation without deviating too far away from their relative positions.

1.5 Ion Detection

At the end of any mass spectrometer is a detector, transforming ion events into usable signal. The incident ions impact the detector, generating an electric current proportional to the ion abundance. There are two key classes; point ion counters,

which count ions of a single mass at a time, and array collectors, which have the ability to count multiple masses and detect the arrival of all ions simultaneously along a plane [44].

The first detector used in mass spectrometers was the photographic plate. Ion impacts on the plate would result in a spot, the position of which indicated the m/z, and the darkness of the spot provided an approximate value of relative abundance. This detector has been rendered obsolete today with the advent of more quantifiable detectors.

An example of a point ion detector is the Faraday cup [102]. Made up of a metal cup or cylinder with a small orifice, it is designed to catch charged particles in a vacuum. When ions hit the cup, they are neutralised as the charge is transferred to the metal walls. This charge transfer produces a current through a connected resistor. This discharge current is amplified, detected, and provides a measure of ion abundance. The Faraday cup is simple and robust, however is limited by its low sensitivity and slow response time.

Another point ion detector is the electron multiplier, widely used in mass spectrometry. Consisting of a series of dynodes, an ion impact on the first dynode causes the emission of secondary particles, which are converted to electrons and amplified by a cascade effect in the electron multiplier to output a current [44]. There is a dependence on ion impact velocity and the nature of the ion, rendering the electron multiplier less precise than the Faraday cup, but it offers an exceptionally high gain and sensitivity.

An array collector variation of the electron multiplier is the Microchannel Plate (MCP) detector. A MCP comprises of a large array of cylindrical channels of 5-25 μm diameter. By applying a positive potential difference of about 1 kV between the front and back faces of the MCP, each channel behaves as a continuous dynode electron multiplier, with electron multiplication caused by ion impacts on the semiconductor substance coating each channel. MCPs offer precise arrival times and a large detection area, with the disadvantages of fragility, air sensitivity, and cost.

Coupling the MCP with a phosphorescent screen enables the extraction of positional information of each ion event. A cluster of electrons produced by an ion event and output from the back of the MCP can proceed to impact on the screen, producing photons. The photons can then be detected by a photomultiplier and a CCD, or CMOS camera, supplying both ToF and positional information.

There are a number of options for recording the ion image produced, the most traditional being the CCD camera. The CCD camera has no time-stamping ability, thus is used by time-gating the camera over the desired peak. This acquires an image for a particular m/z. While the CCD had a significant quality advantage in the field, the development of fast sensors such as the delay-line anode, PImMS, and Timepix, allow for acquisition of both ToF and position for the entire spectrum to be obtained simultaneously [80, 103].

One such fast sensor is a Delay-Line Detector (DLD), which can be paired with an MCP without a scintillator. The electron cloud emitted from the back of the MCP stack can induce a signal in a wire. In a DLD, the wire is arranged in serpentine path wound around a base plate along the x and y axis [104]. The induced current from an electron impact travels in two directions along the wire, at the end of which are time-to-digital converters. Based on the difference in time from either end of the wire, the arrival time and position of the ion event can be determined. The advantages offered by a DLD include excellent signal-to-noise and high time resolution, however this comes with a cost of a 10-100 ns pixel dead time between impacts, making it unsuitable for high ion count detection.

Complementary Metal-Oxide Semiconductor (CMOS) sensors work by converting photons from the phosphorescent screen into electrical signals. The Pixel Imaging Mass Spectrometry (PImMS) sensor is an example of a CMOS sensor, with a fast time-stamping and multi-pixel sensor [80]. Each pixel contains both a photodetector, and an active amplifier, with each pixel capable of recording up to four arrival times per pixel, allowing multiple events to be detected per time-of-flight cycle. There are two generations of the PImMS sensor, with the first having 72×72 pixels and the second with 324×324 pixels. Only ion events which exceed a predefined

pixel threshold can trigger the time-stamping, with a timing precision of 12.5 ns, corresponding to a 80 Mfps frame rate on a conventional camera. The ability to record four arrival times per pixel makes the PImMS camera more suitable for higher ion count detection than a delay line detector.

A similar camera which has been developed uses the TimePix sensor [103]. This sensor is able to record time-of-arrival, and time-over-threshold simultaneously in each pixel. The Timepix3 sensor has 256×256 pixels and can achieve a timing resolution of 1.5625 ns. Like PImMS, Timepix also employs thresholding on individual pixels to minimise the storage of null data, which is especially important when operated in ToF mode, where the time-of-arrival of an incident photon is recorded and large amounts of data must be transferred efficiently to a computer.

This thesis focuses on microscope mode mass spectrometry imaging. The motivation for this has been driven by the development of multi-mass imaging sensors becoming available. The ion detection methods used in this thesis will be described in more detail in Chapter 2.

1.6 Summary

Mass spectrometry is a powerful analytical tool, supplying information on what molecules are present in a sample, and the distribution of those molecules within the sample. Within this chapter, the history of the technique has been presented, followed by a discussion on time-of-flight MS and developments of the technique. A number of different ionisation sources exist, with the key methods being explored. Finally, the process of ion imaging and means for ion detection were introduced.

The two key ion imaging methods are microprobe mode, and microscope mode. These modes each have their own advantages and disadvantages, with microprobe mode typically attaining higher mass and spatial resolution, but at the expense of acquisition time. Microscope MSI can reach high mass and spatial resolutions, the challenge primarily lies in achieving these simultaneously, and covering a wide mass range. It has been shown that an effective mass range of 300-600 Da can be

achieved with the time-variable PEDA technique, achieving a simultaneously high mass resolution (8,000 $m/\Delta m$) and spatial resolution (18 $\pm$ 6 μm) [30].

Notable work in the field of microscope mode mass spectrometry imaging has been done by the Toyada Group, at Osaka University, acquiring a simultaneous mass resolution $\sim$10,000 $m/\Delta m$ and a spatial resolution of 1 μm with a MULTUM instrument [95]. Additionally, the Heeren group, at Maastricht University, used a BioTrift instrument to produce a 1.2 gigapixel image in 33.3 minutes [73]. Both are significant steps within the field, increasing the capability of microscope mode imaging.

This thesis aims to improve two microscope imaging mass spectrometers, with the experimental methods used within this thesis will be described in Chapter 2, presenting two different microscope MSI instruments. The rest of this thesis will discuss approaches to improve various aspects of the microscope MSI systems. Chapter 3 explores improvements on a MALDI-ToF instrument, offering a high spatial resolution potential arrangement, followed by an investigation on a variable zoom lens using simulations. Chapter 4 proposes a method of improving time-stamping precision using Timepix3 camera paired with a novel triggering method, and explores a technique to improve the mass resolution achieved using the camera experimentally. Chapter 5 discusses and compares the two microscope MSI instruments, one utilising laser ablation, another using SIMS, exploring the differences between them. Finally, Chapter 6 concludes the thesis, recapping the key outcomes, as mentioned above, and proposing areas for future work.

2
Experimental Methods

Contents

2.1 Reflectron ToF Mass Spectrometer 36
2.1.1 Ion Optics 37
2.1.2 Laser 40
2.1.3 Triggering 43
2.2 SIMS MSI 44
2.2.1 Preparation Chamber and Sample Plate 47
2.2.2 Ion Optics 47
2.2.3 C_{60}^{+} ion gun 50
2.3 Sample preparation 52
2.3.1 Electrosprayer 52
2.3.2 Dried droplet 56
2.4 Detector assembly 56
2.4.1 Microchannel plates 58
2.4.2 Scintillator screen 59
2.4.3 Photomultiplier Tube 61
2.5 Cameras 63
2.5.1 CCD 63
2.5.2 Timepix3 camera 65
2.5.3 Image processing 67
2.6 m/z calibration 68
2.7 Summary 71

This chapter describes the equipment used for experiments presented within this thesis. Firstly, a reflectron Time-of-Flight (ToF) ion microscope paired with a Nd:YAG laser will be detailed, followed by a Secondary Ion Mass Spectrometry

(SIMS) ToF ion microscope with a C_{60}^{+} primary ion beam. Following this, the details for the sample preparation methods are laid out. Next, the detector assemblies used in both MSI instruments are explained, after which a number of different cameras capable of obtaining images from the detectors are discussed. Finally, the calibration methods are presented.

2.1 Reflectron ToF Mass Spectrometer

The reflectron ToF mass spectrometer instrument is a home-built instrument, consisting of four main regions: a sample loading chamber, an ion source chamber, a reflectron, and a flight tube (see Figure 2.1) [30, 105]. This is held under a high vacuum using two turbo-molecular pumps (Leybold TMP 600 and SL300), backed up by two rotary pumps (Leybold TRIVAC B). The pressure is monitored by two different types of vacuum gauges, a Pirani gauge (KJLC 275 Convection Enhanced Pirani), and a hot filament ion gauge (KJLC 392 Series Wide-Range Combination Gauge).

A pirani gauge is a thermal conductivity gauge, operating at pressures from 1 $\times 10^{-7}$ to 1,000 mbar. The hot filament ion gauge uses a heated filament to produce electrons which are then attracted to a cylindrical grid cage, held at a positive potential, which is open to the vacuum chamber. Most electrons pass through the grid and collide with gas molecules, ionising some of them. The gas ions formed are attracted to the a fine wire at the centre of the ionisation volume, producing a current proportional to the gas density at the gauge. At a constant temperature, the current is linearly related to the gas pressure. The reflectron MSI instrument is typically held at a pressure of 1 $\times 10^{-7}$ mbar.

The sample loading chamber is separated from the main body of the instrument with a manual gate valve. This isolates the sample chamber, allowing it to be vented while retaining the vacuum in the rest of the instrument. An additional rotary pump is used to reduce the pressure in the small sample chamber to 1×10^{-3} mbar, before the gate valve is opened to reconnect the two sections.

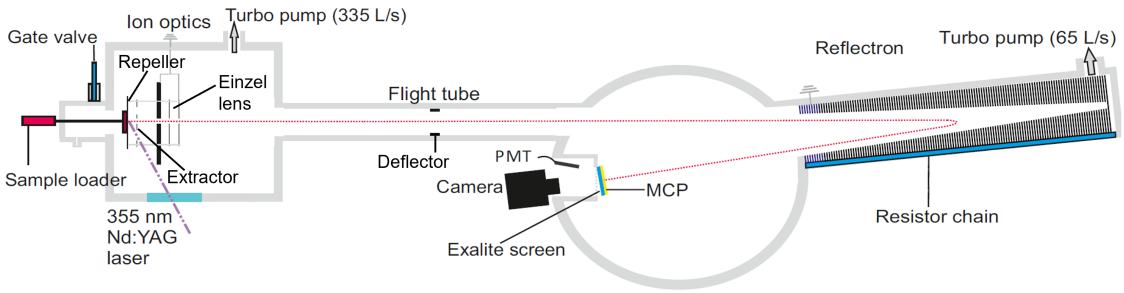


Figure 2.1: Schematic of the reflectron ToF mass spectrometer. The red line indicates the ion trajectory. Adapted from [101].

Once vented, the sample loading chamber can be removed and pulled away from the main chamber using wheels located at its base for ease of movement. This section consists of a small chamber approximately 2 dm^3 in volume, with a sample arm and round plate with four square inserts (sample holder plate) for sample loading. The sample chamber is located off-centre to allow for one of the four sample plates to align with the central time-of-flight axis. The sample arm can be extracted and rotated to allow for changing between the four loaded samples while still under vacuum. The samples are prepared on Indium Tin Oxide coated glass slides and loaded into the 25 mm $\times$ 25 mm $\times$ 1 mm inserts cut into the section of the repeller plate attached to the sample arm. The slides are affixed using copper tape to remove excess surface charge from the slide; excess charge can cause aberrations to the image and broaden the mass peaks.

Using the sample arm, samples can be transferred from the sample chamber into the ion source chamber. Here the sample can be ionised by a laser. The ions pass through a series of ion optics, travel down the flight tube and reflectron, before colliding with the detector assembly. The signals generated at the detector are then recorded using a photomultiplier tube and camera, then saved on to a computer.

2.1.1 Ion Optics

Within the ion source chamber, there are a series of ion optics: 5 circular metal plates consisting of a repeller, extractor, and a three-plate einzel lens (see Figure 2.2). The five plates are mounted on four stainless steel rods insulated by ceramic

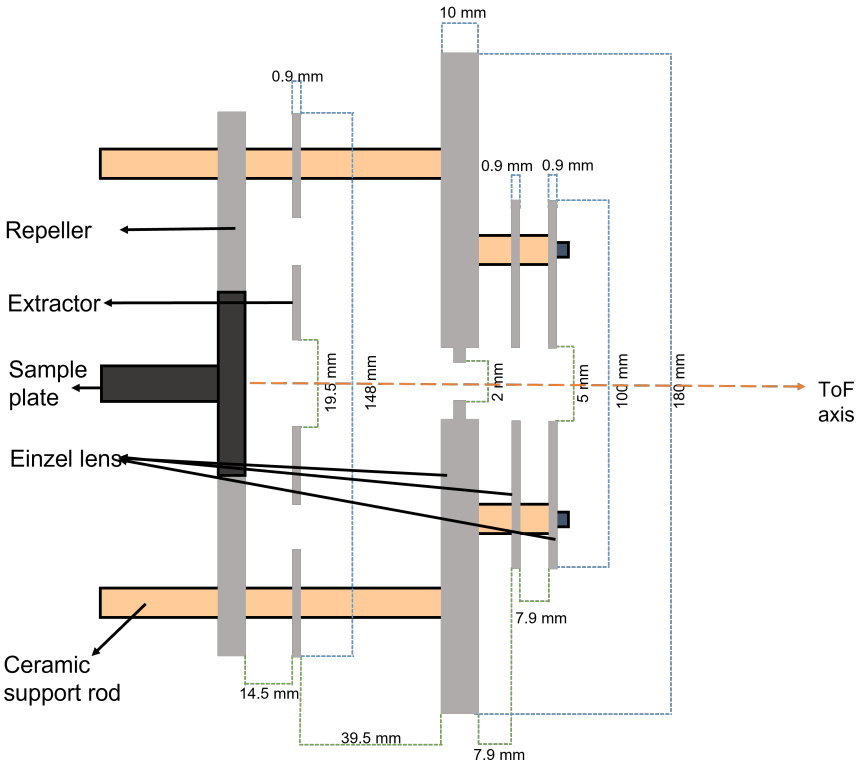


Figure 2.2: Details of the ion optics in the ion source chamber. The electrodes shown in the blue are (left to right): repeller, extractor, and three-plate einzel lens, consisting of grounded electrode one, einzel electrode, grounded electrode two. The black section indicates the sample holder plate, and orange indicates the ceramic support rods.

(Macor) spacers mounted to the chamber walls. The repeller plate consists of a solid plate with a 148 mm diameter and a large opening, into which the sample plate is loaded. The extractor plate has a thickness of 0.9 mm, the same diameter as the repeller, and is separated by a distance of 14.5 mm, with a central aperture of 19.5 mm for ion flight following ablation off the repeller. Finally, the einzel lens is located at a distance of 39.5 mm away from the extractor. Consisting of three plates - a grounded plate, and charge plate, and a final grounded plate. The first of which has a 10 mm thickness, 180 mm diameter, and 2 mm aperture. The second and third plates are both 0.9 mm thick, with a diameter of 100 mm, and 5 mm apertures.

The repeller plate is held at a high positive electric potential, serving to accelerate cations away from the sample plate and along the ToF axis. This plate has a sample plate inset, which can be removed from the repeller plate using the sample holder plate arm. The sample plate is not centrally located, instead offset such that one

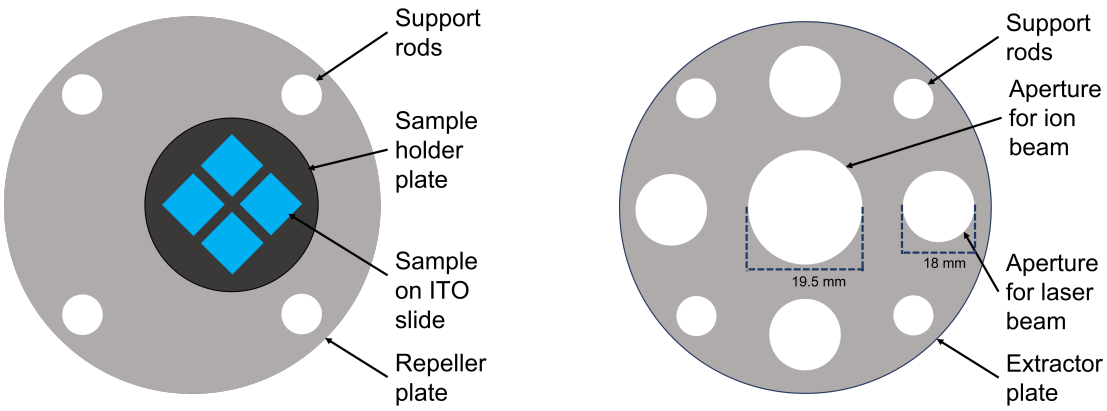


Figure 2.3: a) Repeller electrode with inset sample holder plate and ITO slides and b) extractor plate showing the apertures used for the ion and laser beam.

of the four ITO samples slides is located centrally and aligns with the ToF axis (see Figure 2.3a). Rotation of the sample arm by 90° allows for a different sample to be centrally located, thus each sample can be analysed in turn. Changing to new samples requires extraction of the sample holder plate by pulling the sample arm back, this places the sample holder plate inside the sample loading chamber. Only then can the gate valve be closed, isolating the main chamber. After venting, the sample chamber can be opened, the samples changed, and the sample chamber then reconnected to the main chamber and pumped down with a rotary pump.

Following the repeller plate is the extractor plate. This plate has the same diameter as the repeller, positioned using ceramic support rods. The extractor plate features a large aperture at its centre, to allow for the ion beam to pass along the central ToF axis (see Figure 2.3b). It also has four additional symmetric apertures. One of the apertures is used to allow a laser beam to pass through at an angle and irradiate the sample on the repeller. The other three maintain the symmetry of the electric field.

The einzel lens assembly is made up of three electrodes, the first of which is a grounded 10 mm thick plate with a removable 2 mm aperture at its centre. This narrow opening helps block ions of large initial transverse velocities, acting as a contrast diaphragm [105] and reducing chromatic aberrations in the output ion

image. The second and third electrodes in the einzel lens assembly have identical dimensions, with only the second electrode having a potential supply, while the outer two electrodes are grounded.

Following the ion optic stack in the sample chamber is a cylindrical field free flight tube of length 1,436 mm. Within this are located two sets of deflector electrodes; parallel plates with length 30 mm, and positioned 721 mm away from the final plate within the einzel lens. These electrodes are used to deflect ions and steer the ion beam into the reflectron.

The reflectron follows after the field free flight tube, consisting of sixty three individual electrodes separated by ceramic spacers. The first eight plates in the stack are grounded, with the remainder connected to a resistor chain creating a linearly decreasing potential gradient. The electrodes within the reflectron have linearly decreasing irides, beginning with 90 mm and ending as a solid plate. The solid plate has the full reflectron potential applied to it.

At the end of the flight path is a detector, comprised of dual-stack microchannel plates and an Exalite-404 scintillator screen. The detector set up is discussed in further detail later in this chapeter, in Section 2.4.

2.1.2 Laser

The ablation method for this instrument is a frequency tripled output of a neodymium-doped yttrium aluminium garnet laser (Nd:YAG, Continuum Powerlite 8000 Precision II) running at 355 nm. Nd:YAG is a commonly used lasing media for solid-state lasers. Within the yttrium aluminium garnet (YAG), a small percentage ($\sim$1%) of the yttrium ions are replaced with the dopant Nd(III) ions. The presence of the neodymium ion provides the lasing activity in the crystal. The laser is optically pumped using flash lamps, one of which is located in the Nd:YAG medium within the oscillator, the other two located within the amplifier. This induces a population inversion with 808 nm light, the subsequent electron relaxation emits light with a wavelength of 1064 nm (see Figure 2.4). This emitted light is then reflected

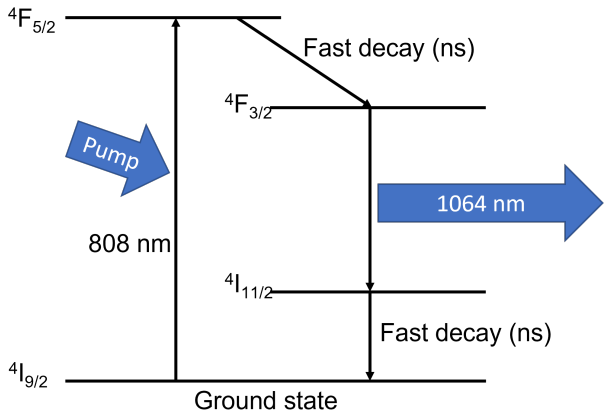


Figure 2.4: Simplified energy level diagram showing the energy levels and transitions for a Nd:YAG laser.

back and forth through the active medium in an optical cavity, amplifying the light and creating coherent 1064 nm light.

To achieve pulsing, the laser is operated in Q-switching mode. This generates 3-7 ns laser pulses of the 1064 nm light with a much higher peak power relative to continuous wave lasers. The process of Q-switching begins with a population inversion - the gain medium is pumped and the light allowed to leave. This population inversion occurs without any feedback as the stimulated emission is suppressed, corresponding to a low Q factor (an indicator of high light transmission). This population inversion resets after each pulse and the amount of energy stored in the gain medium increases. The second phase occurs after the medium is gain saturated and the system changes from a low to a high Q factor - the duration of this high Q factor period dictates the length of the laser pulse. Feedback is thus allowed, the output pulse is stored by a second gain medium (amplifier) and stimulated emission begins. The final phase utilises the high energy stored in the gain medium, the intensity of light in the resonator builds up, firing a short pulse of light with a high peak intensity. The laser beam path within the Continuum Powerlite 8000 is depicted in Figure 2.5.

The power of this pulse is controlled via the delay time between the Q-switch in the oscillator and the amplifier flash lamps. This is done using a Quantum Composer 9520 pulse generator. The power is tuned depending on the sample -

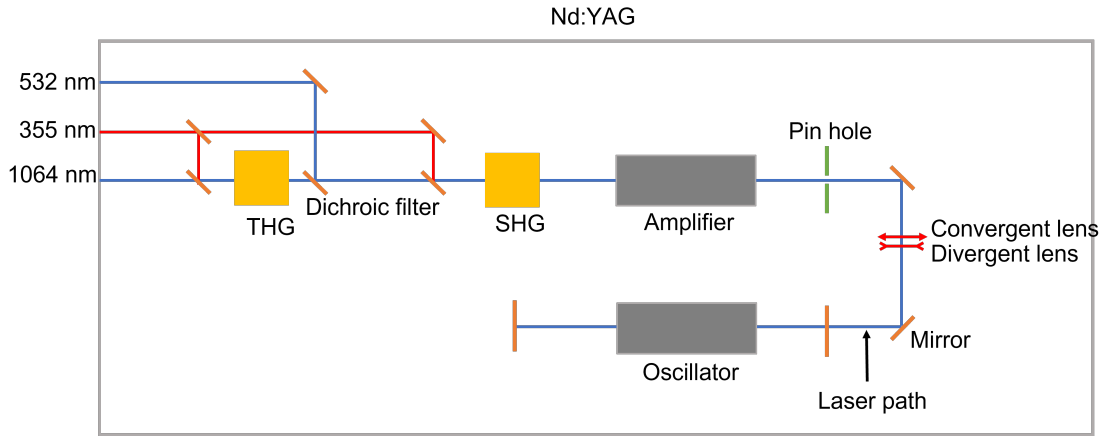


Figure 2.5: Schematic of Nd:YAG Contiuum Powerlite 8000 Precision II laser. The blue trace indicates the laser path beginning at the oscillator. 1064 nm photons are produced, travelling through the divergent and convergent lenses to refocus the beam. The amplifier increases photon emission before passing the photons through a second harmonic generating (SHG) crystal, doubling the frequency and producing 532 nm photons. A dichroic filter in the beam path filters out 532 nm light. The remaining 1064 nm photons are frequency tripled through a third harmonic crystal (THG) to produce 355 nm light, which are then filtered and subsequently used in the experiments presented in this thesis.

optimal laser fluence is reliant on surpassing a minimum sample ionisation threshold which is low enough to prevent ion trajectory distortion caused by space charge effects during flight. This reduces the mass and spatial resolution, thus optimal laser power is defined as the minimum fluence such that sufficient ions are produced to acquire an image and mass spectra.

The output 1064 nm light is frequency-doubled (532 nm) and tripled (355 nm) using a Potassium Dihydrogen Phosphate (KDP) crystal. For use in the experiments described in this thesis, the third harmonic was used for its efficiency at ionising molecules. The laser operates at 10 Hz, limiting the experimental repetition rate, with a pulse width of 3-7 ns. The laser is capable of operating at 3 W, however that is attenuated significantly using a 50:50 beam splitter, prisms, and mirrors prior to reaching the sample surface (Figure 2.6). Combined with the Q-switch settings determined by the pulse generator, the operational pulse energy is between 1 to 10 mJ/pulse. While a higher pulse energy could be used, doing so would result in a greater number of ions being generated, which may lead to strong space charge effects and distort the ion trajectory.

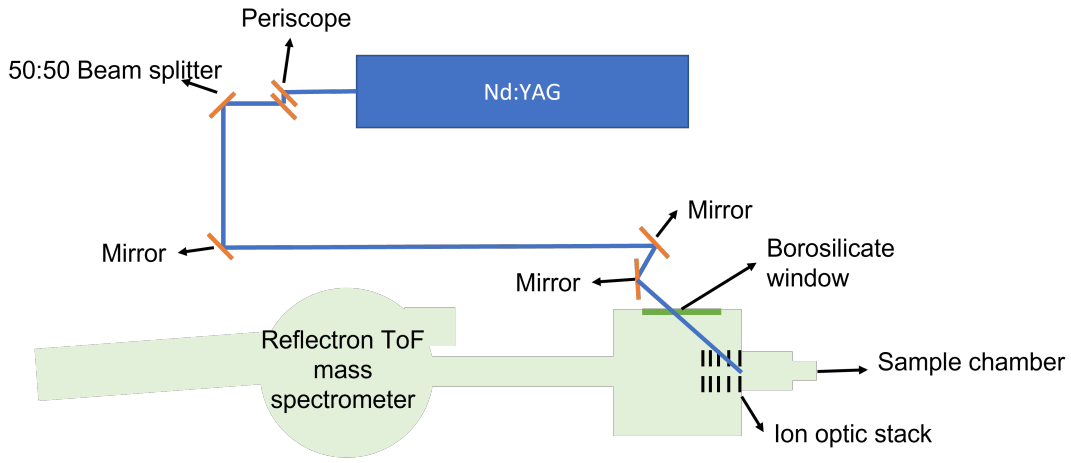


Figure 2.6: Schematic of the Nd:YAG 355 nm laser beam path. The blue trace indicates the laser path beginning at the exit of the Nd:YAG Continuum Powerlite 8000. The beam path is directed to the reflectron ToF mass spectrometer using a periscope, 50:50 beam splitter, and three before passing through a borosilicate window and an aperture in the extractor lens before reaching the repeller plate.

In addition to the external optics required to propagate the beam, the pulse must also enter the vacuum chamber via a borosilicate window. In order to minimise in-homogeneity in the laser profile as it enters the vacuum chamber, the window has a λ-5 flatness. The beam must also travel through one of the holes in the extractor plate, allowing the laser beam to reach the sample plate at a small incidence angle ($\approx$ 20°).

2.1.3 Triggering

The pulse generator used offers a 250 ps time resolution, enabling accurate triggering timings for the experiment which has an experimental cycle of 50 μs. Transistor-transistor logic (TTL) 5 V pulses are used in this experimental setup, with 3.4 V being used for the CCD camera.

The order of operation is as follows: a TTL pulse switches on the Nd:YAG flash lamp, a second pulse is then used to activate the Q switch 45 μs later, designated as t_{zero}. With this pulse, the laser fires and ionises the sample. The next pulse sent out is 2.85 μs later, causing a high-voltage switching box to increase the voltage applied to the extractor plate. A fourth and final pulse is then sent, 65 μs after the Q-switch. This pulse is to trigger a CCD camera to begin recording. The

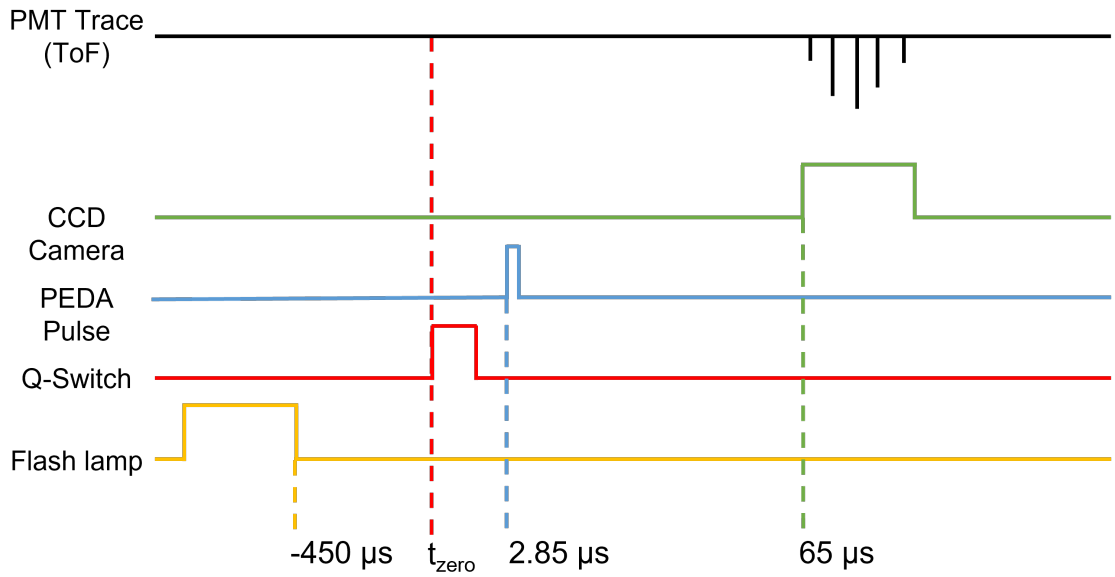


Figure 2.7: Cartoon showing the timings of pulses sent from the delay generator to the laser, extractor plate (PEDA pulse), and CCD camera. Timings displayed are relative to t_{zero}.

width of the pulse determines the image time window recorded for that particular shot. The pulse start and width is set such that the window overlaps with the sample peaks recorded via PMT (also displayed on the oscilloscope). All of this is displayed using a LeCroy DDA-260 oscilloscope with a 65 GHz sampling rate. This process is depicted in Figure 2.7.

2.2 SIMS MSI

A C_{60}^{+} primary ion beam can be used to ablate a sample surface and generate secondary ions, acting as a soft ionisation method with little fragmentation [106]. The advantage of SIMS is large biomolecules are more likely to remain intact and therefore produce simpler spectra which can be more easily characterised. It is for this reason that a microscope mode instrument using SIMS, instead of MALDI, would be desirable.

A second microscope mode instrument has also been developed and used in this thesis. Unlike the reflectron ToF mass spectrometer instrument, which is entirely home-built, the SIMS ToF mass spectrometer instrument was designed in collabo-

ration between Ionoptika, the Rosalind Franklin Institute (RFI) and the Oxford University Chemistry Department. The chamber design of the instrument is based on the Ionoptika J105 SIMS, using the sample analysis chamber (SAC) as the base around which the rest of the SIMS microscope-mode ToF-MSI instrument is built.

Both instruments act as microscope-mode imaging mass spectrometers, with two major differences: the SIMS ToF mass spectrometer instrument has no reflectron attached and is a simple linear ToF instrument, and the ionisation method has changed from laser ablation to a C_{60}^+ ion gun. SIMS, when compared to MALDI, exhibits extensive fragmentation of secondary ions and a low secondary ion yield [107]. It offers the advantage of reduced sample surface damage while maintaining sputtering rate, making it an ideal ionisation source for microscope-mode MSI.

The instrument comprises of a prep chamber, SAC chamber, a C_{60}^+ ion beam, a ToF tube, with a detector assembly, and a Secondary Electron Detector (SED) (see Figure 2.8). The entire footprint of the instrument is 205 × 110 × 180 cm (H × W × L). In addition to this, an optical camera has been fitted outside of the vacuum to a port on the SAC chamber, providing a real-time image of the inside of the chamber.

The system is kept under vacuum, held at a pressure of 10^{-9} mbar, using two rotary pumps (Edward, nXDS6i scroll pump), and three turbos (Lleybold TurboVac SL80, Pfieffer HiPace 300 Plus, Pfieffer HiPace 80). There are pneumatic gate valves between the SAC and the prep chamber, which allows for venting of the prep chamber and sample loading; a manual gate valve in front of the C_{60}^+ ion gun; and a pneumatic gate valve part way along the ToF tube, to protect the Microchannel Plates (MCPs) and screen, keeping them under vacuum at all times. There are also gate valves between the entire instrument and the two rotary pumps.

The C_{60}^+ ion gun is positioned at an angle of 40° to the surface, and has a length of 95 cm from ion source to SAC chamber. The ion gun is a refurbished commercial model designed by Ionoptika (IOG 660-40 Ion Beam System) and re-purposed to run with a defocused beam, rather than the more traditional highly focused beam. A more detailed description of the ion gun is given in Section 2.2.3.

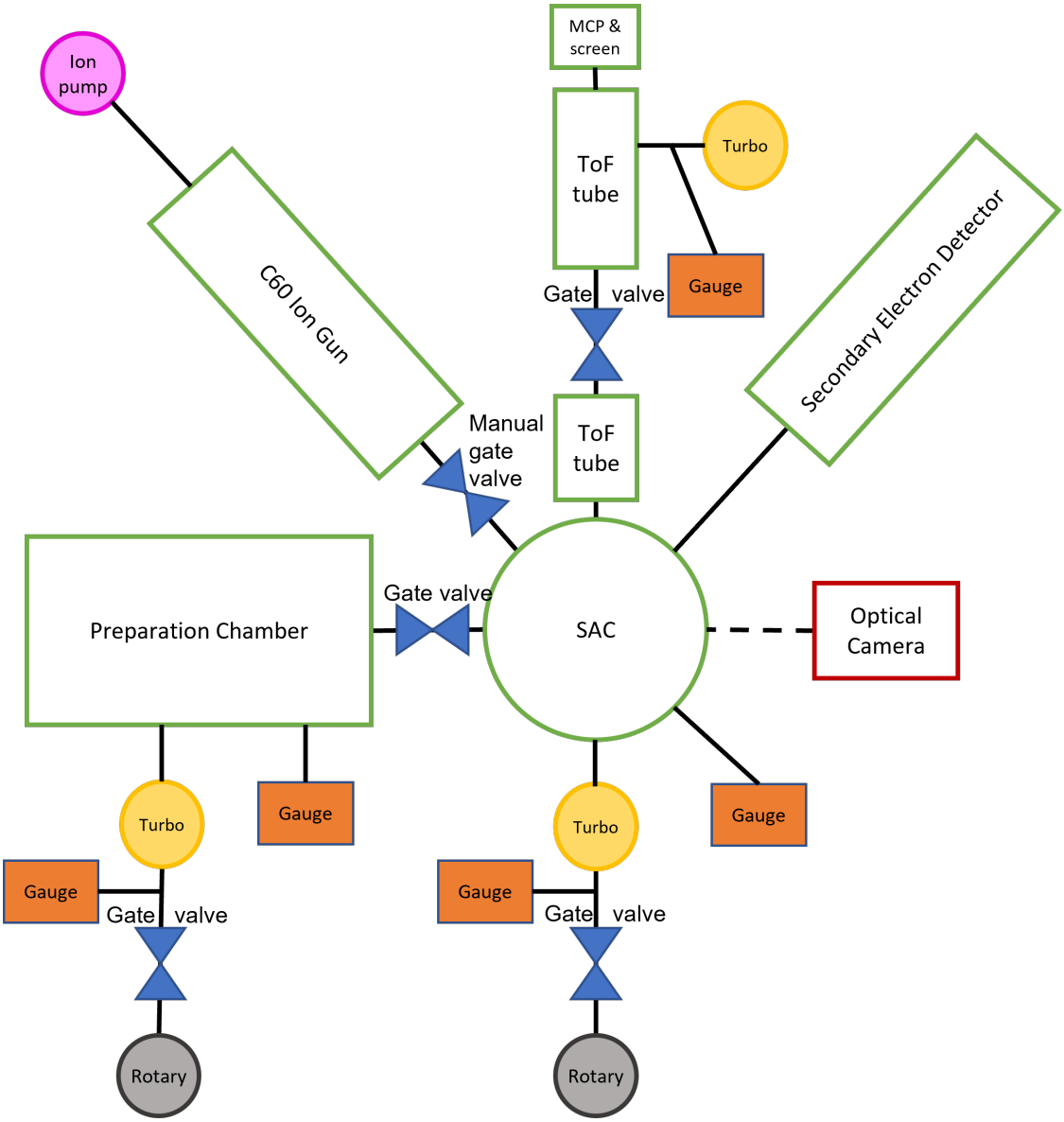


Figure 2.8: Schematic depicting the SIMS instrument.

At the end of the C_{60}^{+} ion beam path is the SAC chamber, housing the extraction optics and leading to the flight tube. The primary ion beam collides with the sample, generating secondary ions, which are then accelerated vertically through the ToF tube using the extraction optics. The ToF tube has a length of 100 cm, at the end of which, the secondary ions collide with a detector, made up of a dual stack Microchannel Plate (MCPs) assembly and a scintillator screen, located at the top of the flight tube. One of the turbos branches off the ToF tube, and a gate valve is located within the ToF tube, 25 cm from the SAC chamber. Also connected to

the main chamber is a SED (Ionoptika, SED03) to provide a topographical image of the surface, a viewing window, the optical camera, and the prep chamber.

The majority of the instrument can be controlled electronically, via a computer. This supplies the pressure readout from the gauges, controls the pumping and venting procedure, and is the interface for the C_{60}^{+} ion gun, SED, sample stage, and optical camera. The additions made to the Ionoptika J105 design include all components included within, or attached, to the ToF tube, and these are controlled manually using individual power supplies.

2.2.1 Preparation Chamber and Sample Plate

The preparation loading chamber consists of a small chamber with a horizontal sample loading arm of length 1294 mm. At the end of this arm are two prongs, which insert into a copper sample plate designed by Ionoptika. The preparation chamber is separated from the main chamber via a gate valve and has a pressure gauge connected. This chamber is also connected to the C_{60}^{+} ion gun to share the vacuum pumping load. The preparation chamber can be isolated from the main body of the instrument using the gate valve between the prep and SAC chambers, and the gate valve between the prep and C_{60}^{+} ion gun.

Sample loading can be performed by isolating the prep chamber, venting the chamber to atmosphere, and access to the chamber is provided by a door on the side of the chamber. The sample plate is loaded onto the sample arm prongs with the aid of a viewing window, located above the intersection of the chamber door and sample arm.

Samples are either mounted directly on to the copper sample plate surface and affixed with conducting copper tape, or prepared on an ITO slide (more details given in 2.3.1), which sits on the surface of the sample plate and is affixed with copper tape.

2.2.2 Ion Optics

The ion optics within the main chamber are similar to that of the reflectron instrument; consisting of a repeller plate, and extractor, and an einzel lens. The

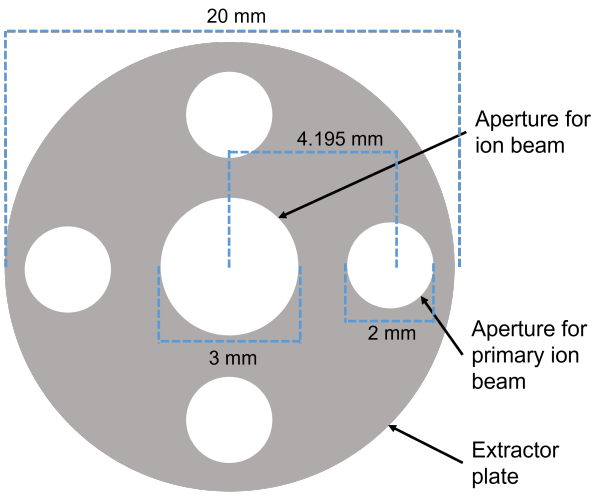


Figure 2.9: Schematic of the SIMS ToF mass spectrometer extractor plate

plates are considerably smaller than the reflectron instrument, resulting in a different electric field being formed. The extractor having a diameter of 20 mm and a secondary ion beam aperture diameter at 3 mm. The sample plate is transferred from the preparation chamber into the SAC onto a sample stage using the sample arm. Within the SAC is a sample stage with three dimensional movement, controlled via the computer to load the plate onto the stage.

This sample stage is connected to the copper sample plate, and thus the sample plate acts as the repeller plate. The stage is also connected to an ammeter. The sample plate has a Faraday cup embedded, allowing for the current from C_{60}^+ beam to be measured. The stage height can be adjusted to account for larger objects, such as ITO slides, to be mounted, and the stage can be easily moved to allow for the desired area to be ionised.

Above the sample plate is an extractor plate, which has four symmetrical holes surrounding a central hole (see Figure 2.9). One of the outer holes allows the C_{60}^+ ion beam access to the sample surface, and the central hole is aligned with the secondary ion beam flight path. As the C_{60}^+ ion beam enters through one of the side holes on the extractor lens, the defocused ion beam is restricted by the diameter of the holes on the lens (discussed in more detail in Chapter 5), however the extractor plate can be exchanged for a different one should it be deemed necessary in the

future. Above this is the einzel lens, comprising of a two outer plates, which are grounded, and a central plate to which a potential is applied.

The beam collides with the surface at an angle of 40° normal to the surface. The sample stage can be moved to align the region of interest to be the primary ion beam impact location. Positioning of the sample plate is guided by the optical camera, positioned such that it can view the stage through a different hole in the extractor plate. Upon ablation with the primary ion beam, the secondary ion beam is repelled from the repeller plate, and guided vertically through extractor and einzel lens by the electric fields produced, entering a field free ToF tube.

Also within the SAC is a Secondary Electron Detector (SED), located towards the sample plate surface. A SED is used to detect, and quantify, secondary charged particles produced after bombardment of a sample surface with a primary ion beam. The bombardment produces electrons or ions, originating from the sample surface, with a significantly lower energy than the primary ion beam. A grid electrode with a positive potential attracts secondary electrons, causing these electrons to drift towards the SED. The grid potential can be adjusted to improve the collection of electrons emitted from the sample surface, or it can be reversed to collect only high energy electrons or detect positive secondary ions.

After passing through the grid electrode, the electrons are impacted onto the front of a multiplying detector. This multiplying detector is a continuous dynode electron multiplier, the same as that used in a PMT (discussed in detail in Section 2.4.3). At the end of the electron multiplier, the signal is collected and fed into a pre-amplifier, amplifying the signal to a voltage suitable for connection to a computer for displaying the output image. The image is acquired by raster scanning the surface, with a higher resolution image acquired with a slower raster speed.

On the sample plate is a Faraday cup. The Faraday cup is a small metal cup, designed to catch charged particles in a vacuum. This allows for the C_{60}^{+} ion beam current to be measured, determining the number of charged particles hitting the cup. This is used to verify the gun is working as expected. There is

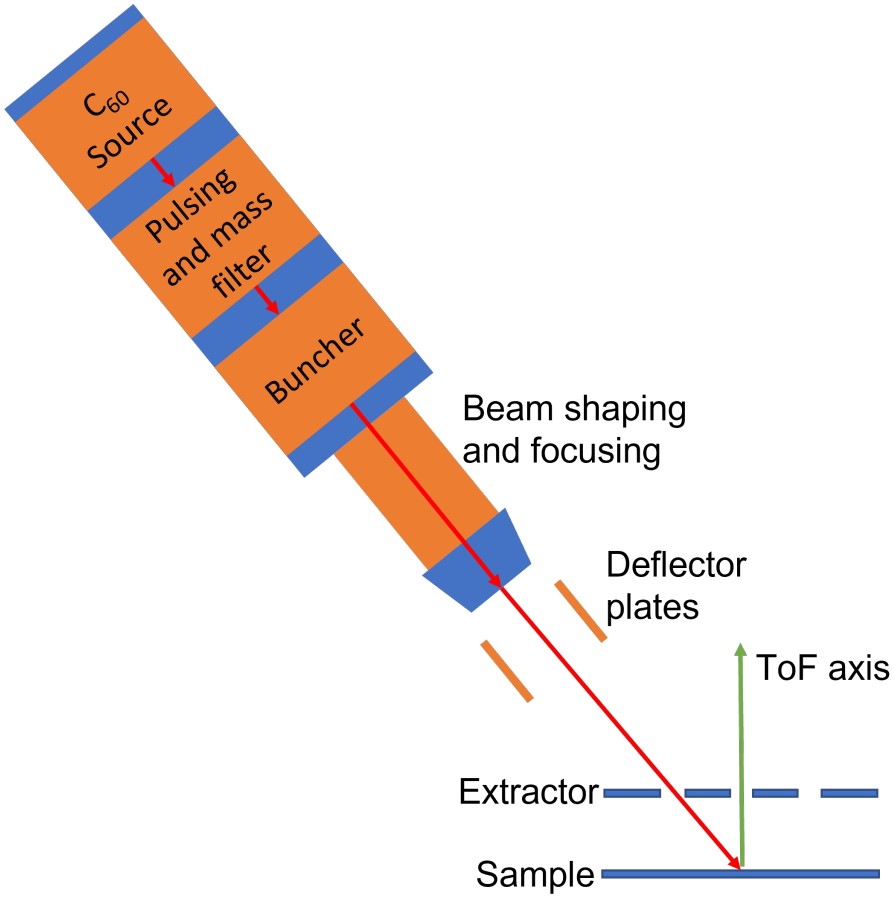


Figure 2.10: Cartoon of the IOG C60-40 C_{60}^+ ion gun.

a singular external connection from the sample stage which can either connect to the ammeter or supply a potential.

2.2.3 C_{60}^+ ion gun

The C_{60}^+ ion gun (IOG C60-40) is the ionisation source for the instrument, supplying the primary ion beam from a C_{60}^+ source at a continuously adjustable range of kinetic energies between 10 keV and 40 keV (Figure 2.10). Originally designed to operate as a focused beam for microprobe MSI, the beam would have a diameter between 300 nm and 20 μm. For the purpose of this research however, the beam has been defocused to a diameter of 1.8 mm so that it can be used for microscope MSI instead.

Within the ion gun lies a C_{60} source, a small charge of the C_{60} powder at the rear of the source is heated, producing a vapour. This vapour can then pass into an electron bombardment chamber, producing C_{60}^+ ions and other positively

charged fragments. Using a series of electrodes, these ions are accelerated through the optical column.

The optical column comprises of two lenses, which collimate and focus the beam. A pair of plates are used to control the pulsing; there is a 1° bend in the flight axis, and applying a potential to the pulsing plates allows the ion beam to travel around the bend and on to the sample. This pulsing operates at a variable rate up to 1 kHz. This has an added advantage of filtering out any neutral molecules which may be present in the beam.

The beam is also mass filtered using a Wien Filter [108]. This consists of perpendicular electric and magnetic fields, which can select ions based on their velocity. Charged ions within the field will feel a force proportional to the charge and field strength:

$$\overrightarrow{F} = q\overrightarrow{E}, \tag{2.1}$$

where F is force, q is charge, and E the electric field strength. Likewise, the magnetic field will exert a force proportional to the velocity and charge of the particle:

$$\overrightarrow{F} = q\overrightarrow{v} \times \overrightarrow{B}, \tag{2.2}$$

where v is the velocity of the particle, B the magnetic field strength, and $\times$ the cross product. Given the magnetic field is 90° to the velocity, this becomes

$$F = qvB \tag{2.3}$$

in the direction of the cross product, which is perpendicular to both B and v.

Setting the two forces as equal in magnitude but in opposite directions,

$$\frac{E}{B} = v. \tag{2.4}$$

Hence only a single velocity is allowed through, depending upon the combination of electric and magnetic fields applied. This is used to isolate the C_{60}^{+} species.

The ion gun is also capable of pulse bunching, done using a pulsed plate, the timing of this pulsing is a function of beam energy. By bunching the beam, the energy spread of the pulse is reduced. Additionally, beam rastering can be done using a set of deflector plates to adjust the beam position.

The ion gun is operated under vacuum and has a manual gate valve to isolate the ion source chamber. This gate valve allows for easy access to the source, necessary for routine maintenance. The result is a C_{60}^{+} primary ion beam, typically accelerated to 40 keV, and aimed at the centre of the sample plate having entered through one of the side holes in the extractor plate. The beam shaping and focusing lenses include Lens 2, which is typically used to focus the ion beam, however for the purpose of microscope-mode MSI, it is instead used to defocus the beam. Additionally, the deflectors used to raster scan are also not used in microscope mode.

2.3 Sample preparation

Instrument characterisation with both the reflectron ToF mass spectrometer and the SIMS ToF mass spectrometer have been performed primarily using dye molecules, as these are easy to ionise and prepare. Additionally, a number of solid metal samples were used within the SIMS ToF instrument; these are simply affixed to the sample plate surface using copper tape. With the dye molecules, it is possible to produce well-defined patterns using a home-built electrospray device and metal mesh. Doing so allows for a thin, uniform later of dye to be deposited in a pattern, such that the spatial mapping capability of each instrument can be recorded.

For the testing of samples which don't require any spatial mapping information, another method of dried droplet deposition is employed. This is a very quick and efficient way of producing a sample when only investigating mass resolution.

2.3.1 Electrosprayer

Electrospraying is a process in which electrical forces cause liquid nebulisation [109, 110], enabling the deposition of a thin, uniform layer of sample on a surface. Liquid flows from a capillary nozzle, a high electric potential is applied to the nozzle,

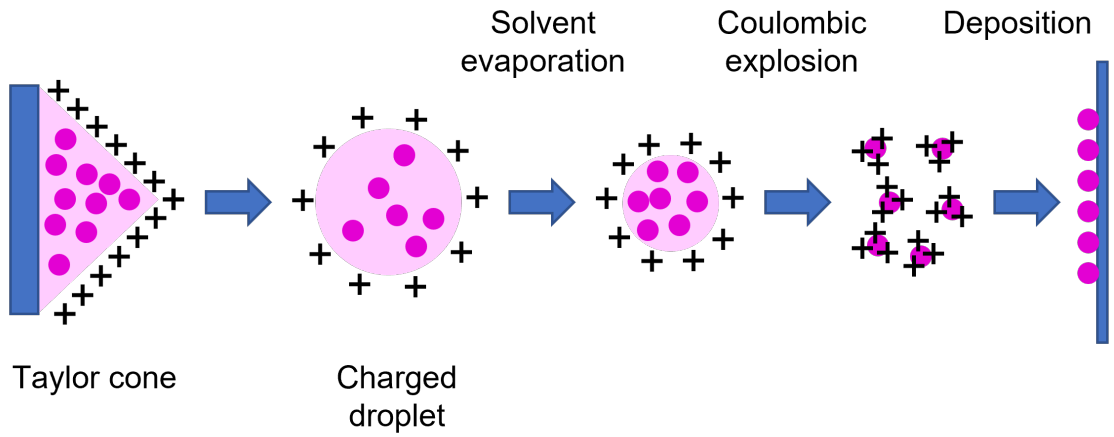


Figure 2.11: Diagram of electrospray sample deposition. Under a high voltage, the Taylor cone produces a mist of liquid drops. The solvent in these droplets evaporates gradually, continuing until a coulombic explosion occurs. The ions of sample molecules formed are then deposited on the sample surface.

generating a a strong electric field and subjecting the liquid to these forces. This electric field acts as a driving force, pushing the electric charge carriers in the liquid to distribute under the liquid surface of the meniscus.

The natural surface tension generating the meniscus in a liquid is thus deformed into a conical shape, called a Taylor cone. The cone is a consequence of equilibrium surface tension, and electrical and gravitational forces. At the apex of this cone, the electric charge accumulates. Eventually, this will generate an electric field sufficiently high to produce electrodynamic pressure, which exceeds and overcomes the liquid surface tension. The result of this is a thin liquid jet emerging from this apex point, removing the excess charge. The electric field accelerates the electrically charged jet, disrupting into droplets at the opposite end due to electrical repulsion (Figure 2.11).

The process can be controlled with the electric potential applied and the liquid flow rate. A continuous flow rate is required to attain the liquid flow from the meniscus; the optimal flow rate is dependent on the physical properties of the liquic [111].

A home-built electrospraying instrument was used to prepare the majority of dye samples in this thesis [109]. The device consists of an injection needle (BD Microlance 3, filed flat) suspended above a grounded plate. The needle has an outer diameter of

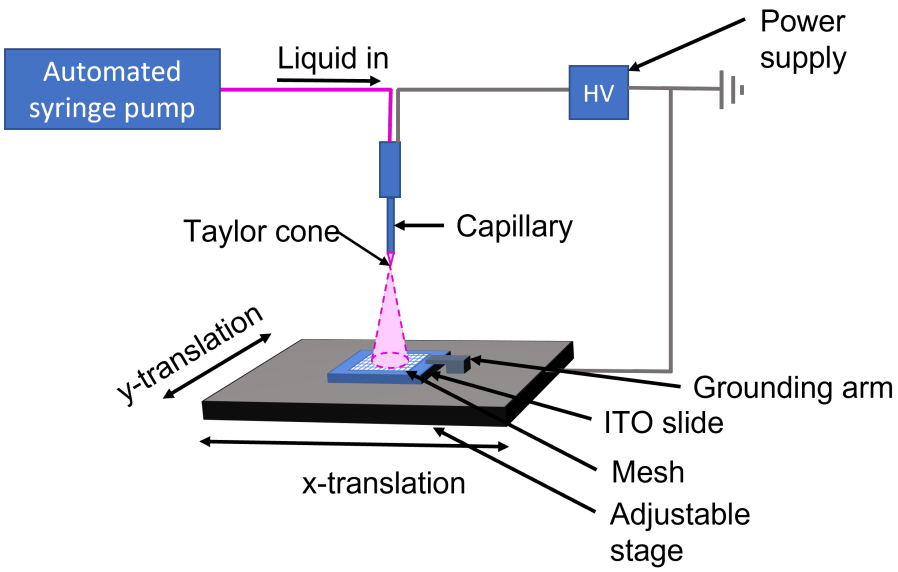


Figure 2.12: Schematic diagram of home-built electrosprayer. This prepares samples by depositing dye on an ITO slide in a homogeneous layer. Grids can be made by placing a mesh on the slide, electrospraying, then removing the mesh to leave a grid pattern of dye.

0.81 mm, a length of approximately 30 mm, and is held at a high potential (5.2 kV). It is connected to a capillary tube with a diameter typically less than 1 mm. The capillary is attached to a syringe containing the analyte, which is fitted to a syringe pump (Legata 100, KD Scientific Inc) operating at a flow rate of 30 - 60 μL/h.

Indium tin oxide (ITO) coated glass slides (25×25×1.1 mm, Sigma-Aldrich) are used as sample substrates. The ITO slide is placed conductive side up on the grounded plate, acting as a counter electrode located 1 - 3 cm below the tip of the needle. This grounded plate can be adjusted in three dimensions, allowing for easy positioning of the sample slide. The ITO slide is necessary to prevent charge build up both within the electrosprayer, which would repel incoming droplets, and for use within the instruments. When used in either of the instruments, any surface charging can alter the initial ion velocity, which can negatively impact the spatial and temporal resolution. As such, the ITO slide within the electrosprayer is grounded to the adjustable base plate via a small metal arm.

A grid pattern of the analyte is formed using electroformed nickel mesh on the ITO slide as a stencil. Two different size grid patterns are used, (Industrial Netting BM0400-49 with 63 μm pitch and 14.2 μm wire width, and Industrial

Netting BM0181-01 with 101 μm pitch and 38.1 μm wire width) were utilised to characterise the magnifications and spatial resolutions achieved in the two instruments. Prior to spraying, a droplet of solvent (typically methanol) is applied to the mesh so that it will lay flush against the conductive side of the ITO slide. Doing so prevents any warping in the mesh surface which could deform the analyte spray. The electrosprayer will deposit dye onto the slide until the desired sample thickness is achieved (usually about 20 minutes), after which the nickel mesh can be removed to reveal the analyte grid.

The quality of the sample prepared is dependent on the size of particles of droplets that form, as well as their distribution. In order to produce the most complete dye layer, with minimal defects, small droplets with a narrow distribution in size are desired. For layer thickness, the homogeneity of the dispersion is essential. Electrostic forces between the capillary tip and the substrate help produce this even dispersion - made better by very fine droplets. With the correct setup, electrospray dispersion is highly reproducible and simple due to the automated nature with the syringe pump.

As such, the electrosprayer is very effective in producing a homogeneous layer when the analyte is a highly soluble dye, however, parameters need to be adjusted by trial-and-error to produce optimal results. Electrospraying is dependent on the dye sample solution, flow rate, concentration, and solvent. Other solutes are less effective, in particular matrix solutions, as the matrix crystallises in varying sizes and results in some droplets being released from the electrosprayer. This disrupts the Taylor cone, causing large droplets to be deposited. These larger droplets contain larger quantities of solvent, which land on the surface and cause the already deposited analyte to travel to new locations, distorting the sample. An additional issue is posed in the local matrix concentration - inhomogeneity can alter the ionisation of the sample.

The sample produced by the electrosprayer is a full circle because of the mutual Coulomb repulsion - the charged droplets output from the Taylor cone repel each other, expanding in space as a spherical cloud. The position of the capillary tip

relative to the sample surface can be adjusted, giving control over the size of the circle produced. This distance will alter the density of the dye deposited, as a smaller distance results in a smaller circle but with the same quantity of dye deposited. The density can also be adjusted using the flow rate or increasing the spray time, creating a large amount of flexibility with sample preparation.

2.3.2 Dried droplet

Another sample preparation method used is known as the dried droplet method. This involves dissolution or suspension of a solute in a volatile solvent, such as methanol, then using a micropipette to extract a small volume of the solution, and depositing a single drop onto the sample plate. The solvent is allowed to evaporate, leaving the sample behind on the surface. Depending on sample, concentration of the solution, and desired sample thickness, subsequent droplets can be added on top of the original. Doing so would redissolve the original quantity of sample deposited, but by adding the solution to the surface in a drop-wise procedure, the sample thickness can be increased without expanding the area significantly. Adding multiple drops at once will result in a larger area being covered.

This method is an inhomogenous sample preparation technique which offers the advantage of being very quick, and can be done with multiple samples at the same time. It is typically used for samples which a) do not require any spatial information, and b) samples which do not electrospray well. This includes any analytes which aren't especially soluble, therefore they can be deposited and affixed onto a slide via a suspension and thus used in vacuum.

2.4 Detector assembly

The detector assembly is similar in both the reflectron ToF and SIMS ToF instruments; consisting of a dual Microchannel Plate (MCP) stack and a scintillator screen. This is paired with a photomultiplier tube (PMT), to obtain time-of-flight information, and a camera.

The expectations of a detector assembly is to convert the ion events at the end of ToF path into electronic signal. This signal should provide positional data (x and y coordinates) for ion events, as well providing a time stamp with high precision, preferably on the order of nanoseconds. Each event should be detected, with the number of events proportional to the electronic signal recorded. The detector setup utilised in these instruments is capable of outputting all the necessary information, with differences between the two introducing different resolutions in each case.

For the reflectron ToF mass spectrometer, there are dual-stack MCPs with a 32.75 mm outer diameter, 0.42 mm thickness and a 12° chevron bias angle (B1425, Photek, UK). This instrument also uses a home-built fast screen with exalite 404, made via sublimation onto an ITO plate. This method produces an even thickness of the dye, ensuring homogeneous fluorescence across the screen. The SIMS ToF mass spectrometer uses a detector assembly (Photonis 39042PS-P47) consisting of 40 mm diameter imaging quality Chevron MCPs, and a fiberoptic phosphor screen with P47 phosphor mounted to a 6" vacuum flange. The Exalite 404 screen is preferred over the P47 as the rise time offered by Exalite 404 ($\approx 3.5 \pm 0.2$ ns) is shorter than that of P47 (6.7 ± 0.2 ns), as well as an increased fluorescence and longevity [109].

The SIMS instrument detector assembly is mounted in a standard vacuum flange, however the reflectron ToF instrument differs in that the detector is mounted on a mobile platform to allow movement in two dimensions. This platform is controlled using two dials outside of the reflectron chamber, easily adjusting the angle of the detector within the chamber without breaking the vacuum. An adjustable detector allows for more control over the angle, so as to ensure the detector is perpendicular to ion flight path and minimising the lateral spread of ions across the detector.

The screen decay time can prove to be a limiting factor for each instrument with respect to its mass resolution. The mass resolution is inversely proportional to the FWHM of the ion ToF, with the reflectron ToF mass spectrometer having a FWHM of less than 8 ns. A 70 ns decay time offered by a P47 phosphor screen would significantly hamper its mass resolution, hence Exalite 404 is preferred to allow for high mass resolution experiments. The SIMS experiment is partially limited by

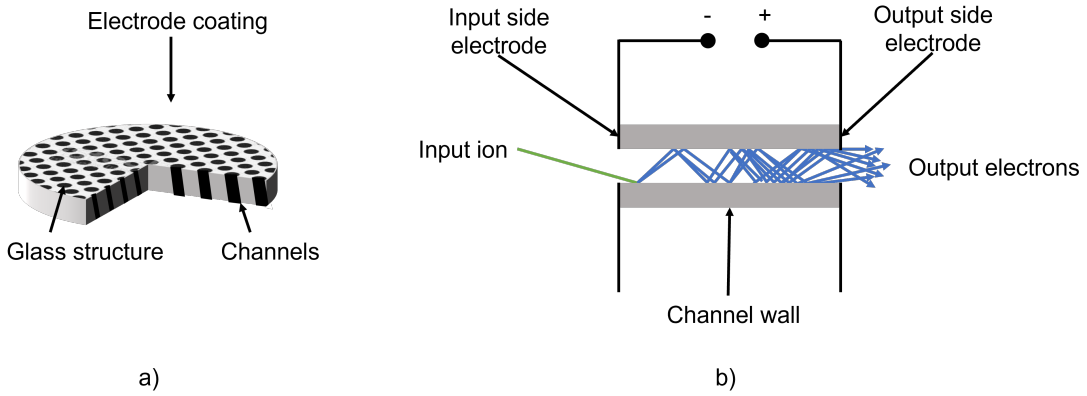


Figure 2.13: MCP assembly, a) displays a schematic of the structure, b) shows how the channels result in signal amplification.

the P47 phosphor screen, a choice made due to available resources upon assembly however an upgrade to a faster screen will occur in the near future.

2.4.1 Microchannel plates

The MCPs serve to amplify the signal received, comprising a circular glass slab with cylindrical open pores (microchannels) running throughout. These pores are in a regular array across the MCP, running parallel and at an angle to the surface (Figure 2.13). MCPs are used in position sensitive detection because of the ability to preserve positional information while amplifying the ion event. The large surface area with a high density of microchannels means events arriving at the entrance face are output at the same location, retaining the spatial information of the events. The active region of the reflectron instrument MCPs have a 12.2 μm centre-to-centre spacing between two adjacent pores, with a pore diameter of 10 μm. The inner walls of the microchannels are covered with a semiconductor, enabling the secondary emission process.

The front and rear faces of the MCP have a metallic coating (chrome), allowing these faces to act as electrodes. By applying a potential difference to these faces, each channel acts as a continuous dynode electron multiplier with a strong electric field across it. Firstly, ions will collide with the grounded front face of the MCP, entering the channels. An ion within a channel will experience the strong electric field, accelerating it. The channels lie at a 12° angle normal to the surface of the place, as

a result, the ion will collide with the channel wall. This initial collision will begin a cascade of secondary electron emission within the channels and propagates through the pore channel. The result is an amplified signal; the extent of the amplification is dependent on the electric field strength and MCP geometry. Operating the MCP with a grounded front face and its rear face held at 1 kV (maximum voltage), the gain is of the order of 10^4. Owing to the short channel length, the time required for this cascade to finish is very short, ideal for ToF analysis.

Within both instruments, there are two MCPs (dual-stacked) turned 180° along their axes with respect to each other, producing a chevron geometry. Stacking MCPs increases gain further, as the electron avalanche exiting the first plate will enter the second and begin a cascade in the next, further intensifying the signal. The geometry maximises collisions and secondary emission, producing more gain at a given voltage. The two MCPs are powered by a single power supply with a split of a 2:1 ratio (front:back) created using resistors. The rear face of the second MCP is held at the full voltage (V_{MCP}), the front face of the second MCP and the rear face of the first MCP are held at $V_{\mathrm{MCP}}/2$, and the front face of the first MCP is grounded. Provided the MCPs are operated under a high vacuum, and operated below their maximum voltage, ion collisions with the back plate of the MCP can result in a 1×10^6 electron gain leaving the back face of the MCP [110].

2.4.2 Scintillator screen

Exiting the back plate of the MCPs, the electrons are then accelerated towards the scintillator screen. The electrons collide with the Exalite 404 or P47 molecules, emitting photons via impact-induced fluorescence. The high energy electrons collide with the scintillator screen, transferring their energy to the phosphor molecule. At room temperature, the majority of electrons within the phosphor molecule will occupy the ground state according to a Boltzmann distribution. These ground state electrons will be excited to a higher energy level, after which they will undergo energy dissipation through vibrational relaxation and internal conversion (both non-radiative). Of the excited electrons, the majority electrons will now exist in

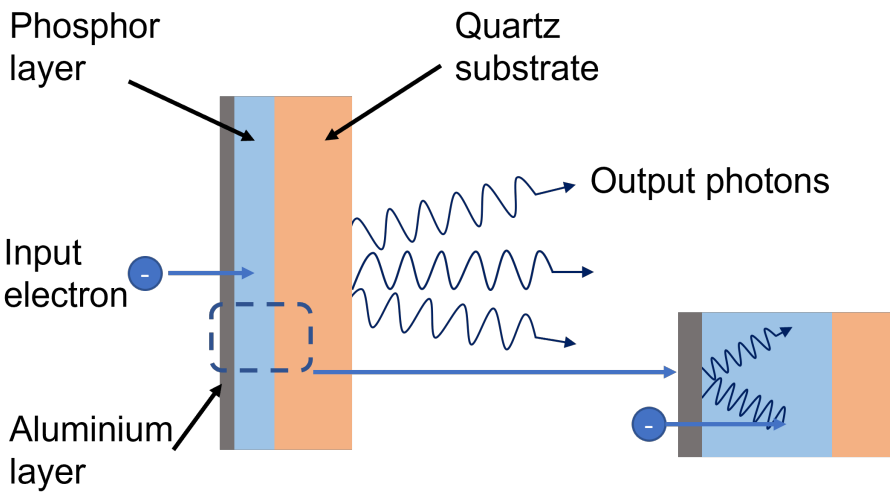


Figure 2.14: Structure of a phosphor screen. Electron impacts result in fluorescence and photons, output with the aid of an aluminium layer to reflect photons in the desired direction.

the first excited electronic state, from which they return to the ground vibrational level of the first excited electronic state, emitting a photon in the process.

The structure of a typical phosphor screen consists of an aluminium layer, phosphor layer, and a quartz substrate (Figure 2.14). The aluminium layer maximises the visible light output by reflecting photons towards the back face, where it can be detected by a camera or PMT. Without this reflection, these photons would otherwise be lost and not enter the camera or PMT, reducing intensity.

The phosphor molecule chosen for the scintillator screen can impact a range of parameters, which will affect the quality of the data recorded. The most relevant of these parameters is the fluorescence lifetime (the time spent in the excited state before decaying to the ground state via spontaneous emission). This lifetime, τ, is defined as the time taken for the number of excited electrons to drop to 1/e of the original population, and can be determined by the time taken for the fluorescence intensity to drop to 1/e of its initial value, as given by:

$$I = I_0 \mathrm{e}^{-t/\tau} \tag{2.5}$$

where I represents the fluorescence intensity at time t, and I_0 the initial intensity.

Table 2.1: Fluorescence lifetimes, τ, for a selection of phosphor molecules. The upper limit for fluorescence rise (t_{rise}) and fall (t_{fall}) time have also been listed as the rise and fall between 10% and 100%, adapted from [112].

Compound	τ (ns)	t_{rise} (ns)	t_{fall} (ns)	Signal strength
Exalite 404	3.7 ± 0.2	3.5 ± 0.2	7.7 ± 0.3	Strong
Exalite 398	9.8 ± 0.4	5.1 ± 1.1	26.1 ± 1.9	Strong
Exalite 384	4.7 ± 0.5	4.2 ± 0.8	9.3 ± 1.5	Strong
P47	69.3 ± 0.8	6.7 ± 0.2	13.0 ± 1.3	Strong

The relevance of τ in ToF-MS lies in its effect on mass resolution. With P47, the fluorescence lifetime is approximately 60 ns, meaning ion events arriving at the detector are dispersed over 60 ns, reducing the theoretically achievable mass resolution significantly after the FWHM of a ToF peak has been convolved with τ. Hence, selecting a phosphor molecule with a short fluorescence lifetime is very important for experimental mass resolution. Additional factors to consider are brightness, the emission spectrum, and the spatial resolution of the scintillator screen, all of which impact the cameras ability to detect photons and the spatial resolution of the image acquired.

Winter *et al.* studied a selection of materials, with the fluorescence times summarised in Table 2.1 [112]. The fluorescence lifetimes listed were determined as the upper limits for each material, due to other factors likely contributing to the broadening of a ToF peak (such as the ionisation laser pulse width, temporal spread of the ion pulse, and response time of the PMT). Hence the real τ is probably smaller than what is presented.

As a result of this research, an Exalite 404 screen was prepared and fitted on the reflectron ToF mass spectrometer, providing a fluorescence lifetime of 3.7 ns, and producing photons at a wavelength $\lambda \approx 400$ nm. The SIMS instrument is fitted with a P47 screen, providing a fluorescence lifetime of 69.3 ns.

2.4.3 Photomultiplier Tube

Photon emission from the scintillator screen can be recorded by a photomultiplier tube (PMT). The PMT can convert the optical signal into current, multiplying the current produced as much as 8 orders of magnitude, outputting the information

in the form of data. A PMT is able to detect light in the UV range through to the near-infrared range, able to to detect individual photons with low flux. It can measure with a combination of high gain, low noise, ultra fast response (of the order of 1 ns), and large collection area (∼1 cm), making it an excellent choice for the two mass spectrometers discussed in this thesis.

Photomultipliers are typically constructed with an evacuated glass tube, with an entry window on one side. Incident photons will enter the window, which is coated internally with a thin layer of a photocathode material. This photocathode material is layer of a photosensitve semiconductor material, which upon being struck by an incident photon, emits photoelectrons by the photoelectric effect, and releases them into the vacuum tube. The photocathode is held at a negative potential (about -1 kV) to help accelerate the photoelectrons away from the surface. The number of photoelectrons produced per incident photon is proportional to the photon energy.

With the help of a focusing electrode, these photoelectrons are then directed towards an electron multiplier. This electron multiplier is made up of a series of electrodes called dynodes (Figure 2.15). Using a resistor chain, the dynodes increase in potential by ≈+100 V with each subsequent dynode. The group of primary electrons output from the photocathode are directed to the first dynode, accelerated by the electric field, gaining kinetic energy. They collide with the first dynode, generating more low energy electrons via secondary emission, which are then accelerated towards the second dynode. This process continues, with an exponentially-increasing number of electrons produced at each stage.

At the end of the electron multiplier is an anode. At this stage, there are a large number of electrons arriving. The electrons arriving at the anode produce a sharp current pulse, which can be displayed on an oscilloscope. A PMT is capable of recording and amplifying even a low photon count, generating a precise record of when a photon is emitted from the scintillator screen, and thus generating a time-of-flight mass spectrum. A black shroud is used over the detector and PMT to minimise the amount of ambient light incident on the PMT.

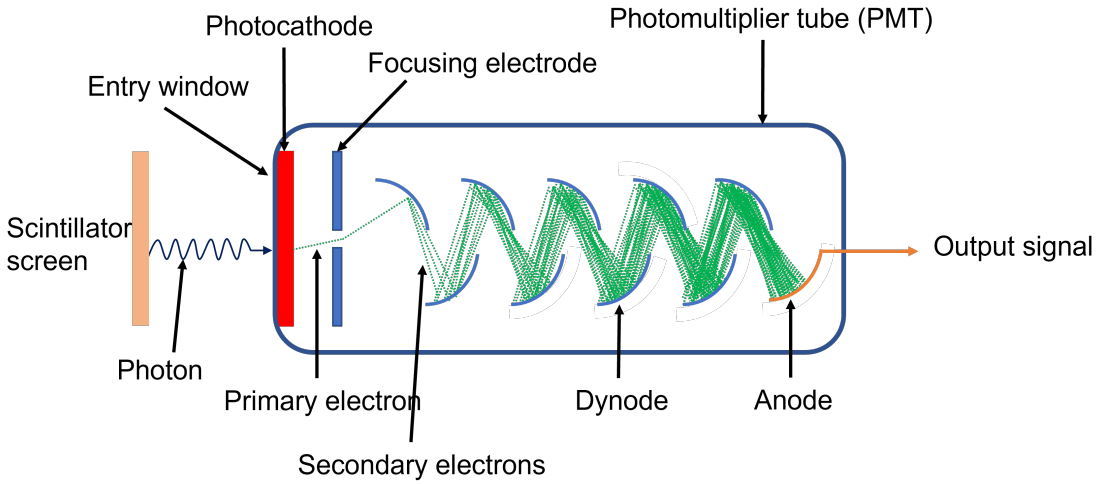


Figure 2.15: Schematic of a photomultiplier tube (PMT)

2.5 Cameras

To extract the spatial information from the screen, a camera is used. Two different cameras are used in this thesis: a Charged Coupled Device (CCD), and a Timepix based camera known as the Timepix3 camera. The CCD camera has the advantage of a large pixel array, and thus can be used to record highly spatially resolved ion images. It does not however have the ability to record time information, which is where the Timepix3 camera comes in; the CMOS sensor can be used for multi-mass ion imaging. While capable of providing time stamping information, the Timepix3 chip has a smaller pixel array than the CCD, and with a reduced active area, resulting in a worsened spatial resolution. This is a result of the circuitry which enables multiple ion hits to be recorded within each experimental cycle.

2.5.1 CCD

CCD cameras can record two dimensional optical images from photons emitted off the scintillator screen. An intensified CCD camera (Photonic Science) is used for both instruments, with a 768 × 576 pixel array and a temporal resolution of 50 ns. This camera is intensified through the use of additional MCPs to further amplify signal received from the phosphor screen.

Photons are incident on a pixel within the CCD camera, which converts the incident photon into electrons. The process for this is once again the photoelectric effect - each pixel is constructed by etching an integrated circuit into a semiconductor surface. The CCD is an array of coupled capacitors, such that the electrons produced are stored in the capacitors within the pixel until it is converted until a digital signal. This conversion occurs by movement of an electron packet from the original pixel, to the measurement electronics at the serial output. This creates a voltage, by which the packet can be quantified. These signals are then compiled into a corresponding image for each experimental cycle, producing a two dimensional plot of the electrical signal.

CCD cameras have a slow readout speed, with a typical frame rate less than one hundred frames per second. Given a time-of-flight with peak separation of the order of microseconds, this frame rate is insufficient for acquiring time-of-flight data. Instead, the CCD camera is gated over a particular time window, determined by the trigger delay and width set by the pulse generator (as discussed earlier). Setting this time window over a particular ToF peak, the CCD camera can record the spatial information for that species only. In addition to the time window, the pulse generator also sets a threshold voltage for the CCD camera. This threshold serves to minimise background signal, a pixel is activated only if the threshold voltage is exceeded.

The physical arrangements for the reflectron ToF mass spectrometer and the SIMS instrument differ. The reflectron ToF instrument is horizontal, and thus the CCD camera is positioned horizontally in front of the detector on a scissor jack to allow for easy position adjustment and a stable platform. The screen is 25 mm in diameter, requiring a camera lens position of 175 mm away for optimal focusing. The SIMS instrument differs in that it has a vertical flight path, thus the camera must point downwards towards the detector. It rests on a mount elevated 55 mm from the detector. In both cases, the detector, camera, and PMT, are covered with a black shroud to reduce ambient light detection and maximise contrast on the screen.

The CCD is connected to a CRT TV, converting the analogue video signal into real-time ion images. This aids in the laser alignment on the sample surface for the

reflectron instrument; the intensity distribution across the surface can be seen to vary when the laser position is adjusted with the final optics, having a live video feed allows for fine tuning of the position until an even intensity distribution is achieved.

In addition to this, the CCD camera is connected to a computer. The conversion from analogue to digital data is done using a frame grabber (Pleoras iPORT AnalogPro External Frame Grabbers). This device captures individual still frames (8-bit, 768×576 pixels) from an analogue video signal. A defined threshold discards (sets to zero) any pixel below a certain intensity, classifying it as noise, and improving the image quality. This threshold needs to be carefully set to avoid discarding real ion events, while also effectively filtering out the unwanted noise. The computer can then process these frames, and will be described in Section 2.6.

2.5.2 Timepix3 camera

Mass spectra images were recorded using the Timepix3 camera (Figure 2.16), an event-triggered, time-stamping complementary metal-oxide-semiconductor (CMOS) device [76, 113]. CMOS devices have enabled the collection of spatial distribution for multiple ToF peaks within one experimental cycle. CMOS chips contain large arrays of transistors, which are composed of a photodiode and amplifier. The photodiode accumulates the charge from a photon, and these charges are then converted to a voltage, amplified, and transmitted. Compared to a CCD, a CMOS sensor uses little electrical power, requiring only one power source. The simultaneous collection of (x, y, t) means that microscope MSI can be applied to irreproducible samples, since each mass peak can produce an image and be recorded all within one experiment. A time-stamping camera is essential for utilising the high-throughput capability of microscope-mode MSI.

The CMOS detector within the Timepix3 chip has a 256 × 256 pixel array (14 mm × 14 mm), with each pixel being 55 μm × 55 μm [114, 115]. It is capable of recording multiple ion events within each experimental cycle and has a timing precision of 1.5625 ns [116]. The Timepix3 chip allows for readout of each hit pixel and can achieve a throughput of up to 40 MHits s^{-1} m^{-2} [117]. This chip evolved

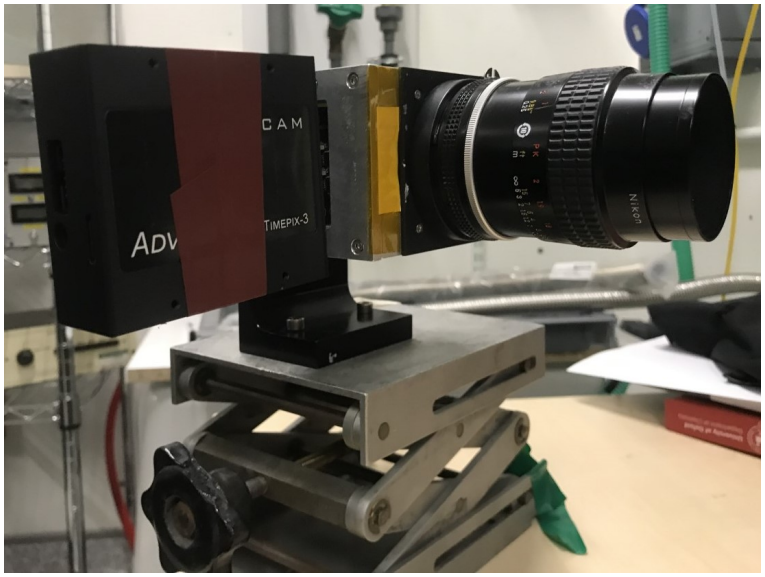


Figure 2.16: Image of the Timepix3 camera. Positioned on a scissor jack, with a lens and connected to the AdvaDAQ readout system.

from the Timepix chip, with the key difference is the event-based readout rather than a frame-based readout. The Timepix3 chip instead outputs a continuous stream of data, requiring a USB 3.0 connection to a computer to sustain the necessary speed. The other distinguishing feature is the ability to measure the hit amplitude simultaneously with time of arrival - this is output in the form of time-over-threshold (ToT), a measure of the time taken for the signal to fall back below the threshold.

The readout from the chip is provided by the USB 3.0 AdvaDAQ system, paired with PiXet-Pro pixel acquisition software to control Timepix3 camera for the experiments in this thesis, [118]. PiXet controls the real time display, viewable in multiple different modes, and allows for chip calibration to ensure all pixels across the chip have the same threshold and response to photon event. PiXet also records the Timepix data, which consists of five columns: Matrix index, Time-of-Arrival (ToA), Time-over-Threshold (ToT), fine Time-of-Arrival (fToA), and overflow. All of this is output as a .t3pa file, recorded using a USB connection to a computer. Optimal operation for the experiments conducted had data files of 5 s duration (50 laser shots). This was chosen to keep the file size small, each file was typically less than 4 MB, and eased data processing time.

Like the CCD camera, the Timepix3 camera is also positioned on a scissor jack close to the scintillator screen with an F-mount Nikon (55 mm f/2.8 AI-s) lens to maximise photon flux at each pixel. Within PiXet, the threshold is set to 1.39 eV, minimising the effect of ambient light and cosmic rays on the sensor. Similarly to the CCD camera set up, the detector, camera, and PMT, are all covered in a black shroud. At present, the Timepix3 camera has only been used on the reflectron instruments due to limitations in its operation, which are discussed in detail in Chapter 4.

2.5.3 Image processing

When an ion impacts the front MCP face, it produces a electron packet at the back face of the MCP. There is a gap between the two MCPs, during which the electron packet has time to spread out in space. The result is multiple channels on the second MCP will receive electrons, generating additional electron cascades. There is also a gap between the back face of the second MCP, and the scintillator screen, during which the electron packets will once again continue to expand in space. This results in a small area of the scintillator fluorescing, rather than one spot, which is then recorded as a group of pixels on the cameras (see Figure 2.17). The result of this is a blurring of the final image, as the pixel intensity of what is a single pixel event, is spread over multiple pixels.

The photons emitted from the scintillator have a two dimensional Gaussian distribution, which is observed approximately among the group of pixels illuminated. By locating the centre of this Gaussian distribution, the blurring effect can be minimised. This method is called “centroiding”, and assigns a single pixel position to each event, rather than accepting every pixel event in the summated image.

With the CCD camera, Labview IMAQ “Find Circles function” is used to centroid the binary data (intensity information is ignored to account for inhomogeneity across the detector). The ion event when detected by the CCD camera typically has a circular shape, owing to the regular arrangement of pores across the MCPs. The Labview function will inspect an image, identify any circles and pinpoint the centre, even if it overlaps with multiple other circles. The function also allows for a minimum

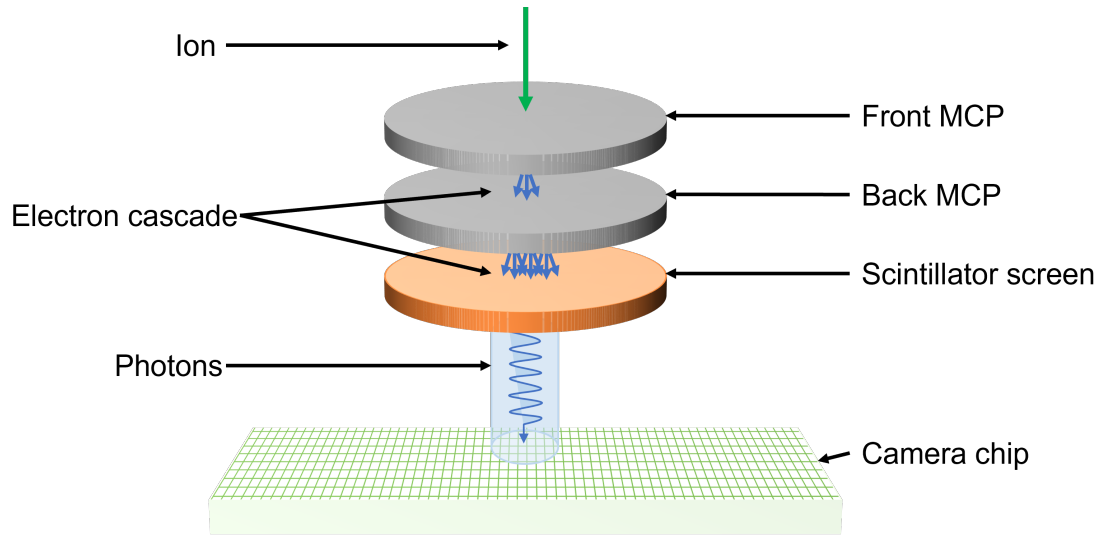


Figure 2.17: Cartoon depicting the cause of blurring from a single ion event. One ion event can be recorded across multiple pixels on the camera.

circle radius to be defined, preventing background noise from being included in the process. The centre of the identified circles is then set as the origin pixel for an ion event. The centroiding process for Timepix3 data works in the same way, however, is applied in post processing rather than during data acquisition and performed using a Python script, written by Wood *et al.* [81].

Centroiding is done to each frame of the images output by the cameras, after which the frames are summated. In event counting mode, the value for each coordinate (x, y) gives the total number of ion events at that particular location during the data acquisition. Centroiding is performed in real-time with the CCD camera, outputting only the centroided ion image, while Timepix3 data is centroided in the post-processing stage.

2.6 m/z calibration

Both instruments are ToF-MS and output data in the same way - a string of time against intensity from the PMT, in addition to an image from a camera. The PMT and Timepix3 data needs to be converted from time-of-flight, into m/z information. The conversion is dependent upon the specific setup and parameters chosen for

the experiment, thus a calibration must be performed each time an instrument parameter is changed for good mass accuracy.

In order to convert from time-of-flight to m/z, a calibration equation can be applied. This calibration equation can be collected by recording a mass spectrum of a well known sample with clearly defined m/z peaks. These defined peaks can be used to determine the relationship between the two variables, valid for that particular experimental setup. Any change in experimental parameters requires a new calibration equation to be determined.

As discussed in Section 1.2, the relationship between m/z and a particles' time-of-flight, t, can be described with:

$$t = k\sqrt{\frac{m}{z}}, \tag{2.6}$$

such that there is linear proportionality, k, between t and $\sqrt{m/z}$. The function between time and the mass to charge ratio can be fitted with a linear equation,

$$y = a + bx, \tag{2.7}$$

where y corresponds to t and x to $\sqrt{m/z}$. The slope, b, describes the linear dependence between the two variables, and the y-intercept, a, accounts for factors which may shift the entire time-of-flight, such as the Q-switch timing and electric field strength.

To utilise Equation (2.7), a ToF spectra with known m/z peaks needs to be produced. Examples of some calibration compounds include: Red Phosphorus, laser dyes, perfluorotributylamine, perfluorotripentyl, and polyetheylene glycol. Initial calibrations within the reflectron instrument were conducted using Rhodomine B, while the SIMS instrument typically uses metallic samples due to the highly characteristic and broadly spaced m/z peaks. Rhodamine B was chosen as it ionises easily and has been extensively characterised, thus its peaks are well defined [79, 109]. Red phosphorus can also be used as a calibrant, as its fragments are multiples of phosphorus (30.9 Da) and spans a wide range of masses, however it produces a less consistent ToF spectra.

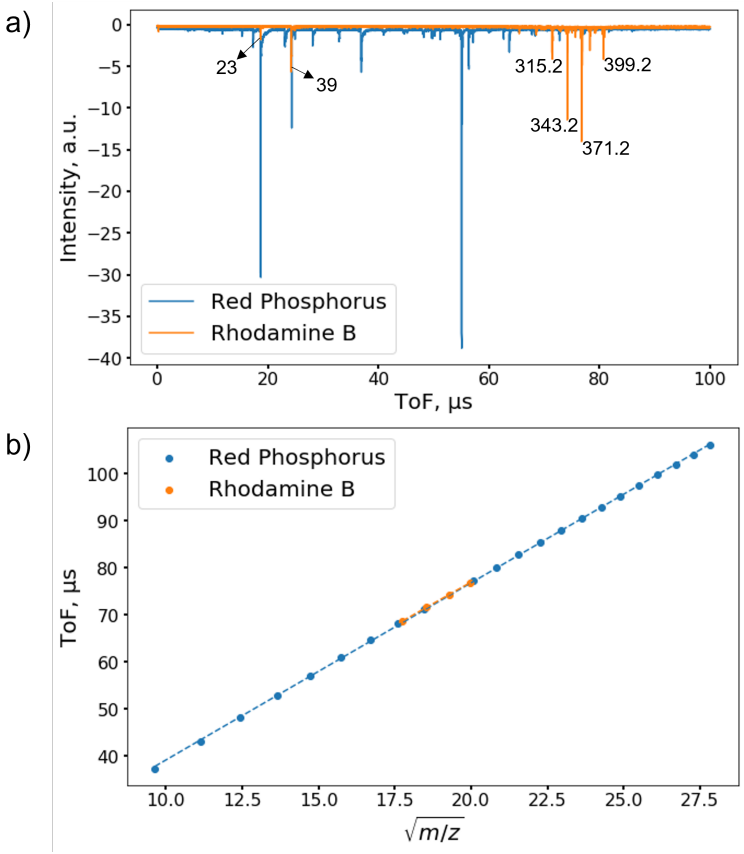


Figure 2.18: Converting a ToF spectrum to a mass spectrum. a) shows reference ToF spectra for red phosphorus and Rhodamine B, with key Rhodamine B peaks labelled with the peak mass, Da. b) shows the calibration line obtained from known peaks.

The major peaks are identified from the spectra, four of which are from the laser dye Rhodamine B (315.2 Da, 343.2 Da, 371.2 Da, 399.2 Da) and two from Na^+ (23 Da) and K^+ (39). Between these six peaks, a linear regression line can be plotted using Equation (2.7). The same procedure is applied to the red phosphorus spectra, with peaks expected at $n \times 30.9$ Da, where n is the number of phosphorus atoms in the fragment ion. The approximate peak location was determined, after which each ToF peak is assigned to the expected mass and a regression line plotted. Both of these calibration plots are shown in Figure 2.18.

The regression line for each compound is:

$$\text{Rhodamine B: } y = 2.9 + 3.7x, \mathrm{R}^2 = 0.999 \tag{2.8}$$

$$\text{Red phosphorus: } y = 1.5 + 3.8x, \mathrm{R}^2 = 0.998 \tag{2.9}$$

Both spectra were obtained under identical conditions, and have only minor differences which can be attributed to the number of peaks assigned in red phosphorus compared to Rhodamine B - a larger range offers greater confidence in the linear regression. As such, when investigating spectra which exceed the bounds of the Rhodamine B peaks, red phosphorus should be used as the calibrant. However, due to ease of ionisation and reproducibility, Rhodamine B is otherwise used.

Using these functions, m/z can be estimated using:

$$\frac{m}{z} = \left(\frac{t-a}{b}\right)^2 . \tag{2.10}$$

This can be applied to any spectra, provided they are obtained under the same experimental conditions, to determine the mass of any peak within the range from which the calibration was obtained. If extrapolated outside of this range, it is not possible to be confident in its application, as it may cease to be a linear relationship.

2.7 Summary

This chapter has outlined two different instruments, both of which are complex systems. The reflectron ToF mass spectrometer instrument is an ion microscope time-of-flight mass spectrometer paired with a reflectron and can use laser ablation or MALDI. The SIMS ToF mass spectrometer instrument is also an ion microscope time-of-flight mass spectrometer, however without a reflectron, and using a C_{60}^+ ion gun to generate secondary ions.

Methods for sample preparation have been described, followed by a description of the detector assemblies used in each instrument. The different cameras have been detailed, as well as how the data produced from the instruments is calibrated. The instruments and methods outlined in this chapter will be used in the experiments described later in this thesis, with the goal of improving the capabilities of the two imaging mass spectrometry instruments.

3

Characterisation of a Reflectron Ion Microscope

Contents

3.1 SIMION 75
3.1.1 Potential Arrays 75
3.1.2 Defining Ions 77
3.1.3 Workbench 80
3.1.4 LUA 81
3.1.5 Output Results 81
3.1.6 Genetic Algorithm 84
3.2 Improving the Spatial Resolution 85
3.2.1 Theory 86
3.2.2 Simulations 87
3.2.3 Experimental Results 89
3.3 Zoom lens 92
3.3.1 Reflectron lens 93
3.3.2 Additional einzel lens 101
3.3.3 Using the existing einzel lens as a zoom lens 113
3.4 Conclusion 118

This chapter focuses on the reflectron ToF instrument, beginning by introducing the modelling software, SIMION, and how the simulation software accurately models an ion flight path within electric and magnetic fields. A simulation of the reflectron ToF mass spectrometer has been prepared using this software, produced by Guo

and Burleigh [30, 105], and further developed in the subsequent sections of this chapter to investigate the capabilities of the instrument.

Previous work on the reflectron ToF mass spectrometer in our laboratory has involved the addition of a reflectron to a linear ToF mass spectrometer, followed by the implementation of firstly a single-field pulsed extraction differential acceleration (PEDA), then double-field and time-variable PEDA, as described in Section 1.4 [30, 105]. Consequently, the reflectron ToF mass spectrometer can attain an effective mass range of 300-600 Da with the time-variable PEDA technique, achieving a simultaneously high mass resolution (8,000 $m/\Delta m$) and spatial resolution (18 $\pm$ 6 μm) [101].

Previous work has focused on attaining the best mass and spatial resolution simultaneously, however this does not reflect the true capability of the instrument if one of these factors is prioritised over the other. Section 3.2 seeks to explore if a better spatial resolution can be obtained using the reflectron ToF mass spectrometer, while maintaining a high mass resolution.

As discussed in Chapter 2, samples within the reflectron ToF mass spectrometer are placed on a sample plate, which can be rotated to allow a maximum of four samples to be loaded into the instrument. This design however has the samples in a fixed location, thus only a specific area of the surface can be imaged - which may not necessarily be the region of interest. It would expand the utility of the instrument if locating and imaging a specific region of interest were possible.

A step towards achieving this could be done by increasing the field of view. The instrument currently obtains a magnification of $\times$93, producing a field of view ~270 μm [30], which allows for high spatial resolution images, however does restrict images to a very small region of the sample surface. Introducing an adjustable sample stage would allow for more of the surface to be imaged, however this would take a long time at this magnification. If variable magnification can be introduced to the instrument, reducing the magnification would result in the field of view increasing, allowing for a larger portion of surface to be imaged and a region of interest identified. After this, the instrument could be returned to the

greater magnification to produce a high spatial and mass resolution image of the desired region. A range of methods to achieve variable magnification is explored using simulations in Section 3.3, utilising existing electrodes already present, and investigating the addition of an einzel lens along the flight path.

3.1 SIMION

SIMION is a commercial ion optics simulation program capable of modelling ion trajectories within electric and magnetic fields [119]. The program was originally developed in the late 1970s as part of a Ph.D thesis by Don McGilvery at La Trobe University, Melbourne, Australia [120]. David Dahl later adapted it for PCs in 1985 at the Idaho National Laboratory, followed by Adaptas SIS for version 8.0 onwards.

SIMION has the capability to calculate the electric and magnetic fields of complex systems, followed by calculating the motion of charged particles (ions or electrons) within these fields. Additionally, the fields can exist as either static or time-varying. It is an incredibly powerful tool, and is able to predict experimental results accurately and aid in electrode design of ion optics.

It is for this reason that it was chosen to model the two experiments in this thesis: one for the SIMS instrument, another for the reflectron instrument. This section uses the reflectron instrument set up to describe the SIMION features.

3.1.1 Potential Arrays

To generate a magnetic or electric field within SIMION, a potential array (PA) needs to be created. Within the software, a potential array consists of a series of points which defines the potential and type of field. This can be produced using a mathematical geometry as described by a geometry (GEM) file, thus modelling an electrode within the system. The GEM file uses constructive solid geometry (CSG) to define electrode geometries; CSG allows for the creation of a complex surface or object from the combination of simpler objects (e.g., a rectangular slab with a cylinder hole cut through it). An electrode is defined by its origin

(X, Y, Z), shape, length, width/radius, symmetry, and axis of rotation (elevation, rotation, and azimuth angle).

As previously mentioned, a PA is a 2D or 3D representation of the potential for an experimental setup composed of electrode or non-electrode points. The potential array can utilise symmetry (planar, cylindrical, or mirroring) to ease creation as well as reducing the computational load - each grid point increases the amount of RAM required, which can increase significantly with large volume arrays if symmetry isn't utilised. An electrode point acts as a Dirichlet boundary condition, which specifies the value at the boundary of the domain. The electrode points restrict the potential at the surface of the electrode, can be set to a specified value, and is uniform over the surface of the entire electrode. Additionally, the PA electrode points emulate a physical boundary; if a particle collides with it, the particle will "splat" and end its flight path.

To determine the field existing in the empty space between the electrode points, the Laplace equation is used. There are two boundary conditions specifying the domain of the function; the Dirichlet boundary condition, defining the voltage on the surface of the electrodes, and the Neumann boundary condition, which describes the electric flux through the electrodes. During refinement, Laplace's equation is solved and the electrostatic potential at any point is calculated as a function of the potential of the surrounding points. In this case, the field is calculated when no particles exist in the space, following the zero charge density assumption [121].

The Laplace equation is

$$\vec{\nabla} \cdot \vec{E} = \nabla^2 V = 0 \tag{3.1}$$

$$\frac{\delta^2 V}{\delta x^2} + \frac{\delta^2 V}{\delta y^2} + \frac{\delta^2 V}{\delta z^2} = 0 \tag{3.2}$$

for electric field, E, and potential field, V. Laplace's equation states that the divergence of the electric field is zero everywhere. Once a PA has been designed, any non-electrode PA points are taken as Neumann boundary conditions, as determined from the first derivative of the Laplace equation, and is taken to be zero for the purpose of this simulation setup.

In order to calculate the electric field in the empty space, SIMION undergoes a process termed "refining". This process uses the potential of the electrode array points to estimate the potentials of non-electrode points to solve the Laplace equation numerically. The average potential of the nearest four (2D arrays) or six (3D arrays) neighbour points is used as the basis for estimate the potential of each non-electrode point in the array. This will occur for each point in the array in the iteration. Successive iterations refine the estimates until the array converges. The quality of the estimated potentials is determined by the grid density, however, as mentioned previously, a higher grid density has a computational cost, thus is a balance between the two factors.

Following refinement, all points within the PA have been calculated, completing the array. The PA can then be viewed in either potential energy (PE) view, allowing for the field to be visualised as a surface map, or as a simple equipotential array. Any charged particle can then be flown through the PA, experiencing the effect of the field on the particle, as calculated using Newtons second law.

Given the simulation is designed to replicate the experimental set up, the reflectron instrument simulation contains four PAs: the ion optics stack, deflector plates, reflectron stack, and detector. These groupings are made up of multiple individual PAs to account for every electrode used experimentally. An example of a SIMION workbench is shown in Figure 3.1, with each of the labels indicating the separate PAs.

3.1.2 Defining Ions

Within SIMION, the initial conditions of particles can be defined in a FLY2 file. This file contains a number of parameters, with the key parameters being the charge, mass, and initial velocity. The initial velocity is determined by specifying a source position and a directional distribution that particles should fly in, for example, in a cone shape or by using specific azimuth and elevation angles (Figure 3.2).

The flexibility provided by SIMION for initial particle conditions allows one to easily simulate experimental behaviour. This allows for the ions created by

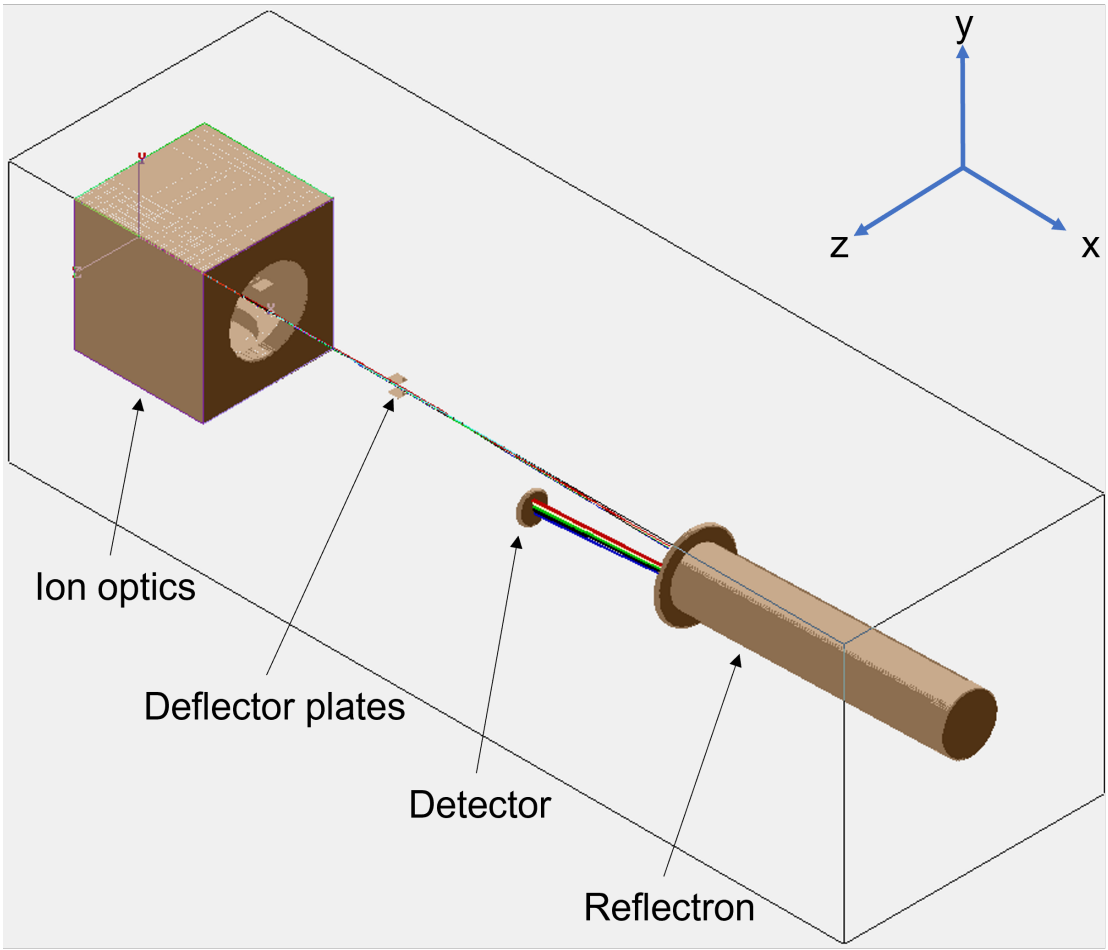


Figure 3.1: SIMION workbench designed for the reflectron ToF mass spectrometer. Each labelled component depicts a separate potential array. The coordinate axes of the workbench is indicated in the top right corner. The ion flight path has also been displayed.

the MALDI/LDI ionisation process to be readily replicated. Given the nature of the laser ablation method, the generated ions have a non-zero range of initial velocities. This spread of velocities results in a reduction of mass and spatial resolution for ToF mass spectrometers.

Two key factors need to be determined: what is a realistic initial velocity, and how does this vary with m/z value? A number of studies looking at polypeptide molecular ions, covering a mass range between 1000 to 15,600 Da, found an initial ion velocity distribution of approximately 300 to 800 $\mathrm{m\,s^{-1}}$ [122], and across a mass range of 200 - 16,00 Da, a mean axial velocity (along the ToF axis) of 500 $\mathrm{m\,s^{-1}}$ [123–125]. Thus it was concluded that in MALDI experiments, mass may affect

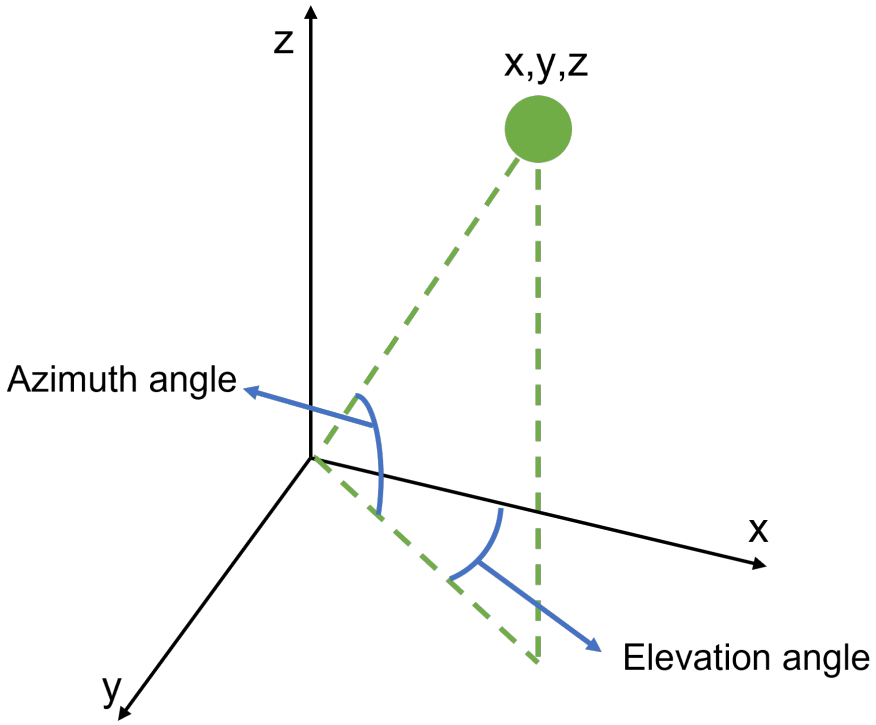


Figure 3.2: SIMION coordinate axis used to define an ion position

Table 3.1: Initial ion velocities of analytes ions with different matrices, adapted from [122]

Analyte	Matrix	Ion	m/z	v_0
Maltotetraose	2,5-DHB	[M+Na]+	689	187 ± 97
Human-milk oligosaccharide 1	2,5-DHB	[M+Na]+	730	340 ± 10
Maltoheptaose glycosylamine	2,5-DHB	[M+H]+	1154	515 ± 66
Melittin	2,5-DHB	[M+H]+	2848	530 ± 52
Bovine insulin	SINA	[M+H]+	5735	332 ± 29
Bovine insulin	αCHCA	[M+H]+	5735	291 ± 51
Bovine insulin	THAP	[M+H]+	5735	306 ± 32
Bovine insulin	2,5-DHB	[M+H]+	5735	543 ± 40
Carbonic anhydrase	2,5-DHB	[M+H]+	29025	599 ± 119

the average initial velocity (as demonstrated by Table 3.1), but has no effect on the mean initial ion axial velocity distribution. The largest effect influencing the velocity distribution was found to be matrix choice and factors which may impact crystallisation, such as solvent choice or additives [124]. It was found that the velocities were largely independent of the molecular mass, laser fluence, and ion charge state and polarity [123–125].

Zhang and Chait investigated the radial velocity distribution from MALDI, which found that the radial component was considerably smaller than the axial component, producing a strongly forward peaked (self collimated ion beam) MALDI plume [125, 126]. This suggests that the initial angular distribution of ions are also strongly forward peaked, and the result lends support to proposals of a jet expansion model for ion generation with MALDI. This jet expansion model proposes a layer of the matrix is excited by the laser, after which the matrix molecules experience a rapid phase transition to a high pressure fluid and expands adiabatically in the vacuum into a jet. The jet carries the large analyte ions into the gas phase, resulting in the contents of the jet having a similar mean velocity.

The angular velocity was fitted with a $cos^n\theta$ distribution, where n is shown to be dependent on mass. The distribution for protonated dynorphin 1-13 (1,605 Da) is fitted well when $n = 28$, whereas a protonated CHCA dimer (379 Da) appears best fit with $n = 12$. They concluded that heavier peptides exhibit a higher degree of forward peaking than a light matrix ion.

As such, the initial ion directions given by the azimuth and elevation angle should therefore be defined with a $cos^n\theta$ distribution, with the mean direction normal to the sample surface. However, SIMION does not have an option for a $cos^n\theta$ distribution of angles, instead it is approximated by a Gaussian function. In order to replicate a $cos^n\theta$ function, the FWHM is set to 60°, and modal direction is equal to zero, as based on previous investigations estimating the resolutions of a Rhodamine B peak (343 Da) [109, 122, 127].

3.1.3 Workbench

Most systems modelled in SIMION utilise multiple potential arrays (PAs). This is where the ion optics workbench comes in - acting as an empty 3D rectangular volume of space in which potential arrays can be placed and manipulated in space. The PAs are arranged in space in the order in which a particle would experience each field. The positions of which can be easily adjusted and manipulated, allowing for easy testing and optimisation of electrodes along the flight axis.

This work bench is saved as a .IOB file, which connects together the potential arrays, the ions contained within the .FLY2, and the LUA code which operates the entire simulation. The IOB specifically defines the simulation universe, including the dimensions, scaling, rotation, and translation of PAs. The IOB can also operate the PAs by applying the voltages on fast adjust PAs.

A basic PA has its electrode potentials defined, it is then refined to solve for non-electrode potentials. A fast adjust PA is similar, except the electrode potentials are not explicitly defined, and instead are defined later after refining. This feature utilises the additive property of the Laplace equation, whereby each independent solution is linearly combined for the desired combination. Doing so allows for quick adjustment of the electrode potentials but does not require the time-intensive re-refinement step.

3.1.4 LUA

Operating the simulation is a user program written using LUA. Other programming languages can be used, but LUA was chosen due to its efficiency and simplicity.

The LUA program performs a number of roles, starting with initialising the variables and the system - setting the potential for each electrode. Additionally, any functions required later in the code are defined. The next phase is initialising ion flight, alongside the application of any time-dependent voltages to electrodes, such as time-variable PEDA, as discussed in Chapter 1. The final phase is the outputting of data, and any desired calculations.

3.1.5 Output Results

Ions travel from the repeller, guided through the system under the effect of the various PAs, until a collision occurs with either a "wall" or a detector plane. At this point, the particle "splats", resulting in the termination of the trajectory. If this splat occurs on the detector plane, the ToF and positional coordinate (X,Y,Z) are recorded. From this, it is possible to determine the field of view, ion transmission efficiency, the magnification, mass resolution, and spatial resolution.

For this simulation, the initial ion positions are defined as five equally spaced discrete point sources, with the first point source set as the centre of the repeller and the rest aligned along the y-axis. Owing to the cylindrical symmetry of the ion optics, this one dimensional arrangement of ion sources can be used to represent the two dimensional nature of the sample surface.

The simulation can record the flight time for each ion, from which we can calculate the mean time ($\bar{t}$) and the standard deviation of the arrival time distribution (σ_{ToF}) for the entire collection of ions flown. For a single mass and charge, the mass resolution of this simulated arrangement is defined as

$$m/\Delta m \approx \frac{\bar{t}}{2\Delta t} = \frac{\bar{t}}{2 \cdot 2\sqrt{2ln2} \cdot \sigma_{ToF}} \approx \frac{\bar{t}}{4.71\sigma_{ToF}}, \tag{3.3}$$

where Δt is the full width half maximum (FWHM). Assuming a normal distribution for arrival time, $\Delta t/\sigma_{ToF} = 2\sqrt{2ln2}$. Another assumption is made for this expression to be valid: it requires the detector response time to not be a limiting factor, i.e. with a response time negligible compared with Δt.

As discussed in Chapter 2.4.2, the fluorescence lifetime of the scintillator screen is a key contributor to the overall detector response time. Consequently Equation 3.3 must be convoluted with the detector distribution. Assuming both ToF distribution and the detector lifetime distribution are close to Gaussian-like functions, the convoluted standard deviation of the observed ToF signal, σ_t, will also be Gaussian and can be described by:

$$\sigma_t = \sqrt{\sigma_{ToF}^2 + \sigma_{det}^2}. \tag{3.4}$$

Hence, the mass resolution with convolution is given by

$$m/\Delta m \approx \frac{\bar{t}}{4.71\sigma_t} = \frac{\bar{t}}{4.71\sqrt{\sigma_{ToF}^2 + \sigma_{det}^2}}. \tag{3.5}$$

where σ_{det} is the standard deviation of the detector response time.

As a result of the scintillator temporal spread, a maximum mass resolution limit exists:

$$\lim_{\sigma_{ToF} \to 0} \Delta t_t = 2\sqrt{2ln2} \cdot \sigma_{det} = 2.355\sigma_{det}. \tag{3.6}$$

From the ion splats, the instrument magnification can also be determined. As with an optical microscope, the ion image is enlarged during the ions flight to the detector plane. The magnification, M_i, is defined as the distance between the i^{th} splat centre (Y_i) and the first splat centre (Y_1), divided by the distance between the two point source locations, where d is the distance between two adjacent point sources:

$$M_i = \frac{Y_i - Y_1}{(i-1)d}(i = 2, 3, 4, 5). \tag{3.7}$$

The splat centre is determined as the mean Y position for each cluster of ions originating from the same point source. Thus the mean magnification $\bar{M}$ is taken from the mean of individual cluster magnifications, M_i.

The final quantity required from the simulation is the spatial resolution. Given that there are five discrete point sources, which upon flight through the simulation, arrive as five groups distributed along the y-axis of the detector plane. The standard deviation, σ_y^i, for the position along the y-axis for each cluster of ions originating from a point source can be calculated. Using σ_y^i, the FWHM of distribution for each cluster at the detector plane, $\Delta R_{50\%}^i$, can be given by:

$$\Delta R_{50\%}^i = 2\sqrt{2ln2} \cdot \sigma_y^i \approx 2.355\sigma_y^i(i = 1, 2, 3, 4, 5). \tag{3.8}$$

Hence the spatial resolution across the surface, $\Delta r_{50\%}^i$,

$$\Delta r_{50\%}^i = \frac{\Delta R_{50\%}^i}{M_i}(i = 1, 2, 3, 4, 5). \tag{3.9}$$

As M_i has been calculated relative to M_1, when using Equation 3.9, M_1 must be estimated by either taking the value to be the same as M_2, or $\bar{M}$.

Experimentally, the spatial resolution is determined from the distance between 20% to 80% of the maximum intensity of an image edge. It is for this reason that well defined patterns (such as one of the grid patterns described previously) are often used to determine the spatial resolution for an instrument. Provided the size of the grid pattern is an order of magnitude greater than the spatial resolution, the rising edge can be clearly distinguished and convolved with a Gaussian response function.

As such,

$$\Delta R^i_{20-80\%} \approx 1.683\sigma^i_y \approx 0.715\Delta R^i_{50\%} (i = 1, 2, 3, 4, 5). \tag{3.10}$$

describes the relationship between the standard deviation σ^i_y and the 20% to 80% distance, $\Delta R^i_{20-80\%}$, quantifying the spatial resolution [128].

3.1.6 Genetic Algorithm

A genetic algorithm (GA) is based on a natural selection process and uses biologically inspired operators to solve constrained optimisation problems [129]. Due to the complex nature of the simulations used in this thesis, it has been necessary to use a GA to find the optimal values for instrument variables in order to improve the performance.

Within this thesis, the GA is used to narrow down the search field when investigating many variables. The reflectron ToF mass spectrometer simulation contains a large number of parameters which are difficult to explore without the use of a GA. The algorithm is used to narrow down the search field, in order to later run finer simulations based upon the results.

Step one of the algorithm is initialisation; after upper and lower limits for the desired variables have been defined, the first generation is created. This initial population is made up of random values chosen for each variable within a defined range (its chromosomes). Step two is then selection; each chromosome in the existing population is applied to the fitness function, measuring the quality of the particular chromosome. Those which have a better fit are more likely to be selected to breed a new generation.

Once the entire population has gone through the selection process, the next step is to generate a second population, firstly by crossover, then mutation. Similarly to natural selection, two "parent" chromosomes are selected based on their fitness, breed, and produce two "child" chromosomes. The value for each variable on the parent chromosomes is treated as a "gene", and the child is produced by a uniform crossover method. Each gene has an equal probability of being chosen

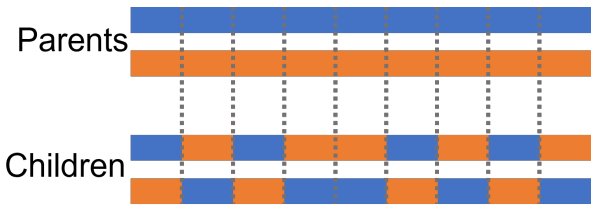


Figure 3.3: Cartoon depicting uniform crossover. The dashed grey lines represent crossover points.

from either parent, hence each gene is treated separately in the crossover phase, as depicted in Figure 3.3. The output is a child chromosome with genes taken from each parent chromosome at random.

To prevent falling into a local minima and to maintain genetic diversity amongst the new population, a mutation operator is applied to the child chromosome. The mutation operator sets the probability that a mutation will be applied to a gene. It does this by generating a random variable, if this random variable is within the mutation probability range, the gene will be mutated and changed to a random value within the variable parameters. If the random variable for mutation is outside of the mutation probability range, the gene remains as that obtained from the parent chromosome.

The parent chromosomes are selected semi-randomly, with a weighting towards those that are better fits in the selection process. Having both semi-random parents, and mutations, prevents the populations from becoming too similar to each other and converging - this increases the likelihood of finding the global optimum.

This process is repeated until a termination condition is reached, which is typically a maximum number of generations having been reached, but could also be a solution having been found or the highest ranking chromosomes have reached a plateau. This procedure is depicted in the flow chart shown in Figure 3.4.

3.2 Improving the Spatial Resolution

As discussed in Chapter 1, microscope MSI offers high throughput compared to microprobe-mode, however, the technique typically provides this at a lower mass and spatial resolution since both must be acquired simultaneously. Previous work on the

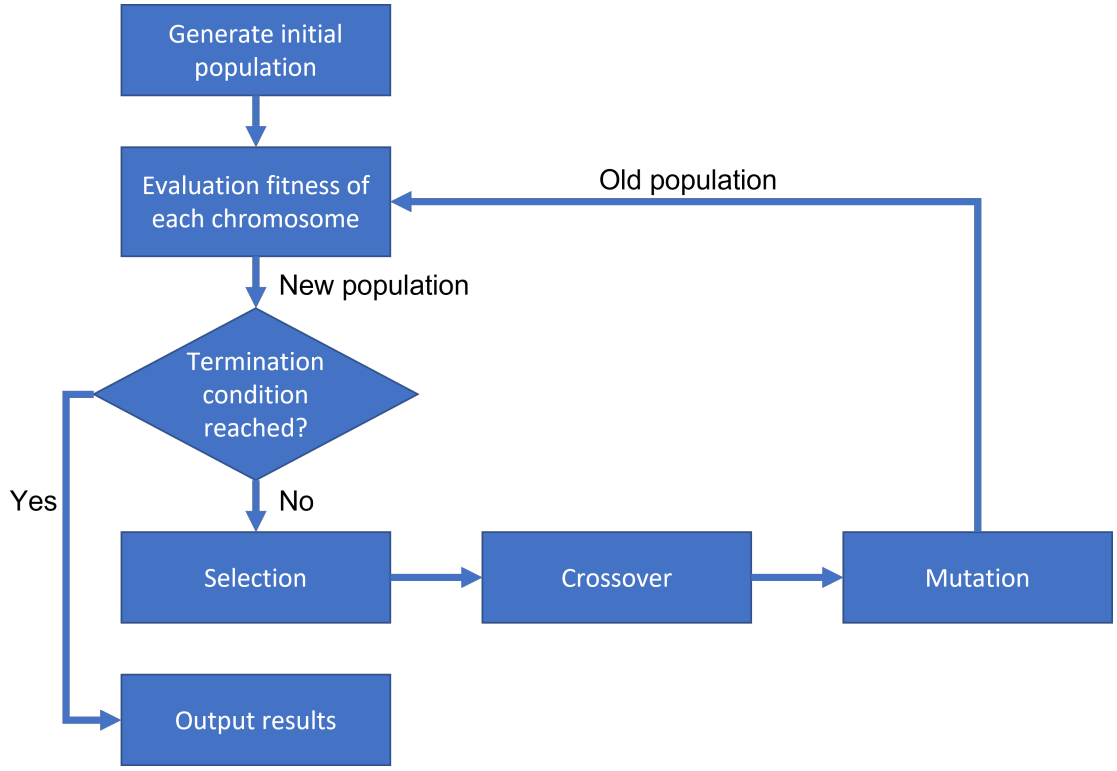


Figure 3.4: Genetic algorithm operating procedure.

reflectron ToF mass spectrometer has attained a spatial resolution of 18 $\pm$ 6 μs with a mass resolution of 8,100 $\pm$ 700 $m/\Delta m$ for a 343 Da ion [101]. This section seeks to use the simulator to improve the spatial resolution offered by the reflectron ToF mass spectrometer, while maintaining an adequate mass resolution (>3,000 $m/\Delta m$).

3.2.1 Theory

Spatial resolution, as described in 3.1.5, is determined from the minimum distance at which two objects can be distinguished from each other. For a microscope MSI instrument to be comparable with microprobe MSI instruments which have achieved sub-micron resolution [72], the spatial resolution must be optimised as far as reasonably possible.

For ions moving through an electric field, $\vec{E}$, the force experienced, $\vec{F}$, can be described using

$$\vec{F} = q\vec{E} \tag{3.11}$$

where q is the ion charge. Increasing the electric field strength results in a greater force applied to the ions, thus

$$\vec{F} = m\vec{a} \tag{3.12}$$

for a constant mass, m, the acceleration of the ions, $\vec{a}$, increases proportionally.

Thus by operating at higher potentials, and generating a stronger electric field relative to the previously established parameters, ions experience a faster acceleration along the ToF axis. As a result, they have less time to deviate from their starting position before reaching the detector. Consequently, a higher spatial resolution could be achieved, while also preserving the same mass resolution [63].

3.2.2 Simulations

Exploration of this was initially performed using SIMION, with a simulation of the reflectron ToF instrument set up as described earlier in this chapter with single-field PEDA. The simulation was paired with the genetic algorithm, restricted with a maximum potential of 10 kV applied to the reflectron voltage power supply - this being a physical maximum due to power supplies available at the time. All of the electrode parameters were allowed to vary within the genetic algorithm, with a range of approximately ~6 kV.

The optimisation equation chosen for the genetic algorithm is:

$$\text{Optimise} = \frac{\text{SR}^2}{(\text{MR}/1000)^2}. \tag{3.13}$$

Where SR is the spatial resolution, and MR the unconvoluted mass resolution output from a single simulation. This equation sets the spatial and mass resolution to be of the same order, as MR is typically >10,000, while SR is usually >100. In order to maximise MR and minimise SR, SR is the numerator, while MR/1000 is the denominator. Both the numerator and denominator are squared, which drives the optimisation factor more quickly towards the successful chromosomes. As a result, the optimisation seeks to approach 0 as the SR decreases and MR increases, but with a heavier weighting towards SR. This results in the spatial resolution decrease

being prioritised by the genetic algorithm over the mass resolution. Using this optimisation equation, the genetic algorithm was programmed to favour simulations with an optimisation term closer to zero.

When used with ions of 343 m/z, simulations with 10 kV limitations indicate an achievable spatial resolution of 9 μm with the new voltages, which can be compared to 18 μm simulated by the original voltages. An arrangement produced by the genetic algorithm is shown in Table 3.2, alongside the original voltages typically used with single-field PEDA on the reflectron ToF mass spectrometer.

Table 3.2: Simulation results from the genetic algorithm using 343 Da ions. The value for each parameter is listed, along with the spatial resolution, mass resolution, and magnification. Results obtained with original optimised parameters, 10 kV GA boundaries, and 40 kV GA boundaries are shown, with the former being experimentally attainable with the power supplies available.

Parameter	Original voltages	10 kV limited	40 kV limited
Repeller	5000 V	6295 V	36269 V
Extractor	4685 V	5948 V	16404 V
Einzel lens	1715 V	2027 V	15332 V
PEDA	5300 V	6730 V	14577 V
PEDA delay time	2.85 ns	2.65 ns	1.34 ns
Deflector	55 V	61 V	166 V
Reflectron	8750 V	9800 V	32034 V
Spatial resolution, μm	18.1	9.0	6.7
Mass resolution, $m/\Delta m$	30356	25221	13053
Convoluted mass resolution, $m/\Delta m$	8157	6435	3149
Magnification	$\times$81	$\times$82	$\times$74

Additionally, the genetic algorithm was used to explore the attainable spatial resolution when not limited by available power supplies. Thus the genetic algorithm was repeated with the parameter boundaries increased up to 40 kV. Simulations suggest a spatial resolution of 6.7 μm can be achieved, however this is at the expense of convoluted mass resolution, which has decreased to 3,149 $m/\Delta m$. This suggests that the instrument is close to its upper limit of spatial resolution in its current design.

3.2.3 Experimental Results

To test the simulation results experimentally, samples of Rhodamine B were prepared. Solvated in methanol, Rhodamine B is electrosprayed through a nickel mesh, onto an ITO slide, as described in chapter 2. The homogeneous layer of dye produced a grid pattern of squares with a width of 49 μm, and pitch of 63 μm, as shown in the optical image in Figure 3.5.

The value assigned for each variable (Table 3.3) was guided by the simulation and optimised experimentally, conducting a rough search of parameters until the spatial resolution no longer improved. The sample of Rhodamine B was imaged with a CCD camera, gated over the time-of-flight range covering the five main Rhodamine B peaks. The original parameters optimised for single-field PEDA were used to obtain Figure 3.6(a), with which a direct comparison can be made with the results using the new voltages, which produced the image shown in Figure 3.6(b).

Table 3.3: The value assigned to each parameter with the original PEDA values compared to the new high spatial resolution values.

Parameter	Original Value	New Value
Repeller	5000 V	6295 V
Extractor	4685 V	5920 V
Einzel lens	1715 V	2000 V
PEDA	5300 V	6730 V
PEDA delay time	2.85 ns	2.65 ns
Deflector	55.0 V	61.0 V
Reflectron	8750 V	9800 V

The images have been centroided and a Fourier transform applied, removing noise introduced during the image acquisition. From these images, intensity profiles

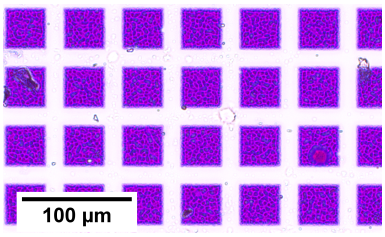


Figure 3.5: x20 optical image of Rhodamine B electrosprayed through a 63 μm pitch nickel mesh onto an ITO slide.

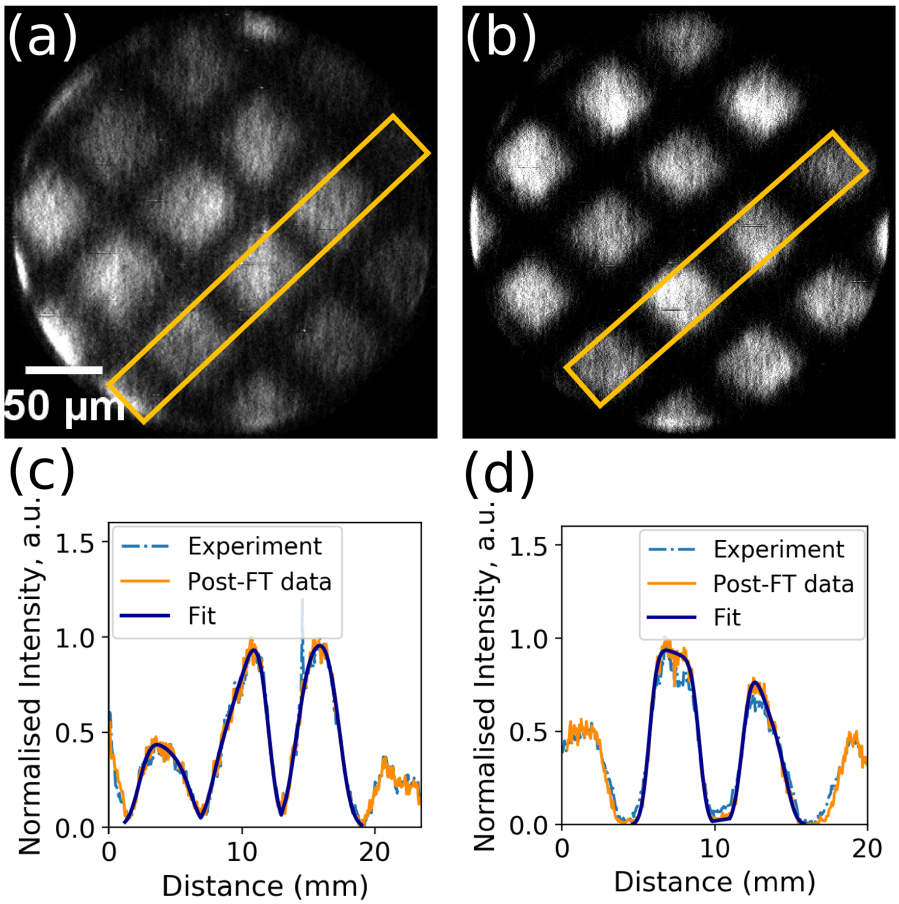


Figure 3.6: The centroided CCD images of Rhodamine B at the original (a) and new (b) voltages respectively, gated on the four peaks shown in Figure 3.7. The spatial resolution is determined from the 20-80% intensity rises observed along profile lines running perpendicular to the wire silhouettes of each image. Each profile (c) and (d), corresponding to the orange box highlighted in (a) and (b) respectively, is fit with a Gaussian function convolved with a rectangular function representing the grid, and a linear function to account for the 20° incidence angle of the laser.

running perpendicular to the wire silhouettes in the images are extracted. The intensity profile is fit with a rectangular function, convolved with a Gaussian, to match the grid pattern (Fig. 3.6 (c) & (d)). The functions are convolved with a Gaussian function and a linear function to account for the ~20° incidence angle of the laser pulse on the sample surface, which causes a shadowing on the acquired image, and hence decreasing intensity across each intensity profile.

From the acquired image, the magnification, M, can be established and the spatial resolution, R_s, calculated from the average 20-80% intensity rise of each dye grid [130, 131]:

$$R_s = \frac{1.68\sigma}{M}, \tag{3.14}$$

using the Gaussian standard deviation, σ.

The magnification is calculated from the number of pixels required to image the 25 mm diameter of the scintillator screen and comparing the pitch of the imaged grid pattern with the 63 μm pitch of the nickel mesh. The magnification changes from $\times$92 to $\times$93 with the new high spatial resolution voltages. The small increase in magnification is inline with that predicted by the simulation results. A decrease in magnification is to be expected, as the faster ions should deviate less from the central ToF axis, however, the small increase in magnification calculated is not significant enough to disagree with this.

The spatial resolution changes from 13 $\pm$ 1 μm to 8 $\pm$ 1 μm for the original and new parameters in Table 3.3 respectively. This is in line with simulations, and the optimised experimental parameters used were similar to those listed in Table 3.2, differing only by ~30 V with the extractor and einzel lens potential. This suggests that the simulation is working correctly, and proves that higher spatial resolution images can be attained experimentally with the use of stronger electric fields.

Alongside Figure 3.6(b), a ToF mass spectrum of the higher spatial resolution setup was acquired using a photomultiplier tube (PMT). Figure 3.7 demonstrates that an average mass resolution of 3888 ± 370 $m/\Delta m$ can be obtained alongside the higher spatial resolution. This is approximately a factor of two smaller than what has been obtained experimentally with the original parameters and disagrees with the simulated results, which predicts a value closer to 6,000 $m/\Delta m$. This discrepancy can likely be attributed to single-field PEDA optimisation. With additional experimentation, the focused mass window produced by single-field PEDA can be better positioned to align with the Rhodamine B peaks, producing a mass resolution closer to that expected from simulation.

As shown in Figure 3.6, it has been proven that a higher spatial resolution of 8 $\pm$ 1 μm is achievable with the use of higher voltages. This change is associated with a decrease in mass resolution, however this could be improved with optimisation

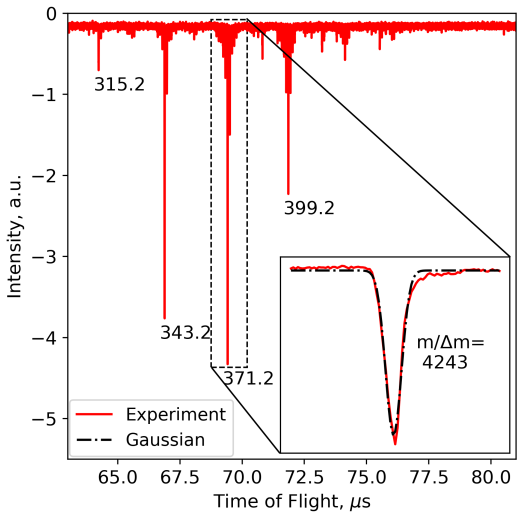


Figure 3.7: A time-of-flight mass spectrum of Rhodamine B, taken with a PMT at the new higher spatial resolution parameters listed in Table 3.3. The labels indicate the m/z value for each key peak. The inset image shows an expanded view of the 371 Da peak and the Gaussian fitted to the peak to provide a mass resolution of 4,243 $m/\Delta m$.

of the single-field PEDA application. Theoretically, the spatial resolution could reach 6.7 μm with the use of higher voltage power supplies.

3.3 Zoom lens

The reflectron instrument in its current set up has a magnification of ~×92, and a field of ~270 μm [30]. This high magnification is largely due to the reflectron, which increases the flight path significantly, and hence the ion deviation from the ToF axis also increases. Without the reflectron, a linear ToF variation achieves a magnification of approximately ×20 [30]. While a high magnification is excellent for the spatial resolution and getting a clear view of the sample, it is restrictive. With the current instrument design, the sample slide cannot be translated to allow for other areas of the surface to be imaged. If slide translation were possible, it would still require locating a region of interest, or one may not even know what their region of interest is until after imaging. Thus, having the option to decrease the magnification and expand the field of view, would allow for more of the surface to be imaged. From there, the exact region desired can be located, and a second image of higher quality (mass and spatial resolution) could be obtained at the ×92 magnification.

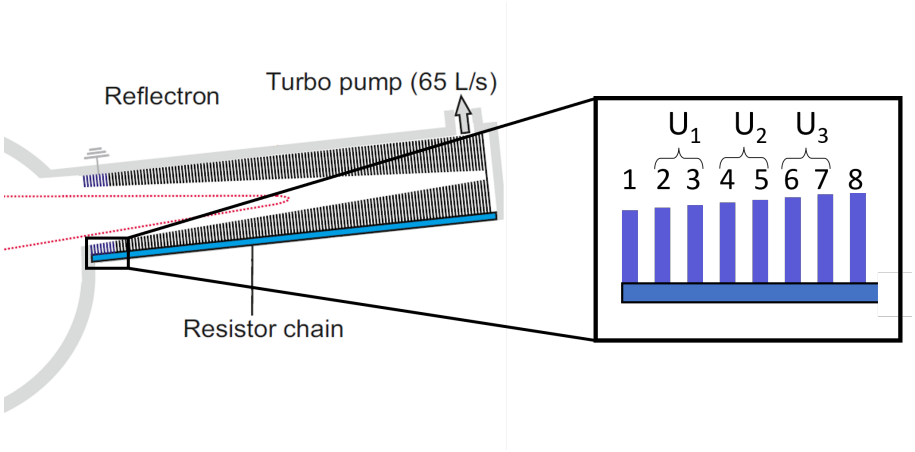


Figure 3.8: The first eight electrodes in the reflectron stack, labelled 1-8 with 1 being at the entrance of the reflectron, and additional labels pairing the electrodes: U_1 (2 and 3), U_2 (4 and 5), and U_3 (6 and 7).

This would ultimately save time in the imaging process, exploiting the advantage microscope-mode MSI has over microprobe-mode MSI. Such control could potentially be achieved using an electrostatic zoom lens within the current setup [132–134].

This section details the simulations performed investigating the instrument magnification. A number of options were investigated, including: utilising the grounded reflectron electrodes, the addition of another einzel lens in different locations along the ToF axis, and using the existing einzel lens plates.

3.3.1 Reflectron lens

Using the SIMION 8.1 model of the mass spectrometer, the reflectron electrodes voltage on the entrance and exit can be varied using the first eight electrodes in the reflectron stack. Standard operation has the first eight electrodes grounded, however by applying a voltage to these electrodes, we can create a three-electrode immersion lens. Of the eight electrodes investigated within the simulation, the outer electrodes (1 and 8) are grounded, and the remaining six are paired up and assigned a variable: U_1 (2 and 3), U_2 (4 and 5), and U_3 (6 and 7), as indicated in Figure 3.8. All other parameters were kept the same as the original values used in Section 3.2, as listed in Table 3.3.

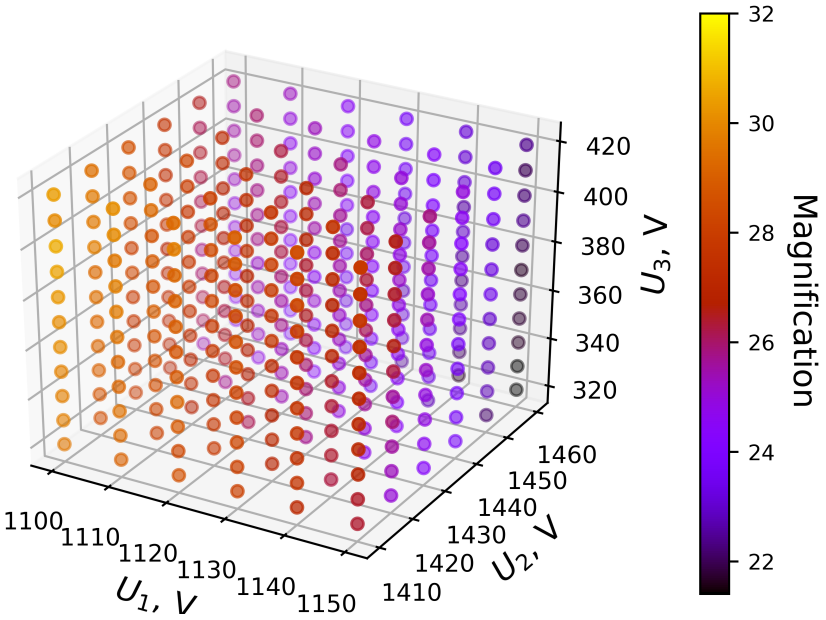


Figure 3.9: The simulated magnification as functions of the U_1, U_2, and U_3 potentials applied to the electrodes in the reflectron stack.

The three pairs, U_1, U_2, and U_3, were simulated at a range of static voltages, applied to a low mass ion (343 Da) generated from the five locations distributed along the y-axis (as described in 3.1). Guided by broad preliminary simulations, the search range was narrowed down to U_1=1100 - 1150 V, U_2=1410 - 1460 V, and U_3=320-420 V, simulated with steps of 10 V. As can be seen in Figure 3.9, a range of magnification can be achieved, spanning from 30 to 22. This is quite a significant decrease in magnification from 92. There is little variation with respect to U_3, suggesting the absolute value of electrodes 6 and 7 are not a significant factor. The mass resolution averages 6772 ± 34 $m/\Delta m$ and the spatial resolution averages 22 ± 4 μm within the entire search range, however this could likely be improved by adjusting the other parameters.

Following on from this, a pulsed field was explored. With a static field, the ions will experience the field on both the entrance and the exit to the reflectron, however more control over the ion movement could be obtained with a field applied only once along the path. The simplest method to achieve this is a step pulse with a set trigger time and pulse width. This pulse can then be easily adjusted to apply to only the entrance, or only the exit, of the ion flight path. This of course will have

limitations depending on the ion mass and its respective time-of-flight, however, simulations suggest the amount of time spent in the reflectron is approximately 50% of the entire ion time-of-flight. This corresponds to an entrance time of the reflectron of ~27 μs, and an exit time of ~55 μs for a 250 Da ion, thus the pulsed field can be set up to apply to only ions within this window.

In order to apply to pulsed field on the entrance to the reflectron, targeting the ions >250 Da, a pulse start time of 0 μs (relative to ion generation time) and width of 55 μs was chosen. To apply the pulse on the exit, a start time of 50 μs from t_0, and a duration of 40 μs (operated from 50-90 μs relative to t_0), was used. The magnification, mass resolution, and spatial resolution, were obtained over a 200-1000 m/z mass range. The potentials applied to the pairs of electrodes were determined using the genetic algorithm, guided by the trends indicated in Figure 3.9. A configuration which showed promising results was used, the following simulation data uses U_1=1500 V, U_2=-1500 V, and U_3=0 V. An ideal result is one which presents a consistent magnification against m/z, while maintaining a good spatial and mass resolution.

Simulations were subsequently performed with the reflectron zoom lens pulse on the entrance (0-55 μs), exit (50-90 μs), and statically, exploring a range of 200-1,000 m/z values, as shown in Figure 3.10. All other parameters have been kept the same. Notably, the pulse set to apply at the exit of the reflectron can be clearly seen to change upon the pulse ending at 90 μs, with the magnification changing suddenly at approximately 700 Da, attributed to the heavy mass ions arriving at the reflectron entrance after the pulse has begun. Pulsing at the entrance and exit seem to have limited impact on magnification, achieving ~×65 for most of the mass window, meanwhile the static pulse is <×40. This suggests that the static pulse is the best option, however this is at the expense of the spatial resolution. The static lens shows a significant worsening of spatial resolution above 500 m/z, while the pulsed version remain below 100 μm until approximately 800 m/z. The mass resolution strongly favours the pulse on the entrance, but with convolution, the variation is minimal. It is likely that the optimal parameters have yet to be found,

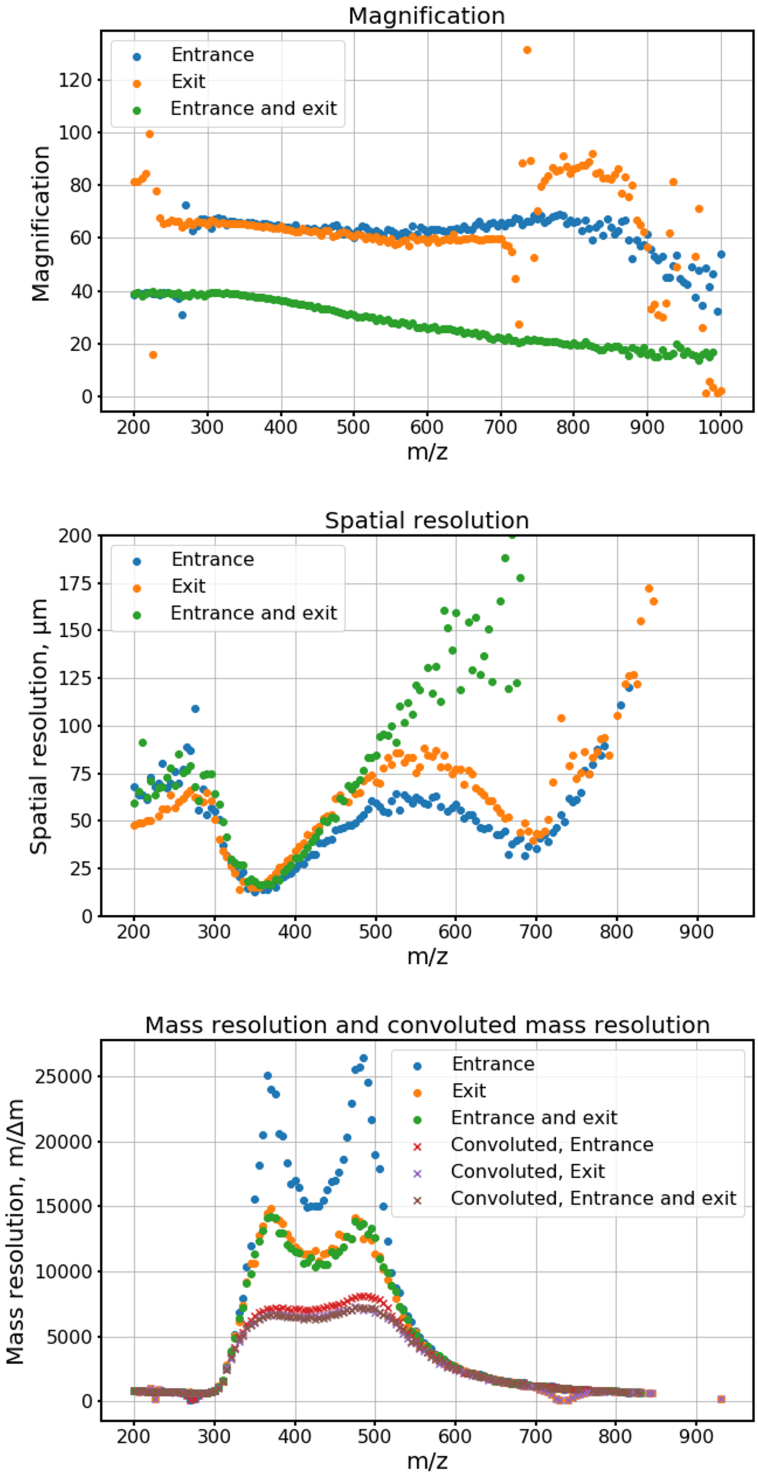


Figure 3.10: Simulation results using the reflectron zoom lens while varying the zoom lens pulse timing against m/z. "Entrance" denotes a pulse on the entrance at 0-55 μs, "Exit", a pulse as ions exit the reflectron from 50-90 μs pulse, and "Entrance and exit", refers to a static pulse. Displaying magnification (top), spatial resolution (middle), and mass resolution and convoluted mass resolution (bottom), convoluted with the screen fluourescence lifetime. A deflector voltage of 45 V was used for each simulation.

which could reduce the magnification further on the entry pulse, while retaining spatial resolution over a wide mass window.

To try optimise the simulation parameters, the deflector voltage were investigated further by applying a number of different deflector potentials and scanning a mass range of 200-1000 Da. The results are shown in Figure 3.11 and suggests a lower deflector voltage can decrease the magnification as low as $\times$20 at 15 V. Voltages lower than this cause the ions to collide with the reflectron upon entrance. The magnification also appears to remain relatively constant for most potentials, 52 V being an exception, explained by ions passing too close to the reflectron edge upon exit, resulting in aberrations. Additionally, there appears to be $<$100 μm spatial resolution and $>$5000 $m/\Delta m$ from the convoluted mass resolution from the majority of the simulations.

Upon close inspection of the ion flight path to the detector, it was observed that the ions were being distorted as the deflector voltage decreased, which can be demonstrated by Figure 3.12. From this, we can see that there is an optimal deflector voltage to retain the correct arrangement of ion groups: too little deflection, the ion groups begin to overlap with each other; too much deflection, the ions can collide with the reflectron plates before reaching the exit. Instead, a deflection which allows the beam to exit the reflectron close to central on the detector, while retaining the correct spatial arrangement, is optimal. This appears to be at a deflection voltage of 35 V.

The results from Figure 3.11 are misleading, as once the ion groups cross paths during flight, the arrival order is incorrect and the magnification calculation fails. However, Figure 3.12 does suggest that a valid decrease in magnification is occurring as the deflection shifts from 52 V to 35 V. The results thus far have been acquired with the ion starting locations distributed along the y-axis of the repeller plate, however, we need to know if this behaviour is replicated along both axes. To investigate this, a new .FLY2 file was created to produce a grid pattern. A grid of 9 $\times$ 6 origin locations was generated, each location comprising 100 ions, and with 0.05 mm spacing between each ion. This 54 point grid of ions

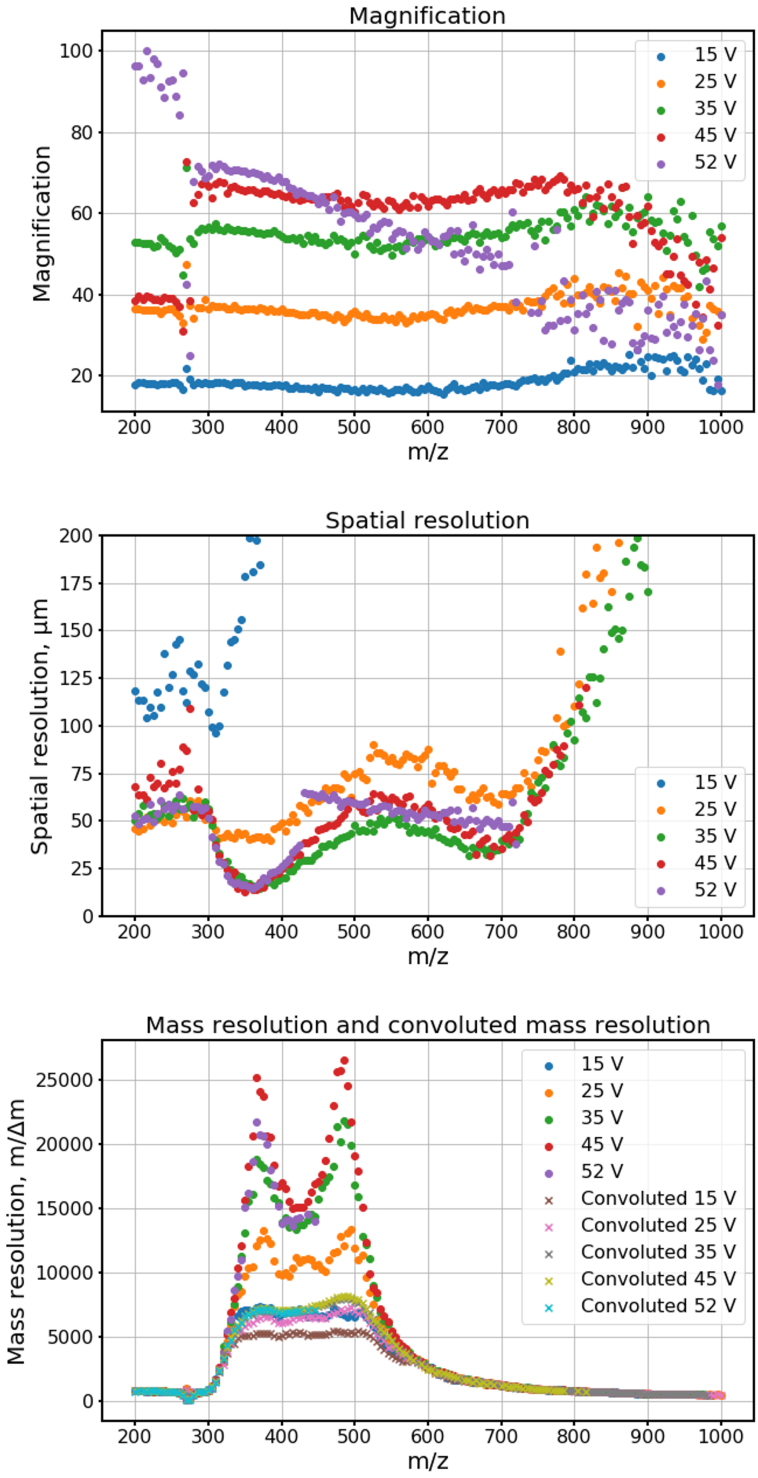


Figure 3.11: Simulation results using the reflectron zoom lens while varying the deflector voltage against m/z. Displaying magnification (top), spatial resolution (middle), and mass resolution and convoluted mass resolution (bottom) convoluted with the screen fluourescence lifetime. The reflectron zoom lens has been applied from 0-55 μs.

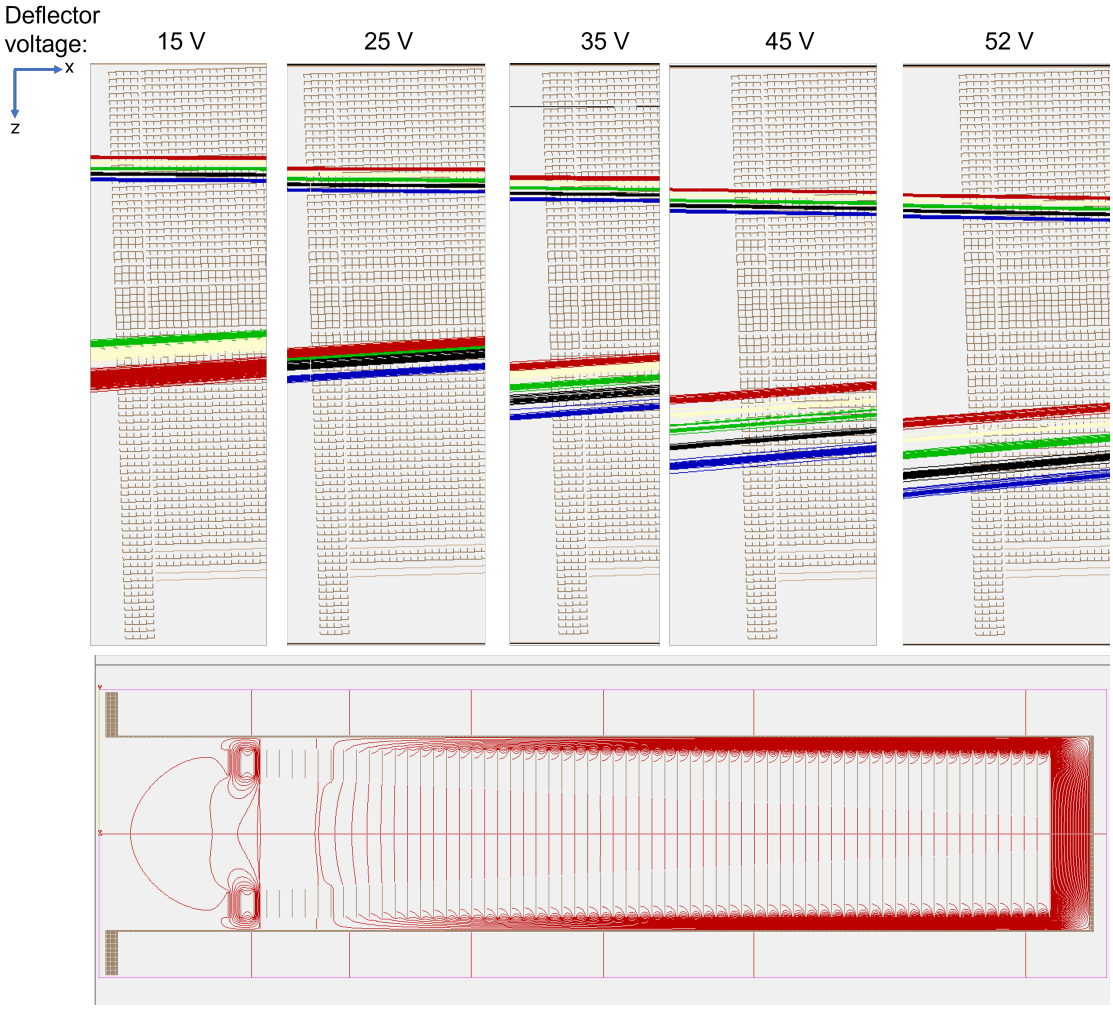


Figure 3.12: Simulations depicting the effect of deflector voltages on the ion flight path with a lens at the entrance to the reflectron. Each colour represents a different ion origin at the repeller, comprised on 100 individual ions. The lower image depicts the electric field generated by the reflectron.

was flown within the simulation, and the resultant image when impacted upon the detector recorded (see Figure 3.13).

While the 5-origin linear point simulation indicated a change in magnification using the reflectron lens, this 54-origin grid point simulation informs that this change is only along the y-axis, as can be observed in the detector impact images. This has been quantified by improving upon the magnification calculation. As described in Section 3.1, the magnification is determined from the distance along the y-axis between the ion groups, relative to the point source location. By transforming from a linear arrangement of ion point sources, to a grid, there are now multiple rows and

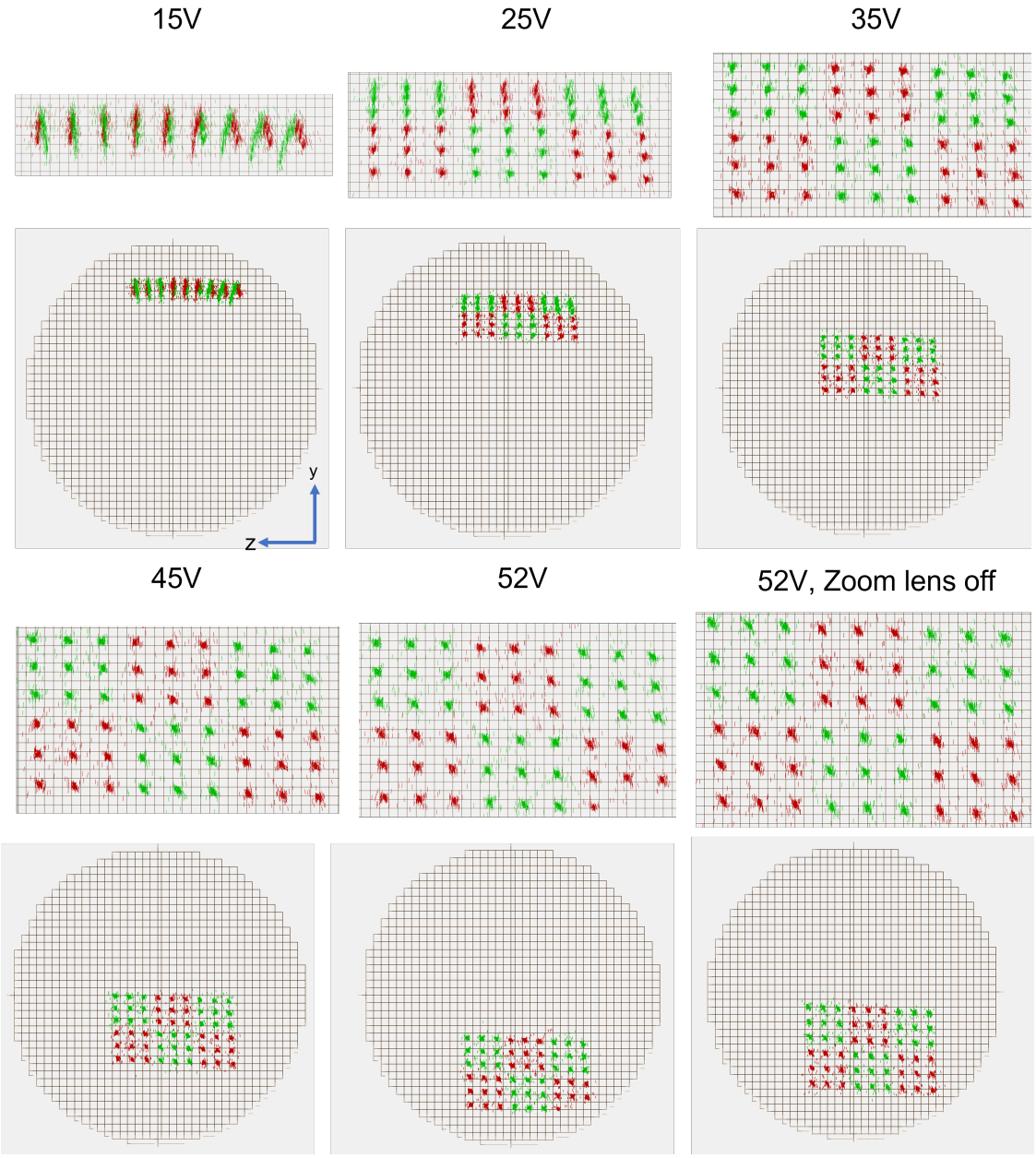


Figure 3.13: Simulated grid pattern created on the detector using the reflectron ToF mass spectrometer. A potential has been applied to the reflectron, creating a lens as the ions enter the reflectron. The spots indicate 54 different ion origin points of 100 ions of mass 343 Da, and their impact points on the detector. Shown above each image is the deflector voltages applied, with images showing the spread of ions across the detector, and the relative location on the detector. The grid pattern without a zoom lens has also been shown for reference. The impact locations indicate that magnification from the reflectron lens is only being altered in one dimension.

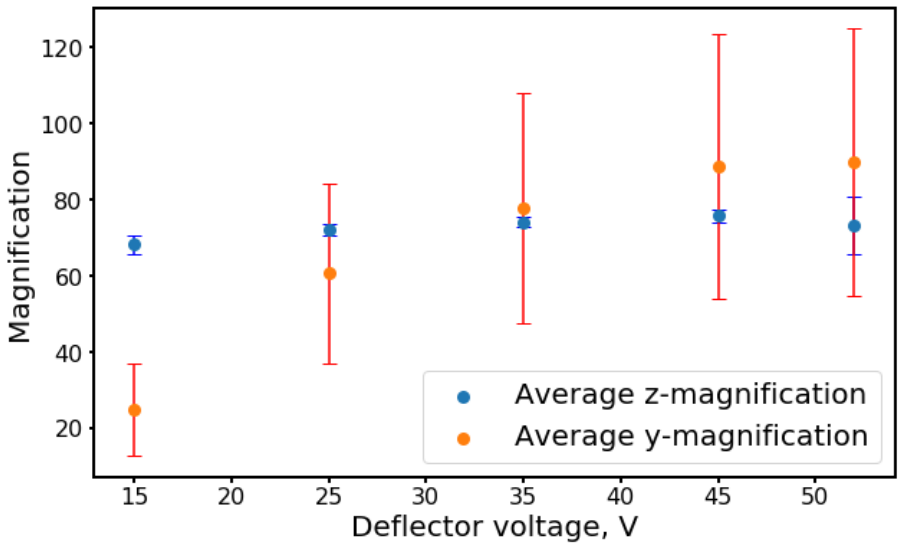


Figure 3.14: Magnification against deflector voltage across the z and y axis of the detector, while the reflectron zoom lens is applied to the entrance of the reflectron. Data obtained with the simulations depicted in Figure 3.13. The magnification is an average in each dimension, with error bars depicted.

columns to provide information about any distortion across the surface of the grid pattern, supplied by the standard deviation across each of these rows and columns.

Using this information, at a deflector voltage of 52 V, a magnification of $\times 73$ was determined in the z-direction, while $\times 89$ was determined in the y-direction. There is a change in magnification in the y-direction as the deflector potential decreases, but there is little change in the z-direction. This effect is also seen with other parameter configurations determined for the new lens. A large degree of distortion is occurring, and the ion flight path can't pass centrally through the reflectron, thus using the reflectron plates as a zoom lens is probably not a viable method for this instrument.

3.3.2 Additional einzel lens

The reflectron zoom lens failed primarily due to the ions passing through the lens off-centre. An alternative to the reflectron plates is simply the addition of another lens, which can be aligned centrally to the ToF axis. The lens could then be located at the entrance or exit of the reflectron, to replicate the same functionality.

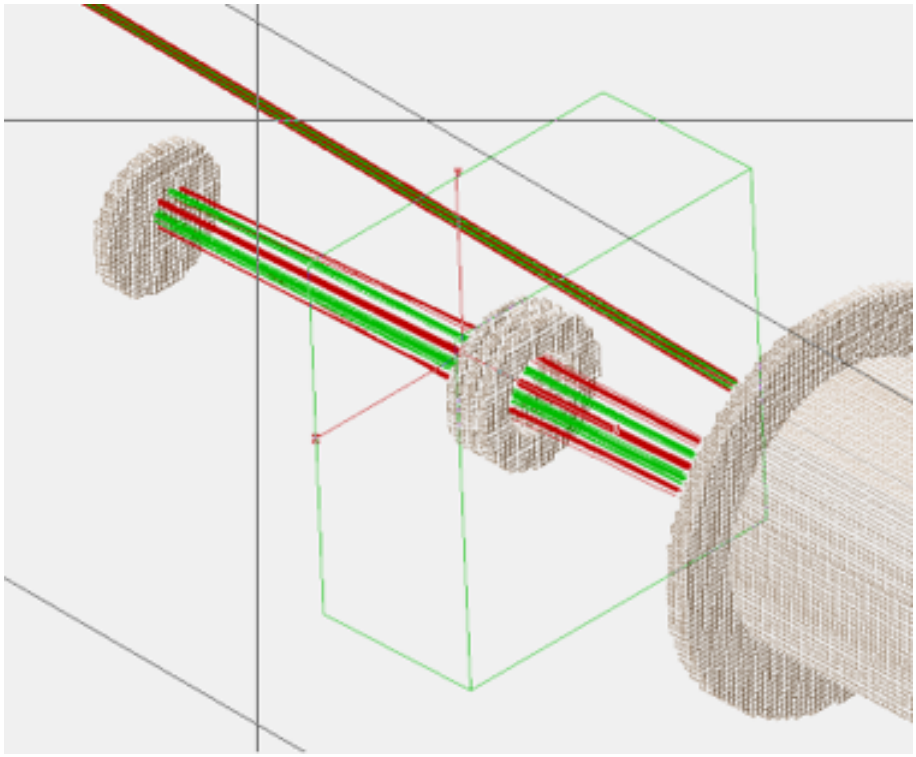


Figure 3.15: Image of the SIMION workbench, expanded to show the detector (left), new einzel zoom lens (centre), and the beginning of the reflectron (right). The ion flight path is shown. A potential of 3200 V has been applied to the new einzel zoom lens, having a clear effect on the ion trajectory towards the detector.

Lens on the exit of the reflectron

Consequently, a three-electrode lens potential array was made in SIMION. This lens can be positioned anywhere along the flight path, including at the exit of the reflectron, as depicted in Figure 3.15. When positioned at the exit, the lens is given an elevation angle of 2.2 degrees, ensuring the field is normal to the ions exiting the reflectron. The size and spacing of this three-electrode lens was set as a plate diameter of 80 mm, aperture diameter of 48 mm, and plate separation of 4 mm. This allows the beam to pass freely through the centre of the electrodes, while also meeting the physical instrument constraints.

Using the genetic algorithm, a range of potentials across each of the three electrodes was explored. A few of these which indicated the best compromise of magnification, mass resolution, and spatial resolution, were selected for further simulations. For these simulations, a typical einzel lens arrangement was employed

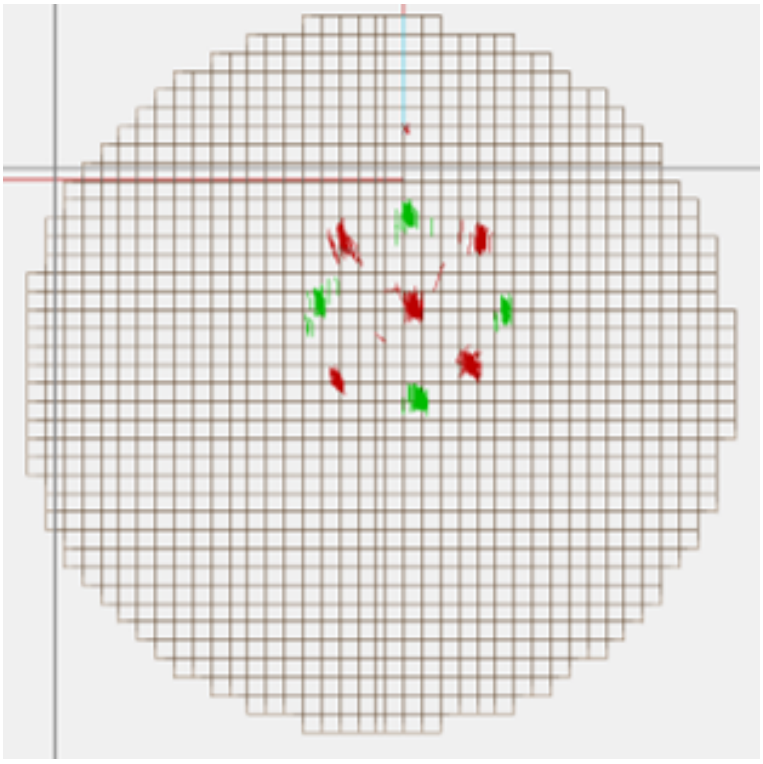


Figure 3.16: Image of the detector plate, taken from the SIMION workbench. A grid of 3×3 ion sources were flown, passing through the new einzel zoom lens which is held at a potential of 3200 V. The ions projected onto the detector have suffered a distortion by the lens, appearing as a circle rather than a square.

for simplicity - the outer two electrodes held at 0 V, the inner electrode held at a positive potential of the order of a few kV. A grid of ion origin points was utilised, however a 3 × 3 grid was flown instead to reduce computational time.

Upon observation of ion impacts on the detector, it is clear that a distortion is occurring due to the lens. The lens is reducing the magnification, however results in the regular grid pattern becoming circular instead (Figure 3.16). This is a consequence of field aberrations caused by ions flying too close to the edges of the einzel lens. A number of different positions along the flight path between the reflectron and detector were tested, with the least deformation occurring with the lens closest to the reflectron exit. This is because the ions continue to expand from the central ToF axis, and the position earlier in the flight path has the lowest magnification, thus ions are closer to the centre of the lens.

The solution to this issue is to make the electrode and aperture larger, such

that the ions can pass through the centre of the lens and field aberrations do not occur. However, in practice, on this instrument is isn't possible as there is limited space in this region, and large enough electrodes cannot physically fit.

Lens on the entrance of the reflectron

The region between the reflectron and the detector is small, accounting for approximately 10% of the ion time-of-flight, however the region before ions enter the reflectron should overcome the issues encountered previously. As ions come to enter the reflectron, they are earlier in their flight path, thus have diverged less from the central axis. This means the original dimensions for the new einzel zoom lens should be appropriate, since the ions will travel more centrally and a large aperture is not necessary. Additionally, there is a greater distance over which to adjust the lens position to allow for ion focusing, offering more flexibility. Applying a lens earlier into the flight path should mean a greater effect on the magnification with a lower potential, as a smaller deviation in the flight path is needed to alter the magnification due to approximately 50% of the path remaining.

The same einzel lens as described earlier was used, moved to a short distance in front of the reflectron, and aligned with the ion path entering the reflectron. The scale of the potential array was changed to 0.7 to prevent the electrodes from crossing into the ion path after exiting the reflectron. All parameters were kept the same as previously described, while the voltage applied to the new einzel zoom lens was varied in steps of 500 V for a 343 Da ion. As can be seen in Figure 3.17, the magnification decreases significantly as the lens voltage is increased, attaining approximately $\times 20$ at a potential of 7 kV. There is a small difference in magnification across the z-axis and the y-axis, the largest difference being at 6.6 kV, with $\sim\times 31$ along z and $\sim\times 26$ along y. This can be explained by the ions not passing perfectly centrally through the lens.

Figure 3.17 also demonstrates the spatial resolution is <20 μm from 0-5000 V. The worsened spatial resolution above 5 kV can also be seen in Figure 3.18, where the clusters of ions at each point spread out further from the spot centre. The ion

points appear to contract with minimal distortion to the grid pattern and with a small decrease in spatial resolution, attaining approximately 63 μm at 7 kV.

The convoluted mass resolution is notably worsened with this lens, halving from ~5,900 $m/\Delta m$ with 0 V, to ~2,600 $m/\Delta m$ with 5 kV. This data was acquired with all other potentials unchanged, thus optimisation of the other electrodes could improve the mass resolution.

To further explore the effectiveness of this lens, a scan of m/z at different lens potentials is shown in Figure 3.19. These indicate a gradual rise in magnification with m/z, attaining minimums of ×65 at 4kV, ×40 at 6kV, and ×20 at 7kV. It is also evident that there is significant variation in the magnification at the higher lens voltage, with increasing error bars. This is expected, as the spatially focused window is approximately 300-700 Da, hence the loss of spatial resolution at high mass distorts the magnification calculation, producing large error bars. Both the spatial and mass resolution follow the expected trend for time-variable PEDA and shows little difference with the applied voltage.

A lens located at the entrance to the reflectron appears to be a reasonable method for creating a zoom lens within the reflectron ToF mass spectrometer. Further simulations must be conducted to further optimise, but it can be seen as a viable approach.

Lens at the beginning of the flight path

As displayed previously, the earlier a lens is along the flight path, the more significant the effect on the magnification will be at the end of the flight path. The ions begin to diverge from the central ToF axis shortly after passing through the einzel lens, hence locating an additional lens after this point should be the most effective. A position 50 cm from the final einzel lens plate was chosen for the additional lens (Figure 3.20).

To begin investigating the effect of the new lens in this location, a simulation scanning through from -10 kV to + 10 kV was performed. The magnification (with error bars indicating the standard deviation in magnification between the rows and columns of the nine groups ions), spatial resolution, mass resolution, and convoluted

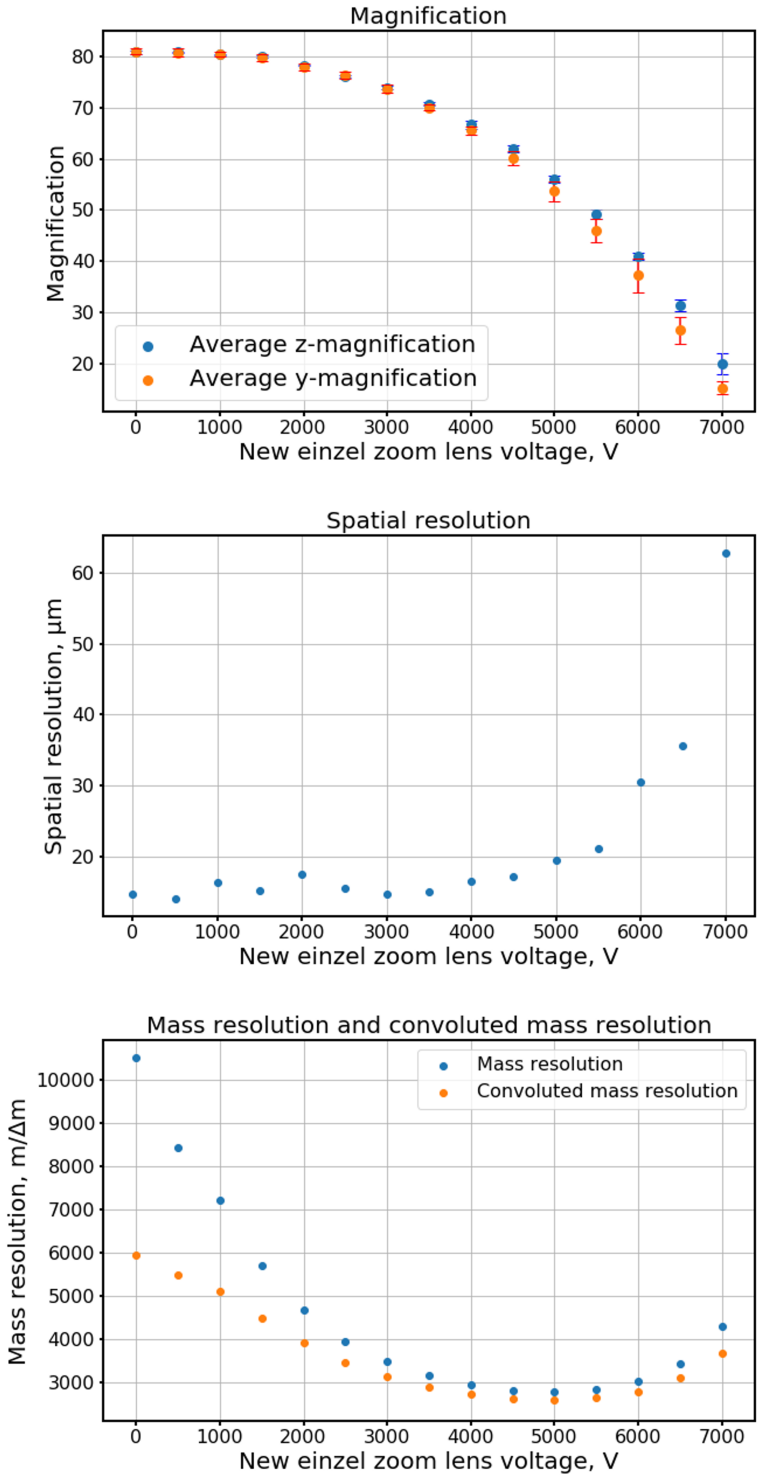


Figure 3.17: Simulation results produced using an additional einzel lens located at the ion entrance to the reflectron. Displaying magnification (top), spatial resolution (middle), and mass resolution and convoluted mass resolution (bottom) against the voltage applied to the new einzel zoom lens.

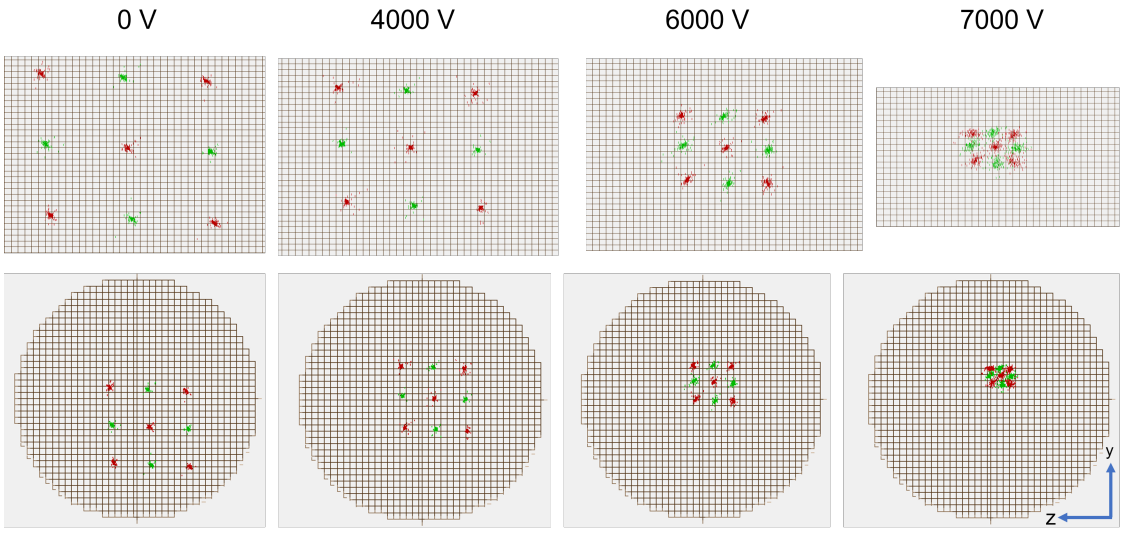


Figure 3.18: Images of the detector plane, taken from the SIMION workbench with different potentials applied to the new einzel zoom lens. There are 9 spots, each comprised of 100 ions, depicting the impact location on the detector.

mass resolution, are shown in Figure 3.21. As can be seen, a positive potential is more effective at reducing the magnification, while also improving the mass resolution. However, this is only true up to approximately 6 kV, after this point, the spatial resolution begins to increase significantly, as does the standard deviation for the magnification. It is worth noting that below 6 kV, the magnification along the z and y axes are very similar at each potential, with small error bars, suggesting the change in magnification is happening evenly across the grid of ions.

Subsequently, simulations exploring the effect of this lens across a range of m/z values were performed. Figure 3.21 indicates 5 kV is a good compromise of magnification, spatial resolution, and mass resolution. As such, ions of mass range 200-1000 Da were simulated to investigate the effect of ion mass on the magnification in conjunction with the new einzel zoom lens (Figure 3.22). The results are promising, indicating a magnification of $\times 60$, which begins to increase at approximately 700 m/z, paired with a spatial resolution window of ~30 μm spanning 250 Da. The convoluted mass resolution also remains greater than 5000 m/Δm for a window of 250 Da.

Continuing from this result, alternative magnifications could be achieved by optimising the existing einzel lens alongside the new einzel zoom lens. The original

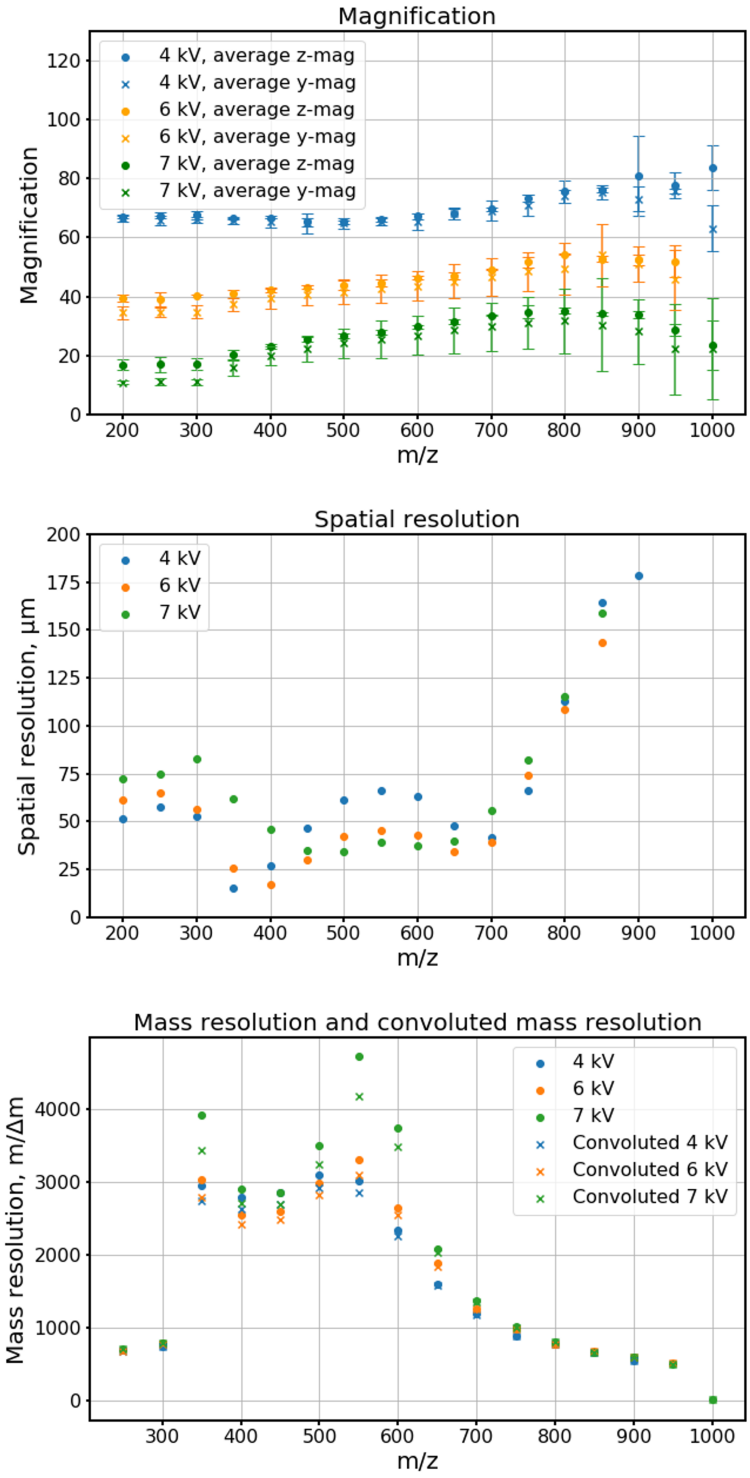


Figure 3.19: Simulation results produced using an additional einzel lens located at the ion entrance to the reflectron. Displaying magnification (top), spatial resolution (middle), and mass resolution and convoluted mass resolution (bottom) against the m/z for different potentials applied to the new einzel zoom lens.

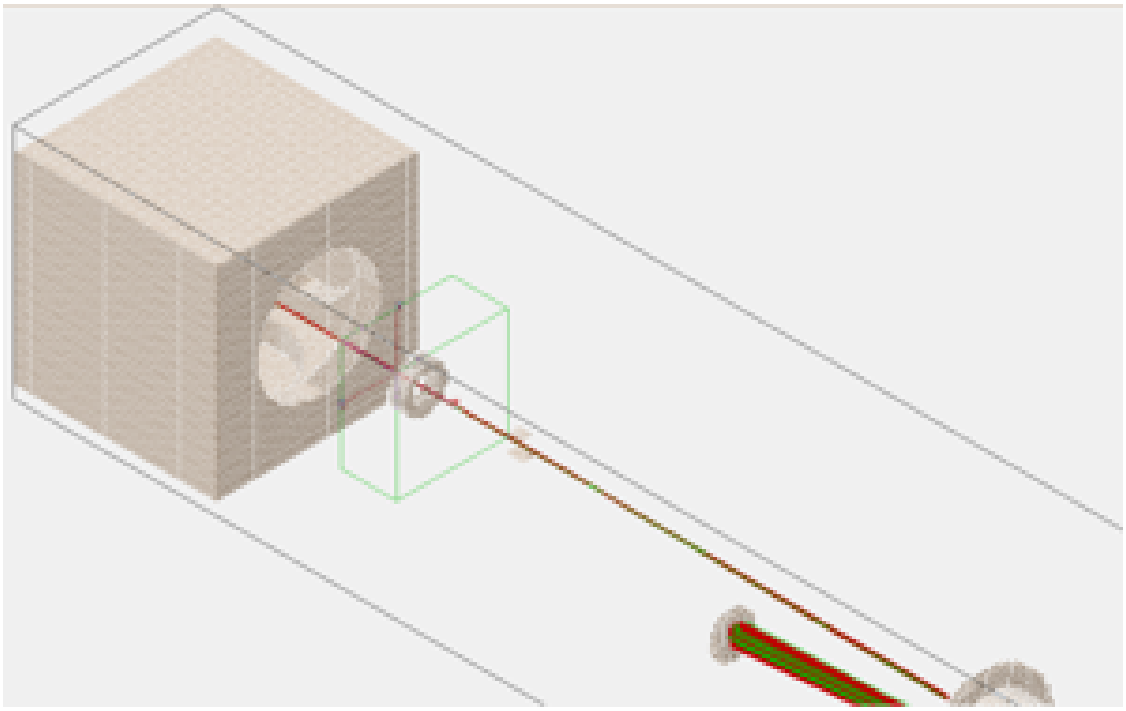


Figure 3.20: Image of the SIMION workbench, cropped to show the ion optics (left), new einzel zoom lens (centre left), deflector (centre), detector (centre right), and entrance to the reflectron (right). The ion flight path is shown.

einzel lens helps to spatially focus the ions, thus one could expect a more optimised setup to produce a different mass resolution alongside an improved spatial resolution. The effect of the original einzel lens can be shown by scanning across a range of voltages while maintaining all other variables (Figure 3.23). This demonstrates that at a mass of 343 Da, the mass resolution and magnification can be held at an approximately constant value, while there is a distinct effect on the spatial resolution. When operating the new lens at a higher voltage (6 kV rather than 5 kV), the optimal spatial resolution is achieved with a lower einzel lens voltage, suggesting an inverse relationship between the two electric fields to achieve the optimal focal window. There is a focal window at approximately 1400 V on the einzel lens when the new einzel zoom lens is held at 6 kV, producing a spatial resolution of 40 μm. The relationship between spatial resolution and mass resolution is exemplified in this figure, as the spatial resolution worsens, the error bars on the magnification increase.

Based on these results with this setup, the conditions resulting in the best spatial resolution, with the lowest magnification, is with an einzel lens voltage

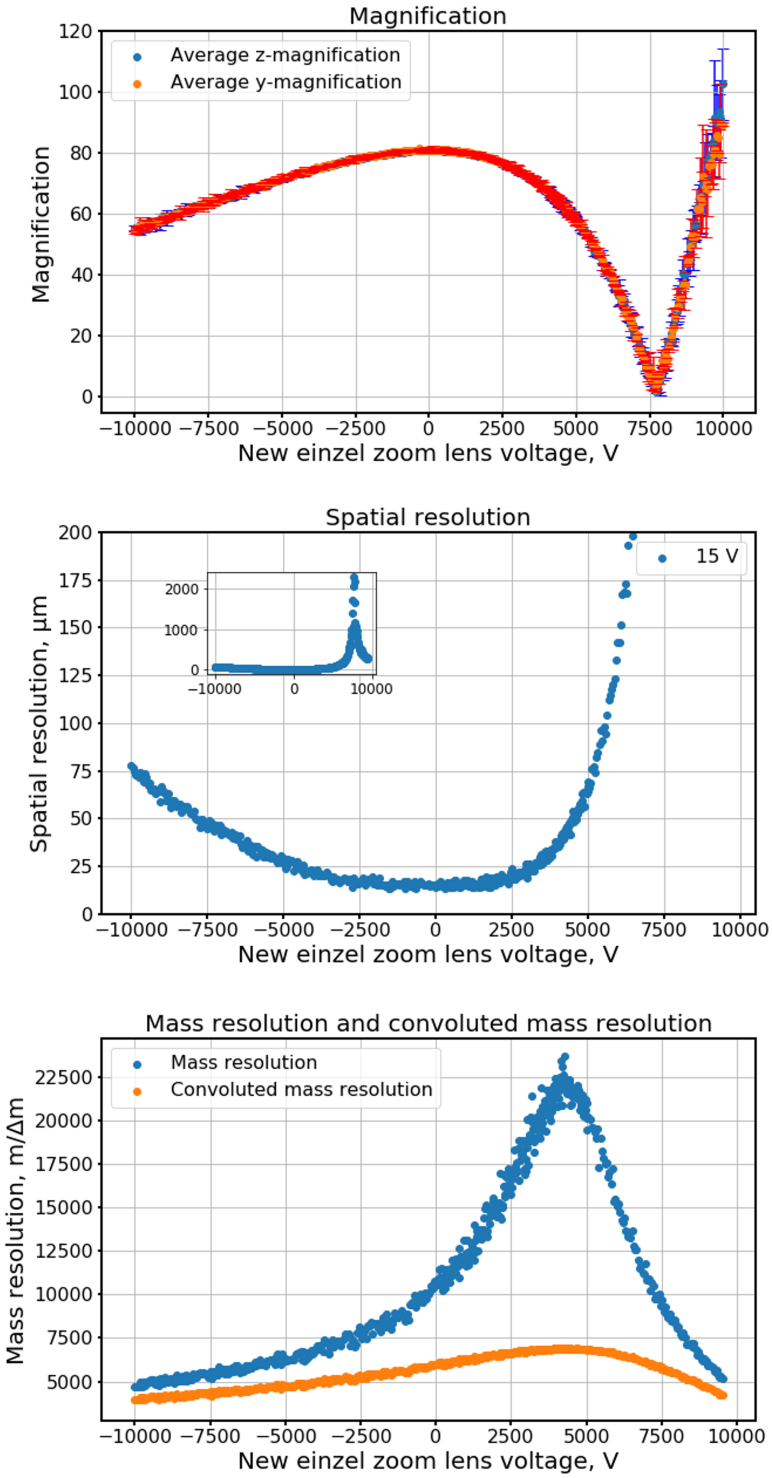


Figure 3.21: Simulation results produced using an additional einzel lens located between the ion optics and deflector. Displaying magnification (top), spatial resolution (middle), and mass resolution and convoluted mass resolution (bottom) against the voltage applied to the new einzel zoom lens. The spatial resolution plot has the full y-axis plot shown as an inset figure.

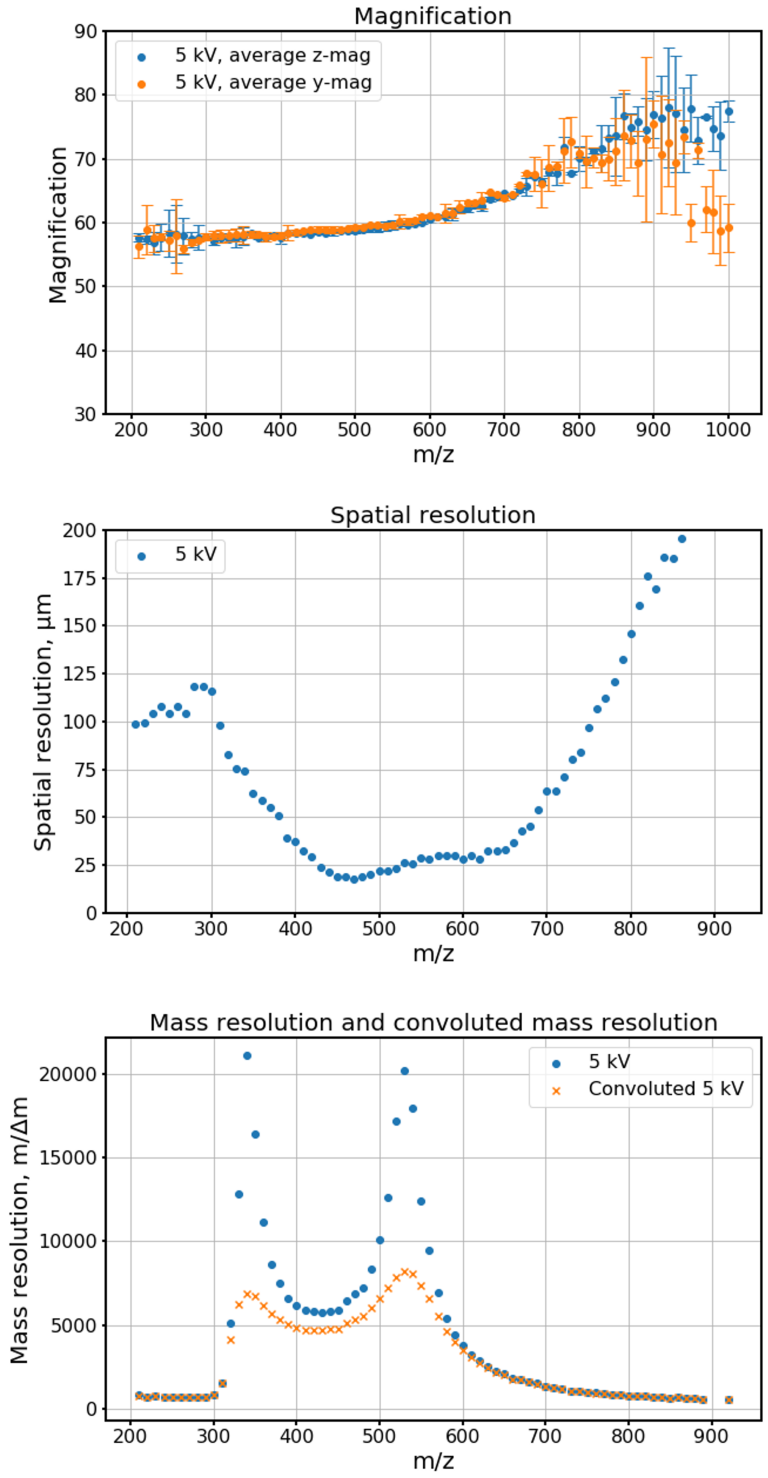


Figure 3.22: Simulation results produced using an additional einzel lens located between the ion optics and deflector. Displaying magnification (top), spatial resolution (middle), and mass resolution and convoluted mass resolution (bottom) against m/z, with 6 kV applied to the new einzel zoom lens.

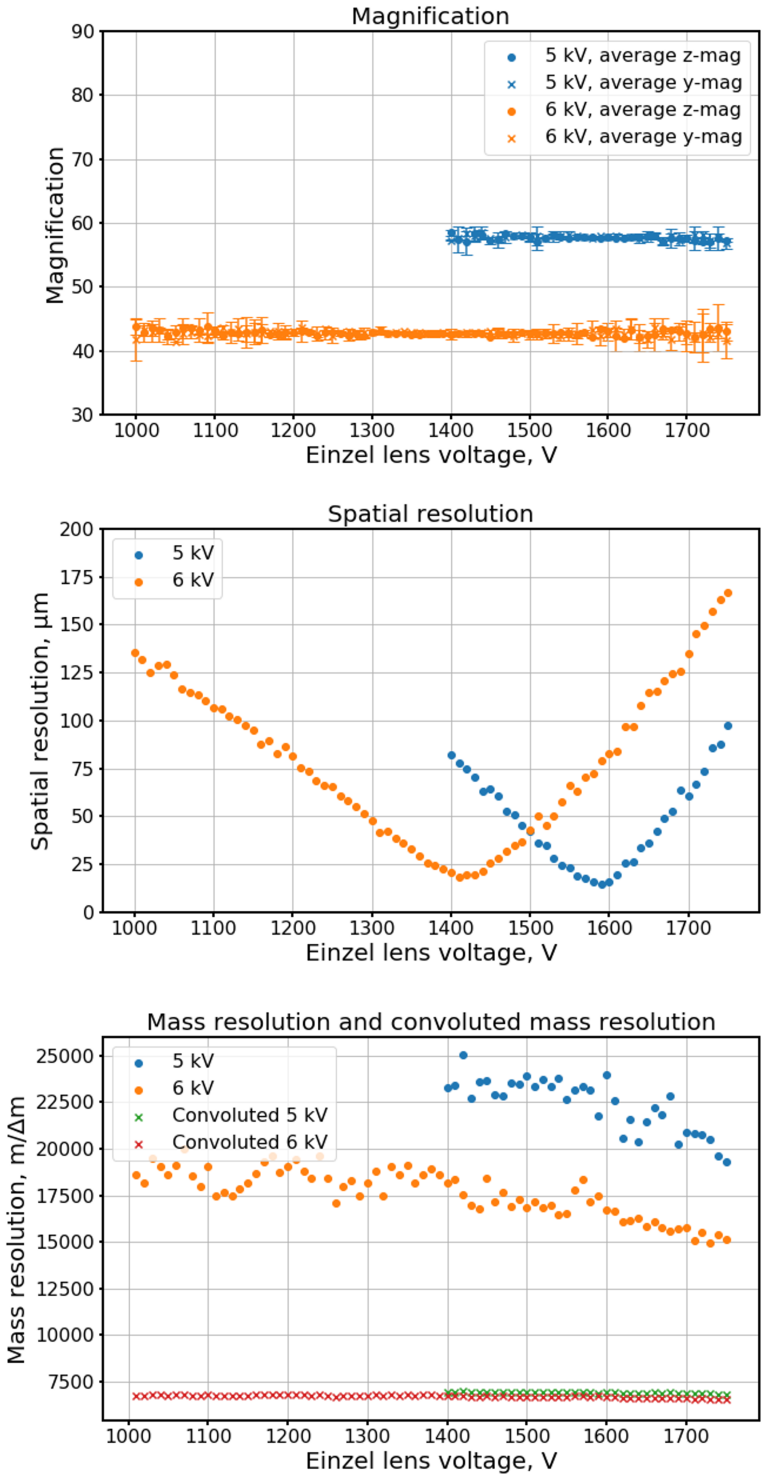


Figure 3.23: Simulation results produced using an additional einzel lens located between the ion optics and deflector. Displaying magnification (top), spatial resolution (middle), and mass resolution and convoluted mass resolution (bottom) against the einzel lens voltage, with 6 kV and 7 kV applied to the new einzel zoom lens, and a mass of 343 Da.

in the region of 1,400 V, and a new einzel zoom lens voltage of 6 kV. This does come at a small cost with the mass resolution, at 6,000 $m/\Delta m$, but the priority with the zoom lens is obtaining a lower magnification image with useful spatial resolution, as such the small decrease in mass resolution is not a limiting factor. Subsequently, this setup has been explored in simulation (Figure 3.24), whereby a lower magnification of $\times 40$ can be achieved at low masses. Unfortunately the magnification increases with mass, likely explained due to the longer time-of-flight. Heavier ions will travel with a lower kinetic energy, thus taking longer to reach the detector and having more time to diverge from the central ToF axis.

There is promise in an additional lens in this location, with simulation indicating a magnification of $\times 40$ being achievable. These early simulations do not consider physical limitations however. For any additional lens installed, it would be preferable for it to be located in the ion optics chamber. This is because it is a large chamber, allowing for easy installation and maintenance. The simulations discussed thus far have the lens located some distance along the flight tube, which is narrow and not very accessible. The natural next stage for the simulations, having proven its viability, is to explore if an additional lens in the ion optic chamber would be effective.

3.3.3 Using the existing einzel lens as a zoom lens

The simplest option, which requires no new electrodes to be installed, would be to utilise the existing einzel lens. We have already seen that in its current set up (outer plates grounded, middle plate held at a voltage), the field can be used to spatially focus the ion flight path. By altering the field through applying a potential to the grounded plates, it should be possible to simultaneously spatially focus the ions, while altering their magnification.

To investigate the effect the einzel lens has, each of the three electrodes was scanned through 0-3 kV, with steps of 25 V and all other variables kept the same, as shown in Figure 3.25. The electrode closest to repeller plate is the third electrode along the flight path, thus is labelled “Lens 3”, the central electrode in the einzel lens is “Lens 4”, and the final electrode is “Lens 5”. When not being adjusted,

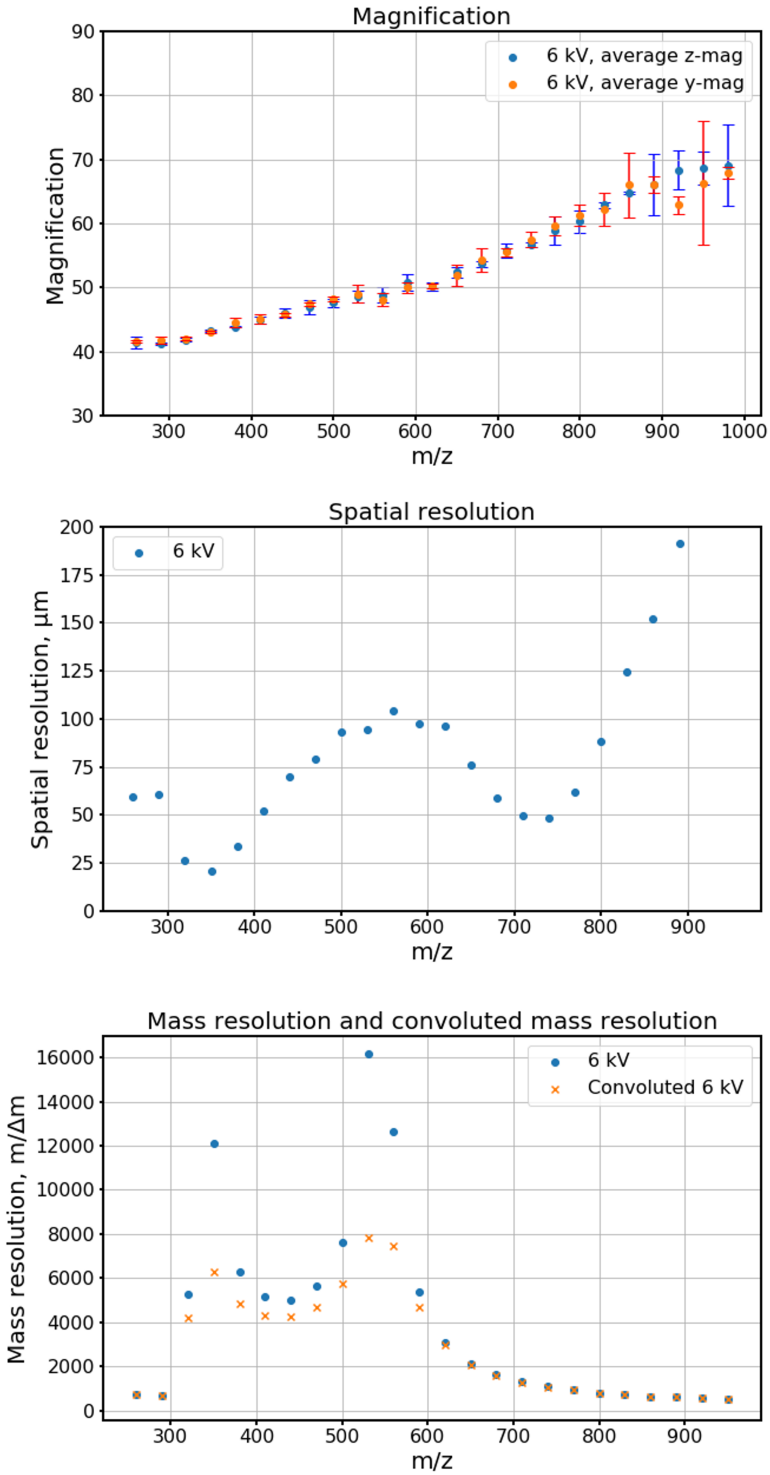


Figure 3.24: Simulation results produced using an additional einzel lens located between the ion optics and deflector. Displaying magnification (top), spatial resolution (middle), and mass resolution and convoluted mass resolution (bottom) against the m/z, with 6 kV applied to the new einzel zoom lens, 1.41 kV applied to the existing einzel lens, and a mass of 343 Da.

Lens 3 and 5 are held at 0 V, Lens 4 is at 1709 V. Ions of mass 343 Da were used. The plots for each electrode only show results when the percentage of ions reaching the detector falls below 90%, below 90% indicates a significant number of ions have diverged from the ToF axis.

From Figure 3.25, it can be seen that Lens 4 alters the spatial focusing window, and that the current potential of 1709 V is the optimal voltage for spatial resolution. This electrode has little effect on the mass resolution, and the magnification change is minor and largely a product of the worsened spatial resolution. Increasing Lens 3 from 0 V significantly worsens the spatial resolution, and the magnification as a result, additionally the mass resolution also decreases. This is likely due to changing the field between the extractor and Lens 3, altering the kinetic energy of the ions from that which the original parameters were optimised for. Using Lens 3 would probably require the other parameters to be re-optimised in order for it to be utilised. Lens 5 shows the most promise at being used for a zoom lens, as the voltage is increased, the mass resolution reaches a maximum at ~2 kV, and two minima for spatial resolution: the first at 25 V with 14μm, the second at 2,400 V with 10μm. While this potential shows an improved spatial resolution and mass resolution when compared to 0 V, there is little effect on the magnification, obtaining $\times$80. It is clear that altering just one of the three electrodes in the einzel lens will not effectively alter the magnification.

To further investigate the use of the einzel lens, the genetic algorithm was utilised. Each electrode in the simulation was varied, using a 343 Da ion. The optimisation conditions were designed to achieve magnifications of $\times$50 (v1, v3), $\times$55 (v4) and $\times$65 (v2), with a few arrangements selected from the simulations listed in Table 3.4, and the 200-1000 Da m/z scan obtained at each configuration in Figure 3.26.

Each of these mass scans dropped below 90% ion hits on the detector after 420 Da. Despite this, it can be seen that a stable magnification of $\times$65, $\times$55, and $\times$47 can be achieved for 200-400 Da. The spatial resolution worsens slightly for each variation, however the most significant change is the reduced mass resolution; the four parameter setups v1-4 all have a convoluted mass resolution of below 4000 m/z.

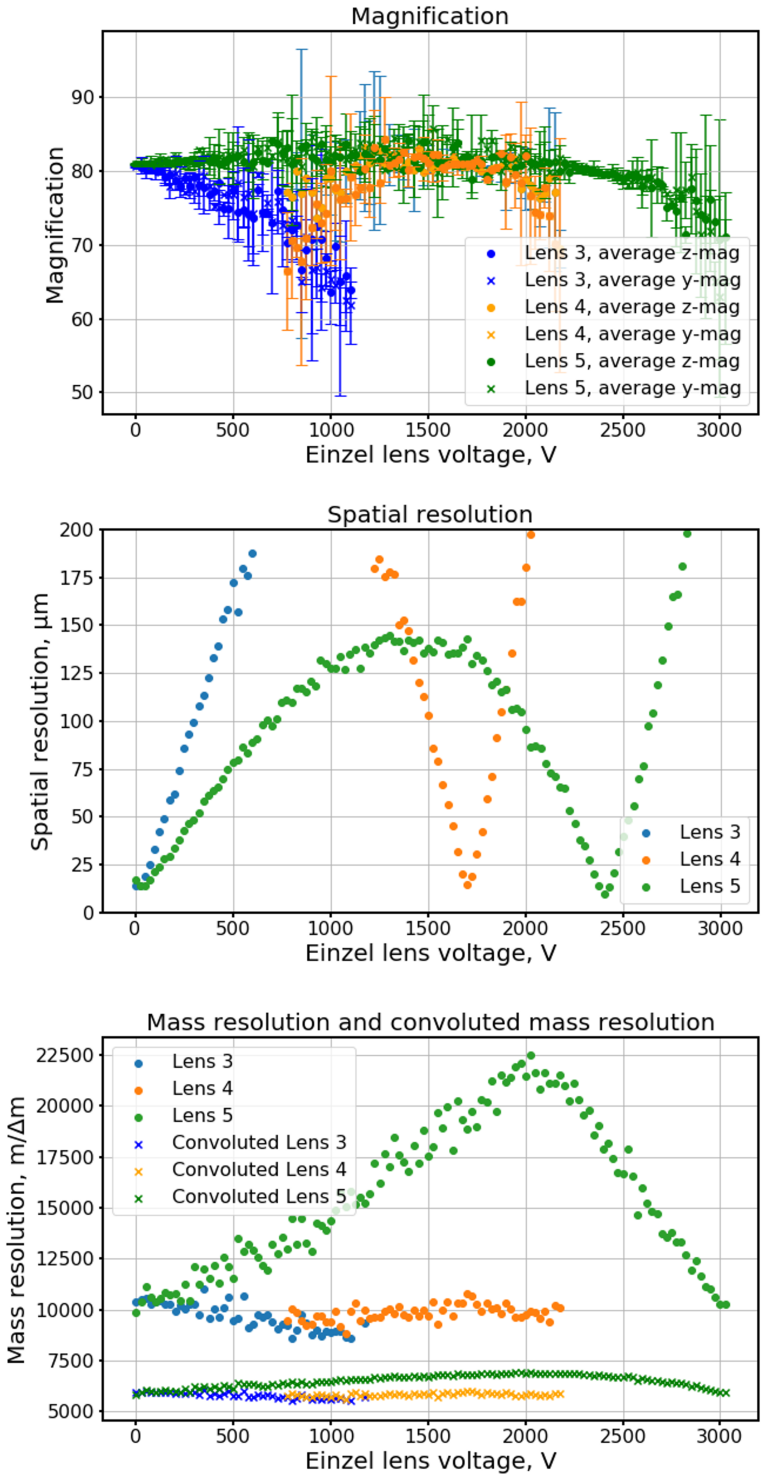


Figure 3.25: Simulation results produced using the existing einzel lens electrodes. Lens 3 refers to the electrode closest to the repeller, Lens 4 the middle electrode, and Lens 5 the electrode furthest away from the repeller. Displaying magnification (top), spatial resolution (middle), and mass resolution and convoluted mass resolution (bottom) against the einzel lens voltage, with a mass of 343 Da.

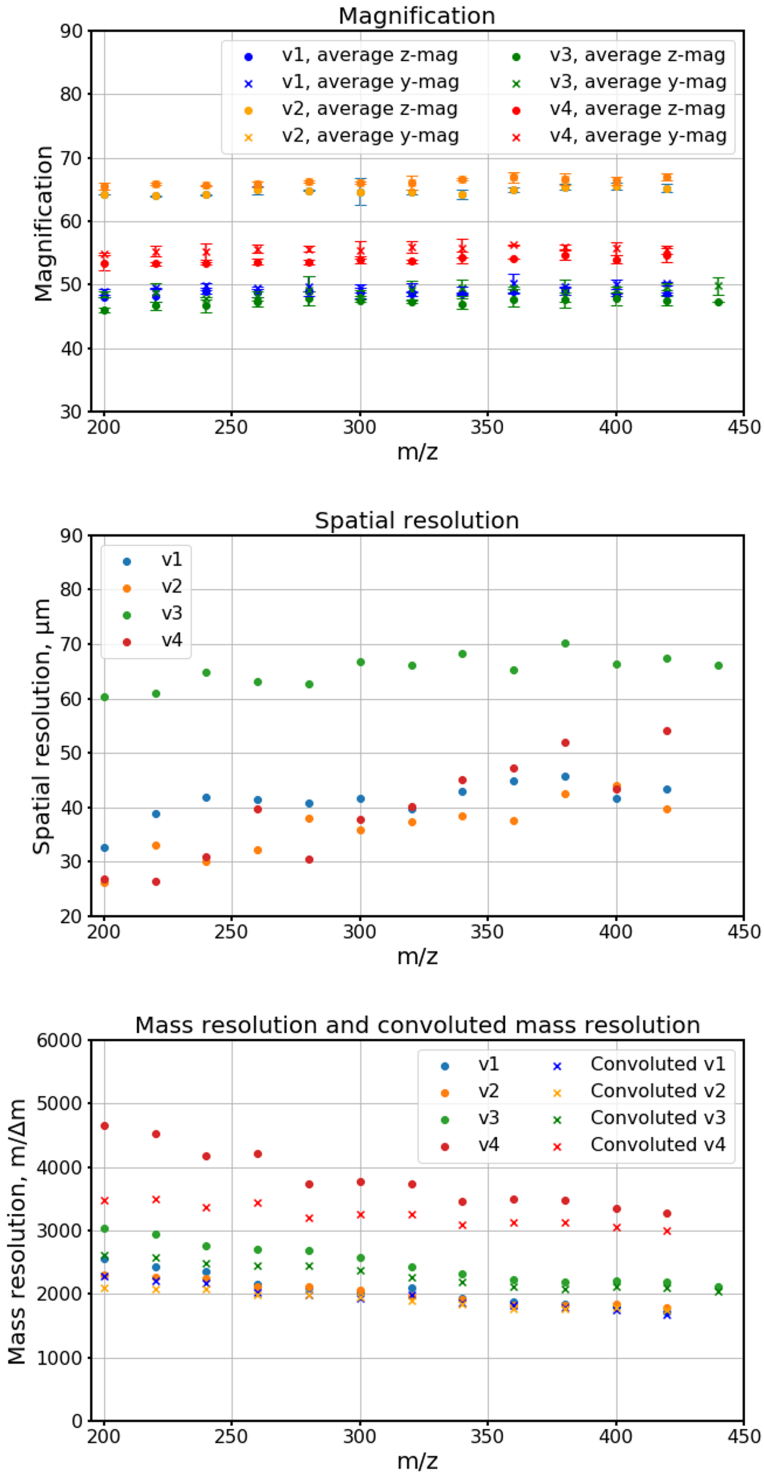


Figure 3.26: Simulation results produced using the existing einzel lens electrodes. v1-4 describes the simulation conditions listed in Table 3.4. Displaying magnification (top), spatial resolution (middle), and mass resolution and convoluted mass resolution (bottom) against m/z.

Table 3.4: The value assigned to each parameter as determined by the genetic algorithm.

Parameter	v1	v2	v3	v4
Repeller	7284 V	8704 V	8027 V	7665 V
Extractor	5928 V	7114 V	6403 V	5072 V
Lens 3	2286 V	2763 V	1865 V	0 V
Lens 4	3889 V	4667 V	4123 V	4263 V
Lens 5	0 V	0 V	0 V	3217 V
PEDA Step	5135 V	5160 V	5040 V	4924 V
PEDA Max	8700 V	8500 V	8526 V	8245 V
PEDA delay time	2.85 ns	2.78 ns	2.80 ns	2.80 ns
Deflector	45 V	46 V	47 V	46 V
Reflectron	8721 V	9006 V	8664 V	8265 V

There is potential for the einzel lens to be used as a zoom lens, however this has been shown to come at a cost to the mass window and mass resolution, as well as the spatial resolution. Improvements could be possible with further optimisation of the other parameters, but it may be limited to only a factor of two change in magnification.

3.4 Conclusion

Simulations showed that the spatial resolution could be improved by increasing the electric field strength, this was proven experimentally on the reflectron ToF mass spectrometer with single-field PEDA. This was verified experimentally, obtaining an ion image with 8 ± 1 μm spatial resolution, compared to 13 ± 1 μm when operating under the original conditions. The mass resolution attained was lower than predicted by simulation at 3,888 ± 370 $m/\Delta m$, thought to be a result of the single-field PEDA pulse not being fully optimised. These experiments were limited to the upper range of the power supplies available, however it is theoretically possible to further improve the spatial resolution with higher potential power supplies.

In order to increase the capabilities of the reflectron ToF mass spectrometer, methods of introducing variable magnification were explored. Firstly using the grounded electrodes at the entrance to the reflectron. This showed promise, however proved effective along one axis only, distorting the image. As the ions do not

pass through the reflectron centrally, trying to alter the magnification with these electrons proved to be an unusable method.

Another method proposed involved the introduction of an additional einzel lens. A new lens could thus be positioned centrally along the axis, avoiding the distortion created by the reflectron electrode lens. The position of the lens proved critical - space after the reflectron is limited, forcing the lens too close to the exit and leading to distortions, while locating it before the deflector achieved a $\times$40 magnification at the expense of mass resolution. The most promising result was obtained with the lens located just before the entrance to the reflectron; magnifications of $\times$65, $\times$40, and $\times$20 were obtained at different potentials. This offers a change in field of view from 270 μm to 1242 μm at $\times$20 magnification, at a cost to mass resolution (<4,000 $m/\Delta m$), however, this could likely be improved by re-optimising the other instrument parameters to realign the mass focal window.

The final option explored involved using the existing einzel lens. Magnifications of $\times$65, $\times$55, and $\times$47 were achieved, but over a limited mass range of 200-450 Da, and with poor spatial (>30 μm) and mass resolution (<4,000 $m/\Delta m$). Further work is necessary to improve these results, but using the einzel lens to alter the magnification is realistic, although it will likely come at a cost of instrument resolution. Using the existing lens is the simplest solution, as there is no need to install new electrodes, but a greater change in magnification was achieved using an additional einzel lens, thus that would be the best method for this instrument.

Ultimately, it can be shown that the alternative magnifications can be obtained, with a reduction from $\times$92 to $\times$20 displayed. Doing so would enable a user to obtain an image of a greater sample surface area, after which an area of interest could be located and then imaged at a higher magnification. To fully employ this variable magnification, further work is needed to optimise the parameters, as well as experimental testing to prove its efficacy. Additionally, an adjustable sample stage would be needed, as currently the samples are held in a fixed location, preventing the sample from being moved towards a region of interest.

4

Improving Time Precision with a Timepix3 Camera

Contents

4.1 Timepix3 Camera and Data Processing 122
4.1.1 Timepix3 Camera 123
4.1.2 Methods 125
4.1.3 Data Processing 126
4.2 Experimental Verification 130
4.2.1 Experimental jitter 131
4.2.2 Laser intensity 134
4.2.3 LED 139
4.2.4 Effects on Mass Spectra 146
4.3 Conclusion 150

The following chapter will discuss how the Timepix3 camera works, and what the data processing entails. This is followed by an exploration in experimental techniques to improve the experimental jitter, options regarding time stamping techniques, as well as the use of time-over-threshold in data acquisition.

In order to fully utilise a time-of-flight microscope-mode imaging mass spectrometer, like the two presented in this thesis, a time-stamping camera is necessary. The previous chapter presents data acquired with a CCD camera, which offers high spatial resolution, but is purely position-sensitive and unable to record the

time at which pixels are activated.

Using a PImMS sensor, it is possible to record an ion image for each peak in a mass spectrum concurrently with a 25 ns timing precision on the CMOS sensor [135]. When paired with the reflectron ToF mass spectrometer, this corresponds to a 1,600 $m/\Delta m$, compared with the PMT which obtains a timing resolution of 4 ns (8100 $m/\Delta m$) [105]. As such, PImMS is limiting the time resolution attainable from this instrument.

As research in time stamping sensors have developed, the Timepix3 chip was released, and it exceeded the capabilities of PImMS, offering a time resolution of 1.5625 ns. Timepix3 has evolved from Timepix and Medipix chips, and extends its functionality by recording events time-of-arrival (ToA) and time-over-threshold (ToT) simultaneously, while also improving the timing resolution [136]. This improvement in timing resolution has been achieved using Voltage Controlled Oscillators (VCOs) inside the pixel matrix, and extends the application of the Timepix3 chip, with its primary uses in particle tracking [137]. Variations of the Medipix and Timepix chips have been used in a range of applications, including neutron imaging, radiotherapy, and astronomy [138–140].

The Timepix3 chip was designed primarily for use as an X-ray detector or particle tracker, where it would typically be bump bonded to a standard silicon sensor. However, for our purpose, it is necessary to detect optical photons produced from the scintillator. Thus the Timepix3 camera was used, consisting of a sensor containing a tinned entrance window and an antireflective coating, paired with a Nikon 55 mm f/2.8 macro lens to focus the light on to the sensor [141]. This setup provides high quantum efficiency over the range 400-900 nm, suitable for the Exalite-404 scintillator, which has an emission maximum at 423 nm [112, 142].

4.1 Timepix3 Camera and Data Processing

The following section will present the Timepix3 camera, detailing the chip and camera properties, followed by the methods used to pair the camera with the

reflectron ToF mass spectrometer and process the output. The methods and data processing were developed by Wood *et al.* [81].

4.1.1 Timepix3 Camera

Timepix3 Chip

The Timepix3 hybrid pixel readout chip comprises of a 256 × 256 pixel array with 130 nm CMOS technology, dimensions of 14.08 mm × 14.08 mm, and square pixels of pitch 55 μm. These pixels are grouped to allow for circuitry to be shared: groups of 4 × 2 pixels are labelled as superpixels (SP), 64 superpixels forms a double column (DC), and 128 of these double columns complete the array (Figure 4.1). Identification of each pixel is done using a 16-bit address, which produces a maximum of 65,536 (256 × 256) unique identifiers. This is then split into 7-bit for the 128 double columns, 6-bit for the 64 superpixel number, and 3-bit for the 4 × 2 pixel number.

The chip operates under two clocks, time-of-arrival (ToA), and fine time-of-arrival (fToA), the combination of which produces a 1.5625 ns timing resolution. The ToA is obtained from a 40 MHz (25 ns) global clock via a 14-bit register; this provides time bins of 409.6 μs. Once the ToA clock for a pixel has been triggered, the fToA clock is activated. This clock operates at 640 MHz (1.5625 ns) on a 4-bit register. Between the two clocks, the fast timing resolution is obtained. Alongside the ToA and fToA information, the time-over-threshold (ToT) is recorded using a 10-bit register. The ToT provides an estimate of the signal amplitude and has an adjustable threshold to cut out unwanted low intensity signal. This is depicted in Figure 4.2. There is a pixel dead time of the pixel ToT + 475 ns, accounted for by the pixel measurement time and data packet transfer time. There is a maximum hit rate of 40 Mhits $s^{-1}m^{-2}$ for continuous operation.

Timepix3 camera

The Timepix3 chip was designed to record electrons and ion events directly, requiring it to exist within the vacuum. However, use outside of a vacuum is important for a range of different purposes and allows for easier access for upgrades and maintenance.

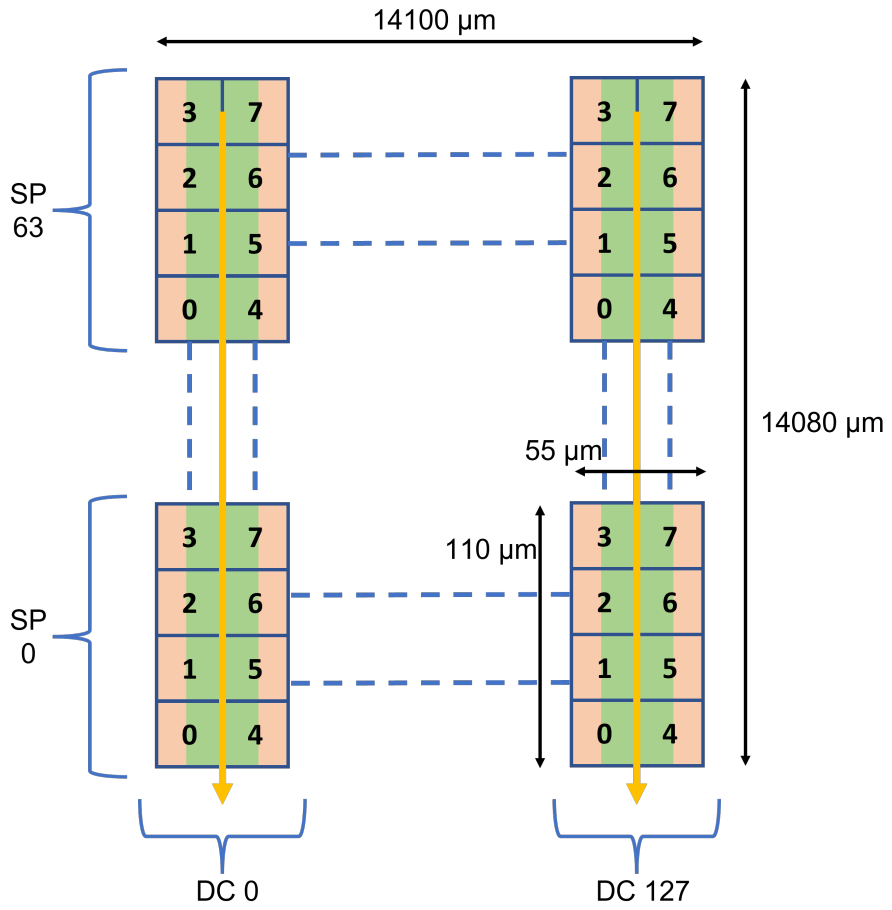


Figure 4.1: Schematic displaying the pixel grouping on the Timepix3 chip. Pixels are shown as the individually numbered squares, superpixels as the rectangles made up of 2 × 4 pixels (labelled SP), and double columns (DC) for a column of 64 super pixels.

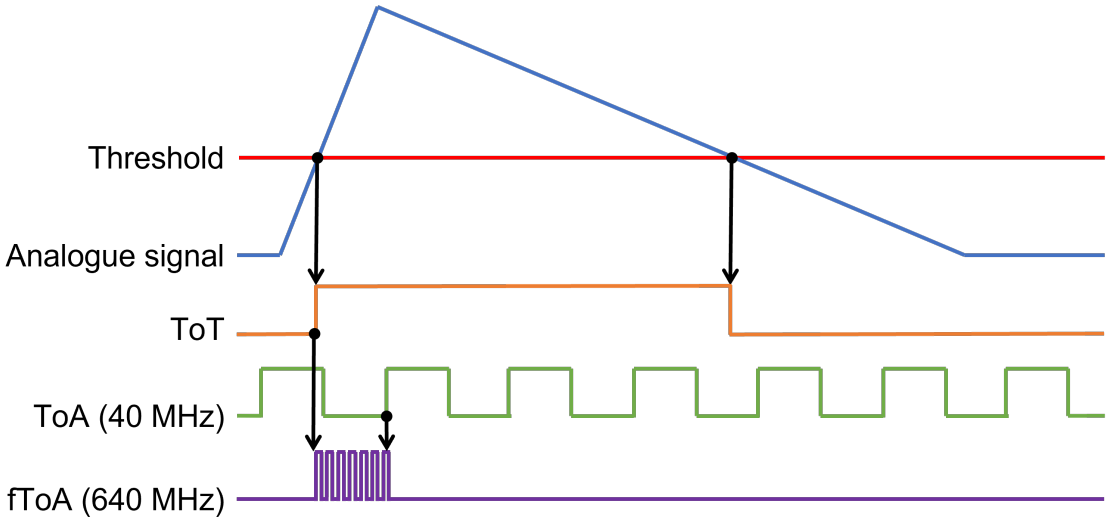


Figure 4.2: Schematic diagram illustrating the ToA and fToA clocks and how ToT is determined from the analogue signal exceeding the threshold set.

Nomerotski *et al.* developed the Timepix3 camera using the Timepix3 chip so it can record visible photons as a fast optical imaging device [143].

This camera comprises of a specialised silicon pixel sensor (a silicon pixel array with greater than 90% quantum efficiency [144]), bump-bonded to the Timepix3 chip. Located behind a window with anti-reflective coating, and paired with a lens. This corresponds to ~61 pixels per 1 mm^2 area of the screen when the Exalite screen fills the field of view of the chip. Transistors in each pixel amplify the charge, then transport this information to the digital readout, provided the charge exceeds the threshold.

Given the increased amount of information the camera is able to acquire, the quantity of data capable of being recorded by the Timepix3 camera is 80 Mhits per chip per second. The Timepix3 camera utilises a general purpose readout system for pixel ASICs (Application-Specific Integrated Circuit) called SPIDR (Speedy PIxel Detector Readout) [145]. This allows for the full bandwidth of the camera to be used, and can accept a time stamp and external trigger pulse. The advantage of such a system is the ability to synchronise the trigger with the laser shot, providing a time reference for the resultant photons. The disadvantage, however, is the SPIDR system is expensive. To combat this, we have utilised an alternative means to trigger the camera, as will be discussed in the subsequent section.

4.1.2 Methods

In order to fully exploit the high timing resolution of the Timepix3 chip, a high performance readout system is required. As the SPIDR system is a costs approximately £80,000, an alternative was utilised: the USB 3.0 AdvaDAQ system. While this system is considerably cheaper than the SPIDR system, it does not accept an external trigger, and thus must operate in continuous mode. The nature of the experiments conducted within this thesis require a trigger in order to overlay and summate the data output, hence a means to bypass this issue was required.

A solution to this problem involves redirecting a portion of the laser beam towards the sensor, and having that serve as the marker for $t_{0,n}$, such that n number

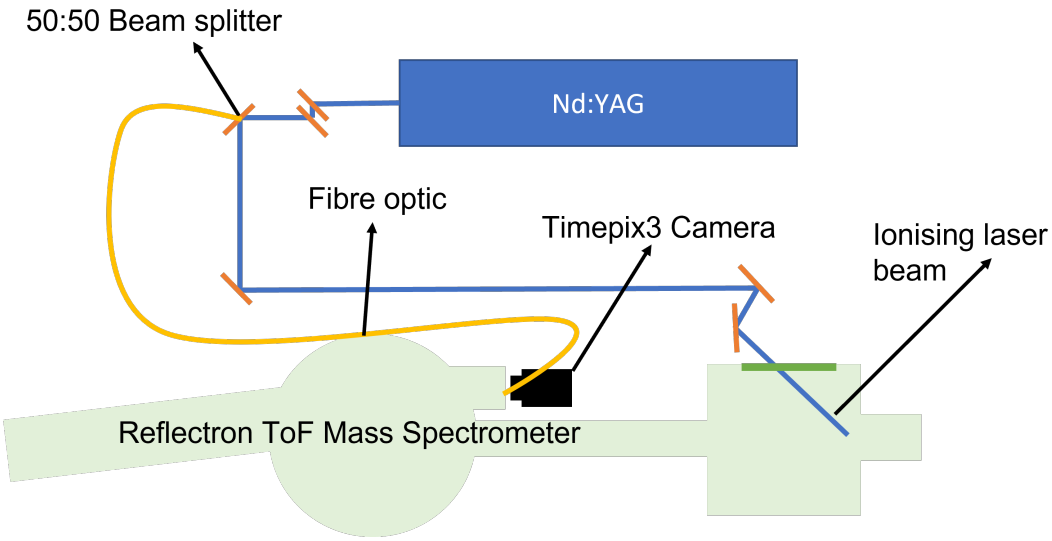


Figure 4.3: Diagram of the laser beam path from the Nd:YAG laser into the reflectron ToF mass spectrometer. For use with the Timepix3 camera, a 50:50 beam splitter is used, and a portion of the beam directed at the camera using a fibre optic .

of spectra can be accurately overlaid [30, 81]. A 50:50 beam splitter (Thorlabs 50:50 UVFS Plate Beamsplitter) located among the external optics (see figure 4.3) is used to direct a portion of the ionising laser beam into a fibre optic cable. This fibre optic is then placed in a location visible to the camera, aimed at a corner of the chip so as to not interfere with any pixels in the active region for the instrument detector.

The AdvaDAQ system and Timepix3 camera can be controlled using PiXet-Pro, software produced by AdvaDAQ. The software is used in continuous mode, which introduces a file size issue - large data files take longer to process and increase the risk of significant data loss. Three actions are implemented to mitigate this: 1) the fibre optic laser spot is positioned such that a minimum number of pixels are activated (approximately 10 to 30); 2) the software is operated in "pixels" mode, which records only the activated pixels, and not the inactive; and 3) the data is saved in files 5 s in duration, which equates to 50 laser shots with the 10 Hz Nd:YAG laser.

4.1.3 Data Processing

The following data processing method was developed by Wood *et al.* using python and operates in 3 phases [81]. Phase 1 is the conversion from the raw output,

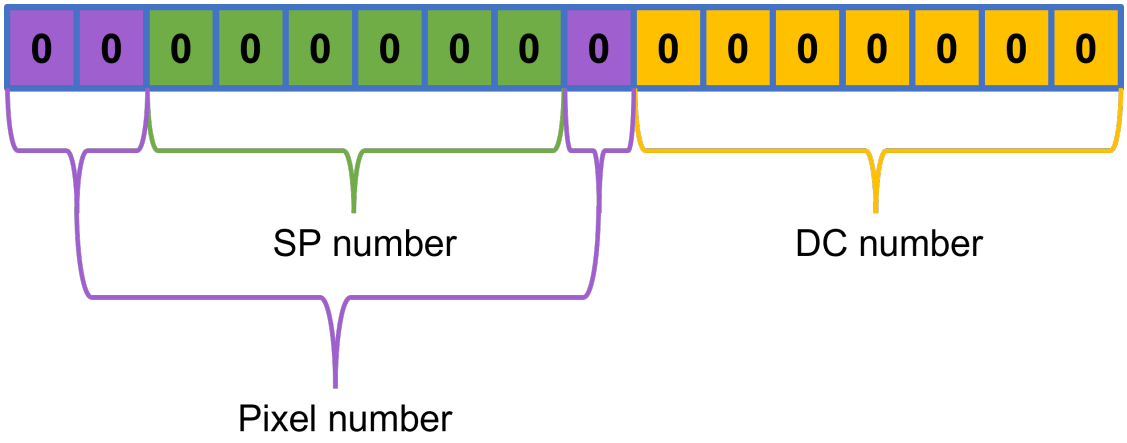


Figure 4.4: An example of a 16-bit address, indicating where information regarding pixel number, superpixel (SP) number and double coloumn (DC) is extracted from.

which comprises of the matrix, ToA, ToT, and fToA, into the desired form of x, y, t, and ToT.

Firstly, the matrix, which is output as a 16-bit register, is converted into positional coordinates x and y. The register is transformed into binary, and the digits separated out. Digits 1-7 identify the double column, 9-14 the superpixel, and 8 & 15-16 the pixel (see Figure 4.4). A combination of pixel number and double column number identifies the x-coordinate - if the pixel number is less than 4, the pixel lies on the left half of the superpixel and the x-coordinate is given by 2 $\times$ double column number + 1. If the pixel number is equal to or greater than 4, the pixel is on the right half, and the x-coordinate is given by 2 $\times$ double column number + 2. The y-coordinate is obtained using the superpixel number and pixel number. Pixel numbers 0 and 4 lie at the bottom of the super pixel, thus the y-coordinate is 4 $\times$ superpixel number + 1. Pixel numbers 1 and 5 are second from the bottom, thus are +2, and the trend continues for the 2 and 6 pairing, and 3 and 7.

The second step in this phase is the conversion from ToA and fToA into 1.5625 ns time bins, T. The ToA output runs on a 40 MHz clock. When a pixel exceeds the set threshold, the 640 MHz fToA clock is activated and runs until the rising edge of the ToA global clock arrives. The fToA clock duration is recorded, as well as the ToA clock met by the fToA. Hence the time can be determined from ToA - fToA. Conversion into time bins is calculated as follows:

$$T = \frac{(25 \text{ x ToA}) - (1.5625 \text{ x fToA})}{1.5625}. \tag{4.1}$$

Conversion into time, t, is given by:

$$t = T \times 1.5625 \tag{4.2}$$

Phase 2 of data processing is clustering. Phase 1 converts the raw data into position and time bins, however, each file output is a continuous string of data spanning 5 s (50 laser shots) due to the absence of an internal trigger. For each new file, the time bin number resets. As such, a method of clustering the data into individual laser shots (frames), is required so that the frames can later be overlaid and summed.

The separation into individuals frames was achieved using a machine learning protocol called KMeans clustering from the Python SciKit package [146]. This clustering technique takes n data points as input and groups them into k clusters. In this case, n describes the number of ion events, and k the number of laser shots per data file [147]. The result is each observation is assigned to a cluster after a number of recalculations.

The procedure follows three key step: initialisation, assignment, and recalculating. The general goal behind k-means is to add k new points to our data, each on of these points is known as a centroid. The centroid will attempt to centre itself in the middle of one of the k clusters. Once the centroid stops moving, the clustering algorithm stops.

The initialisation process involves generating a list of k different means. k is determined based on the number of laser shots, as the goal is to separate the data string into individual frames. A cartoon depiction of a data set is shown in Figure 4.5, in this case, it could be split into two groups, thus it would be reasonable to set $k = 2$. The values for k means is initialised, producing centroids shown as circles on the diagram. The algorithm will then go through each data point, measuring the distance between each point and the two centroids. With the Timepix3 camera data, this is determined from the least squared Euclidean distances between the k

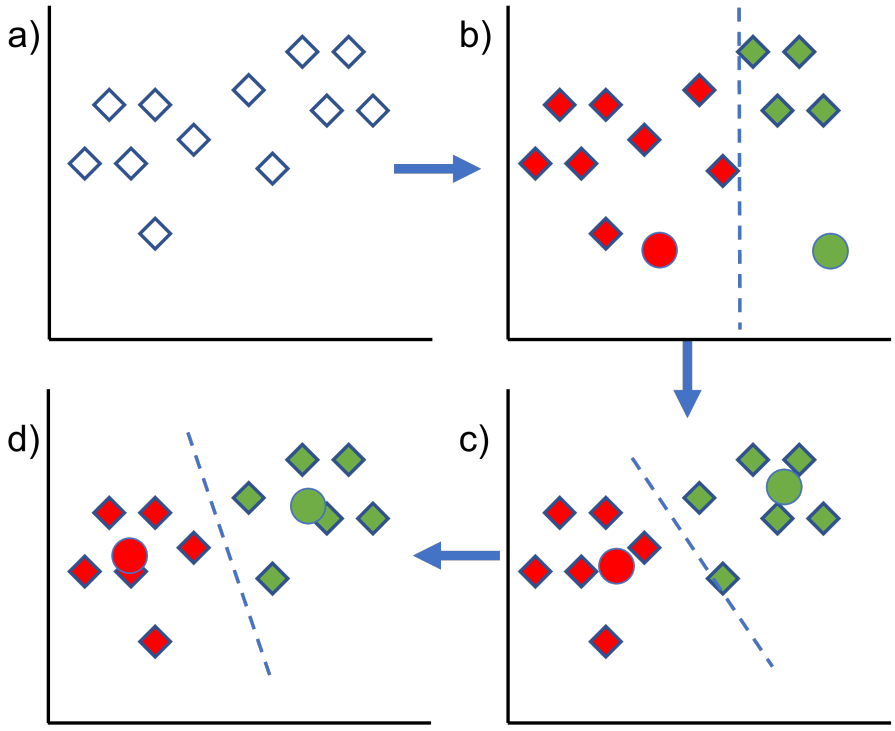


Figure 4.5: Schematic diagram depicted the k-means clustering process. The diamonds represent individual data points, the circles represents the centroids. a)-b) shows the initialisation and assignment step, with the number of centroids determined by k. c) and d) shows subsequent recalculation attempts, moving the centroid to the average value in the group until no further improvement is observed.

mean and the time stamp for each ion event. Once this has been done, each data point is assigned to the nearest centroid. This is depicted in Figure 4.5 b), with the data points being split into two groups and assigned to the closest centroid.

After assignment to a centroid, the means are recalculated in order to optimise the grouping. The new value of the centroid is the sum of all the data points belonging to the centroid group divided by the number of points in the group. This recalculation moves the position of the centroid, as shown in Figure 4.5 c). This repositioning may result in a data point changing centroid groups if a different centroid is a closer match than its initial assignment. This recalculation step is repeated until the centroid no longer changes in value, thus the mean has converged and no further improvements can be made (Figure 4.5 d).

The laser operates at 10 Hz, hence the output data should repeat every 100 ms. The majority of the ion events occur within 100 μs of the laser shot, resulting in

the ion events occurring in concentrated bursts. These concentrated bursts of data points are easily identified via kmeans clustering since there is very little overlap between the groups and hence an unambiguous centroid can be found. As such, this technique is efficient, accurate and computationally inexpensive. The output of this step is an additional column on the output data file, supplying a frame number assigned to each cluster of events recorded, producing 50 frames for each 5 s file.

Phase 3 of the data analysis process is simply identifying the time of ionisation, t_0, for each frame, and subtracting that from the value for t within each frame. An area of pixels is specified, this being the location of the fibre optic laser beam acting as the trigger. The earliest time bin activated is then set as T_0, and this value is subtracted from the rest of the frame. There are a number of factors to be aware of with this process, which will be discussed later in this chapter.

Following these three data processing phases, the final result allows for the time and positional information from the Timepix3 camera to be overlaid and summed. This ultimately bypasses the need for a trigger and the SPIDR readout.

4.2 Experimental Verification

As discussed previously, the Timepix3 camera requires a portion of the laser to be directed at the chip in order for a t_0 to be defined for each laser shot. To obtain the best mass resolution achievable from the pairing of the experimental setup with the camera, t_0 must be as accurate as possible to allow for the best alignment of n spectra. Even a small shift in alignment can cascade and create a summated spectra with significantly poorer resolution.

The rest of this chapter will explore methods in which to improve the timing resolution obtained with the Timepix3 Camera, exploiting its fast time resolution and ToT information, and minimising any effects in our experimental methods which reduce its precision.

4.2.1 Experimental jitter

A means of checking the alignment of t_0 is to look at the time difference between consecutive frames values to check how consistent the separation is. With the reflectron ToF mass spectrometer, a difference of 100 ms is expected, a product of the 10 Hz rep rate from the laser.

Given there is no internal trigger, the compiled data is reliant on t_0 being accurately defined for each laser shot. By looking at a region either side of t_0 in Figure 4.6a), we can see that t_0 is largely assigned as 0, however, it is also clear that some of the frames have been offset by 409.6 μs (262,144 time bins). This is considered to be an artefact of the AdvaDAQ readout software, the exact cause is unknown, but likely related to the nature of the readout occurring in 12-bit clock cycles (4096 counts).

The 409.6 μs offset can be corrected for by simply shifting the data set by the same amount, something easily done as the experimental cycle is typically complete within 0 to 10 μs, thus there is no overlap between the mistakenly shifted data and the non-shifted. However, the shift can begin at any point in the spectra, resulting in part of the spectra being offset, not necessarily just at t_0. This is because the data is collected continuously and the occurrence of the laser flash trigger has no impact on the clock cycle or when the readout system suddenly shifts.

The correction for this offset occurring at any point in the experimental cycle is searching for any points which are outside of an expected window. This was set as <-1,000 and >200,000 timebins (<-1.5625 and >312.5 μs), which does not overlap with the typical ToF collection window of 0 to 64,000 timebins (0 to 100 μs). Any data points between -1,000 and 200,000 time bins were not adjusted. Anything detected within the frame outside of this region and within 409.6 μs of the limits is eligible to be time shifted. Thus any data point existing in the region -411.16 to -1.56 μs and 312.5 to 722.6 μs will have 409.6 μs added or subtracted, respectively, to its ToA. The result of this correction is demonstrated in Figure 4.6 b).

t_0 is selected as being the earliest ion event within the frame. With the 409.6 μs AdvaDAQ shifting, this t_0 can be incorrectly identified as an event which actually

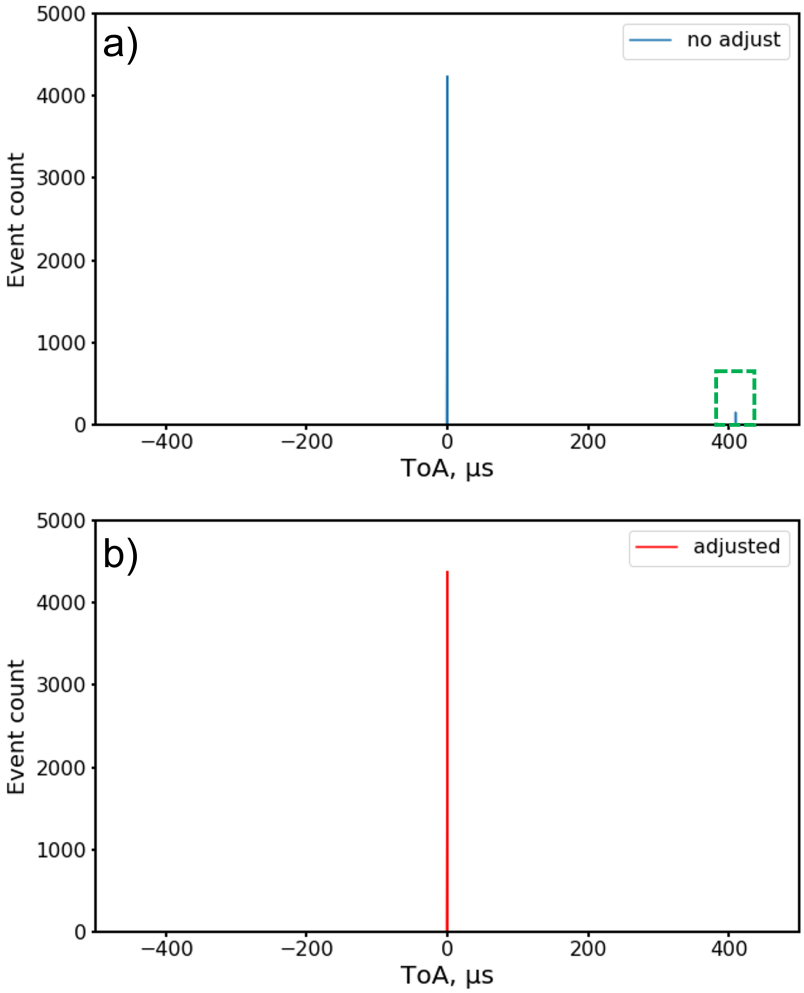


Figure 4.6: Plot of time-of-arrival (ToA) against event count for a laser t_0 pulse on the Timepix3 Camera. a) shows frames with a t_0 at 0 μs and a portion of the frames (highlighted in the green box) are offset by 409.6 μs, b) shows the same plot with the offset corrected.

happens a few time bins before or after 0. This is especially problematic when the shift occurs partway through the laser pulse. This results in frames being misaligned upon summation, broadening the final spectra. To account for this, an initial t_0 is identified (the first ToA in the specified region of each frame), the offset correction is applied, followed by subtraction of the initial t_0 from the ToA's for the rest of the frame. This ensures t_0 is set to zero and the rest of the frame is relative to 0. Applying this correction can save up to 10% of events, improving the intensity as more ion events are included, and improving the accuracy of the ToA distribution.

This correction can be applied to any instrument, provided the shot frequency is no greater than approximately 2 kHz. This is approximated from a data shift of 409.6 μs, plus the ToF window. The ToF window with this shift shouldn't be too long however, as it may result in frames overlapping within the AdvaDaq software, which could introduce issues with the k-means clustering. It is unclear if frame overlapping would occur, as it is currently unknown how exactly the shift works within the software and can't be explored using the reflectron ToF instrument due to only ~100 μs of data being recorded every 100 ms. The SIMS ToF instrument would be usable for lower mass ions; a 400 Da ion has a time-of-flight of approximately 10 μs with the instrument described in Chapter 2, and the C_{60}^+ ion gun can operate at up to 1 kHz, thus 10μs + 409.6 μs « 1 ms.

Another form of jitter to be mentioned is laser jitter. The laser in theory operates at exactly 10 Hz (100 ms), however in practice, it can deviate from this frequency. The expected difference between consecutive T_0's, ΔT_0, is 64,000,000 timebins, which when looked at experimentally actually results in a average laser shot time difference of approximately 63,999,995.5 timebins (100 ms minus 7 ns). This is illustrated in Figure 4.7, which consists of 500 individual laser shots, clustered into bins of 10 frames, with error bars to show the distribution of Δt_0 across the 50 s of data recorded. The laser has an inherent operational jitter for each individual laser shot, listed as 6-10 ns within the manual. It is likely that the jitter described in the manual is the same as that detected by the Timepix3 Camera.

A jitter of ~7 ns is large enough to impact the temporal resolution when multiple spectra are aligned. As t_0 is identified on a shot-by-shot basis, rather than an external trigger, any jitter which occurs from the laser, will also occur to the portion diverted through the fibre optic and onto the camera. This effectively cancels out the jitter, removing the convolution that would otherwise occur.

By correcting and accounting for these two issues, we can reduce data loss and improve the accuracy of t_0 determined for each frame.

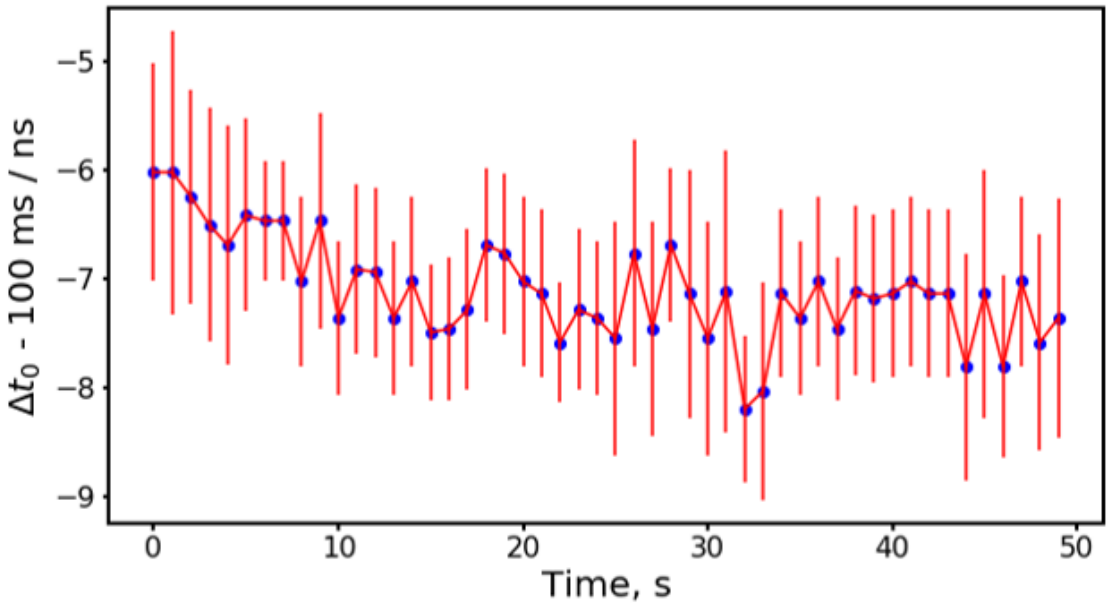


Figure 4.7: Difference between consecutive t_0 time-of-arrivals, Δt_0 with the laser repetition rate (100 ms) subtracted, against time from the first laser shot. The data has been binned into groups of 10, with blue markers indicating the average and red error bars displaying the standard deviation within each bin.

4.2.2 Laser intensity

The accuracy of the t_0 value is dependent on how well defined the laser flash is - a more precise t_0 means better alignment of frames, and a reduction in any broadening caused by the processing. To measure this dependency, the effect of changing the laser flash intensity on t_0 has been investigated.

The fibre optic was positioned on the bench top 16 cm away from the Timepix3 camera, pointed directly at the camera and aimed at a corner of the sensor to minimise the risk of damaging any pixels in the active detector region. The fibre optic was placed behind neutral density filters (Thorlabs, Mounted N-BK7 Reflective) spanning a range of optical densities. Neutral density filters uniformly attenuate the laser beam, thus reducing the beam intensity. This change can be quantified using the optical density (OD), given by the equation:

$$\mathrm{OD} = \log_{10}\frac{1}{T}, \tag{4.3}$$

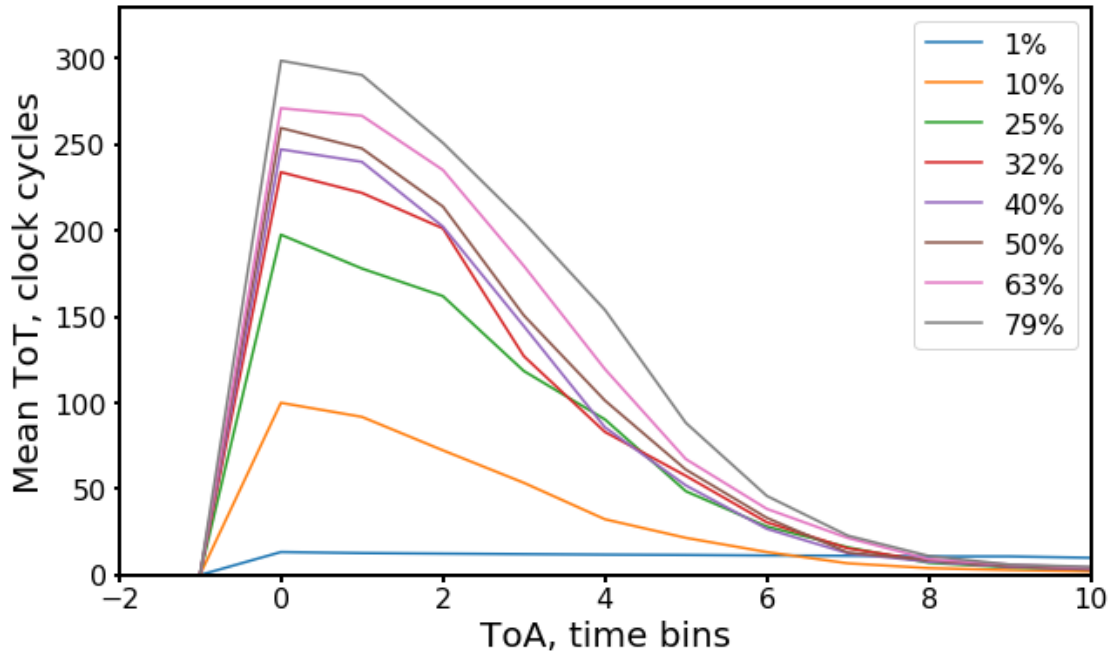
or,

$$T = 10^{-\mathrm{OD}}, \tag{4.4}$$

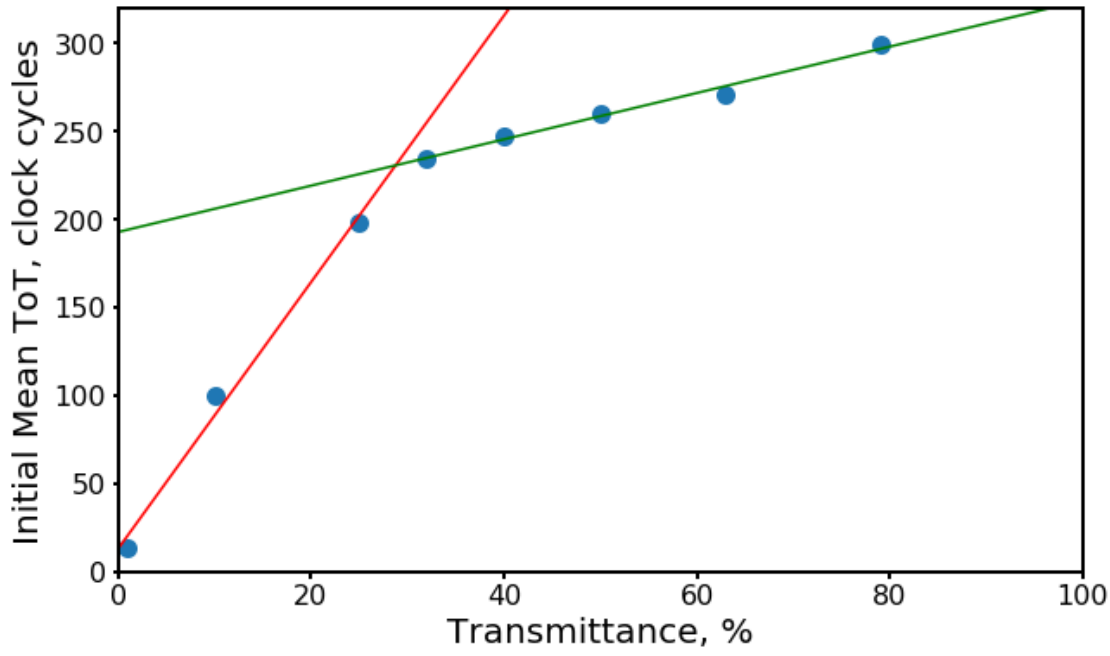
where the transmission, T, is a value between 0 and 1, and is commonly converted into a percentage. The value of OD indicates the attenuation factor provided by an optical filter, such that a higher OD will translate to a lower transmission and greater absorption of the incident light. The transmission is the converse, a higher transmission percentage corresponds to a greater transmission of the incident light.

A range of different optical density filters were placed in front of the fibre optic, and the laser flash recorded by the Timepix3 camera for a total of 500 frames. Following this, the acquired data were processed as discussed above and the results shown in Figure 4.8a, with mean ToT over 500 frames plotted against ToA in time bins for the laser flash pixel region. The results demonstrate that the greater the intensity of the laser beam, the greater the mean ToT recorded. The initial mean ToT is defined as the mean ToT at ToA = 0, plotting this against transmittance produces Figure 4.8b. This plot suggests the presence of two regimes, whereby the initial mean ToT increases with transmittance faster in the low intensity regime (red line), and the gradient decreases in the high intensity regime (green line). This plot resembles that obtained by Ruat *et al.* [148], indicating the laser intensity passes the first ToT regime at approximately 30%.

The significance of Figure 4.8a and 4.8b lies in the time walk effect, which can occur with the Timepix3 camera. Using the AdvaDAQ readout system, a threshold can be set for each pixel, doing so prevents stray light or cosmic rays from impacting on the sensor and adding noise to the data. However, as a threshold must be set, pixels hit by fewer photons will take longer to exceed the threshold, as indicated by Figure 4.9. Consequently, a higher ToT can result in an earlier ToA. An earlier ToA will lie closer to the true value, thus producing a more accurate t_0 value to be recorded. This can be demonstrated by observing the image obtained for each time bin. As time progresses, the laser spot appears to radiate out from the centre with an decreasing ToT (Figure 4.10). The lack of signal in the centre is an artefact of the time-walk effect, distributing the ToA. The laser spot incident on the detector



(a)



(b)

Figure 4.8: a) Plot of mean time-over-threshold against time-of-arrival. The mean is determined from photon events detected at each ToA, after being filtered through a transmission filter as listed in the legend. b) depicts the mean ToT when ToA is equal to zero in a), plotted against transmission percentage. Two lines of best fit are shown to indicate the different ToT regimes.

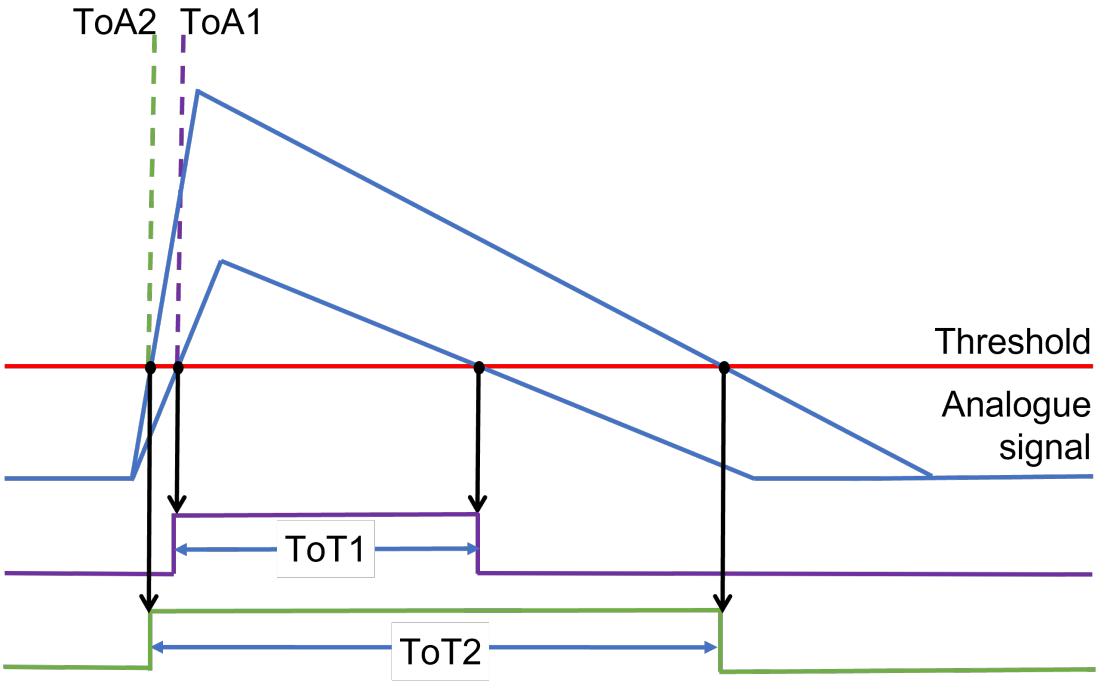


Figure 4.9: Schematic diagram illustrating the timewalk effect. A higher signal results in a greater ToT and an earlier ToA. This effect broadens the time spread, worsening the temporal resolution.

impacts on a cluster of pixels, each receiving a different number of photons. This causes the pixels to reach the threshold voltage at different times, hence resulting in events with larger ToT values producing earlier ToAs.

To investigate the effect of laser flash intensity on events occurring later in the spectra, the same data set was re-processed with a k-means clustering at half its previous value. Doing so causes every other laser shot to be classed as t_0, rather than every laser shot. The subsequent flash is instead categorised as part of the spectra, as shown in Figure 4.11a).

Figure 4.11b) indicates a trend in both ToA and ToT for the secondary flash. As the transmission percentage of the t_0 flash decreases, the secondary flash appears to move further away from the expected 100 ms ToA, approximately 60 ns later with a 10% transmission. This supports the assertion that a more intense laser flash results in more accurately positioned events in the frame. The decaying ToT with decreasing transmission is an effect of the reduction in laser intensity, as the ND filter is also reducing the delayed flash, as well as the t_0 flash.

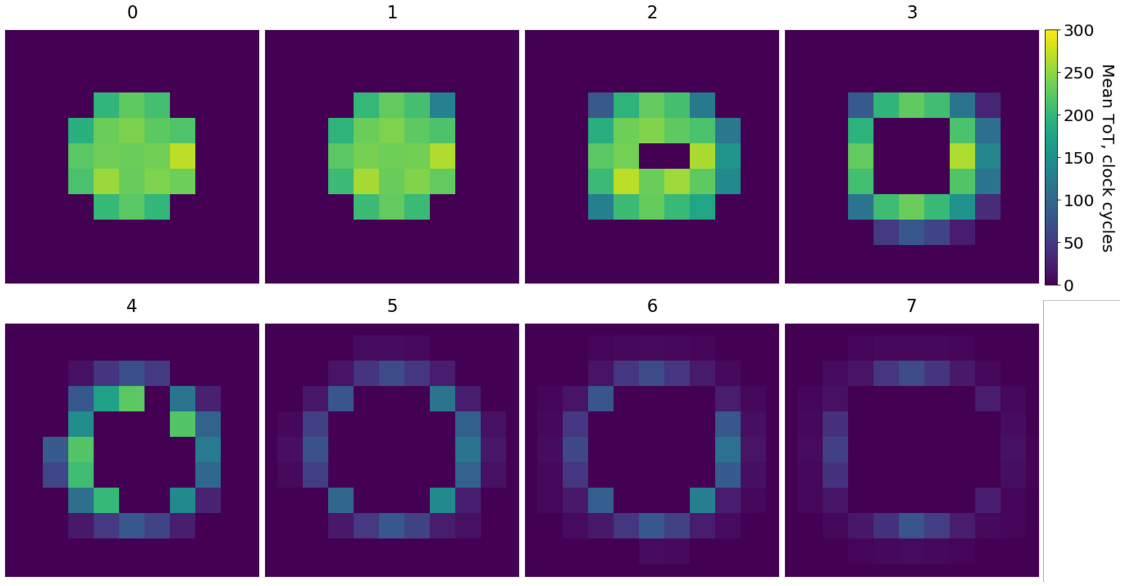


Figure 4.10: Images of a laser spot acquired with the Timepix3 Camera, depicting mean ToT within a single timebin across a 20 × 20 pixel area of the camera. The number above each image indicates the ToA time bin, the colour bar represents the mean ToT value for a laser spot, averaged over 250 frames.

The delayed flash peaks can be fitted with a function to obtain the FWHM and the peak maxima location (Figure 4.12). It can be seen that increasing transmittance reduces the FWHM to a plateau of approximately 4.5 ns (Figure 4.12a), with the standard deviation reducing as well. Additionally, in Figure 4.12b, the peak position trends towards 0 ms (100 ms relative to t_0) with a higher transmittance, indicating a greater accuracy when assigning t_0 with higher transmittance. The location of the peak is closer to the expected location of 100 ms with a greater intensity, suggesting a reduction in time walk. The decreasing FWHM indicates a narrower distribution of ToA's (summed across the pixel region and over 250 laser shots), hence the definition of t_0 is improved with a higher transmittance, making alignment of subsequent laser shots and the following spectra better. It should be possible to attain a FWHM of 1.5625 ns, however this would require a laser shot with a narrower peak and less jitter.

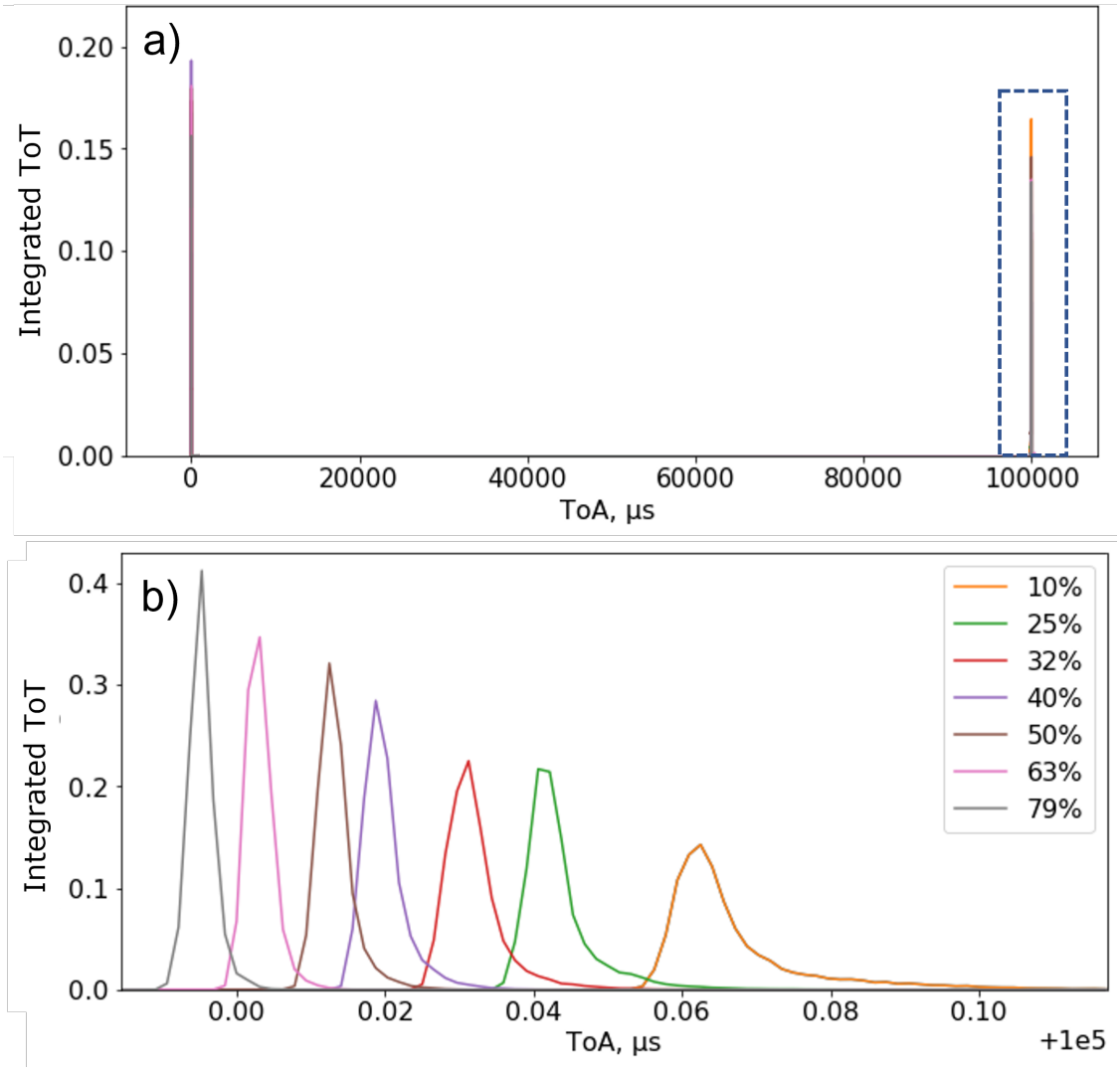
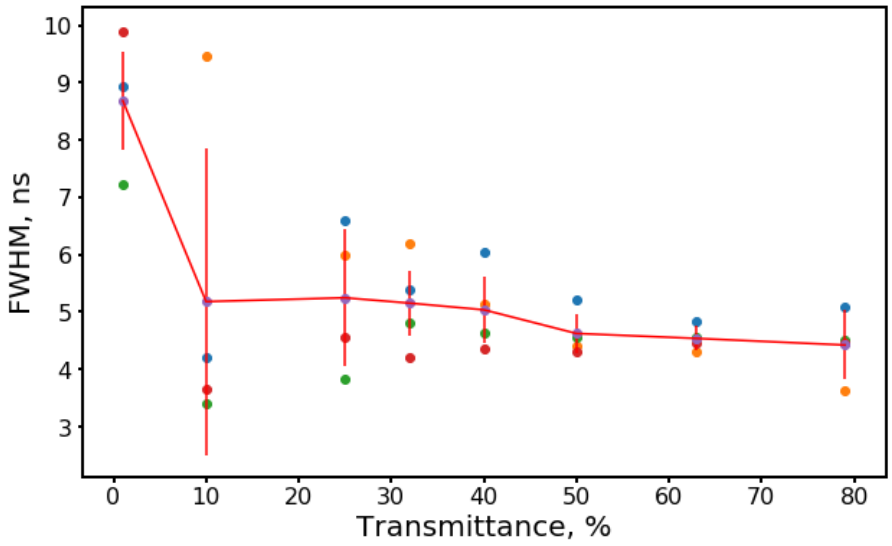


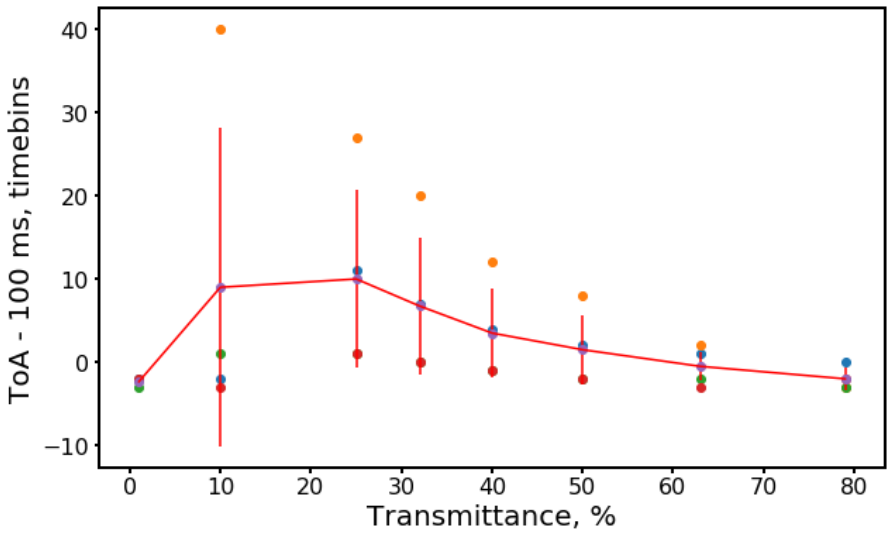
Figure 4.11: a) plot displaying integrated ToT against ToA from a laser pulse operating at 10 Hz, process with the k-means clustering halved. This produces a t_0 peak at 0 μs, and a following laser pulse at 100 ms (blue box). b) displays an expanded view of a) at 100 ms, over a range of different laser transmittance percentages. The y-axis shows the integrated ToT, obtained using the summed ToT for each ToA over 250 laser shots divided by the total ToT.

4.2.3 LED

The laser serves as a trigger for the reflectron instrument; the light sent through the fibre optic arrives at the same time as the sample surface is ablated, hence providing a reliable experimental t_0. However, the SIMS instrument does not have the ability to produce an equivalent optical trigger for the Timepix3 Camera. One option would be using an LED, provided the LED could be synced to the C_{60}^+ ion gun, and



(a)



(b)

Figure 4.12: a) FWHM of the delayed laser flash peak from repeat experiments against transmittance percentage. b) ToA of the delayed peak maxima minus 100 ms from repeat experiments, plotted as timebins against transmittance. The red line depicts the mean across the repeat experiments for each transmittance, and the vertical bars show the standard deviation for each transmittance value.

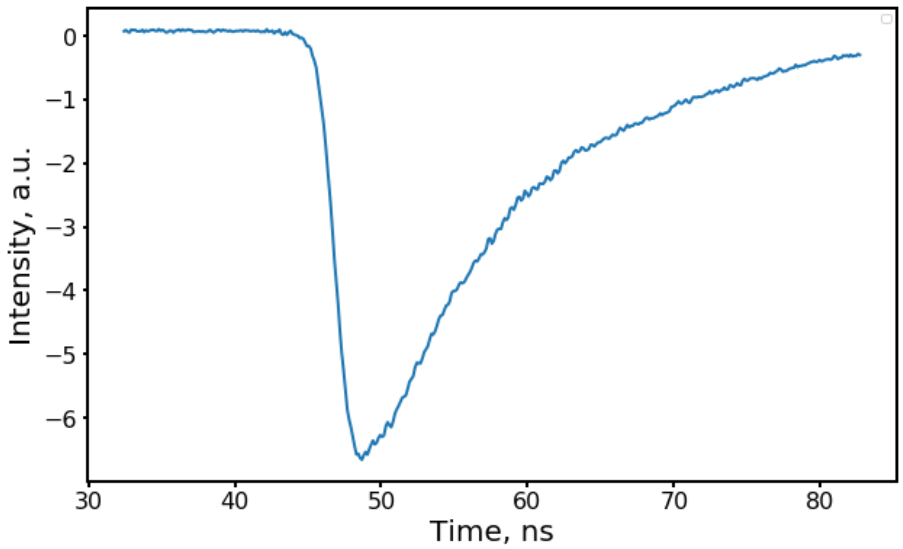


Figure 4.13: PMT trace produced by the LED, with a potential of 5 V, and pulse width of 50 ns.

have a fast rise time and sufficient intensity, it could act as an optical trigger.

To investigate this, an LED assembly was prepared based on a design from Veledar *et al.* [149]. Comprising of two fast radio frequency transistors connected as a regenerative switch, feedback is used to force the transistors either fully on or fully off. When triggered to turn on, a capacitor is rapidly discharged through an LED to produce a fast light pulse. An inductor connected across the LED helps decrease the optical fall time of the pulse as the transistors turn off. This provides a rise time of 1.7 ns rise time observed via PMT and oscilloscope, shown in Figure 4.13.

The LED was then placed in view of the Timepix3 camera, alongside the laser fibre optic, to allow for both the LED and laser flash to be recorded by the camera (Figure 4.14). The LED was set to fire 25 ms after the laser, with a pulse duration of 5 ns, and potential of 5 V. The laser intensity was varied using the ND filters, as described previously, whereas the LED setup remained unchanged in each run. Data was recorded for 50 s and k-means clustered for every other t_0 as described previously, culminating in a total of 250 frames.

Following this, the data were processed in multiple ways. Firstly, with the laser location defined as the trigger source, and hence as t_0. Secondly, the same data set was also processed with the LED location defined as trigger. Doing so demonstrates

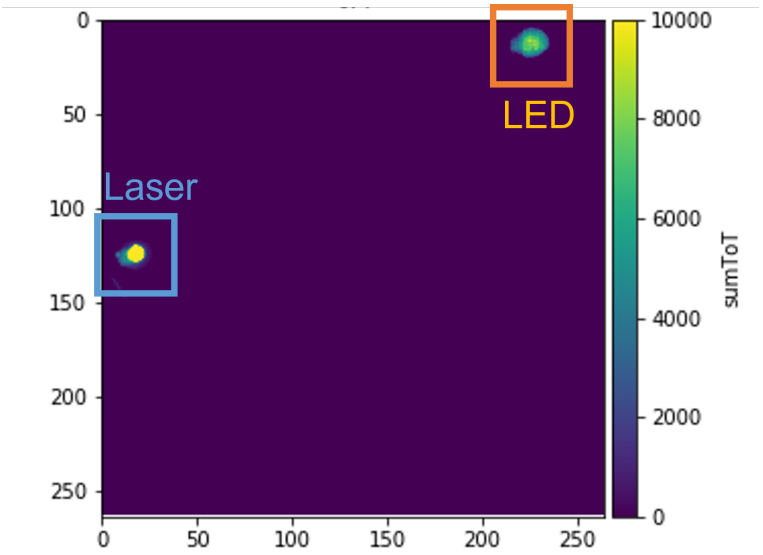


Figure 4.14: Timepix3 Camera image over 250 frames, and 100ms, showing an LED flash and a laser flash at different locations on the camera sensor.

the effect the laser intensity has on subsequent signal, which is independent of the laser, as well as showing the feasibility of using a LED as a trigger source. The results are shown in Figure 4.15.

Figure 4.15 c) shows the LED signal ToA, with a laser pulse trigger at different transmittance percentages. The summed ToT shows very little variation, which is expected as the LED flash does not change in intensity or duration. There is some distribution in the ToA for the LED peak, most significantly with 1% and 10%. This is expected, as shown in Figure 4.12. The peak with the greatest deviation from the expected arrival time is that which has the lowest intensity trigger due to the time walk effect creating a less accurate t_0. The rest of the LED peaks appear at very similar ToA's. This reduced variation compared to the delayed laser peak distribution can be explained by the earlier arrival time resulting in the time walk effect having less impact compared to at 100 ms. The LED flash peaks centre at 24.99991 ms, approximately 90 ns earlier than the expected 25 ms arrival time. This is thought to be a consequence of the delay generator set up, as the LED pulse is triggered relative to the laser Q-switch, and not due to the Timepix3 camera itself.

Figure 4.15 b) shows the ToA spectra with the LED flash location defined as t_0. The laser flash hence appears at -25 ms and at 75 ms when k-means clustered

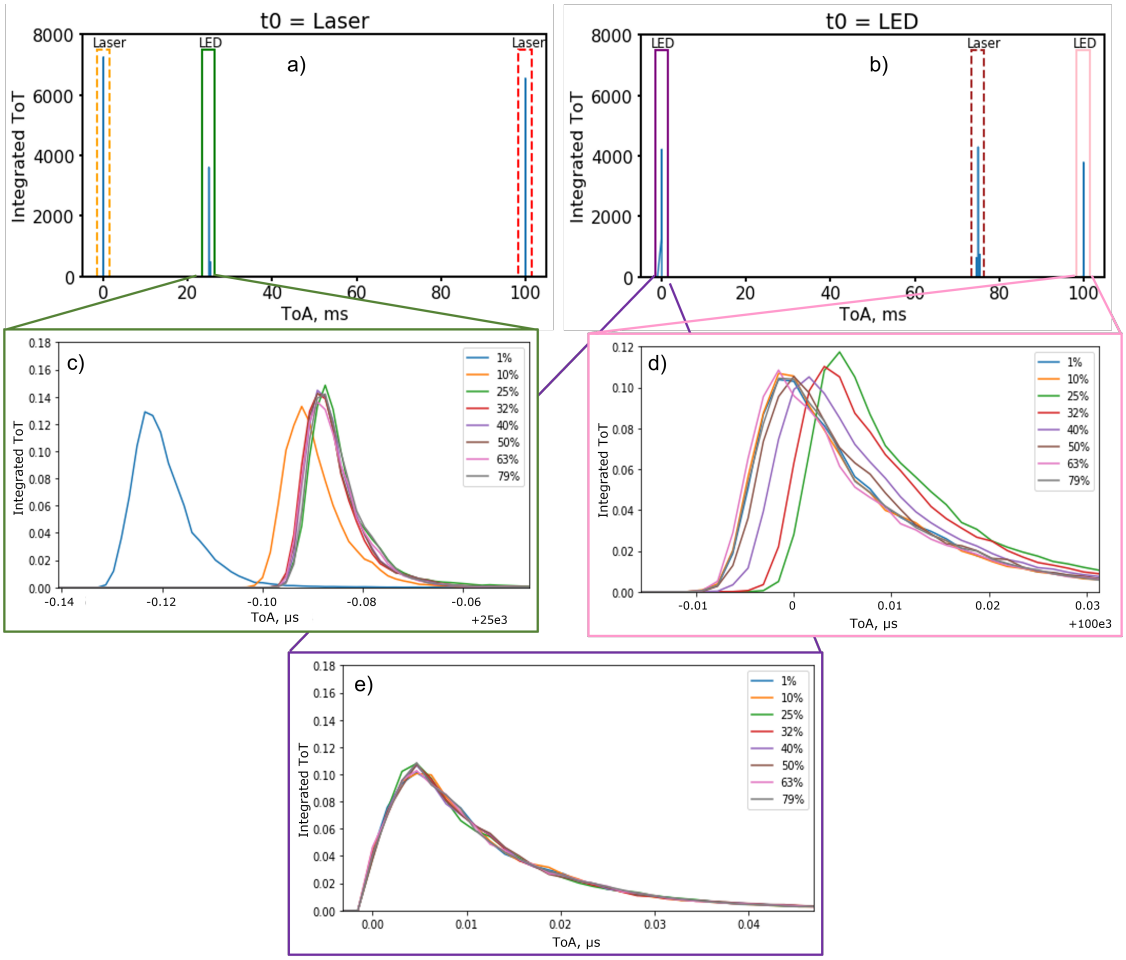


Figure 4.15: a) and b) showing a ToA plot with either a laser flash set as t_0 (a) or an LED flash as t_0, against integrated ToT over 250 frames. Following the t_0 flash is either a laser or LED flash, then at 100 ms is a the subsequent t_0 flash. Peaks produced by the LED are surrounded by a solid box, laser peaks are surrounded by a dashed box. The LED peaks have been expanded in c)-e). c) shows the LED flash when plotted relative to a laser t_0, d) an LED flash 100 ms after the LED flash, and e) an LED flash when set as t_0. The LED signal is identical in each case, the legend indicating the transmittance percentage of the corresponding laser flash from the data set.

for every other trigger flash. The delayed LED flash appears at 100 ms. d) and e) show expanded views of the LED flashes at t_0 + 100 ms and t_0, respectively, over 250 frames. d) shows each data set at t_0 looks almost identical, which is to be expected as nothing changes within the LED flash while the laser intensity changes.

Figure 4.15 d) shows the LED 100 ms after the LED has been used as t_0. There is a small distribution with arrival time, with peaks distributed across approximately a 10 ns window. It is unclear why there is a distribution, as there is no inherent

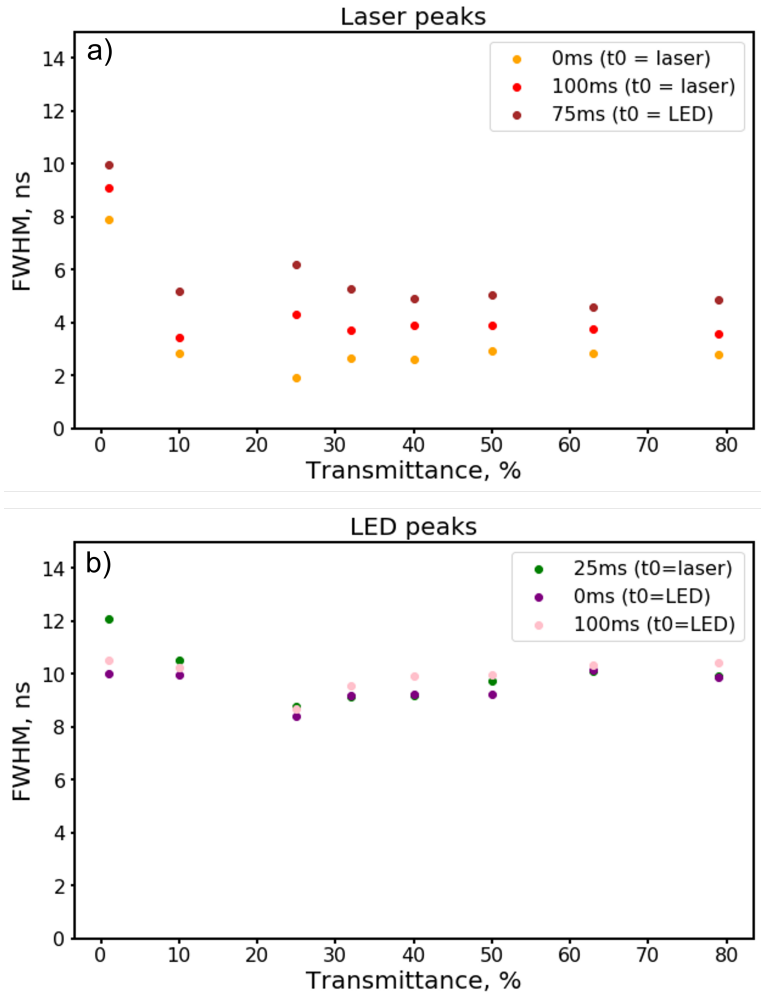


Figure 4.16: Plot of FWHM against transmittance for the peaks displayed in Figure 4.15. a) displays the results from each of the laser peaks, b) displays the results from each LED peak. The colours for each data set corresponds to the colour of the boxes around the peaks in Figure 4.15 a) and b).

change in the LED operation with transmission. This needs to be investigated further, but could be a result of a data processing issue, or a drift occurring within either the Timepix3 camera or the LED laser.

Each of the peaks in the data set from Figure 4.15 a) and b) were fitted to determine their FWHM, the results are shown in Figure 4.16. The data has been separated into signal produced from laser peaks, and signal produced from LED peaks, with the data point colours corresponding to the box colours in Figure 4.15.

The LED is set to have a pulse width of 5 ns, however the FWHM obtained in Figure 4.15 is approximately double. It is unclear why this has occurred, likely

due to the LED electronics not operating as expected. The laser peaks have a smaller FHWM on average when compared to the LED, attributed to the smaller pulse width of the laser. When the LED peaks are compared to each other and at different laser intensities, they show very little variation in the FWHM, which is expected, given there is no change in the nature of the LED pulse. The LED pulse with a laser trigger compared to the LED pulse with an LED trigger show very similar FWHM values, suggesting that the LED as a trigger does not have a negative impact on the alignment of the spectra.

Comparing the laser peaks shows an overall trend in FWHM towards approximately 4 ns as the intensity increases, which is consistent with earlier results in this chapter. Comparing the laser t_0 (laser trigger) FWHM with the laser $t_0 + 100$ms (delayed laser pulse) FWHM displays a small increase, likely due to laser jitter causing broadening of the arrival time for the following flash. The laser flash relative to an LED trigger (LED $t_0 + 75$ms) displays yet another increase in FWHM. This is thought to be due to the laser jitter, as well as the broader LED peak acting as a slightly less precise t_0 compared to the laser. Decreasing the LED pulse width should improve this, as should increasing the LED pulse intensity.

The data suggests an LED could reliably serve as a replacement for the fibre optic laser pulse, with only a small increase in the FWHM. This difference would be observable on the reflectron ToF mass spectrometer instrument, offering an alternative triggering method; the system therefore should also work on the SIMS ToF instrument with its 1 kHz repetition rate. The P47 screen would limit the effectiveness of the Timepix3 camera fast time stamping ability, however the triggering method is independent of the screen as it is aimed directly at the camera, thus could be used regardless. A redesigned LED unit with a shorter pulse width and a more tightly focused beam should be capable of reducing the FWHM recorded using the Timepix3 camera, and hence improve the ToA alignment process to be comparable to the laser triggering method, or better.

4.2.4 Effects on Mass Spectra

Assuming a linear discharge, the relationship between charge, Q, and the mean ToT response can be given by:

$$\text{mean ToT} = p_0 \cdot Q + p_1, -\frac{p_2}{Q - p_3} \tag{4.5}$$

and four free parameters (p_0, p_1, p_2, p_3). This can be fitted to experimental data and gives the conversion from ToT to signal charge [26]. The effect of timewalk on ToT is sketched in Figure 4.9. The implication from this relationship is that ToT can be interpreted as a measure of intensity - directly proportional when in the latter regime. This can be observed in Figure 4.8b.

Traditionally, time stamping CMOS cameras have no direct measurement for intensity, instead this is supplied through single event counting within each time bin and plotting the event count as a measure of intensity. However, if ToT can instead be considered as a measure of photon intensity, the summed ToT could be plotted against time.

As described in Chapter 2, a sample of Rhodamine B dye was prepared with an electrosprayer. The sample was then placed in the reflectron instrument, ablated with the laser, and the results recorded using the Timepix3 camera. In this instance, the fibre optic pulse was positioned in line with the camera, with the beam reflection being recorded as the t_0 pulse. The output data was then processed as discussed above, and the results plotted with two variations: the intensity axis in the form of event count, and as summed ToT (Figure 4.17).

When the Rhodamine B peaks are fitted with a Gaussian and their FWHM calculated, the plots indicate a 5 to 10 ns improvement in FWHM when summed ToT is used (Table 4.1). The peaks appear more defined, with the peak separation increasing between the largest central peak and the smaller peaks surrounding each.

A further step to using summed ToT as a measure of ion intensity, is to use the ToT to filter data points low intensity. A number of thresholds were chosen, and only events which exceed the ToT threshold displayed, presented as summed

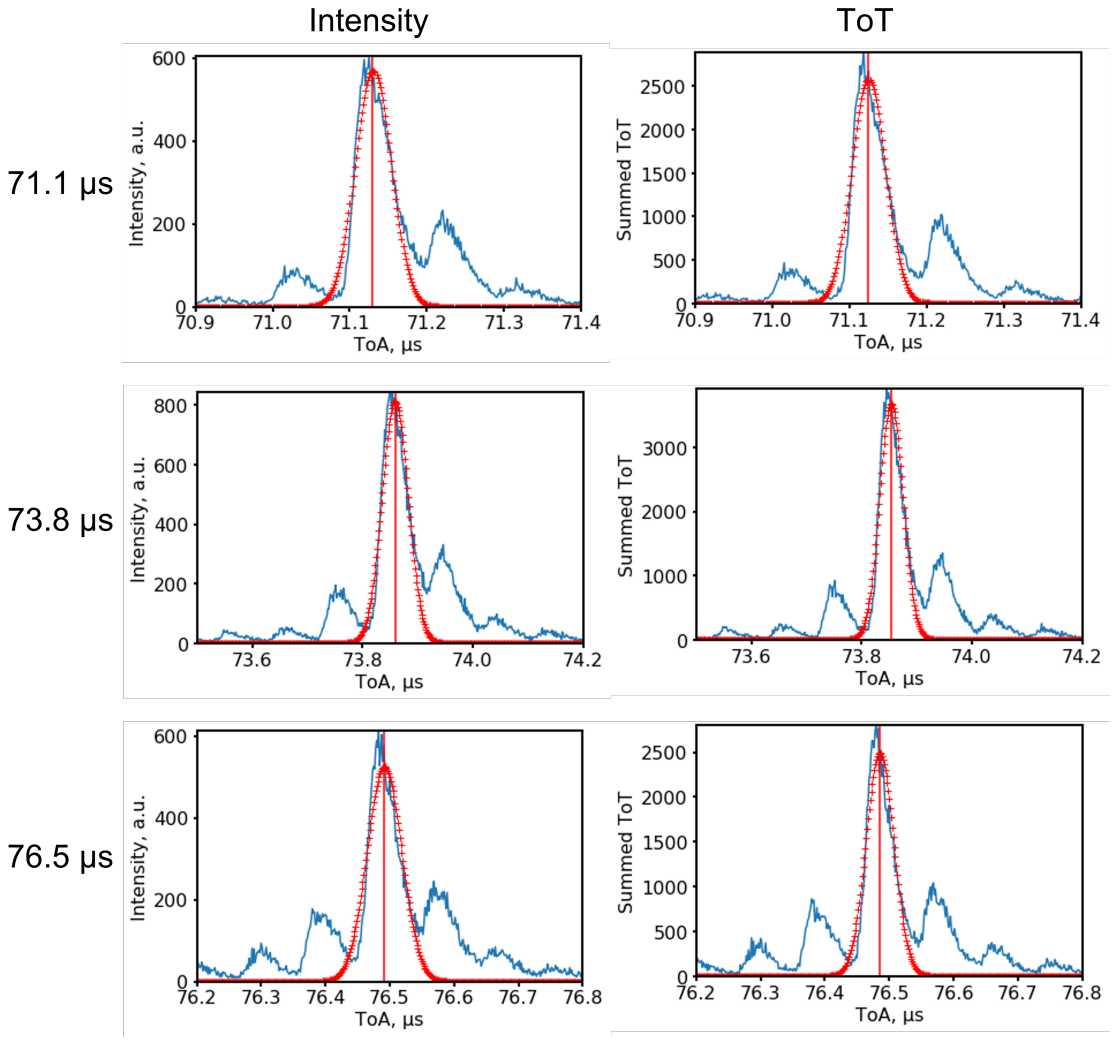


Figure 4.17: A selection of peaks (blue) from a Rhodamine B spectra, acquired using the reflectron ToF instrument paired with the Timepix3 Camera over 15,500 frames. Plots on the left have an intensity scale of event counts, and plots on the right have an intensity scale of summed ToT. All of the peaks have been fitted with a Gaussian curve (red), and the FWHM obtained are shown in Table 4.1.

Table 4.1: FWHM achieved for a range of peak locations in a Rhodamine B spectra recorded using the Timepix3 Camera. The peaks were fit with two different intensity scales: event counting, and summed ToT values. The FWHM achieved using each of these methods are obtained from Figure 4.17.

	FWHM /ns	
Peak location /μs	Event count	Summed ToT
71.1	55.1	51.6
73.8	55.8	50.0
76.5	60.2	49.8

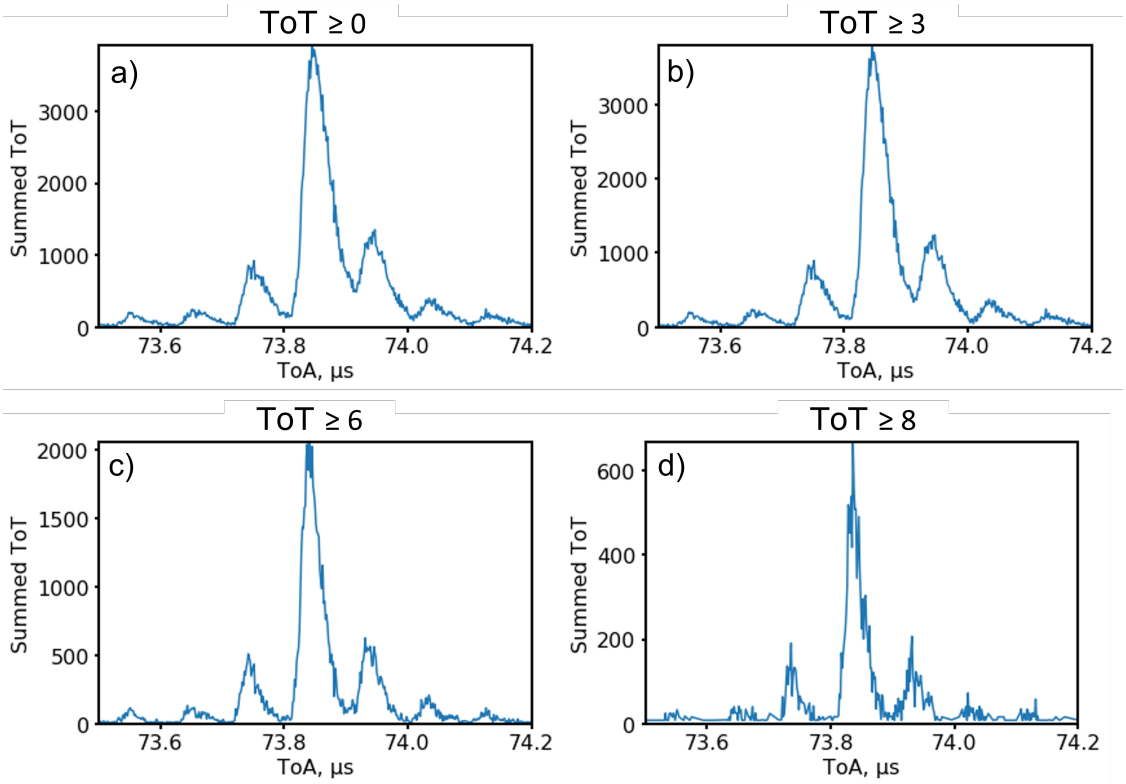


Figure 4.18: Spectra showing a Rhodamine B peak appearing at 73.9 μs, using summmed ToT as intensity, obtained using the reflectron ToF mass spectrometer instrument paired with the Timepix3 Camera. Pixels were filtered according to a range of ToT thresholds, whereby a) has a ToT threshold limit of $\geq$0, b) $\geq$3, c) $\geq$6, and d) $\geq$8. Only pixels which were impacted with a ToT exceeding the threshold are included in each plot.

ToT against ToA. This ToT threshold is in addition to the threshold set within the Advadaq software, which is used during the data collection stage. With a ToT threshold >0, all events are shown, and the maximum event count for the 73.9 μs peak is approximately 600 for this data set (15,500 laser shots). This event count drops to 500 at a ToT threshold of >3, to 200 at a threshold of >6, and 50 when the ToT threshold is set to be >8. This can be visualised using summed ToT (Figure 4.18), showing peak separation increases as the lowest ToT signal is removed from the ToF spectra. However, the spectra quality noticeably decreases upon a ToT threshold of >8, a result of the number of events being included dropping to 10% of the full data set.

The experimental ToT value acquired is approximately 0-10 ToT clock cycles, which is significantly lower than the laser ToT signal of ~0-300 clock cycles seen

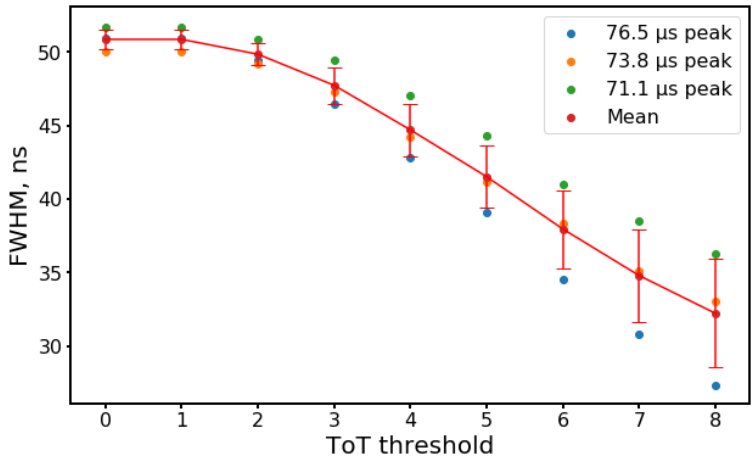


Figure 4.19: Plot of the FWHM from three different Rhodamine B peaks against a ToT threshold applied during data processing. Acquired using the reflectron ToF mass spectrometer and Timepix3 Camera. The three peaks measured are 76.5, 73.8, and 71.1 μs, and are displayed in the legend. The mean is also shown, along with error bars indicating the standard deviation for each ToT threshold.

previously. This can be explained by the laser fibre optic being pointed directly at the camera, supplying a lot of high energy photons, producing a large ToT. The Rhodamine B signal, however, is produced by the Exalite 404 screen generating photons, which are low intensity photons. Increasing the potentials applied over the MCPs and screen help increase the photon intensity, however we have approached the upper limits for this detector set up. It is for this reason that spectra are recorded over a longer period of time to allow for the accumulation of sufficient ion events.

A number of Rodoamine B spectra have been fitted with a Gaussian to investigate the effect ToT thresholding has on the peaks FWHM. This was performed over a number of different peaks and the results plotted in Figure 4.19. There is a very clear trend, as the ToT threshold is increased, the FWHM decreases, suggesting the removal of the lowest ToT ion events reduces the spread of events in time. This can be attributed to the time walk effect: events with the lowest ToT will produce a ToA further from the true ToA when compared with an event with a higher ToT. By removing the lowest ToT events, the distribution in arrival times will decrease, hence reducing the FWHM.

The temporal spread caused by ion events on the detector could be improved by increasing the photon intensity from the screen. As a higher ToT results in

a reduced timewalk effect, increasing the screen intensity would reduce the time walk seen in the ion signal.

4.3 Conclusion

In previous work, a novel method for triggering a Timepix3 camera was developed [81], the work in this chapter has sought to expand upon the use of the Timepix3 camera, and provide a means of triggering the camera without requiring a laser.

The relationship between laser beam intensity and the assignment of t_0 was explored, from which it was shown that a high beam intensity results in a higher time-over-threshold, producing a smaller FWHM and a more accurate t_0. This suggests that simply increasing the laser beam intensity should improve the alignment of consecutive spectra, thus improving the FWHM from sample data. Prior to this, experimental data was acquired with the laser beam spot reflecting off the detector screen before being detected by the Timepix3 camera. With the use of a mirror, the beam could be reflected towards the camera, allowing it to be detected with greater intensity. This intensity would still be limited as the intensity will be the same as that used to ionise the sample, increasing it too high would negatively impact the mass and spatial resolution due to space charge effects.

To extend the use of the Timepix3 camera to the SIMS mass spectrometer, an LED was also investigated. This achieved a 10 ns FWHM, greater than the 4 ns produced with the laser trigger. The work indicates that an LED can be used as a trigger, however, the FWHM would need to be improved further to make it comparable to the laser trigger. If an LED with a faster rise time and smaller pulse width could be made, then the LED could replace the need for a laser entirely, making the trigger a smaller unit and enable the Timepix3 camera to be used with any instrument, without the need for the expensive SPIDR readout system or a laser.

It was established that a higher laser intensity results in a higher ToT, it can also be demonstrated that a higher ToT can produce a reduced time spread for photon events. This information was applied to experimental ion data, which resulted in an improvement to the FWHM by filtering the lowest ToT events out of the

data. This is because the lowest ToT events are likely shifted further from the true ToA due to the lower photon intensity. The ToT filtering is less effective on the experimental ion data than the laser tests as ion impacts on the screen are not able to produce the same intensity as the laser pulse can, producing ~50 ns FWHM from Rhodamine B. A method for improving this could be increasing the screen intensity, thus increasing the ion event ToT. Even with the lower intensity, filtering out the lowest ToT events improves the FWHM, thus improving the spectra.

A combination of a higher intensity trigger and ToT filtering would thus achieving a higher ToT signal and more accurate t_0. With this, a higher mass resolution would be expected for the mass spectra recorded.

An option for future work could be applying a correction to the ToA data, using the ToT. As the ToA is dictated by the ToT, the ToT could be used to calculate the true ToA for an ion event, and thus correct all data points to the true ToA.

5

Comparing the reflectron instrument with the SIMS instrument

Contents

5.1 Ionisation method 154
5.1.1 Nd:YAG Laser Beam 154
5.1.2 C_{60}^{+} Ion Beam 159
5.2 Mass Spectra 172
5.3 Mass resolution 179
5.4 Spatial resolution 180
5.5 Conclusion 184

The two main ionisation techniques used in microscope mode MSI are matrix-assisted laser desorption ionisation (MALDI) and secondary ion mass spectrometry (SIMS). As discussed in Chapter 1, MALDI is a soft ionisation technique, meaning less sample degredation and low fragmentation. SIMS is considered a hard ionisation technique, however, the degree of "hardness" can be altered based on the primary ion source. In the work presented here, a C_{60}^{+} ion source has been used, which, as a poly-atomic ion source, offers softer ionisation than a monatomic ion source would [150].

MALDI is more often used as the ionisation method within imaging mass spectrometry, likely due to the ease of defocusing the laser beam, making it a popular choice in early work [1]. Currently, there are a few microscope mode

imaging mass spectrometers utilising SIMS with CMOS detectors, such as the instrument of Kiss *et al.*, which uses a linear ToF with a Timepix detector [91, 107]. However, the results attained were limited by the early generation Timepix detector, and required peak selection. Hence, an instrument similar to the reflectron ToF instrument introduced in Chapter 2 was developed with the assistance of Ionoptika, the Rosalind Franklin Institute, and the National Physical Laboratory. The SIMS ToF mass spectrometer offers a broadly defocused 40 keV C_{60}^+ primary ion beam, ion optics able to extract and accelerate secondary ions up to 20 keV, time-variable PEDA, and a position-sensitive detector. This instrument could allow for higher throughput, due to the 10 kHz primary ion beam pulsing, and high energy ionisation.

This chapter will discuss the differences between the two microscope mode imaging mass spectrometers, and their ablation methods, and will explore what effect this has on the mass spectra and images acquired.

5.1 Ionisation method

As discussed in Chapter 2, two different ionisation methods are used: a Nd:YAG laser to perform LDI and MALDI with the reflectron ToF mass spectrometer; and a C_{60}^+ ion gun to initiate secondary ion generation with the SIMS ToF mas spectrometer. In order to compare the two instruments, an understanding of their respective ionisation beam profiles needs to be obtained.

5.1.1 Nd:YAG Laser Beam

Investigating the laser beam profile is fairly trivial with the correct equipment. A laser beam profiler (Spiricon SP620U), with an active area of 6.9 mm × 6 mm, was placed in the path of the laser beam. The beam profiler was located in a position which could approximate the sample surface location. This position is after the external optics (including a periscope, 50:50 beam splitter, one prism and two mirrors), and after the borosilicate window. The beam may be subject to a degree of distortion as it passes through multiple optics, but the most notable material

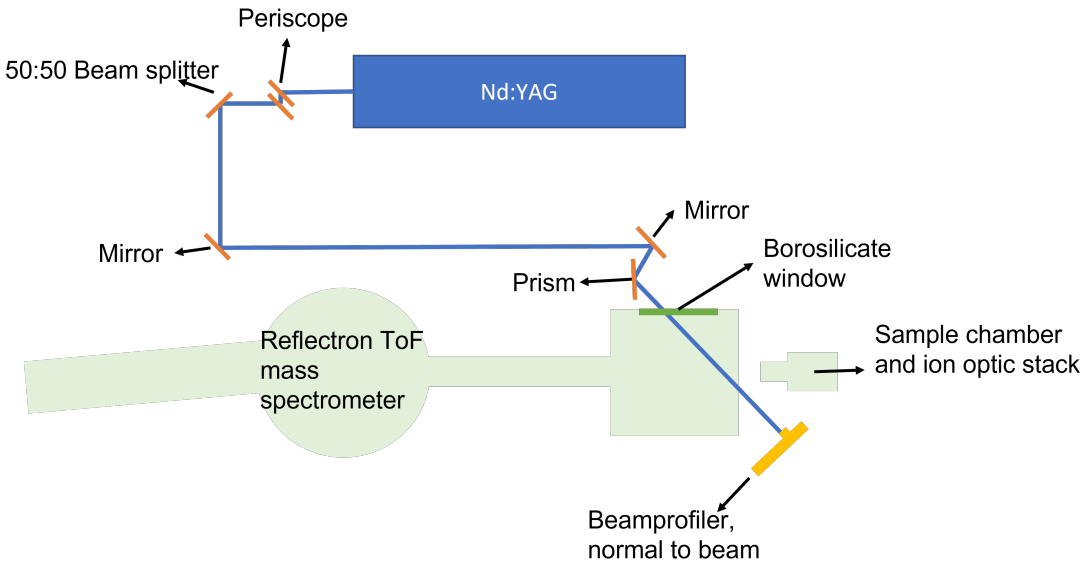


Figure 5.1: Schematic of the Nd:YAG 355 nm laser beam path. The blue trace indicates the laser path beginning at the exit of the Nd:YAG Continuum Powerlite 8000. The beam path is directed to the reflectron ToF mass spectrometer using a periscope, 50:50 beam splitter, and two mirrors, and a prism, before passing through a borosilicate window and out an open flange. The open flange is a result of the sample chamber and ion optic stack being removed, allowing the beam to exit the chamber. A beam profiler is positioned normal to the beam as the beam exits the ion source chamber.

which can cause distortion is the borosilicate window - as such, it was important to profile the beam after it has passed through the window.

The profiler can't be positioned within the chamber in the exact same location as the repeller plate due to the size of the chamber openings and the size of he profiler. It was instead mounted outside of the instrument, with the sample chamber and ion optic stack (consisting of the repeller, extraction, and einzel lens) removed from the ion source chamber. This allows the beam to pass through the window and then exit the chamber again, upon which it is incident on the beam profiler, as depicted in Figure 5.1.

The beam profiler is positioned approximately normal to the beam (Figure 5.2a), as well as at the approximate angle of the repeller plate (Figure 5.2b) to investigate the beam profile at the same angle as a sample surface would observe it. The laser is expected to have a Gaussian profile, however, as can be seen in the beam profile images, there is a considerable degree of inhomogeneity in

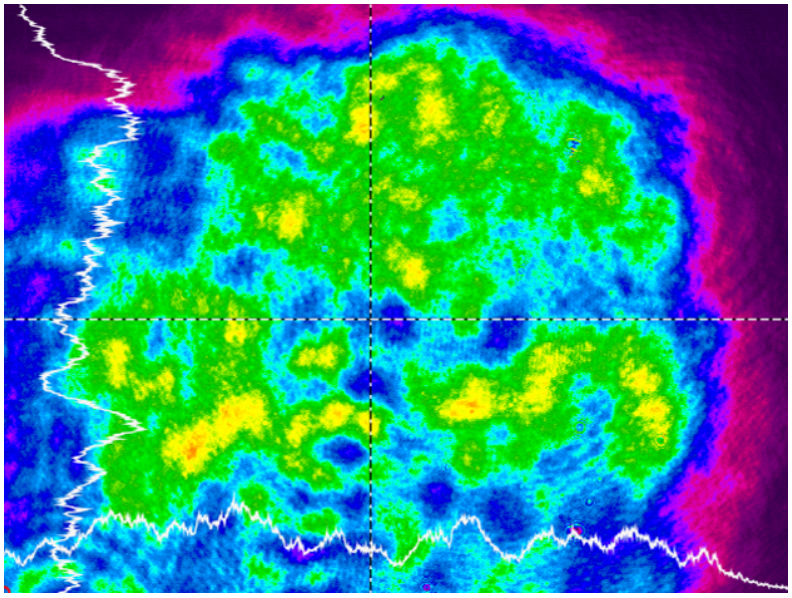
the profile, most notably on the profile with a sample surface angle. These hot spots could be a result of the borosilicate window or the ion optics, or it could be an sign of a degraded Nd:YAG rod, indicated by a poor performance in output wattage. Hot spots are visible in Figure 5.2b, which aligns with what has been seen experimentally: When conducting an MSI experiment using the reflectron ToF instrument, the laser can be observed covering the majority of the sample surface, however small adjustments of the position can lead to an improvement/worsening of the observed signal intensity. This suggests that these small adjustments are simply showing the movement of a laser hot spot on/off the region of the sample which generates the ions able to make it to the detector.

The diameter of the laser beam is approximately 8 mm. The laser defocusing allows the entire sample surface to be exposed to laser ablation, thus enabling microscope-mode to operate. However, the current beam size is greater than is necessary experimentally, given our field of view is ~250 μm with a $\times$92 magnification. As such, experimentally, we are instead aligning a hot spot with the relevant region rather than the entire beam, and thus the beam inhomogeneity has a less significant impact upon the imaged area. If the magnification of the instrument is reduced as discussed in Chapter 3, this inhomogeneity would have a greater impact on the image and create intensity differences across the image. This could likely be mitigated by improving the internal laser alignment, and upgrading the external optics used. Alternatively a spatial filter could be used, consisting of focusing the beam, passing it through a pinhole, then collimating [151]. This has the effect of removing unwanted noise in the beam profile and outputting a clean Gaussian beam.

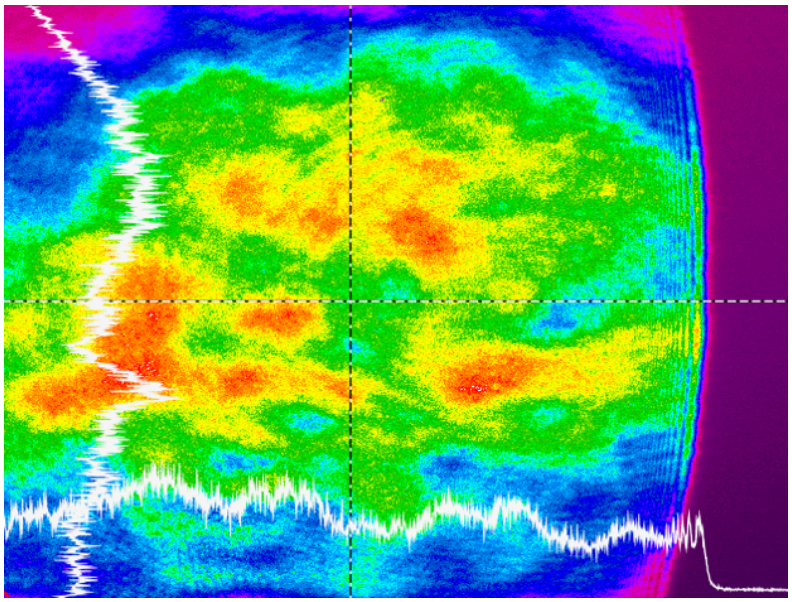
Using the same setup as described in Figure 5.1, an energy meter (StarLab v3.80) was placed in the beam path after the beam had passed through the borosilicate window. The beam energy was measured over a range of Q-switch delay times, from which the laser fluence can calculated:

$$\text{Fluence}\left[\frac{\text{Joules}}{\text{cm}^2}\right] = \frac{\text{Laser pulse energy [J]}}{\text{Effective focal spot area [cm}^2\text{]}} \tag{5.1}$$

.



(a)



(b)

Figure 5.2: Profile of the Nd:YAG beam, measured with a Spiricon SP620U beam profiler, with an active area of 6.9 mm × 6 mm. a) positions the profiler normal to the beam and b) at a 20 degree angle, approximating the angle of the beam on the sample surface. Red indicates high energy regions, blue indicates low energy regions.

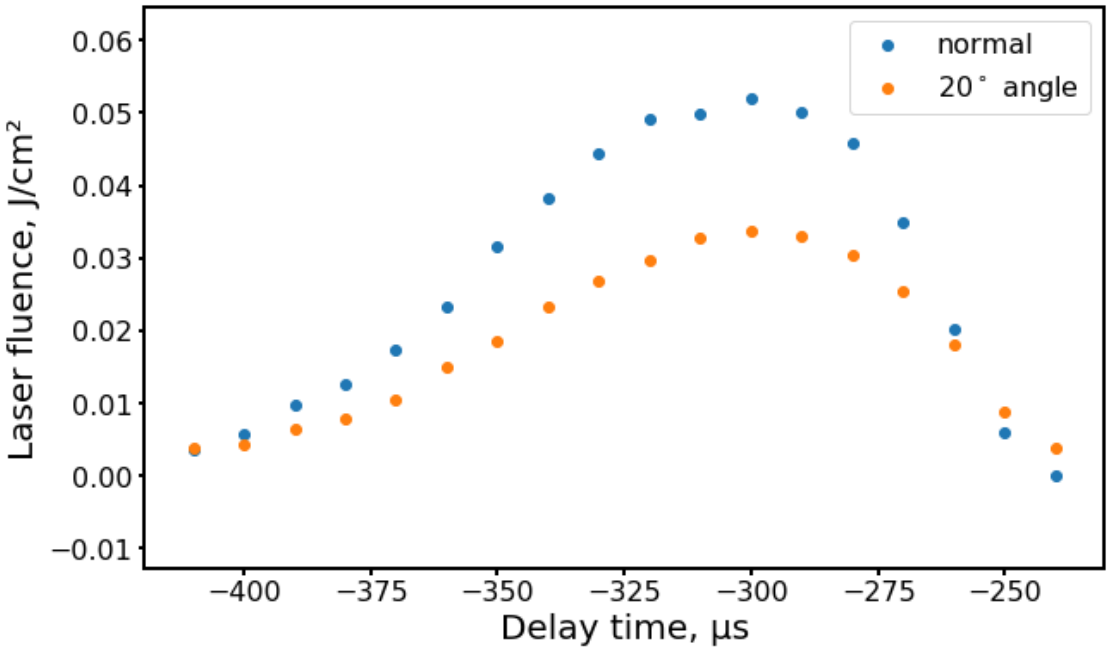


Figure 5.3: Laser fluence per pulse, acquired normal to the beam (blue) and at a 20 degree angle (orange), after passing through the borosilicate window, as a function of the delay time between flash lamp and Q-switch ($t_{\text{flash}} - t_Q$). The typical range of delay time used is -400 to -350 μs.

Given the laser is incident on the sample at a 20° angle, the area, A, of the resultant ellipse can be calculated with:

$$A = \pi R^2 \sec(\theta) \tag{5.2}$$

where R is the radius of the beam normal to the beam path, and θ is the angle incident to the surface. The beam angle is approximately 20° relative to the sample surface, and combined with a 0.4 cm radius, the ellipse area is determined to be 0.53 cm^2.

The power, and thus the flux per pulse, of the laser can be adjusted using the delay time between the flash lamp and Q-switch ($t_{\mathbf{flash}} - t_Q$). The fluence after the borosilicate window can then be measured as a function of the delay time, as shown in Figure 5.3. When the fluence normal to the beam and at a 20° angle are compared, a reduction of 30 - 40% is observed when the laser beam is angled.

The maximum laser pulse energy produced is 235 mJ/pulse (measured at the exit of the laser), however it suffers a significant loss in energy as it passes through the external optics (Table 5.1). A large loss is experienced after the periscope,

Table 5.1: Energy recorded by an energy meter when located at different positions along the external beam path. The percentage of beam energy remaining relative to position one has also been determined for each position. The large loss after the periscope is likely due to low quality optics.

Position	Position	Energy (mJ/pulse)	% remaining
1	Immediately after laser exits	235.7	100
2	After periscope	93.0	39.5
3	After 50/50 beam splitter	36.0	15.3
3b	Back of 50/50 beam splitter	44.9	19.0
4	After mirror 1	32.4	13.7
5	After mirror 2	29.7	12.6
6	After prism	27.8	11.8
7	After window	26.1	11.1

likely due to poor quality optics. Replacement of the two prisms should increase the energy retained per pulse, providing a greater range of energy to be used if desired in future work. Culminating with a 1 to 10 mJ/pulse used experimentally - corresponding with a laser fluence of 0.0065 to 0.0105 J/cm^{-2} at 20° to the surface. This can be compared to a fluence of 0.0097 to 0.0173 J/cm^{-2} when positioned normal to the beam.

Alignment of the laser on the sample surface is a simple matter, done by adjusting the final external optic and moving the large beam across the sample surface with the use of a window above the ion source chamber to visually confirm the location. Fine adjustment is done with the aid of the photomultiplier trace (PMT) trace, displayed on the oscilloscope, as well as with the camera. Alignment on the sample is complete once the PMT trace has sufficient intensity, displaying the expected peaks with a high signal-to-noise ratio, and the camera has an approximately even distribution of ion events across the detector region.

5.1.2 C_{60}^{+} Ion Beam

Positioning of the primary ion beam is particularly important, as it must pass through a 2 mm hole in the extractor plate, as depicted in 5.4. If the positioning isn't correctly aligned with the ToF axis, the beam may be partially or fully blocked by the ion optic. If the primary ion beam isn't impacting the area directly below

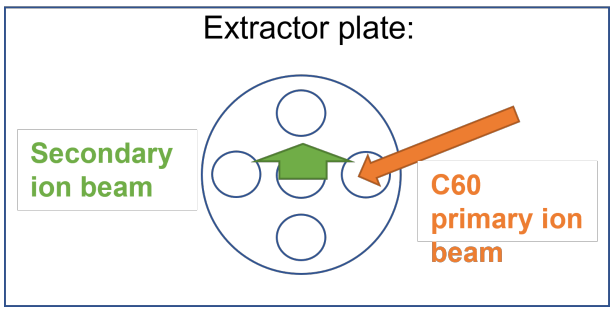


Figure 5.4: Schematic diagram depicting the primary ion beam path (orange) and secondary ion beam path (green) through the extractor plate in the SIMS instrument

the central hole of the extractor (the ToF axis), the secondary ion beam will likely fail to make it through the extractor plate aperture. Consequently, it is important to be able to manipulate the beam location.

With the SIMS ToF instrument, positioning of the primary ion beam on the sample surface can't be visually confirmed, as the ion beam isn't observable like the laser beam is on a surface. Hence, in order to determine its size, shape, and location on the surface, a different method is needed. The position of the primary ion beam on the sample surface could be found using the secondary ion beam and detector, however, this adds complications in the form of the secondary ion beam extraction optics impacting on the primary ion-beam path. Distinguishing the effect of the C_{60}^{+} ion-beam optics, and the secondary ion-beam optics, becomes difficult, so an alternative means is preferred.

If the continuous C_{60}^{+} ion beam is allowed to ablate the copper sample plate surface for a long enough time, a burn mark is made on the surface. This burn mark is a result of easily ionisable surface contaminants being ablated, producing a mark which can be imaged using the secondary electrode detector (SED). By applying different conditions to the beam, and measuring the burn relative one produced without the use of deflection plates (hence aligned to the secondary ion axis), the impact of different electrodes can be determined. In order to preserve the surface of the sample plate and to allow for multiple rounds of generating burn spots, a layer of copper tape is applied to the surface of the sample plate.

This SIMS ToF mass spectrometer is in its infancy, as such, a large degree of characterisation is needed to fully understand the defocused primary ion beam and how to manipulate the ion gun in order to achieve the desired beam profile. This section will discuss how different sets of deflectors impact the primary ion beam, as well as exploring the effect of stage potential, along with the characteristics of the beam surface itself.

Raster Deflector Plates

The C_{60}^+ gun is a refurbished ion gun from the National Physical Laboratory; as such, it was designed to produce a highly focused beam of a few microns in diameter. This highly focused beam would be used for microprobe mode MSI, and rastered across the surface using he two pairs of deflector plates located near the C_{60}^+ source. With microscope mode MSI, the beam is in a defocused state and ablates the entire imaging region at once. Consequently, these raster deflector plates are not needed, and can therefore be used to bend the ion path, and hence position the primary ion beam instead.

To quantify the effect these raster deflector plates have on the C_{60}^+ beam, the focused beam was allowed to ablate the copper tape surface for a duration of 5 minutes, over a range of different raster deflector potentials - the raster deflectors are supplied as a percentage within the C_{60}^+ ion gun control software. This is performed with the secondary beam ion optics switched off so as to remove any effects these additional fields would have on the primary ion beam path. The surface was then imaged using the SED.

Using a focused C_{60}^+ ion beam, burn marks were produced while testing a range of x and y shift potentials, ranging from -100% to +100%. Figure 5.5 shows the experimental effect on the the primary ion beam position. The plot shows the measured change in position, relative to zero deflection, while the images show the SED images of the burn marks from which the deflection has been measured. Note, the x-axis deflection images have been rotated for ease of illustration, and

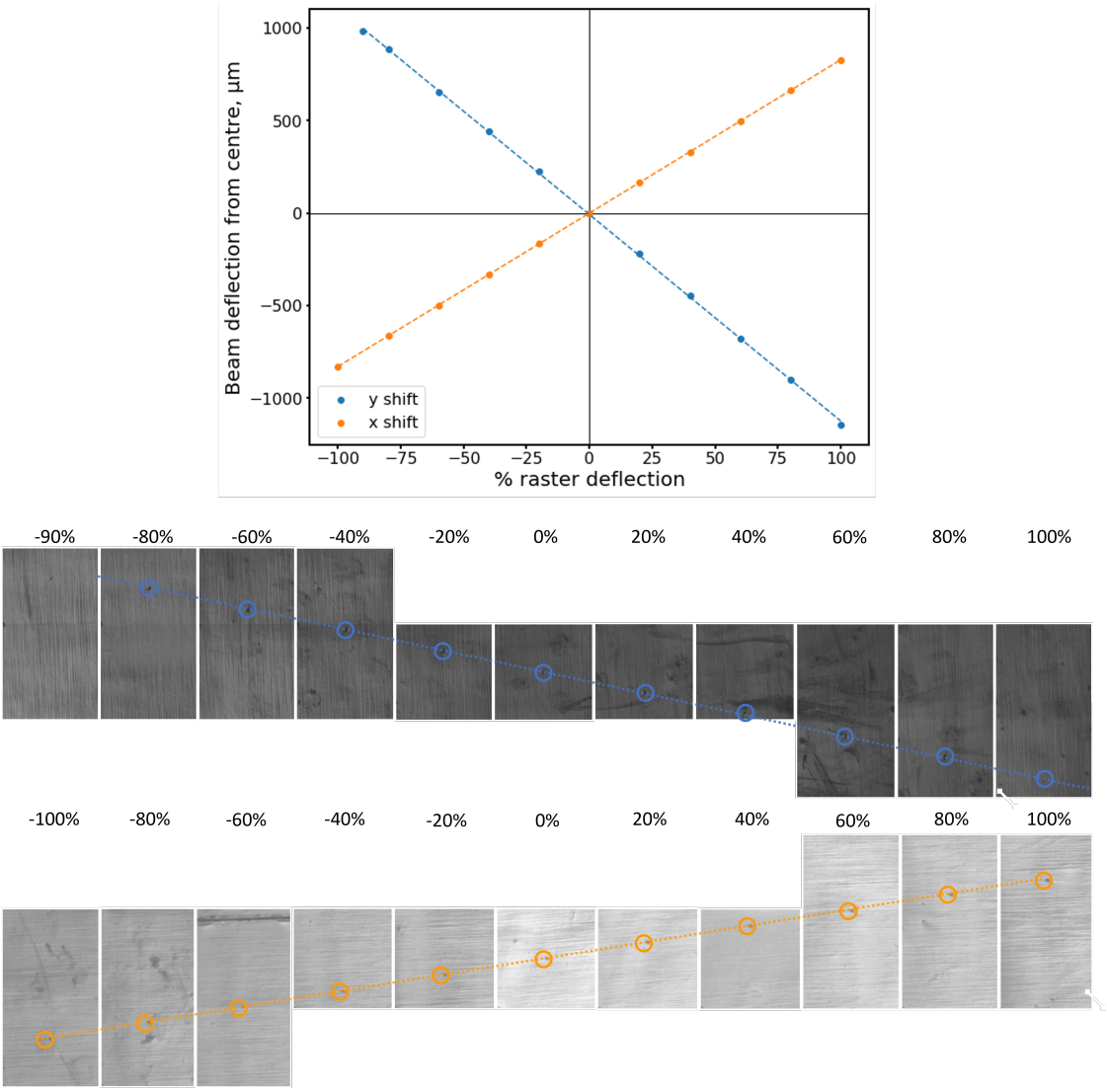


Figure 5.5: Primary ion-beam deflection against % raster deflection with x (orange) and y (blue) deflection plates. The deflector plates typically used for rastering the C_{60}^+ beam across the sample surface have been used to adjust the beam location. The plot shows the range of linear beam shift available in the x and y axis. The SED images show the burn spot (circled) produced by allowing the focused and continuous beam to impact the surface for a period of 5 minutes. The movement of the spot with % raster deflection is tracked across the surface relative to 0 deflection. Note, the lower image set has been rotated 90° relative to the upper image for ease of illustration.

the -100% y-shift failed to ablate on the surface, likely due to the beam failing to pass through the extractor plate hole, and colliding with the plate instead.

The results indicate a linear relationship between the % raster deflection applied by the plates within the ion gun. This clear trend means these plates could be used to adjust the primary ion beam position and the translational shift of the ion beam

could be predicted. However, the amount of deflection at each potential is different along the axes, with more deflection along the y-axis than the x-axis. It is unclear why there is a difference, perhaps a result of the ion gun refurbishment.

This deflection ability can be used to correct any position changes which may occur due to the extraction optic field, providing a lot more flexibility in the beam location.

Outer Deflector Plates

The C_{60}^+ ion gun has a second set of deflector plates, located between the primary ion beam and the sample surface. This deflector is made up of only two plates, meaning adjustment can only occur along the y-axis. A similar experiment to the one discussed above was conducted, with burn marks being made using a defocused beam instead.

The SED has a field of view of 1000 μm $\times$ 1000 μm, and thus areas exceeding this must be pieced together by moving the stage and acquiring multiple images. To aid reconstruction when using a larger defocused beam, images were taken with overlapping regions of 200 μm width, and the features on the surface aligned. Following this, the sample stage would be moved to another region, far enough away to ensure no overlap of burn marks would occur, and another burn spot made with a new raster deflector potential.

The ToF axis is identified as the centre point of the initial image, as depicted by the blue cross in Figure 5.6. The reconstructed image is fitted with a circle around the visible portion of the burn mark (yellow circle). The centre of this circle is located and measured relative to the centre point of the ToF axis.

The burn mark formed is not circular, suggesting it is being clipped by its passage through the hole in the extractor plate. Additionally, this edge appears in a consistent position relative to the ToF axis and suggests there are some machining defects along the edge of the hole drilled through the extractor plate - confirming that the beam must be hitting the extractor plate, rather than passing cleanly through the hole (green circle). The beam passing too close to the edge of the extractor hole

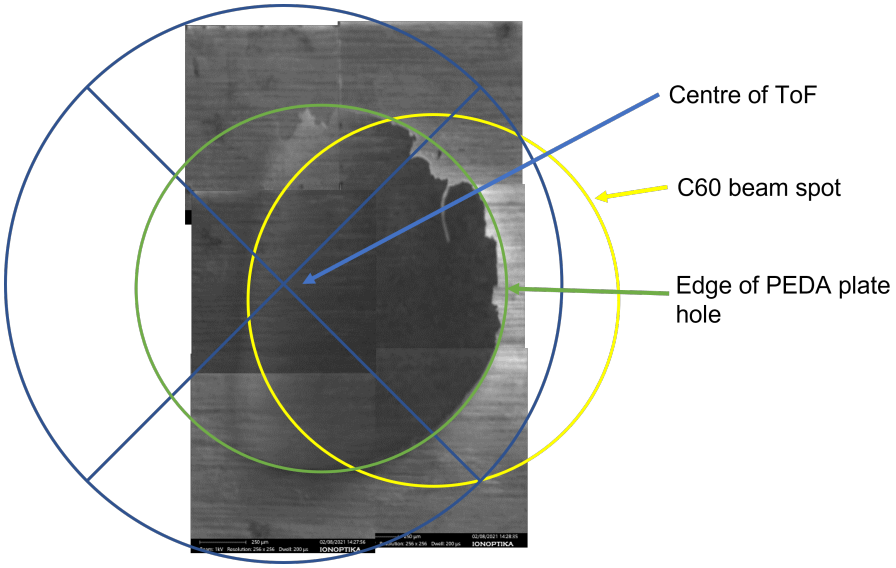


Figure 5.6: Image of a burn mark produced using a defocused primary ion-beam. The centre of the time-of-flight axis has been located (blue cross), the ion beam spot identified with a circle (yellow), and the edge of the PEDA plate is clearly visible (green).

will result in aberrations when a potential is applied to the lens in the primary ion beam profile, which will lead to an inhomogenous beam acting on the surface.

The beam was allowed to ablate the surface for ten minutes, and covered a deflector potential range of 0 to 1,000 V with steps of 200 V. The shift of the spot centre relative to the ToF axis are shown in Figure 5.7.

The beam centre deflection shows a linear shift in the negative y-direction, with only a small degree of variation in the x-direction also occurring, as the deflector potential increases. This trend offers another means of manipulating the beam position, but only in the y-direction. In order to clear more of the extractor plate and pass through the hole, the defocused ion beam needs to be moved in the negative x-direction using the raster deflection plates.

Beam focus

The beam clipping the edge of the extractor plate is further exemplified through adjustment of the beam focus (Figure 5.8). By adjusting the focus, the diameter of the beam can be changed. This can be done using the final focusing ion optics at the end of the C_{60}^{+} ion gun, denoted as Lens 2. Further burn marks were obtained with the same procedure as discussed above, varying the potential applied to Lens 2.

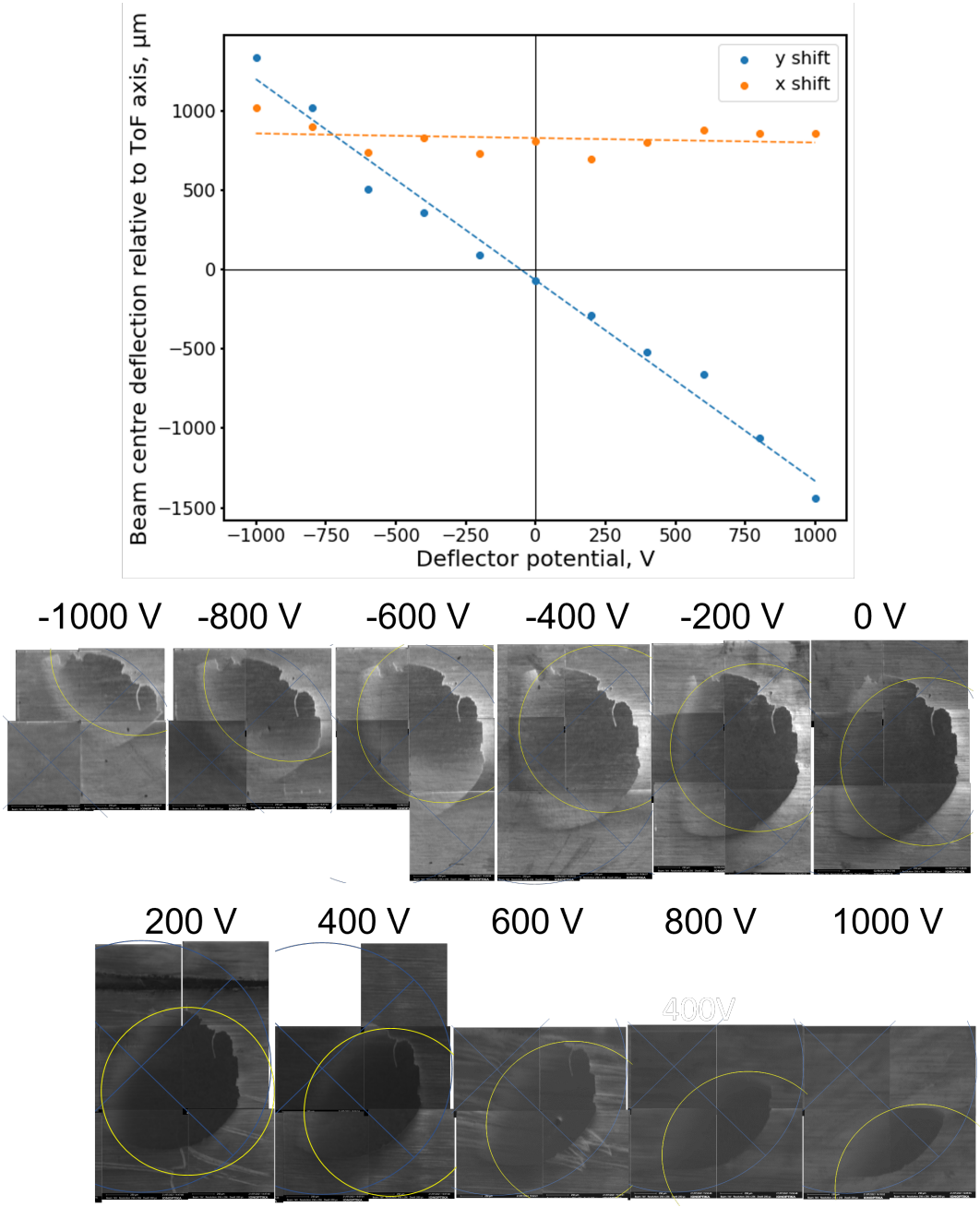


Figure 5.7: Beam centre relative to the ToF axis against deflector potential, using deflector plates located at the exit of the C_{60}^{+} ion gun. A defocused beam was used to generate spots on a copper surface, and the distance of the centre of the defocused spot (yellow circle) was measured relative to the centre of the ToF axis (blue circle and cross). The position was measured relative to the ToF axis in both the x and y direction.

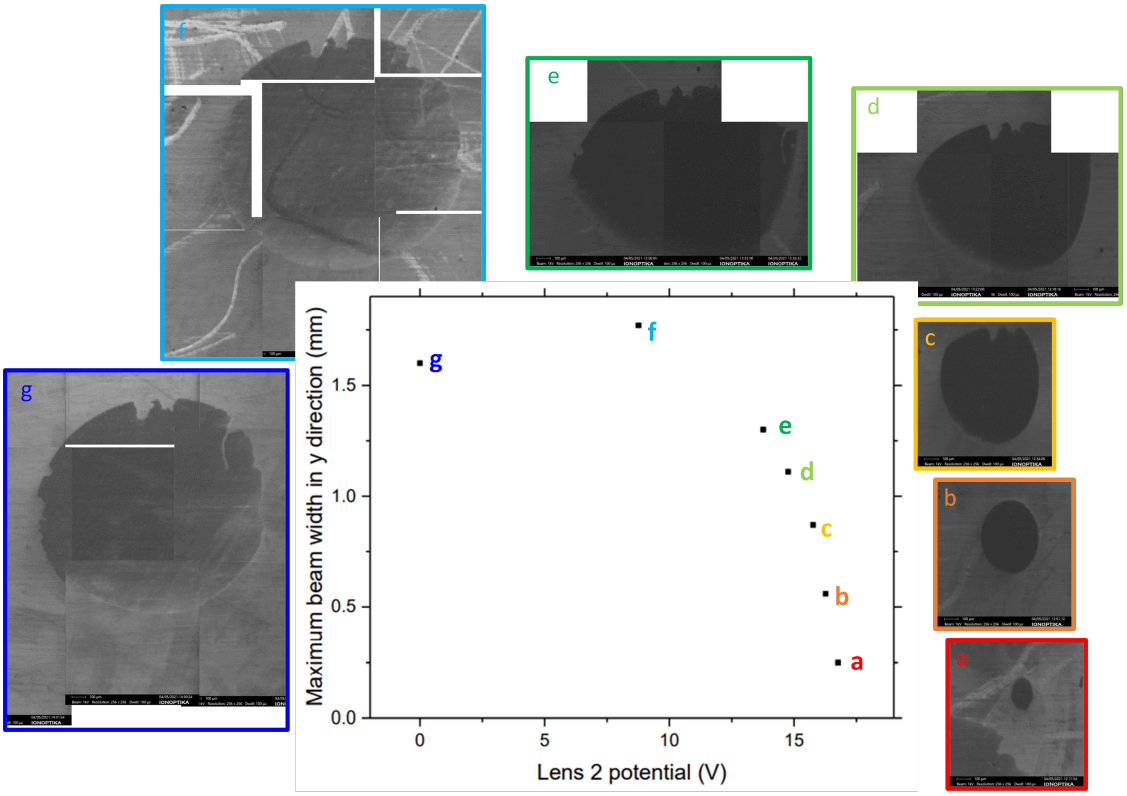


Figure 5.8: Maximum beam width in the y-direction against Lens 2 potential [a]. Note, some of these images were taken without overlap, resulting in some gaps between the compiled images.

Note, some of the the SED images acquired have no overlap, resulting in some misalignment of the reconstructed images.

When looking at the burn marks, the primary ion beam can be seen to become smaller and more focused as the Lens 2 potential is increased from 0 V to 17 V. This reflects the range of beam sizes available and adds additional flexibility to the primary ion beam - a more focused primary ion beam has a greater flux, thus the beam size can be selected based on the ablation area and flux needed. Despite being clipped by the extractor plate, a beam diameter up to 1.8 mm was achieved. Adjustment of the position to produce a larger beam could be done, however this results in the lower edge of the beam being clipped instead. As a result, the true size of the fully defocused beam is unknown, with a maximum spot size of 2.5 mm^2 attainable currently.

[a] Experimental data collected with and processed by Felicia Green.

The beam clipping isn't necessarily a limitation in the current setup, as the secondary ions emitted will (at least initially) match the diameter of the primary incident beam. The secondary ion beam must also pass through a 3 mm diameter hole in the extractor plate, thus is restricted to a maximum diameter in a second location. Additionally, a secondary ion beam too great in diameter would introduce aberrations caused by secondary ions passing too close to the edges of the electrode. It would be possible to increase the primary ion beam diameter with the development of another extraction plate with larger holes.

The size of the beam can thus be tuned to the desired diameter, allowing for easy adjustment of ion flux and charge density across the sample surface. A large area can be covered to allow for a wide field of view in microscope mode MSI. The 1.8 mm beam is the most suitable for use in this instrument, thus will be used as the defocusing primary ion.

Effect of Stage Potential on Beam Position

Depending on the polarity, a potential on the stage can act as an attractive or a repulsive force for the C_{60}^+ ion beam, hence deflecting it before impacting on the sample surface. The extent of this can be measured using a focused ion beam, producing burn marks, and tracking the effect upon application of different stage potentials have on it, as shown in Figure 5.9.

The spot can be seen to move significantly in the positive y-direction, and a small amount in the x-direction. This is in line with what is expected given the primary ion beam lies on the zy-plane. Additionally, the spot also appears to increase in size with a more negative potential. This is likely due to the beam angle changing close to the surface, thus spreading out the ions and creating a larger, more ellipsoid, spot.

This deflection caused by the sample stage would always occur when using the secondary ion beam optics, hence the two sets of raster and outer deflectors could be used to correct for the bend in the primary ion flight path.

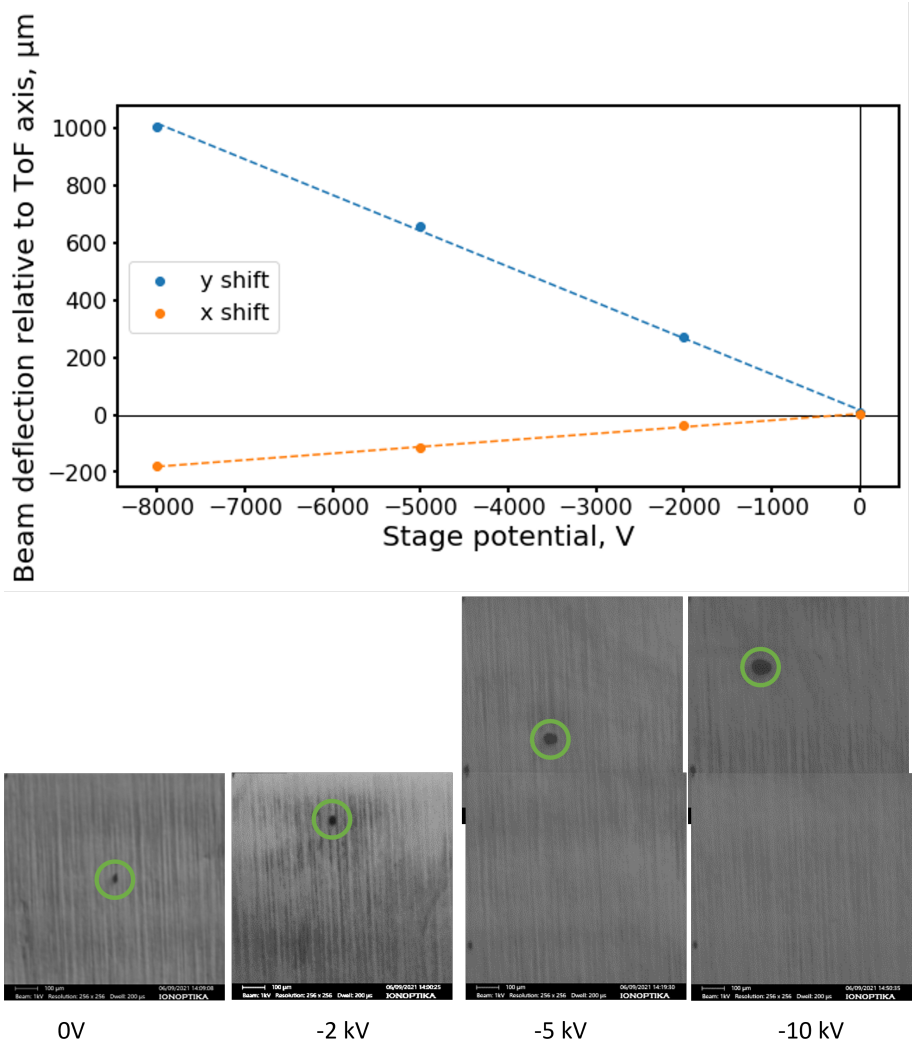


Figure 5.9: Beam deflection relative to ToF axis against stage potential. A focused beam was used to generate spots on a copper surface, and the distance from the burn spot (green circle) was measured relative to the centre of the ToF axis (at 0V), in both the x and y direction.

Beam surface profile

Profiling the C_{60}^{+} ion beam is not as straightforward as profiling a laser beam. This is because of two factors; 1) the ion beam operates entirely within a vacuum, making it difficult to physically add and position a device in the beam path to look at the beam directly, and 2) the primary ion beam passes through a plate which has a potential applied, bending the path slightly and adding another complication in fitting in a sensor.

To combat this, the ammeter connected to the sample plate is utilised in

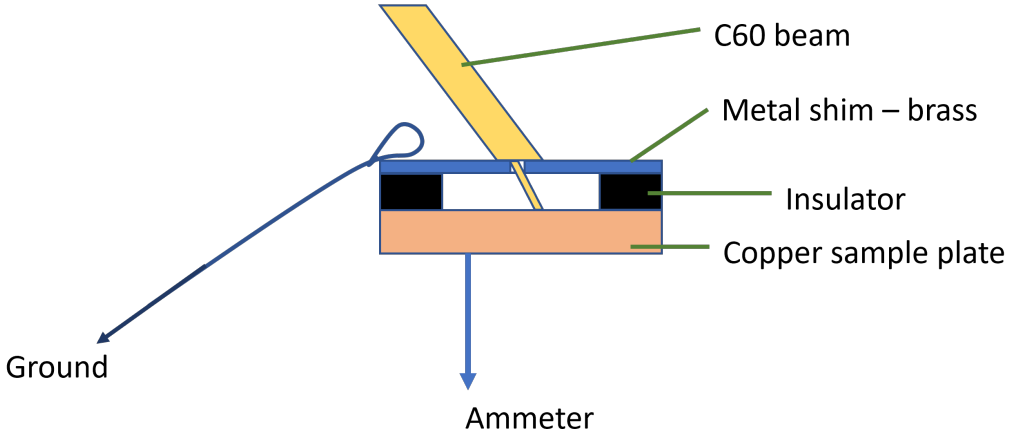


Figure 5.10: Schematic of modified Faraday cup for measuring current of the C_{60}^{+} beam.

conjunction with a modified Faraday cup (Figure 5.10). A thin plate of brass (0.18 mm thickness) with a pinhole in its centre, placed on top of 5 mm of an insulating material, is mounted on the sample plate with four small screws. The stage must be moved down by 5.18 mm in the z-axis to account for the additional height and avoid collision with the extractor optic.

The purpose of this setup is to act as a pinhole for the C_{60}^{+} ion beam. The entire beam, which would ordinarily impact on the sample plate, instead impacts on the thin copper plate. A small portion of the beam is allowed through the pinhole to impact on the sample plate, from which the current can be measured with an ammeter. By moving the sample plate along the x and y axes, the beam surface can be effectively profiled.

Early experiments indicated that charge build up on the thin copper plate was an issue and distorted the profile. To combat this, the vacuum was broken via a viewing port to affix a copper wire between the sample chamber wall and the sample plate, grounding the copper plate (see Figure 5.11).

Three different beam settings were investigated: a fully defocused beam, a partially focused beam, and a fully focused beam. The fully focused beam had a diameter too small to usefully profile using this method. The defocused and partially focus beams however are larger and shown in Figure 5.12.

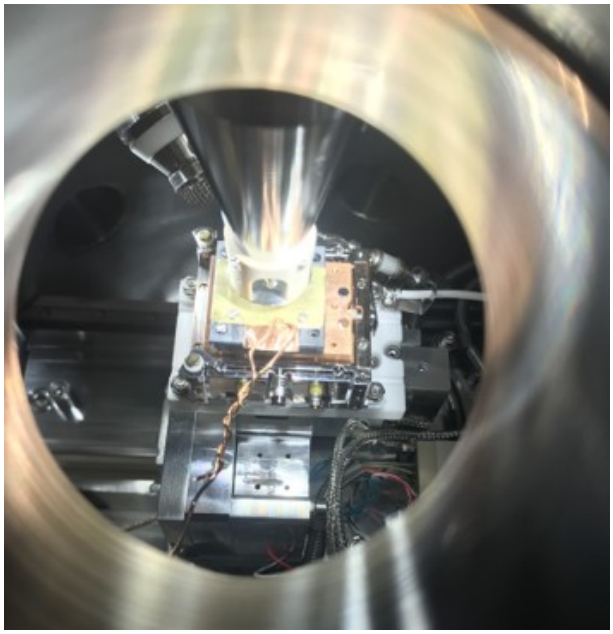
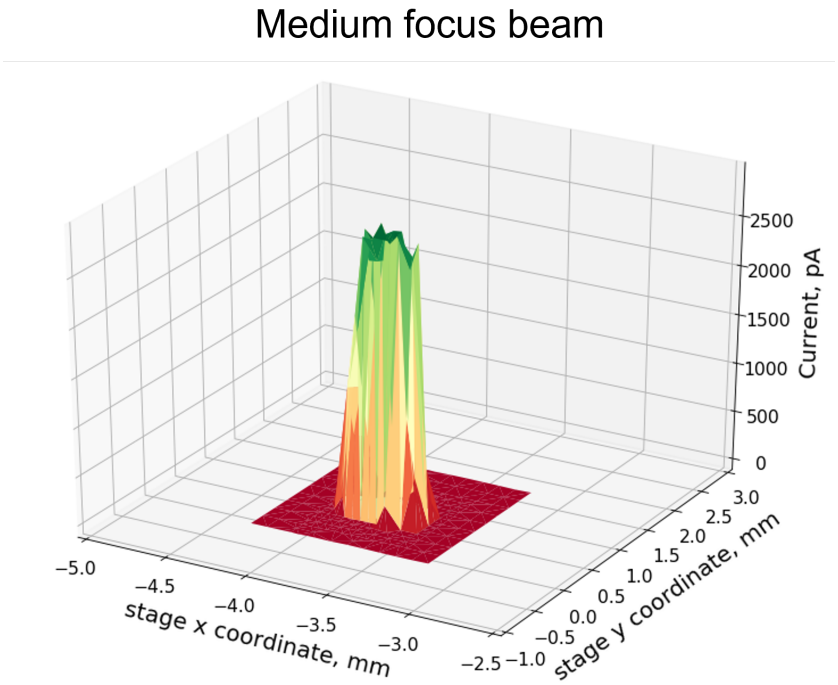


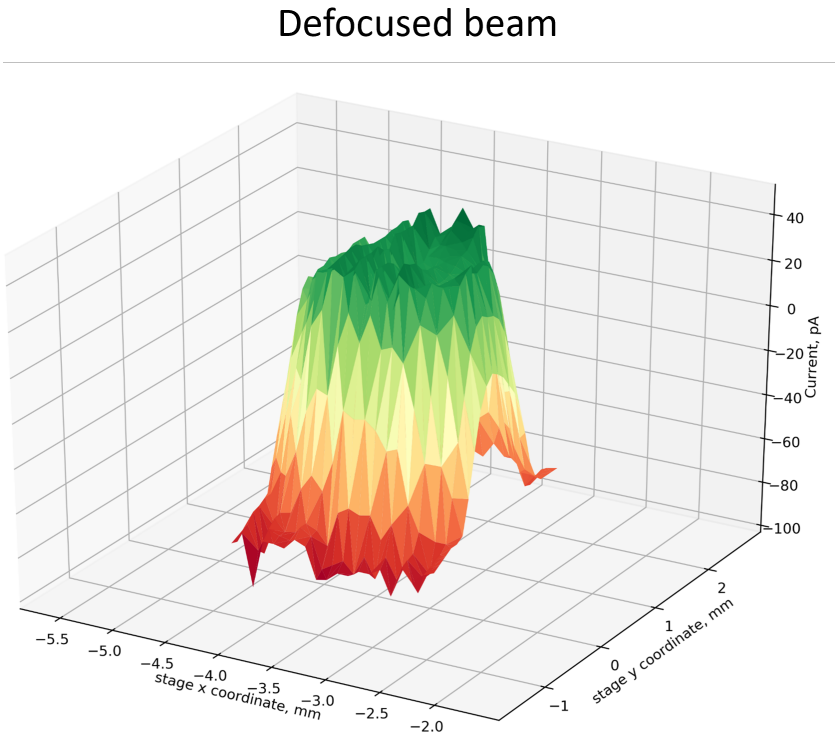
Figure 5.11: Image of the pinhole setup, with grounding wire resting on upper brass sheet, insulated from the sample plate.

The defocused beam has a diameter of 1.8 mm (Figure 5.12b) and the medium focused beam has a diameter of 0.18 mm (5.12a). The profiles indicate that the beam profile is uniform and homogeneous. The current recorded from the medium focused beam is ~2000 pA, while the defocused beam plateaus at ~20 pA, equating to the same total amperage across the area for both beams and confirming that the signal has not been saturated in Figure 5.12a).

Any beam inhomogeneity is more significant on the SIMS ToF mass spectrometer than on the reflectron ToF mass spectrometer, owing to its lower magnification and increased field of view. Any "hot spots" within the primary ion beam would amplify any differences in energy across the secondary ion beam, resulting in significant variations in ion impacts on the detector. However, as the primary ion beam has been shown to be uniform, this is not of concern. As a result, the primary ion beam can be confirmed to be uniform, producing uniform ion desorption across the surface of the sample.



(a)



(b)

Figure 5.12: C_{60}^{+} ion beam profiles obtained using the pinhole plate and recording the current on the sample stage. a) Shows the profile of partially focused beam, b) shows the profile of a fully defocused beam.

5.2 Mass Spectra

Both of these instruments are designed to perform microscope-mode MSI, with the key difference being the ionisation method. However, there are also a number of other design differences between the two instruments presented in this thesis; all of these differences impact their ability to obtain time-of-flight mass spectra.

As discussed in Chapter 2, the reflectron ToF mass spectrometer utilises pulsed extraction delayed acceleration (PEDA). The extractor plate has a pulse applied, the most effective being a time-variable pulse, which results in the ions within a mass window to achieve a temporal focus at the detector. This results in a ~8,000 $m/\Delta m$ mass resolution and ~20 μm spatial resolution over a 300 Da window. PEDA can also be applied to the SIMS ToF mass spectrometer, however, it is still being optimised both in simulations and experimentally for this instrument [152, 153]. As a result, mass data acquired using the SIMS ToF mass spectrometer does use single-field PEDA, however is an early example, and could likely be improved through further optimisation.

As detailed in Chapter 2, the design between the ion optics differs significantly. In particular, the SIMS ToF mass spectrometer has a much smaller extractor plate, with considerably smaller apertures in the plate compared to the reflectron ToF instrument. The distance between the repeller and extractor, and extractor and einzel lens also differs greatly between the two instruments. As such, the time spent in these regions also differs - which alters the way in which PEDA might be applied to the SIMS ToF instrument.

An additional factor is the initial velocity. This will vary due to the different ionisation methods - discussed in Section 3.1.2 with reference to ion generation using MALDI and LDI. SIMS is a hard ionisation technique, thus the initial velocity of ions generated will be greater than that experienced using MALDI and LDI. Consequently, the secondary ions spend less time in the region between the extractor and einzel lens than those in the reflectron instrument. This shorter time window means a different pulse is required in order to produce a similar temporal effect within the SIMS instrument.

Yet another complication experimentally is the unknown ionisation time. Using the Nd:YAG laser in combination with a delay generator, t_0 is well defined as the arrival time of the laser on the sample surface. Hence, it is relatively simple to determine a time at which to begin the PEDA pulse; setting it relative to t_{zero} on the delay generator and making small adjustments to optimise. With the SIMS instrument, the exact point of ionisation is currently unknown, as it is dependent on the time taken between the C_{60}^+ gun being triggered, and the primary ion beam reaching the sample surface. This complicates translating simulation results into experimental timing information which describe when the desired ions are in the extraction region.

As discussed in Chapter 1, a reflectron extends the flight path by twice the distance for a given length of ToF instrument. There is a large difference in flight path length between the two instruments, as a result of one containing a reflectron. As a result, the ToF for an ion produced in the SIMS ToF instrument will be shorter than the reflectron ToF instrument. This difference will have an effect on the mass resolution, as ions will have a shorter time window over which to spread out before reaching the detector, thus peaks will be closer together and less distinguishable.

Another difference introduced by the reflectron is the kinetic energy correction offered to the reflectron ToF mass spectrometer. The kinetic energy distribution is reduced by the reflectron, allowing for a mass focal point to form, which can be aligned with the detector. Without a reflectron, the SIMS ToF instrument lacks this additional temporal focusing, which would significantly improve the mass resolution.

A final difference between the two instruments is the detector setup - the reflectron instrument uses an Exalite 404 screen, with a 3.7 ns rise time. The SIMS instrument however has a Phosphor 47 screen, with a 6.7 ns rise time and 168 ns decay time. This large decay time limits the mass resolution achievable by each instrument, producing a large FWHM.

The combination of these factors results in a number of differences between the attainable mass spectra. To explore these differences, a number of laser dyes (Figure 5.13) were tested in both instruments. Both instruments operated in single

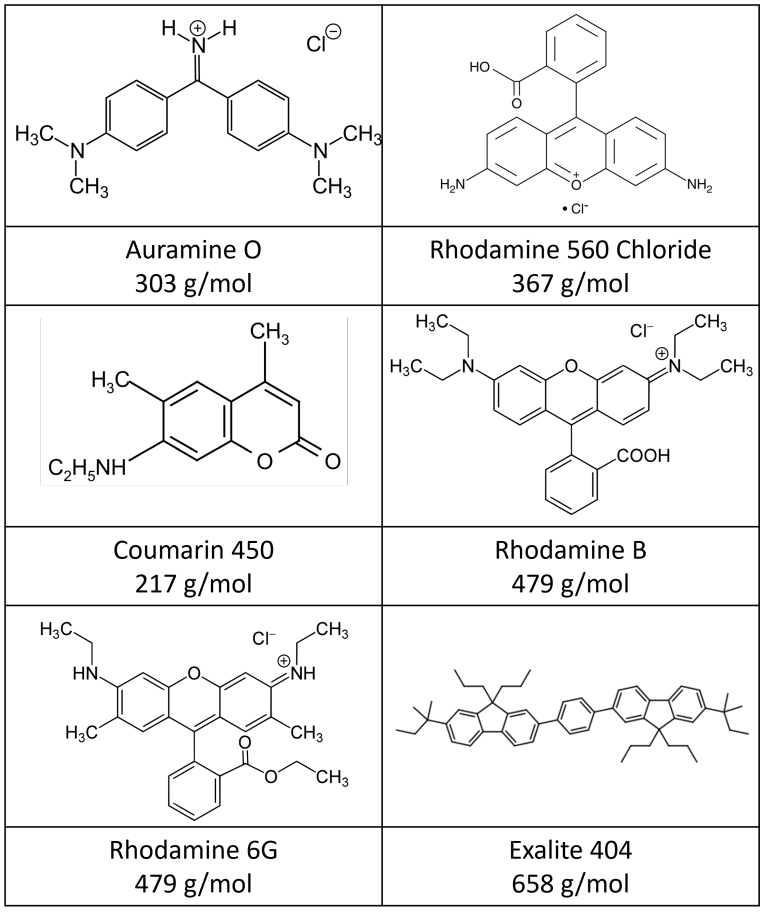


Figure 5.13: Molecular structure of a number of laser dyes tested in the two instruments

field PEDA mode, optimised for 343 Da on the reflectron ToF instrument, and 440 Da on the SIMS ToF instrument. The spectra produced from each instrument are shown in Figure 5.14 and Figure 5.15.

The reflectron ToF mass spectra were calibrated as described in Section 2.6. The SIMS ToF mass spectra have been calibrated using an H^+ peak (~1 Da), Na^+ (~23 Da), K^+ (~39 Da), and the Rhodamine 560 peak(~366.8 Da), as these are the strongest peaks present and can be identified confidently. From the obtained spectra, a 399 m/z Rhodamine B ion had a time-of-flight of 77.6 μs in the reflectron ToF mass spectrometer. Using the calibration equation, an ion of the same mass in the SIMS ToF instrument has a time-of-flight of 24 μs. There is approximately a factor of 3 difference between the ToF for ions of the same mass, a product of the differences between the two flight paths and ion velocities.

The spectra obtained with the reflectron ToF mass spectrometer show the expected peaks within the 200-600 m/z window, with very few lower mass peaks. Often Na^+ and K^+ ions are present, likely from the ITO slide [154], and are prone to producing strong Na^+ and K^+ peaks with the laser, thus the oscilloscope settings were such that the data in that time region was not recorded to avoid saturating the signal.

Comparing the reflectron ToF spectra to that in Figure 5.15 obtained with the SIMS ToF instrument, the results are significantly different. The SIMS ToF spectra show numerous peaks in the 0-150 m/z window with few peaks of greater mass. A strong peak at 372 m/z is present in the Rhodamine 560 spectra, which is greater than the mass of the neutral species (366.8 Da). This suggests that the calibration is incorrect, however there aren't enough high-mass information with well defined peaks to re-calibrate the spectra.

Auramine O and Coumarin 450 appear to have only noise above ~200 m/z, however, expanding along the y-axis of Rhodamine B, Rhodamine 6G, and Exalite 404, suggest there are low intensity peaks present in the 300-400 m/z range (Figure 5.16). The peak distribution in Rhodamine B is similar to what has been observed with the reflectron ToF mass spectrometer (Figure 5.14), therefore it is likely that these low intensity peaks are laser dye ion peaks. The calibrated m/z once again does not match that in Fig. 5.14, however, adjusting the calibration curve to include these peaks only introduces a minimal change, not sufficiently matching the mass peaks to that expected and the uncertainty over the true value is still high. More experimentation and use of known calibrants needs to be done to confidently assign these peaks.

The intensity of the ions greater than 200 Da in SIMS ToF mass spectra is low, whereas the reflectron ToF mass spectra display a high intensity and signal-to-noise ratio, An explanation for this difference probably lies in the PEDA application. As mentioned previously, the time from triggering a C_{60}^+ pulse, and its arrival at the sample surface, is unknown. The parameters used for the SIMS ToF instrument were obtained using SIMION, thus when selecting the trigger time for the PEDA pulse,

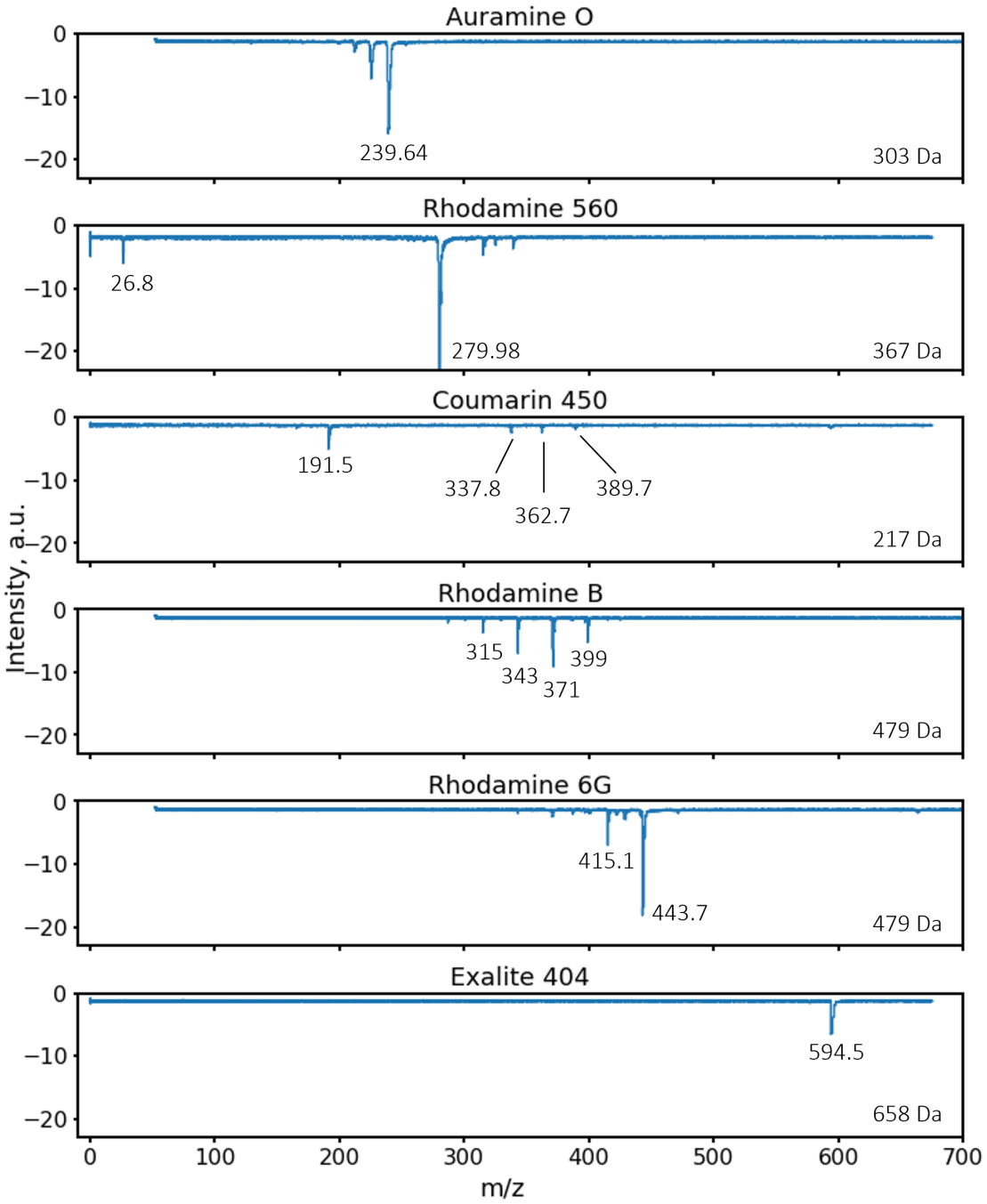


Figure 5.14: Mass spectra obtained with the reflectron ToF mass spectrometer for a selection of laser dyes, acquired with a photomultiplier tube (PMT). A high laser power (100mJ per pulse) was used to increase the signal-to-noise ratio in the spectra presented. Single-field PEDA has been applied, optimised for 343 Da. The mass of each neutral molecule is included in the lower right corner.

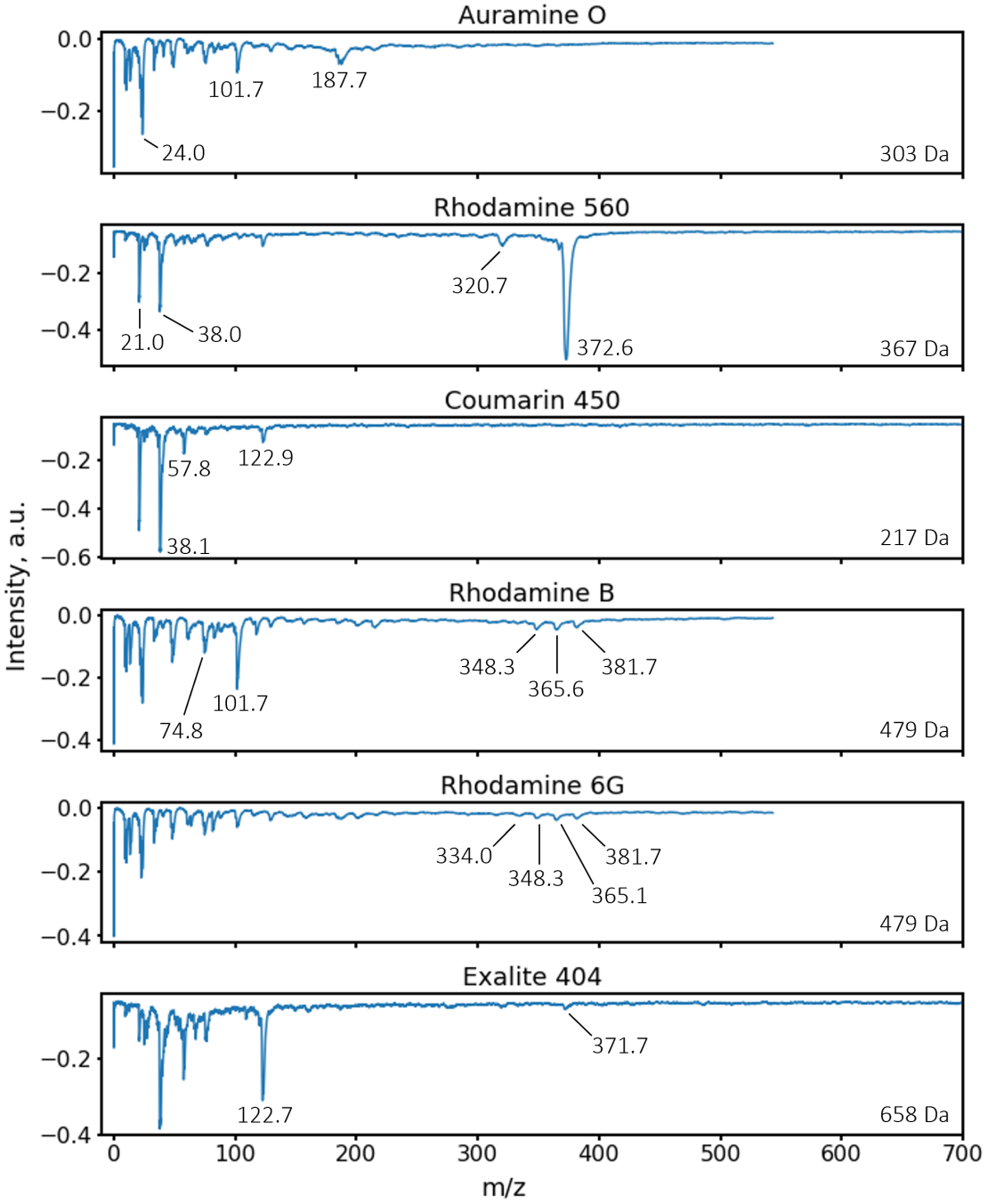


Figure 5.15: Mass spectra obtained with the SIMS ToF mass spectrometer for a selection of laser dyes, acquired with a photomultiplier tube (PMT) [a]. Single-field PEDA has been applied, optimised for 440 Da. The mass of each neutral molecule is included in the lower right corner.

[a]Experimental data collected by Yifeng Jia.

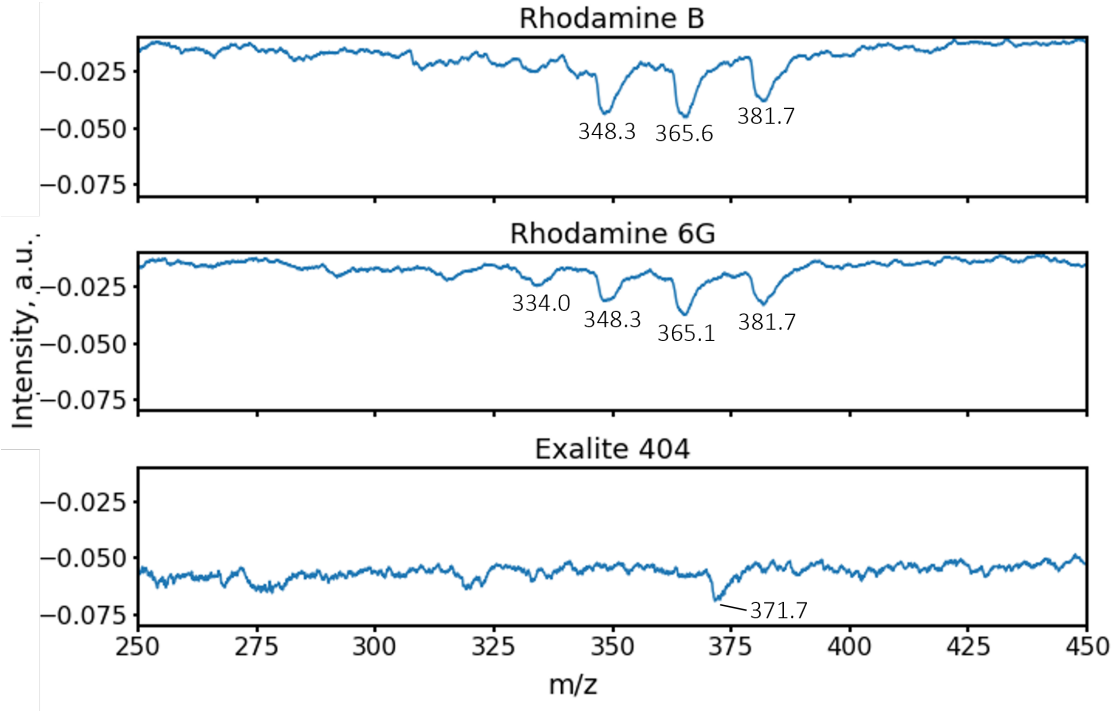


Figure 5.16: Expanded view of Figure 5.15, displaying Rhodamine B, Rhodamine 6G, and Exalite 404 spectra obtained on the SIMS ToF mass spectrometer.

the trigger relative to the C_{60}^+ pulse must be estimated before testing experimentally. It could be that the trigger time selected wasn't optimised, thus preventing the formation of peaks at heavier masses.

Additionally, the potentials applied to the SIMS ToF mass spectrometer have not been fully optimised. The instrument is still being investigated, guided by SIMION simulations. It is highly likely that the mass accuracy and intensity can be improved to favour higher mass ions over the lower, <100 m/z, ions.

Ultimately, the C_{60}^+ pulse simply may not be an ideal method of ionising some of these laser dyes. Either by not successfully ablating the sample and producing none of the laser dye ions, or by the more likely case of heavy fragmentation. SIMS is a hard ionisation method (however C_{60}^+ is a less hard ion source compared to monatomic SIMS ion sources), with expected peaks occurring from C^+, Na^+, and K^+, as well as other lower mass peaks. The laser dyes may have fragmented into lower mass ions and be present in the noisy signal at <150 m/z. Given this is early stage testing, laser dyes were chosen simply because they worked well in the reflectron

Table 5.2: A selection of peaks from Rhodamine 560 and Rhodamine B spectra, obtained using the reflectron ToF and SIMS ToF mass spectra, have been fitted to determine full width half maximum (FWHM) and mass resolution. The FWHM obtained from the reflectron ToF instrument has been fitted with a Gaussian, while the SIMS ToF instrument has been obtained from the 20-80% rise time on each peak.

	Reflectron ToF			SIMS TOF		
Dye	Peak / μs	FWHM / ns	Mass resolution / $m/\Delta m$	Peak / μs	FWHM / ns	Mass resolution / $m/\Delta m$
Rhodamine 560	65.522	52	1262	23.646	36	656
Rhodamine B	72.189	9	8021	23.130	26	889
	74.954	9	7890	23.480	36	652
	77.625	10	7763	23.820	32	744

ToF instrument and could serve as a point of comparison, thus the failure to ionise should not be a point of concern regarding the SIMS ToF mass spectrometer.

The SIMS ToF mass spectrometer demonstrates an ability to generate ions from laser dyes. The peaks produced are of lower intensity, and extrapolation of a low-mass calibration curve is insufficient to calibrate the ToF data. Further work is necessary to improve the spectra, primarily by exploring calibrants of known value, and improving the application of PEDA.

5.3 Mass resolution

Using Figures 5.14 and 5.15, we can acquire mass resolution data by fitting the spectra from each respective instrument. For the reflectron ToF mass spectra, this is done as described in Section 2.6.

The 168 ± 2.3 ns decay time of the P47 screen on the SIMS ToF mass spectrometer can be observed in Figure 5.16, with a sharp rising edge and a long falling edge. This long decay time will be a limiting factor when determining the FWHM of individual peaks. Instead, the 6.7 ± 0.2 ns rise time is utilised instead; by using the 20-80% rise of the leading edge of each peak, this can be used as a measure of mass resolution instead. Doing so minimises the effect of the slow phosphor response time, as the spectra has been recorded using a fast PMT with sub-nanosecond timing resolution.

A selection of FWHM from peaks on Rhodamine 560 and Rhodamine B spectra is listed in Table 5.2. These two were chosen for mass resolution comparison as

Rhodamine 560 has a strong peak in the SIMS ToF spectra, and the reflectron ToF instrument has been optimised for the Rhodamine B peaks in Figure 5.14. The mass resolution within the optimised window for the reflectron ToF mass spectrometer reaches ~8,000 $m/\Delta m$, but drops to ~1,300 $m/\Delta m$ when not focused by single-field PEDA.

The SIMS ToF mass spectrometer achieves a mass resolution of ~600-900 $m/\Delta m$. There isn't a clear optimised window of mass for the SIMS instrument, hence it's not obvious if single-field PEDA is having an impact on ions within this mass range.

While the mass resolution is an order of magnitude smaller than the reflectron ToF instrument, the SIMS ToF mass spectrometer achieves a >600 $m/\Delta m$ resolution for ~350-400 m/z with single-field PEDA. This is with several factors negatively impacting the attainable resolution, hence it should be possible to improve the resolution further from this early stage.

5.4 Spatial resolution

As discussed in Chapter 4, use of the Timepix3 camera is currently dependent on a laser flash to act as t_0. The SIMS ToF mass spectrometer does not operate with a laser, and thus has no optical source to act as a trigger for the Timepix3 camera (see Chapter 4). Hence the Timepix3 camera hasn't been tested on the SIMS instrument, but should be possible with the implementation of the LED trigger. Instead, a CCD camera is used to determine the spatial resolution of the instrument.

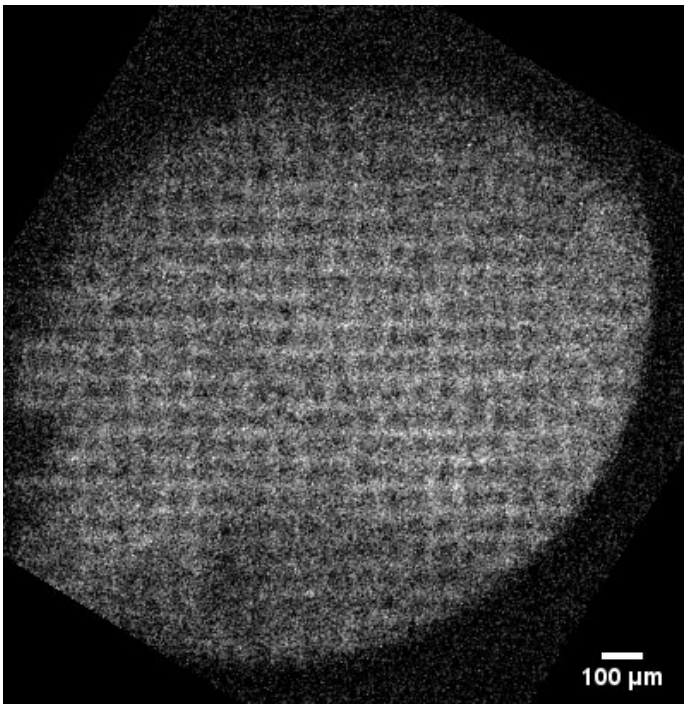
Two grid patterns, of pitch 63 μm and 140 μm, were prepared on an ITO slide with Rhodamine B, as described in Chapter 2. These ITO slides were then affixed to the surface of the SIMS sample plate using copper tape, which allows for conductance between the ITO coating on the slide and the sample plate. Once loaded into the instrument, the vertical position of the sample stage was reduced by 1 mm, such that the sample surface would be at the same height as the stage typically is.

Figure 5.17 shows the secondary ion images detected from each of the mesh patterns. While features are discernible on the smaller grid, it is not sufficient to produce a useful intensity profile across the surface. The larger grid at a pitch of

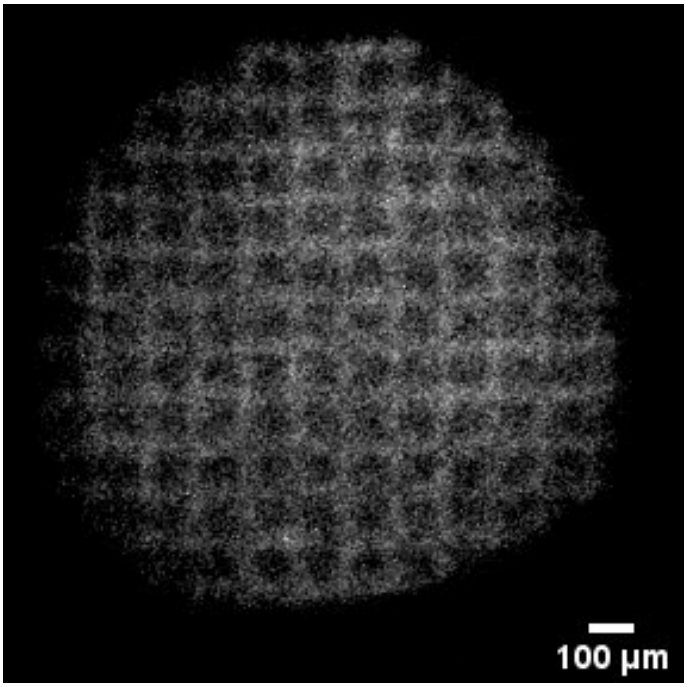
140 μm however has much more distinct features. When the images are compared to those in Figure 3.6, the image appears inverted, with the grid being bright rather than the squares. This suggests that the ion signal is not coming from Rhodamine B ions. A possible explanation is that it's actually sodium ions from the ITO slide being imaged. These images were acquired at a very early stage and without any mass spectra, shortly after which the screen degraded to an extent that further clear images were unattainable, however, Figure 5.15 shows a significant number of low mass ion peaks and a low number of Rhodamine B peaks, making this explanation quite likely.

An intensity profile for the grid was taken across the surface of Figure 5.17b, the results of which are plotted in Figure 5.18. Due to the image inversion, the profile is also inverted. By fitting a box function convoluted with a Gaussian, the rising edge is calculated from the intensity profile. Using the 20 - 80 % of this rising edge, a spatial resolution of 23.8 $\pm$ 8.2 μm is obtained. This is comparable to the SIMION model, which gives a spatial resolution of 25 μm. These images were taken using a static extractor potential, i.e. without PEDA. With the application of PEDA, simulations suggest a sub-micron spatial resolution should be achievable.

Another piece of information offered by these images is the field of view and the magnification. In Figure 5.1.2, the beam spot size for the fully defocused beam was determined to be 1.8 mm, however that does not necessarily mean that is the size of the secondary ion beam which makes it through the extractor opening, and successfully through the ToF tube on to the detector. Given the pitch size of 140 μm in Figure 5.17b, approximately 11 squares can be seen spanning the width of the image in both directions. This corresponds to a diameter of approximately 1.5 mm, which is only 0.3 mm smaller than the primary ion beam ion diameter determined with the corresponding copper burn spot. This suggests that the centre of the primary ion beam is well aligned with the centre of the ToF axis; the secondary ion beam is well aligned with the centre of the ToF tube and few ions are being deflected by the comparatively (to the reflectron instrument) small extractor hole. Using the 1.5 mm diameter, the magnification can be determined to be $\sim \times$ 7-8.



(a)



(b)

Figure 5.17: Secondary ion images acquired on the SIMS ToF mass spectrometer, using a CCD image of a Rhodamine B grid with a) 63 μm pitch and b) 140 μm pitch.

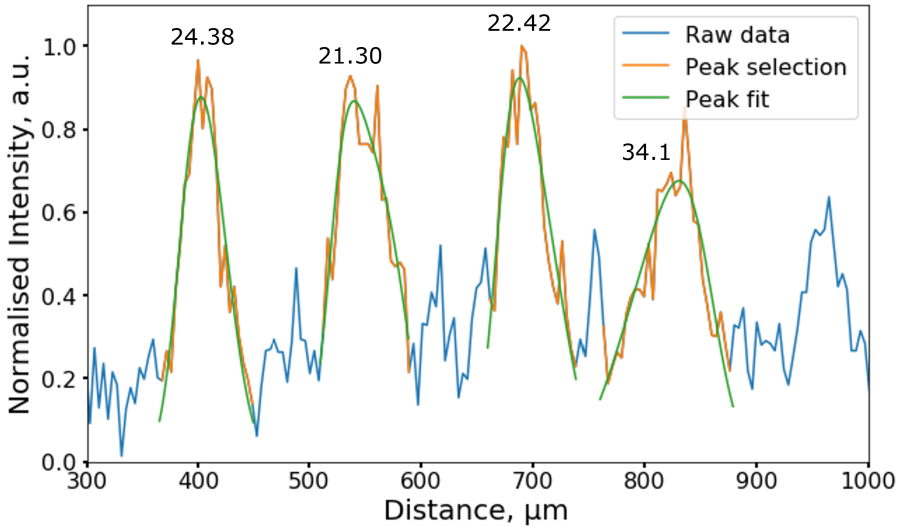


Figure 5.18: Example of an intensity profile taken across the surface of a grid imaged by the SIMS ToF mass spectrometer (Figure 5.17b). Each peak selected (orange) has been fitted with a box function convoluted with a Gaussian to produce a peak fit (green). The spatial resolution, given by the 20-80% rise, is written above each peak.

When grids of the same pitch are imaged using a CCD camera in the reflectron instrument, a spatial resolution of approximately 8 ± 1 μm has been achieved, with a magnification of $\times 93$ (as discussed in 3.2.3). The difference in magnification between the two instruments can be largely attributed to the reflectron. Not only does the reflectron increase the flight path of the ToF axis in the reflectron, it also increases the separation of the ions originating from neighbouring locations.

As discussed in Chapter 3, the path through the reflectron causes the magnification to change from approximately $\times 20$ on the entrance to the reflectron, to $\times 93$ after exiting and impacting on the detector. This is because of the mirroring action of the reflectron - a longer flight path will inevitably result in an increase in magnification. Additionally, the entrance to the reflectron could be acting in a similar way to a convex mirror - the potential surfaces around the reflectron opening is curved, which may be diverging the beam.

Alongside the flight path, the ion velocity also plays a role. Faster ions will have a shorter ToF, thus have less time to deviate from the central ToF axis. The ToF within the SIMS instrument for a 400 Da ion is approximately 20 μs. Comparatively, the reflectron instrument has a ToF of approximately 70 μs for the same mass. Thus

the SIMS instrument, with its high energy ionisation method, generates secondary ions with a higher initial velocity, and paired with a shorter flight path and lack of reflectron, results in a smaller magnification.

The spatial resolution differences can in part be attributed to PEDA and the reflectron. The images acquired using the SIMS ToF mass spectrometer were taken with a static potential on the extractor plate, while a time-variable pulse is applied to the reflectron ToF instrument. As a result, the ions experiencing the time-variable pulse are more spatially focused on the detector plane over a wider mass range. Paired with the difference in magnification between the two instruments, the difference in spatial resolution is understandable.

5.5 Conclusion

A comparison of two different instruments was performed, beginning with an investigating of the laser beam and C_{60}^+ ion beam. It was shown that the laser beam has a 8 mm diameter, but a non-Gaussian profile with hot spots. These hot spots do not appear to impact the ion distribution, as the magnification is high enough to limit the field of view to within a hot spot, however, should the variable magnification be introduced in the future, this non-Guassian profile may introduce. The SIMS mass spectrometer is a newer instrument, thus needed additional characterisation to understand the primary ion-beam and how to adjust it. It was shown that the C_{60}^+ ion beam can produce a range of sizes, with a maximum attainable diameter of 1.8 mm. This has greatly expanded the detection area relative to that previously achieved [91]. The surface of the ion beam appears homogenous, with little variation in the current across beam. This supplies confidence that when using the C_{60}^+ ion beam, all areas of the sample surface are receiving approximately the same kinetic energy.

The extent to which the C_{60}^+ ion beam can be moved across the sample surface was characterised. There are a number of methods for deflection, which offer up to $\pm$ 1000 μm of deflection relative to the central ToF axis. This will allow for the primary ion beam position to be corrected if deflected from the centre of the ToF axis by the secondary ion optics. Given that the defocused primary ion-beam is

clipped by the hole in the PEDA extractor plate, being able to alter the beam path is essential to ensuring a large area of the sample can be ionised.

A selection of laser dyes were explored in each instrument, highlighting a difference in ionisation between the two methods. The reflectron ToF mass spectrometer produced high-intensity mass peaks, with a low signal-to-noise ratio and little fragmentation. The SIMS ToF mass spectrometer contrasted with low-intensity mass peaks >150 Da, and higher fragmentation and background signal. PEDA has not yet been optimised for the SIMS ToF instrument, thus the best mass resolution achieved is ~900 $m/\Delta m$. The reflectron ToF mass spectrometer reaches a maximum at ~8,000 $m/\Delta m$. The SIMS ToF instrument could improve this value with further optimisation of the secondary ion optic parameters and utilising time-variable PEDA. The instrument is limited by P47 screen, replacing the screen with an Exalite 404 screen would significantly reduce the convolution created by the fluorescence time and help bring the experimentally achievable results closer the values predicted in simulation.

The spatial resolution was determined to be 23.8 ± 8.2 μm with the SIMS ToF mass spectrometer, offering a magnification of ~×7-8. The reflectron ToF instrument can achieve a 8 ±1 μm, at a ×92 magnification. This difference can be attributed to the reflectron and time-variable PEDA. Implementing these on the SIMS ToF mass spectrometer should help increase the spatial resolution, enabling the instrument to be achieve comparable resolutions to that of the reflectron ToF instrument.

The long term aspiration with the SIMS ToF instrument is for a sample to be imaged under both the reflectron ToF and SIMS ToF instrument, each ionisation provides a different distribution of ions, which could be pieced together to identify unknown compounds and therefore learn more about a particular analyte within a sample.

6
Conclusions and Future Work

This thesis has presented work on a reflectron ToF mass spectrometer, and a SIMS ToF mass spectrometer, which are capable of simultaneously acquiring mass and spatial information. Both theoretical and experimental research has been conducted with the intention of improving the capabilities of both imaging mass spectrometers.

A genetic algorithm was used to investigate the spatial resolution limits of the reflectron ToF mass spectrometer. The simulations show that by accelerating the ions to a higher velocity, it is possible to improve the spatial resolution from ~18 μm to ~9 μm when simulated within the physical constraints of the instrument. This was verified experimentally, achieving 8 $\pm$ 1 μm with a mass of ~37 Da, while retaining a mass resolution of 3888 $\pm$ 370 $m/\Delta m$. If the constraints are changed from 10 kV to 40 kV, a spatial resolution of ~7 μm could be attained in simulations. These experiments prove a higher spatial resolution is attainable, bringing the instruments range closer to the 1 μm achieved with the MULTUM [95]. In the future, higher voltage power supplies could be used to further expand the versatility of the instrument.

Next, the introduction of a zoom lens on the reflectron ToF mass spectrometer was investigated using SIMION, with the goal of reducing the magnification and expanding the instruments field of view. By doing this, a larger surface area could be imaged at once, allowing the region of interest to be identified. If paired with an

adjustable sample stage, the magnification could then be increased to allow high magnification imaging of the region of interest with minimal sample ablation. To do this, a number of options were explored, including using plates on the reflectron electrode stack, introducing an additional einzel lens, and manipulating the existing einzel lens. The reflectron introduced distortions to the simulated grid as a result of ions passing through the lens off-centre, while the existing einzel lens limited the mass range to <450 Da. The best option proved to be an additional einzel lens, located before the reflectron. If positioned between the deflectors and reflectron, magnifications of ×65, ×40, and ×20 could be attained, reduced from ×92 without a lens. A <50 μm spatial resolution and >2,500 $m/\Delta m$ mass resolution was calculated, which could likely be optimised further using the other electrodes. The next step in this endeavour should be optimising the location of the additional einzel lens, as well as the potentials applied to the extraction optics in order to improve the mass and spatial resolution further. This could then be followed by experimental testing and optimisation. In order for variable magnification to be most effective, the installation of an adjustable stage should be considered. This would allow for a wider field of view image to be acquired, followed by zooming back in and positioning the sample in the desired location.

The timing precision of the Timepix3 camera is explored in Chapter 4. The Timepix3 camera has previously been paired with the reflectron ToF mass spectrometer, using a portion of the laser beam and a fibre optic to act as a trigger for the camera. This early work could be further optimised through improving the timing precision with the use of a more intense laser beam spot. When using a low intensity laser spot (10% transmittance), a difference of ~16 ns from the expected time-of-arrival (ToA) for a peak at 100 ms was found. A high intensity laser spot (79% transmittance) produced a full-width half maximum (FWHM) of ~4.5 ns, approximately three timebins. This variation with laser intensity negatively impacts the alignment of successive spectra, therefore broadening the peak. If a more intense beam spot could be employed, this can increase the mass resolution towards the true instrument resolution.

This work was expanded on with the use of an 510 nm LED, the purpose of which is to allow this method of triggering the Timepix3 camera to be used on the SIMS ToF mass spectrometer. The LED proved to have a FWHM ~8 ns, which when used as the trigger resulted in peaks with a FWHM ~6 ns. The LED is a viable method of triggering the Timepix3 camera, however it currently results in broader peaks when compared to the laser trigger. Decreasing the LED pulse width and focusing the LED on to the camera should improve this. If a fast LED pulse can be generated. this pulse could be used to trigger the Timepix3 camera on other systems (such as the SIMS ToF instrument), removing the need for a laser and fibre optic trigger.

The Timepix3 camera supplies time-over-threshold (ToT) information, which could be interpreted as a measure of photon intensity. When looking at Rhodamine B data, collected on the reflectron ToF mass spectrometer using the Timepix3 camera, ToA can be plotted as a function of intensity (event count), or as a function of ToT. Previously, only intensity information has been used, however the ToT information offers another dimension to the data and improves peak separation, reducing the mass resolution from 60.2 μs to 49.8 μs at 398 Da. Secondly, by filtering out events with a low ToT value, the FWHM can be further improved upon by removing the low impact data with a less accurate ToA. The Rhodamine B data was acquired with a low intensity laser spot serving as the trigger. In order to get a more intense trigger spot, a mirror could be used in future experiments. Doing so would allow for a higher precision trigger, and thus better temporal alignment when processing spectra, improving the FWHM further and making the mass spectrometer more competitive with similar instruments.

The C_{60}^+ ion beam was shown to be homogenous, while the laser beam presented hot spots. In the current configuration, this does not appear to have an impact on the image obtained as the field of view is smaller than one of these hot spots, however a spatial filter could be used to produce a Gaussian laser beam should the variable magnification be introduced. The C_{60}^+ ion beam was characterised, identifying a range of beam sizes and how to deflect the beam. Using this, the

beam can be aimed to impact the sample at the central ToF axis, producing secondary ions in the optimal position.

In order to identify any differences between the two instruments, the SIMS ToF and reflectron ToF mass spectrometers were compared. The SIMS ToF mass spectra show low-intensity mass peaks <150 Da, with higher fragmentation and background signal when compared to the reflectron ToF mass spectrometer. A mass resolution of ~900 $m/\Delta m$ is achieved by the SIMS ToF instrument, while the reflectron ToF mass spectrometer attains ~8,000 $m/\Delta m$. The spatial resolution was determined to be 23.8 ± 8.2 μm with the SIMS ToF mass spectrometer, with a magnification of ~×7-8. The reflectron ToF instrument reached a spatial resolution of 8 ±1 μm, at a ×92 magnification. This discrepancy has been attributed to the application of PEDA not being optimised on the SIMS ToF instrument, as well as the P47 screen which supplies a long fluorescence lifetime, hampering the time resolution. Future work should include replacing the SIMS ToF instrument detector with a faster scintillator (e.g., Exalite 404) to reduce the convolution, as well as the application of time-variable PEDA to improve the mass resolution. This would help make the instrument more comparable to the reflectron ToF instrument, thus capable of supplying additional spectral information. A more ambitious project would be the addition of a reflectron to the SIMS ToF mass spectrometer, which would make the instrument more comparable to the reflectron ToF mass spectrometer by increasing its flight path and helping to temporally focus the ions.

Overall, the combination of these developments improves the performance of these microscope mode mass spectrometry imaging instruments, increasing functionality with a theoretical study into variable magnification, and providing an option for high spatial resolution imaging. The timing precision provided by the Timepix3 camera has also been improved upon, improving the mass resolution capability of the camera when paired with the reflectron ToF mass spectrometer, and the a new SIMS ToF mass spectrometer has been introduced and characterised.

References

[1] A. R. Buchberger, K. DeLaney, J. Johnson, L. Li, *Analytical chemistry* **2018**, *90*, 240.

[2] J. T. Merz, J. T. Merz, *A history of European thought in the nineteenth century*, W. Blackwood, Edinburgh, **1907**, pp. 1–484.

[3] A. J. Dempster, *Proceedings of the National Academy of Sciences of the United States of America* **1925**, *11*, 552–554.

[4] E. O. Lawrence, D. H. Sloan, *Proceedings of the National Academy of Sciences of the United States of America* **1931**, *17*, 64–70.

[5] D. C. Faircloth, *CERN Accelerator School: High Power Hadron Machines CAS 2011 - Proceedings* **2013**, 369–407.

[6] P. F. Dahl, *Flash of the Cathode Rays* **1997**.

[7] H. E. Gove, *Measuring Mass: From Positive Rays to Proteins*, *Vol. 94*, The University of Chicago Press, **2003**, pp. 348–349.

[8] J. J. Thomson, *Proceedings of the Royal Society of London. Series A Containing Papers of a Mathematical and Physical Character* **1913**, *89*, 1–20.

[9] J. Griffiths, *Analytical Chemistry* **2008**, *80*, 5678–5683.

[10] K. M. Downard, *Eur. J. Mass Spectrom* **2007**, *13*, 177–190.

[11] J. De Laeter, M. D. Kurz, *Journal of mass spectrometry : JMS* **2006**, *41*, 847–854.

[12] A. O. Nier, *Journal OF Chemical Education* **1989**, *66*, 385–388.

[13] C. Reinhardt, *Shifting and rearranging: Physical methods and the transformation of modern chemistry*, Sagamore Beach, MA., **2006**.

[14] H.-F. Grützmacher, *Encyclopedia of Spectroscopy and Spectrometry* **1999**, 637–648.

[15] K. Biemann, *Journal of Proteomics* **2014**, *107*, 62–70.

[16] K. Biemann, *Annual Review of Analytical Chemistry* **2015**, *8*, 1–19.

[17] H. Budzikiewicz, C. Djerassi, D. Williams, *Interpretation of mass spectra of organic compounds*, **1964**.

[18] R. S. Gohlke, F. W. McLafferty, *Journal of the American Society for Mass Spectrometry* **1993**, *4*, 367–371.

[19] R. S. Gohlke, *Analytical Chemistry* **1959**, *31*, 535–541.

[20] W. C. Wiley, I. H. McLaren, *Review of Scientific Instruments* **2004**, *26*, 1150.

[21] M. B. Comisarow, A. G. Marshall, *Chemical Physics Letters* **1974**, *25*, 282–283.

[22] J. B. Fenn, *Journal of Biomolecular Techniques : JBT* **2002**, *13*, 101.

[23] M. Dole, L. L. Mack, R. L. Hines, D. O. Chemistry, R. C. Mobley, L. D. Ferguson, M. B. Alice, *The Journal of Chemical Physics* **2003**, *49*, 2240.

[24] F. Hillenkamp, M. Karas, *International Journal of Mass Spectrometry* **2000**, *200*, 71–77.

[25] M. Karas, D. Bachmann, F. Hillenkamp, *Analytical Chemistry* **1985**, *57*, 2935–2939.

[26] K. Heijhoff, K. Akiba, R. Bates, M. Van Beuzekom, P. Bosch, A. P. Colijn, R. Geertsema, V. Gromov, M. L. Heidotting, L. S. Hendrikx, D. Hynds, H. Snoek, *Journal of Instrumentation* **2021**, *16*.

[27] I. Newton, *Philosophiae naturalis principia mathematica*, **1687**.

[28] M. Moniatte, F. G. Van Der Goot, J. T. Buckley, F. Pattus, A. Van Dorsselaer, *FEBS Letters* **1996**, *384*, 269–272.

[29] J. H. Gross, *Mass Spectrometry*, Springer International Publishing, Cham, **2017**.

[30] R. J. Burleigh, PhD thesis, University of Oxford, **2019**.

[31] J. J. Thomson, *Rays of positive electricity and their application to chemical analyses*, *Vol. 42*, John Wiley & Sons, Ltd, **1923**, pp. 861–861.

[32] F. W. Aston, *Proceedings of the Royal Society of London. Series A - Mathematical and Physical Sciences* **1937**, *163*, 391–404.

[33] S. D. Shi, C. L. Hendrickson, A. G. Marshall, *Proceedings of the National Academy of Sciences of the United States of America* **1998**, *95*, 11532–11537.

[34] SG Alikhanov, *Soviet Phys. JETP* **1957**, *4*.

[35] B. A. Mamyrin, V. I. Karataev, D. V. Shmikk, V. A. Zagulin, B. A. Mamyrin, V. I. Karataev, D. V. Shmikk, V. A. Zagulin, *JETP* **1973**, *37*, 45.

[36] K. K. Murray, File:Reflectron schematic.gif - Wikimedia Commons, **2017**.

[37] E. V. Moskovets, *Applied Physics B 1991 53:4* **1991**, *53*, 253–259.

[38] T. Quenzer, J. Robinson, B. Bolanios, E. Milgram, M. Greig in Proceedings of the 50th Annual Conference on Mass Spectrometry and Allied Topics, **2002**.

[39] N. R. Council, *Monitoring at Chemical Agent Disposal Facilities*, National Academies Press, **2005**, pp. 1–84.

[40] A. J. Dempster, *Physical Review* **1918**, *11*, 316.

[41] J. T. Watson, *Electron Ionization Mass Spectrometry*, John Wiley & Sons, Ltd, **2000**.

[42] A. G. Harrison, *Chemical Ionization Mass Spectrometry*, 2nd ed., Routledge, **1992**.

[43] B. Munson, *International Journal of Mass Spectrometry* **2000**, *200*, 243–251.

[44] S. V. Hoffmann Edmond de, *Mass Spectrometry: principles and applications, 3rd Edition - Edmond de Hoffmann, Vincent Stroobant*, **2007**, pp. 1–4.

[45] J. N. Bilton, N. Kyriakidis, E. S. Waight, *Principles of field ionization and field desorption mass spectrometry. Vol. 13*, John Wiley & Sons, Ltd, **1978**, pp. 490–490.

[46] M. Karas, F. Hillenkamp, *Analytical Chemistry* **1988**, *60*, 2299–2301.

[47] S. Okuno, M. Nakano, G. E. Matsubayashi, R. Arakawa, Y. Wada, *Rapid Communications in Mass Spectrometry* **2004**, *18*, 2811–2817.

[48] M. Karas, D. Bachmann, U. Bahr, F. Hillenkamp, *International Journal of Mass Spectrometry and Ion Processes* **1987**, *78*, 53–68.

[49] M. J. Stump, R. C. Fleming, W. H. Gong, A. J. Jaber, J. J. Jones, C. W. Surber, C. L. Wilkins, *Applied Spectroscopy Reviews* **2007**, *37*, 275–303.

[50] X. Chen, J. A. Carroll, R. C. Beavis, *Journal of the American Society for Mass Spectrometry* **1998**, *9*, 885–891.

[51] M. Karas, R. Krüger, *Chemical Reviews* **2003**, *103*, 427–439.

[52] R. Knochenmuss, *Journal of Mass Spectrometry* **2002**, *37*, 867–877.

[53] K. Dreisewerd, The desorption process in MALDI, **2003**.

[54] R. Zenobi, R. Knochenmuss, *Mass Spectrometry Reviews* **1999**, *17*, 337–366.

[55] R. Knochenmuss, R. Zenobi, *Chemical reviews* **2003**, *103*, 441–452.

[56] Creative Proteomics, MALDI-TOF Mass Spectrometry, **2023**.

[57] P. Demirev, A. Westman, C. T. Reimann, P. Håkansson, D. Barofsky, B. U. Sundqvist, Y. D. Cheng, W. Seibt, K. Siegbahn, *Rapid Communications in Mass Spectrometry* **1992**, *6*, 187–191.

[58] J. Kim, *Mass Spectrometry Letters* **2015**, *6*, 27–30.

[59] A. E. Clark, E. J. Kaleta, A. Arora, D. M. Wolk, *Clinical Microbiology Reviews* **2013**, *26*, 547–603.

[60] L. Van Vaeck, A. Adriaens, R. Gijbels, *Mass Spectrometry Reviews* **1999**, *18*, 1–47.

[61] A. Adriaens, L. Vaeck, F. Adams, *Mass Spectrometry Reviews* **1999**, *18*, 48–81.

[62] R. F. Herzog, F. P. Viehböck, *Physical Review* **1949**, *76*, 855.

[63] R. Castaing, G. Slodzian, *Journal of Microscopie* **1962**, *1*, 395–410.

[64] L. Volz, P. Piersimoni, V. Bashkirov, P. Hoppe, J. Leitner, E. Gröner, R. Castaing, G. Slodzian, *Journal of Physics E: Scientific Instruments* **1981**, *14*, 1119.

[65] S. Ninomiya, K. Ichiki, H. Yamada, Y. Nakata, T. Seki, T. Aoki, J. Matsuo, *Rapid Communications in Mass Spectrometry* **2009**, *23*, 1601–1606.

[66] Cameca, Introduction to Secondary Ion Mass Spectrometry (SIMS) technique, **2017**.

[67] A. Bennlnghoven, W. K. Sichtermann, *Analytical chemistry* **1978**, *50*, 1180–1184.

[68] L. A. McDonnell, R. M. Heeren, *Mass Spectrometry Reviews* **2007**, *26*, 606–643.

[69] Z. Takáts, J. M. Wiseman, B. Gologan, R. G. Cooks, *Science (New York N.Y.)* **2004**, *306*, 471–473.

[70] C. Chen, S. R. Laviolette, S. N. Whitehead, J. B. Renaud, K. K. Yeung, *Journal of the American Society for Mass Spectrometry* **2021**, *32*, 1065–1079.

[71] S. Miyamoto, C. C. Hsu, G. Hamm, M. Darshi, M. Diamond-Stanic, A. E. Declèves, L. Slater, S. Pennathur, J. Stauber, P. C. Dorrestein, K. Sharma, *EBioMedicine* **2016**, *7*, 121–134.

[72] S. Ayciriex, D. Touboul, A. Brunelle, O. Laprévote, *Clinical Lipidology* **2011**, *6*, 437–445.

[73] A. Körber, J. D. Keelor, B. S. Claes, R. M. Heeren, I. G. Anthony, *Analytical Chemistry* **2022**, *94*, 14652–14658.

[74] G. H. Morrison, G. Slodzian, *Analytical Chemistry* **1975**, *47*, 932A–943a.

[75] X. Llopart, R. Ballabriga, M. Campbell, L. Tlustos, W. Wong, *Nuclear Instruments and Methods in Physics Research* **2007**, *581*, 485–494.

[76] A. Nomerotski, S. Adigun-Boaye, M. Brouard, E. Campbell, A. Clark, J. Crooks, J. J. John, A. J. Johnsen, C. Slater, R. Turchetta, C. Vallance, E. Wilman, W. H. Yuen, *Nuclear Instruments and Methods in Physics Research* **2011**, *633*, S243–S246.

[77] J. John, M. Brouard, A. Clark, J. Crooks, E. Halford, L. Hill, L. Lee, A. Nomerotski, R. Pisarczyk, I. Sedgwick, S. Slater, R. Turchetta, C. Vallance, E. Wilman, B. Winter, H. Yuen, *Journal of Instrumentation* **2012**, *7*, 8001.

[78] A. T. Clark, J. P. Crooks, I. Sedgwick, R. Turchetta, J. W. Lee, J. J. John, E. S. Wilman, L. Hill, E. Halford, C. S. Slater, B. Winter, W. H. Yuen, S. H. Gardiner, M. L. Lipciuc, M. Brouard, A. Nomerotski, C. Vallance, *The journal of physical chemistry. A* **2012**, *116*, 10897–10903.

[79] M. Brouard, E. Halford, A. Lauer, C. S. Slater, B. Winter, W. H. Yuen, J. J. John, L. Hill, A. Nomerotski, A. Clark, J. Crooks, I. Sedgwick, R. Turchetta, J. W. Lee, C. Vallance, E. Wilman, *Review of Scientific Instruments* **2012**, *83*.

[80] C. Vallance, M. Brouard, A. Lauer, C. S. Slater, E. Halford, B. Winter, S. J. King, J. W. Lee, D. E. Pooley, I. Sedgwick, R. Turchetta, A. Nomerotski, J. J. John, L. Hill, *Physical Chemistry Chemical Physics* **2014**, *16*, 383–395.

[81] D. Wood, R. J. Burleigh, N. Smith, D. Bortoletto, M. Brouard, M. Burt, A. Nomerotski, R. Plackett, I. Shipsey, *Journal of the American Society for Mass Spectrometry* **2022**, *33*, 2328–2332.

[82] J. L. Guerquin-Kern, T. D. Wu, C. Quintana, A. Croisy, *Biochimica et biophysica acta* **2005**, *1724*, 228–238.

[83] M. T. Bernius, S. Chandra, G. H. Morrison, *Review of Scientific Instruments* **1998**, *56*, 1347.

[84] E. De Chambost, *A history of Cameca (1954-2009)*, *Vol. 167*, Academic Press Inc., **2011**, pp. 1–119.

[85] H. N. Migeon, M. Schuhmacher, G. Slodzian, *Surface and Interface Analysis* **1990**, *16*, 9–13.

[86] B. Schueler, P. Sander, D. A. Reed, *Vacuum* **1990**, *41*, 1661–1664.

[87] B. W. Schueler, *Microscopy Microanalysis Microstructures* **1992**, *3*, 119–139.

[88] S. L. Luxembourg, T. H. Mize, L. A. McDonnell, R. M. A. Heeren, *Analytical Chemistry* **2004**, *76*, 5339–5344.

[89] L. A. Klerk, A. F. Altelaar, M. Froesch, L. A. McDonnell, R. M. Heeren, *International Journal of Mass Spectrometry* **2009**, *285*, 19–25.

[90] J. H. Jungmann, L. MacAleese, R. Buijs, F. Giskes, A. de Snaijer, J. Visser, J. Visschers, M. J. Vrakking, R. M. Heeren, *Journal of the American Society for Mass Spectrometry* **2010**, *21*, 2023–2030.

[91] A. Kiss, D. F. Smith, J. H. Jungmann, R. M. Heeren, *Rapid Communications in Mass Spectrometry* **2013**, *27*, 2745–2750.

[92] J. H. Jungmann, L. MacAleese, J. Visser, M. J. Vrakking, R. M. Heeren, *Analytical Chemistry* **2011**, *83*, 7888–7894.

[93] H. Hazama, J. Aoki, H. Nagao, R. Suzuki, T. Tashima, K. i. Fujii, K. Masuda, K. Awazu, M. Toyoda, Y. Naito, *Applied Surface Science* **2008**, *255*, 1257–1263.

[94] H. Hazama, H. Yoshimura, J. Aoki, H. Nagao, M. Toyoda, K. Masuda, K. Fujii, T. Tashima, Y. Naito, K. Awazu, H. Hazama, H. Yoshimura, J. Aoki, H. Nagao, M. Toyoda, K. Masuda, K. Fujii, T. Tashima, Y. Naito, K. Awazu, *JBO* **2011**, *16*, 046007–046007.

[95] T. Hondo, M. Toyoda, *Mass spectrometry (Tokyo Japan)* **2021**, *10*.

[96] J. Aoki, H. Hazama, M. Toyoda, *Journal of the Mass Spectrometry Society of Japan* **2011**, *59*, 57–61.

[97] R. S. Brown, J. J. Lennon, *Analytical chemistry* **1995**, *67*, 1998–2003.

[98] S. M. Colby, T. B. King, J. P. Reilly, D. M. Lubman, *Rapid Communications in Mass Spectrometry* **1994**, *8*, 865–868.

[99] A. Guo, PhD thesis, University of Oxford, **2018**.

[100] A. Guo, M. Burt, M. Brouard, *International Journal of Mass Spectrometry* **2018**, *429*, 121–126.

[101] A. Guo, R. J. Burleigh, N. Smith, M. Brouard, M. Burt, *Journal of the American Society for Mass Spectrometry* **2020**, *31*, 1903–1909.

[102] K. L. Brown, G. W. Tautfest, *Review of Scientific Instruments* **1956**, *27*, 696.

[103] T. Poikela, J. Plosila, T. Westerlund, M. Campbell, M. D. Gaspari, X. Llopart, V. Gromov, R. Kluit, M. V. Beuzekom, F. Zappon, V. Zivkovic, C. Brezina, K. Desch, Y. Fu, A. Kruth, *Journal of Instrumentation* **2014**, *9*.

[104] A. Oelsner, O. Schmidt, M. Schicketanz, M. Klais, G. Schönhense, V. Mergel, O. Jagutzki, H. Schmidt-Böcking, *Review of Scientific Instruments* **2001**, *72*, 3968–3974.

[105] A. Guo, M. Burt, M. Brouard, *International Journal of Mass Spectrometry* **2018**, *429*, 121–126.

[106] K. Chughtai, R. M. Heeren, *Chemical Reviews* **2010**, *110*, 3237–3277.

[107] A. Kiss, J. H. Jungmann, D. F. Smith, R. M. Heeren, *Review of Scientific Instruments* **2013**, *84*.

[108] Wien filter - Wikipedia, **2022**.

[109] B. Winter, PhD thesis, University of Oxford, **2014**.

[110] J. Ladislas Wiza, *Nuclear Instruments and Methods* **1979**, *162*, 587–601.

[111] A. Jaworek, *Encapsulations* **2016**, 1–45.

[112] B. Winter, S. J. King, M. Brouard, C. Vallance, *Review of Scientific Instruments* **2014**, *85*.

[113] A. Nomerotski, Imaging and time stamping of photons with nanosecond resolution in Timepix based optical cameras, **2019**.

[114] R. Ballabriga, M. Campbell, E. H. M. Heijne, X. Llopart, L. Tlustos, *IEEE Transactions on Nuclear Science* **2007**, *54*.

[115] D. Niederlöhner, C. Bert, J. Giersch, K. F. Pfeiffer, G. Anton, *Nuclear Instruments and Methods in Physics Research Section A: Accelerators Spectrometers Detectors and Associated Equipment* **2003**, *509*, 138–145.

[116] A. Zhao, M. V. Beuzekom, B. Bouwens, D. Byelov, I. Chakaberia, C. Cheng, A. Nomerotski, P. Svihra, J. Visser, V. Vrba, T. Weinacht, A. Zhao, M. V. Beuzekom, B. Bouwens, D. Byelov, I. Chakaberia, C. Cheng, E. Maddox, A. Nomerotski, P. Svihra, J. Visser, V. Vrba, T. Weinacht, **2017**, *113104*.

[117] D. Turecek, J. Jakubek, P. Soukup, *Journal of Instrumentation* **2016**, *11*, C12065–C12065.

[118] H. Hazama, J. Aoki, H. Nagao, R. Suzuki, T. Tashima, **2008**, *255*, 1257–1263.

[119] D. A. Dahl, *International Journal of Mass Spectrometry* **2000**, *200*, 3–25.

[120] D. C. McGilvery, PhD thesis, La Trobe University, **1978**.

[121] S. Gil, M. Saleta, D. T. .-. A. J. o. Physics, u. 2002, *American Journal of Physics* **2002**, *70*, 440.

[122] M. Karas, R. Krüger, *Chemical reviews* **2003**, *103*, 427–439.

[123] R. C. Beavis, B. T. Chait, *Chemical Physics Letters* **1991**, *181*, 479–484.

[124] S. Berkenkamp, C. Menzel, F. Hillenkamp, K. Dreisewerd, *Journal of the American Society for Mass Spectrometry* **2002**, *13*, 209–220.

[125] W. Zhang, B. T. Chait, *International Journal of Mass Spectrometry and Ion Processes* **1997**, *160*, 259–267.

[126] M. S. Rafique, M. Khaleeq-Ur-Rahman, M. S. Anwar, F. M. A. Ashfaq, K. Siraj, *Laser and Particle Beams* **2005**, *23*, 131–135.

[127] M. Gluckmann, M. Karas, *Journal of Mass Spectrometry* **1999**, *34*, 467–477.

[128] E. Halford, B. Winter, M. D. Mills, S. P. Thompson, V. Parr, J. J. John, A. Nomerotski, C. Vallance, R. Turchetta, M. Brouard, *Rapid Communications in Mass Spectrometry* **2014**, *28*, 1649–1657.

[129] M. Mitchell, *An introduction to genetic algorithms*, MIT Press, **1996**.

[130] T. L. Colliver, C. L. Brummel, M. L. Pacholski, F. D. Swanek, A. G. Ewing, N. Winograd, *Analytical Chemistry* **1997**, *69*, 2225–2231.

[131] B. Winter, E. Halford, M. Brouard, *International Journal of Mass Spectrometry* **2013**, *356*, 14–23.

[132] F. H. Read, *Journal of Physics E: Scientific Instruments* **1970**, *3*, 127–131.

[133] T. Mulvey, M. J. Wallington, *Reports on Progress in Physics* **1973**, *12*, 74–81.

[134] F. H. Read, *Journal of Physics E: Scientific Instruments* **1983**, *16*, 636–642.

[135] I. Sedgwick, A. Clark, J. Crooks, R. Turchetta, L. Hill, J. J. John, A. Nomerotski, R. Pisarczyk, M. Brouard, S. H. Gardiner, E. Halford, J. Lee, M. L. Lipciuc, C. Slater, C. Vallance, E. S. Wilman, B. Winter, W. H. Yuen, *10th International New Circuits and Systems Conference* **2012**, 497–500.

[136] R. Ballabriga, M. Campbell, X. Llopart, *Nuclear Inst. and Methods in Physics Research A* **2017**, *878*, 10–23.

[137] V. Gromov, M. Van Beuzekom, R. Kluit, F. Zappon, V. Zivkovic, M. Campbell, T. Poikela, X. Llopart, C. Brezina, K. Desch, X. Fang, A. Kruth, *Proceedings of Science* **2011**, 046.

[138] J. Jakubek, T. Holy, E. Lehmann, S. Pospisil, J. Uher, J. Vacik, D. Vavrik, *Nuclear Instruments and Methods in Physics Research Section A: Accelerators Spectrometers Detectors and Associated Equipment* **2006**, *560*, 143–147.

[139] A. Rosenfeld, S. Alnaghy, M. Petasecca, D. Cutajar, M. Lerch, S. Pospisil, V. Giacometti, R. Schulte, V. Rosso, M. Würl, C. Granja, M. Martišíková, K. Parodi, *Radiation Measurements* **2020**, *130*, 106211.

[140] O. Siegmund, J. Vallerga, J. McPhate, A. H. Tremsin Oswald W Siegmund, J. V. Vallerga, J. B. McPhate, O. H. Siegmund, J. Vallerga, J. McPhate, A. Tremsin in SPIE 5488, UV and Gamma-Ray Space Telescope Systems, *Vol. 5488*, SPIE, **2004**, pp. 789–800.

[141] M. Fisher-Levine, A. Nomerotski, *Journal of Instrumentation* **2016**, *11*, C03016.

[142] A. Nomerotski, I. Chakaberia, M. Fisher-Levine, Z. Janoska, P. Takacs, T. Tsang, *Journal of Instrumentation* **2017**, *12*, 01017–01017.

[143] A. Zhao, M. V. Beuzekom, B. Bouwens, D. Byelov, I. Chakaberia, C. Cheng, A. Nomerotski, P. Svihra, J. Visser, V. Vrba, T. Weinacht, A. Zhao, M. V. Beuzekom, B. Bouwens, D. Byelov, I. Chakaberia, C. Cheng, E. Maddox, A. Nomerotski, P. Svihra, J. Visser, V. Vrba, T. Weinacht, **2017**, *113104*, DOI `10.1063/1.4996888`.

[144] A. Nomerotski, I. Chakaberia, M. Fisher-Levine, Z. Janoska, P. Takacs, T. Tsang, *Journal of Instrumentation* **2017**, *12*, C01017.

[145] B. V. D. Heijden, J. Visser, M. V. Beuzekom, H. Boterenbrood, S. Kulis, B. Munneke, F. Schreuder, *Journal of Instrumentation* **2017**, *12*, C02040.

[146] F. Pedregosa, V. Michel, O. Grisel, M. Blondel, P. Prettenhofer, R. Weiss, J. Vanderplas, D. Cournapeau, F. Pedregosa, G. Varoquaux, A. Gramfort, B. Thirion, O. Grisel, V. Dubourg, A. Passos, M. Brucher, M. Perrot andÉdouardand, a. Duchesnay, F. Duchesnay, *Journal of Machine Learning Research* **2011**, *12*, 2825–2830.

[147] S. P. Lloyd, *IEEE Transactions on Information Theory* **1982**, *28*, 129–137.

[148] C. Ponchut, M. Ruat, *Journal of Instrumentation* **2013**, *8*.

[149] O. Veledar, S. Danaher, J. Allen, P. Byrne, L. Thompson, *Journal of University of Applied Sciences* **2005**, *9*, 3–6.

[150] G. Arentz, P. Mittal, C. Zhang, Y. Y. Ho, M. Briggs, L. Winderbaum, M. K. Hoffmann, P. Hoffmann, *Advances in Cancer Research* **2017**, *134*, 27–66.

[151] Thor Labs, Spatial Filters Tutorial, **2023**.

[152] Harryson Skelly, Optimisation of Pulsed Extraction in Microscope-Mode Imaging Mass Spectrometers, **2022**.

[153] Anya Eyres, Investigations into microscope mode imaging mass spectrometry, **2021**.

[154] T. K. Yong, Y. Y. Kee, S. S. Tan, S. S. Yap, W. O. Siew, T. Y. Tou, *Applied Physics A: Materials Science and Processing* **2010**, *101*.